Protection of Multi-Terminal HVDC Grids

by

Mohamed Radwan

A thesis
presented to the University of Waterloo
in fulfillment of the
thesis requirement for the degree of
Doctor of Philosophy
in
Electrical and Computer Engineering

Waterloo, Ontario, Canada, 2025

© Mohamed Radwan 2025

Examining Committee Membership

The following served on the Examining Committee for this thesis. The decision of the Examining Committee is by majority vote.

External Examiner:	Prof. Houshang Karimi Professor, Dept. of ECE, York University
Supervisor:	Prof. Sahar Pirooz Azad Assistant Professor, Dept. of ECE, University of Waterloo
Internal Member:	Prof. Mehrdad Kazerani Professor, Dept. of ECE, University of Waterloo
Internal Member:	Prof. Sheshakamal Jayaram Professor, Dept. of ECE, University of Waterloo
Internal-External Member:	Prof. Eihab Abdel-Rahman Professor, Dept. of SYDE, University of Waterloo

Author's Declaration

I hereby declare that I am the sole author of this thesis. This is a true copy of the thesis, including any required final revisions, as accepted by my examiners.

I understand that my thesis may be made electronically available to the public.

Abstract

Aligned with the United Nations' goals of providing affordable and clean energy, achieving net-zero carbon emissions, and mitigating climate change, converter-interfaced renewable energy sources (RESs), such as offshore wind farms, are increasingly integrated into modern power systems. Integrating RESs into the main power grid through high-voltage direct current (HVDC) links presents a promising alternative to traditional high-voltage alternating current (HVAC) transmission systems, particularly over long distances. HVDC links also enable the interconnection of large AC grids operating at different frequencies. Multi-terminal HVDC grids can harvest diversified renewable generations from distant locations and achieve more reliable and robust networks such that unified supergrids can be realized. However, protection of HVDC grids remains a critical challenge, requiring continuous advancements to ensure a highly secure multi-terminal grid resilient to severe fault conditions. DC faults result in a greater risk than AC faults due to the rapid increase of fault current. As a result, HVDC protection schemes must swiftly and accurately detect and differentiate between internal and external faults within a few milliseconds.

HVDC protection schemes are generally classified based on reliance on remote-end data into single-ended (communication-less) and double-ended (communication-based) schemes. This thesis first presents a comprehensive review of the proposed protection schemes in the literature, analyzing and comparing them to highlight their strengths and limitations. The review demonstrates that single-ended schemes are optimal for providing fast primary protection, as they avoid the communication delays inherent in double-ended schemes. In contrast, double-ended schemes are better suited for fault location identification and backup protection schemes.

This thesis next introduces four novel protection schemes for multi-terminal HVDC grids: primary protection, fault location identification, and breaker/relay failure backup protection schemes. The proposed single-ended primary protection scheme employs Hilbert-Huang Transform (HHT) to extract two instantaneous features from local voltage measurements, namely the instantaneous frequency and energy. Abrupt changes in these features during internal faults are detected as outliers. Simultaneous outliers in the extracted features correspond to internal faults, which offers a setting-less fault detection criterion; thus, eliminating the need for simulation-based and grid-specific thresholds. The proposed double-ended fault location identification scheme employs the setting-less outlier-based criterion to capture the arrival instants of the initial fault-induced backward traveling waves (BTWs) at both line terminals, based on which the fault location is identified with high precision.

Primary protection failure can occur when corresponding breakers fail to clear the fault, *breaker failure*, or the primary relay fails to detect the fault, *relay failure*. The basic principle of the proposed single-ended breaker failure backup protection scheme is that a successful breaker trip is always associated with a sudden increase in local voltage measurements corresponding to the counter voltage generated across the breaker during its operation. Therefore, the proposed scheme employs the outlier-based criterion to detect abrupt changes in local voltage measurements, distinguishing between successful breaker operation and breaker failure. On the other hand, the proposed single-ended relay failure backup protection scheme provides local backup protection for internal and reverse external faults. The proposed scheme employs Bayesian Model Averaging (BMA) to reliably and rapidly detect the fault event. Then, the polarity of the local faulted-pole or zero-mode current is utilized to discriminate between internal, forward, and reverse external faults.

Numerous simulations in PSCAD/EMTDC software environment for a four-terminal HVDC grid are executed to demonstrate the rapid and reliable performance of the proposed schemes under various fault conditions, including critical internal faults, *e.g.*, remote-end high-resistance faults, and severe external faults, *e.g.*, solid bus faults. In addition, real-time experimental validation of the proposed primary protection scheme is executed via a hardware-in-the-loop test setup which consists of the OPAL-RT OP5700 target (where the HVDC grid is implemented) and the dSPACE MicroLabBox controller (which acts as the physical primary relay).

Acknowledgements

I would like to express my deepest gratitude to my supervisor, Prof. Sahar Azad, for her invaluable guidance, continuous support, and mentorship throughout my research journey. Her insightful advice, patience, and encouragement have been instrumental in shaping both my academic and professional growth.

I also sincerely thank the respected committee members for their time, effort, and valuable comments. It has been an honor for me to finish my thesis with their support and feedback.

Lastly, I extend my heartfelt appreciation to my family for their unwavering support and encouragement. Their patience and sacrifices have been a constant source of motivation throughout this journey. A special thanks goes to my fabulous kids, Yahia and Hamza, whose laughter and playful energy provided a much needed source of joy and relief from any stresses during my PhD journey. Some of their smiles were more than enough to relieve any stress and recharge for the next day, making even the most challenging moments of this journey more rewarding.

Dedication

To my parents, my sister, my wife, and my kids.

Table of Contents

Examining Committee ii

Author's Declaration iii

Abstract iv

Acknowledgements vi

Dedication vii

List of Figures xiii

List of Tables xviii

List of Abbreviations xx

List of Symbols xxiii

1 Introduction 1

1.1 Background 1

1.2 Protection of Multi-terminal HVDC Grids 4

1.2.1 HVDC protection system requirements 5

1.2.2 Classification of HVDC grid protection schemes 6

1.3 Statement of the Problem 7
1.4 Research Objectives 7
1.5 Research Methodology 8
1.6 Thesis Outline 8

2 Literature Review **9**
2.1 Introduction 9
2.2 Fundamentals of DC faults 9
2.2.1 DC fault stages 10
2.2.2 DC fault clearing philosophies 14
2.3 HVDC grid protection schemes 17
2.3.1 Primary protection schemes 17
2.3.2 Backup protection schemes 19
2.4 Double-ended schemes 19
2.4.1 Differential protection schemes 19
2.4.2 Directional protection schemes 20
2.4.3 Comparison between double-ended schemes 24
2.5 Single-ended schemes 26
2.5.1 Voltage derivative-based schemes 27
2.5.2 Current derivative-based schemes 27
2.5.3 Transient schemes based on voltage and current measurements . . . 28
2.5.4 Boundary reactor-based schemes 29
2.5.5 Traveling wave-based schemes 30
2.5.6 Artificial intelligence-based schemes 31
2.5.7 Special non-unit schemes 32
2.5.8 Comparison between single-ended schemes 32
2.6 Conclusion 35

3 Primary Protection Scheme **36**
3.1 Introduction . . . 36
3.2 Fault-Induced Traveling Waves and Hilbert-Huang Transform . . . 37
3.2.1 Propagation of Traveling Waves . . . 38
3.2.2 Hilbert-Huang Transform . . . 39
3.3 Test Grid . . . 42
3.4 Internal Fault Signature Based on HHT . . . 42
3.4.1 Internal Faults . . . 43
3.4.2 External Faults . . . 45
3.5 Proposed Fault Detection Algorithm . . . 49
3.6 Simulation Results . . . 54
3.6.1 Internal Faults . . . 54
3.6.2 External Faults . . . 56
3.6.3 Impact of Measurement Noise . . . 58
3.6.4 Comparison with Other Schemes . . . 59
3.7 Conclusion . . . 61

4 Fault Location Identification Scheme **63**
4.1 Introduction . . . 63
4.2 Traveling Wave Propagation Theory . . . 64
4.3 Fault Analysis With Hilbert-Huang Transform . . . 65
4.3.1 Test Grid . . . 66
4.3.2 Instantaneous Features Extraction By HHT . . . 66
4.4 Proposed Fault Location Identification Scheme . . . 68
4.5 Simulation Results . . . 69
4.5.1 Solid Internal Faults . . . 70
4.5.2 Fault Resistance Coverage . . . 70
4.5.3 Comparison . . . 71
4.6 Conclusion . . . 72

5 Breaker Failure Backup Protection Scheme **74**
5.1 Introduction . . . 74
5.2 Breaker Failure Backup Protection Scheme . . . 76
5.2.1 Test System . . . 76
5.2.2 Local Voltage Measurement During Breaker Operation . . . 77
5.2.3 IF and IE During Breaker Operation . . . 78
5.2.4 Outlier Detection . . . 78
5.2.5 Proposed Scheme . . . 80
5.3 Simulation Results . . . 80
5.3.1 Fault Location . . . 81
5.3.2 Fault Resistance . . . 86
5.3.3 Boundary Reactors . . . 88
5.3.4 Impact of Measurement Noise . . . 88
5.3.5 Applicability to Other HVDC Grids . . . 89
5.3.6 Comparison with Existing Breaker Failure Backup Protection Schemes 91
5.4 Conclusion . . . 93

6 Relay Failure Backup Protection Scheme **95**
6.1 Introduction . . . 95
6.2 HVDC Test Grid . . . 98
6.3 Fault Detection Component . . . 98
6.4 Fault Directional Component . . . 105
6.5 Proposed Relay Failure Backup Protection Scheme . . . 108
6.6 Simulation Results . . . 111
6.6.1 Performance of the proposed relay failure scheme . . . 111
6.6.2 Sensitivity to the size of boundary reactors . . . 114
6.6.3 Sensitivity to measurement noise . . . 114
6.6.4 Comparison with existing schemes . . . 114
6.7 Breaker Failure Detection Based on BMA . . . 116
6.8 Conclusion . . . 123

7 Real-Time Experimental Validation **126**
7.1 Introduction 126
7.2 Experimental Setup 127
7.3 Experimental Results 130
7.4 Conclusion 140

8 Conclusion and Future Work **141**
8.1 Summary 141
8.2 Contributions 143
8.3 Future Work 144

References **145**

APPENDICES **164**

A List of Publications **165**
A.1 Peer-Reviewed Journal Articles 165
A.2 Conference Proceedings 166
A.3 Submitted Journal Articles 166
A.4 Submitted Conference Papers 166

List of Figures

1.1 Various HVDC transmission schemes. 2
1.2 Protection requirements for HVDC grids. 5

2.1 Four-terminal HVDC test grid. 11
2.2 Positive-pole current during various stages of a DC fault. 12
2.3 RLC equivalent circuit of a half-bridge MMC. 13
2.4 Protection zones of various fault clearing strategies. 15
2.5 Typical mechanical DCCB topologies. 16
2.6 An IGBT-based solid-state DCCB. 16
2.7 A hybrid DCCB. 16
2.8 Classification of HVDC grid protection schemes. 18

3.1 Simplified steps of the EMD sifting process. 40
3.2 Four-terminal HVDC test grid. 42
3.3 V_{13_p} and the corresponding features for F_1. 44
3.4 V_{13_p} and the corresponding features for F_1 with $R_F = 1000\ \Omega$. 45
3.5 V_{13_p} and the corresponding features for F_1 with $SNR = 40\ db$. 45
3.6 EMD of V_{13_p} and the corresponding extracted features for various internal faults along cable 13. 46
3.7 V_{13_p} and the corresponding features for a forward external fault F_2. 47
3.8 V_{13_p} and the corresponding features for a reverse external fault F_3. 47

3.9 V_{13_p} and the corresponding features for F_2 with $L_{dc} = 25\ mH$. 48
3.10 V_{13_p} and the corresponding features for F_3 with $L_{dc} = 25\ mH$. 48
3.11 V_{13_p}, V_{34_p}, and the corresponding features for F_2 considering breaker operation. 49
3.12 V_{13_p} and the corresponding features during the change of the reference DC voltage. 49
3.13 Flowchart of the proposed primary protection scheme. 50
3.14 V_{13_p}, FF_p, and the detect outliers in $IF(t)$ and $IE(t)$ during the fault F_1. . 52
3.15 The extracted instantaneous features and detected outliers for F_1 with various window lengths. 53
3.16 Operating time for various solid PTP faults along cable 13. 55
3.17 Operating time for F_1 with R_F changing from 0.01 Ω to 1000 Ω. 55
3.18 Operating time for a PTP fault at 200 km from bus 1 with R_F changing from 0.01 Ω to 1000 Ω. 55
3.19 $IF(t)$ & $IE(t)$ for external faults under various boundary reactor sizes. . . 57

4.1 Propagation of the fault-induced TWs. 65
4.2 Test Grid. 66
4.3 V_{13_p} and the corresponding features extracted at R_{13} for F_1. 67
4.4 V_{31_p} and the corresponding features extracted at R_{31} for F_1. 67
4.5 Detected outliers at relays and captured arrival instants of BTWs. 68
4.6 Flowchart of the proposed fault location scheme of R_{13}. 69

5.1 Four-terminal HVDC test grid. 76
5.2 Breaker Failure Backup protection system of cable 13. 77
5.3 Positive-pole voltage waveform during successful breaker trip and breaker failure. 78
5.4 The extracted instantaneous features of V_{13_p} and detected outliers during successful breaker trip and breaker failure. 79
5.5 Proposed breaker failure backup protection scheme. 81

5.6 A solid PTP fault at the beginning of cable 13 during successful and unsuccessful breaker trip. 82
5.7 A solid PTP fault at the end of cable 13 during successful and unsuccessful breaker trip. 83
5.8 Instantaneous features and detected outliers under various window sizes for a fault at 0.7 s on cable 13, 50 km from Bus 1. 85
5.9 A PTP fault at the middle of cable 13 with $R_F = 1500\ \Omega$ during successful and unsuccessful breaker trip. 86
5.10 A PTP fault at the end of cable 13 with $R_F = 1500\ \Omega$ during successful and unsuccessful breaker trip. 87
5.11 A solid PTP fault at the middle of cable 13 with a boundary reactor of 10 mH during successful and unsuccessful breaker trip. 89
5.12 A solid PTP fault at the middle of cable 13 with a 40 db white Gaussian noise during successful and unsuccessful breaker trip. 90
5.13 Two-terminal HVDC test grid. 91
5.14 A solid PPTG fault at the middle of the line during successful and unsuccessful breaker trip. 92

6.1 Four-terminal HVDC test grid. 98
6.2 BMA performance during normal operation and an internal PPTG fault at the remote end of cable 13 with $R_F = 1500\ \Omega$. 102
6.3 BMA performance during a solid forward external PPTG fault at the beginning of cable 34. 103
6.4 BMA performance during a solid reverse external PPTG fault at the beginning of cable 12. 104
6.5 Zero-mode current waveforms under internal, forward, and reverse external PPTG faults. 106
6.6 Positive-pole current waveforms under internal, forward, and reverse external PTP faults. 107
6.7 Proposed relay failure backup protection scheme. 109
6.8 BMA optimal model and detected change points for a 5% drop in the reference DC voltage at Bus 1. 110

6.9 BMA performance during successful breaker operation for a solid forward external PPTG fault at the middle of cable 34. 110

6.10 Positive-pole voltage waveform and corresponding BMA models during successful breaker trip and breaker failure. 118

6.11 Proposed BMA-based breaker failure backup protection scheme. 119

6.12 Performance of the proposed BMA-based breaker failure scheme during a solid PPTG fault at the beginning of cable 13 with successful breaker trip and failure. 120

6.13 Performance of the proposed BMA-based breaker failure scheme during a solid PPTG fault at the end of cable 13 with successful breaker trip and failure. 121

6.14 Performance of the proposed BMA-based breaker failure scheme during a PTP fault at the end of cable 13 with $R_F = 1500\ \Omega$ with successful breaker trip and failure. 122

6.15 Performance of the proposed BMA-based breaker failure scheme during a solid PTP fault at the middle of cable 13 with $L_{dc} = 10\ mH$ with successful breaker trip and failure. 123

6.16 Performance of the proposed BMA-based breaker failure scheme during a solid PTP fault at the middle of cable 13 with $SNR = 30\ db$ with successful breaker trip and failure. 124

7.1 Experimental HIL test setup layout. 128

7.2 HIL test setup. 129

7.3 Simplified representation of the experimental setup. 130

7.4 Real-time positive-pole voltage and corresponding trip signal during a solid PTP fault at the beginning of cable 13. 132

7.5 Real-time positive-pole voltage and corresponding trip signal during a solid PTP fault at the middle of cable 13. 133

7.6 Real-time positive-pole voltage and corresponding trip signal during a solid PTP fault at the end of cable 13. 134

7.7 Real-time positive-pole voltage and corresponding trip signal during a PTP fault at the middle of cable 13 with $R_F = 200\ \Omega$. 135

7.8 Real-time positive-pole voltage and corresponding trip signal during an external PTP fault at the beginning of cable 34. 136

7.9 Positive-pole voltage drop during internal and external faults. 137

7.10 HIL real-time positive-pole voltage and corresponding trip signal during a solid PTP fault at the middle of cable 13. 138

7.11 HIL real-time positive-pole voltage and corresponding trip signal during a solid PTP fault at the end of cable 13. 139

7.12 Offline positive-pole voltage during a solid PTP fault at the end of cable 13. 140

List of Tables

1.1 Existing HVDC Projects Overview. 3
1.2 Comparison between LCCs and VSCs. 4

2.1 Common roots of DC faults. 10
2.2 Comparison between existing double-ended protection schemes. 25
2.3 Comparison between existing single-ended protection schemes. 33

3.1 Test grid parameters 43
3.2 Performance of the proposed scheme in the presence of measurement noise 59
3.3 Comparison between the proposed scheme and existing schemes 60

4.1 Fault location calculated by the proposed scheme for various solid internal faults 70
4.2 Fault location calculated by the proposed scheme for various non-solid internal faults 71
4.3 Comparison between the proposed scheme and the existing double-ended schemes 72

5.1 Detection time of successful operation of B_{13} for various fault locations . . 84
5.2 Comparison between the proposed scheme and existing breaker failure backup protection schemes 93

6.1 Performance of the proposed relay failure backup protection scheme under various internal faults 112

6.2 Performance of the proposed relay failure backup protection scheme under various external faults 113
6.3 Performance of the proposed relay failure backup protection scheme under different boundary conditions 115
6.4 Performance of the proposed relay failure backup protection scheme under different noise levels 116
6.5 Comparison between the proposed scheme and existing relay failure backup protection schemes 117

List of Abbreviations

ACCBs AC circuit breakers 14

AFC amplitude-frequency coefficient 64

ANNs artificial neural networks 31

BMA Bayesian Model Averaging 97

BTWs backward traveling waves 63

CNN convolutional neural network 31

DCCBs direct current circuit breakers 4

DFT Discrete Fourier Transform 23

DSPs digital signal processors 91

DWT Discrete Wavelet Transform 20

EMD empirical mode decomposition 39

ENTSO-E European network of transmission system operators for electricity 9

FCFH first carrier frequency harmonic 23

FDI fault detection and identification 28

FFT Fast Fourier Transform 30

FPT first peak time 28

GFS Genetic Fuzzy System 31

HD Hausdorff Distance 23

HHT Hilbert-Huang Transform 23

HIL hardware-in-the-loop 8

HSSs high-speed switches 14

HVDC High-Voltage Direct Current 1

IGBT insulated-gate bipolar transistor 12

IMFs intrinsic mode functions 39

IZSV instantaneous zero-sequence voltage 30

LCCs line-commutated converters 3

LCL inductor-capacitor-inductor 20

LCS load commutation switch 16

MAD Median Absolute Deviation 32

MCMC Markov Chain Monte Carlo 99

MG Morphological Gradient 23

MHS marginal Hilbert spectrum 31

MMCs Modular multilevel converters 3

MMG Multi-resolution Morphological Gradient 23

MOVs metal-oxide varistors 14

MUWD morphological undecimated wavelet decomposition 96

NPTG negative-pole-to-ground 51

PCA Principal Component Analysis 31

PEI Princess Elisabeth Island 1

PMT Phase-Modal Transformation 31

PPTG positive-pole-to-ground 51

PTG pole-to-ground 5

PTP pole-to-pole 5

RESs renewable energy resources 1

RMT random matrix theory 32

ROCOC rate-of-change-of-current 27

ROCOV rate-of-change-of-voltage 27

ROTV ratio of the transient voltages 28

RTI real-time interface 127

SATD surge arrival time difference 31

SNR signal-to-noise ratio 44

STFT Short-Time Fourier Transform 30

SWT Stationary Wavelet Transform 22

TEs transient energies 22

TSOs transmission system operators 9

TW traveling wave 11

UFD ultra-fast disconnector 16

VSCs voltage-sourced converters 3

WPEE wavelet packet energy entropy 96

WTMM Wavelet Transform Modulus Maximum 21

List of Symbols

BR_{13} Backup relay at the beginning of cable 13. 98

C_{eq} MMC equivalent capacitance. 12

FF Fault flag. 50

F_1 A solid internal PTP fault located at the middle of cable 13. 11

F_2 A solid forward external PTP fault located at the middle of cable 34. 45

F_3 A solid reverse external PTP fault located at the middle of cable 12. 45

$IE(t)$ Instantaneous energy. 39

$IF(t)$ Instantaneous frequency. 39

I_{13_p} Positive-pole current waveform measured by the local relay R_{13}. 11

L_{arm} MMC arm inductance. 13

L_{dc}^{min} Minimum boundary inductance per pole. 13

L_{eq} MMC equivalent inductance. 12

M Number of candidate models. 99

N_{SM} Number of submodules of an MMC arm. 12

P_{AC} Probability of detecting an abrupt change. 101

$P_{set,1}$ A threshold used to distinguish between fault events and non-fault conditions. 101

$P_{set,2}$ A threshold used to discriminate between internal and forward external faults. 108

P_{set} A threshold used to distinguish between successful breaker operation and breaker failure. 117

R_{13} Local relay at the beginning of cable 13. 11, 66

R_{31} Remote relay at the end of cable 13. 66

R_{arm} MMC arm resistance. 12

R_{eq} MMC equivalent resistance. 12

R_{on} On-state resistance of an MMC submodule. 12

S_{NPTG} Fault direction during NPTG faults. 105

S_{PPTG} Fault direction during PPTG faults. 105

S_{PTP} Fault direction during PTP faults. 106

$T_{elapsed}$ The time delay of the breaker failure backup protection scheme. 80

V_{R_p} Rectifier-side positive-pole voltage. 90

V_{set} Undervoltage threshold. 51

V_{13_p} Positive-pole voltage waveform measured by the local relay R_{13}. 43, 66, 77

V_{31_p} Positive-pole voltage waveform measured by the remote relay R_{31}. 66

V_{34_p} Positive-pole voltage waveform measured by the local relay at the beginning of cable 34. 48

Y Per unit shunt admittance of the line. 38

Z Per unit series impedance of the line. 38

Z_c Characteristic impedance of the line. 39

i_0 Zero-mode current. 105

i_1 Line-mode current. 105

i_b Backward current TW. 39

i_f Forward current TW. 39

i_n Negative-pole current. 105

i_p Positive-pole current. 105

m Number of change points in the voltage waveform. 99

$r_n(t)$ EMD residue. 40

t_1 Arrival instant of the first fault-induced BTW at R_{13}. 65

t_2 Arrival instant of the first fault-induced BTW at R_{31}. 65

t_c Permissible fault clearing time. 13

t_d The time difference between t_o and t_f. 84

t_f The time instant when the fault is detected by the primary relay and a trip signal is sent to the primary breaker. 84

t_o The time instant when simultaneous outliers in $IF(t)$ and $IE(t)$ are detected indicating successful breaker operation. 84

t_{ac} Time instant when the AC infeed stage commences. 11

t_{dis} Time instant when the capacitor discharge stage commences following fault occurrence. 11

t_{ind} Time instant when the inductive discharge stage commences. 11

t_{cp_r} Time instants associated with the model change points. 99

v_b Backward voltage TW. 39

v_f Forward voltage TW. 39

x Estimated fault location. 65

x_{act} Actual fault location. 70

$z(t)$ Complex-valued signal. 39

ξ_{PTG} Zero-mode current polarity during PTG faults. 105

ξ_{PTP} Positive-pole current polarity during PTP faults. 106

ν_{TW} TW propagation velocity. 39

γ TW propagation constant. 38

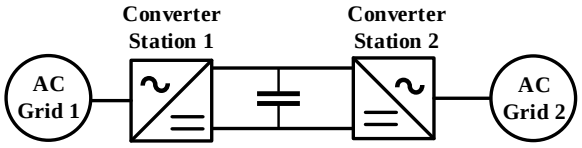
Chapter 1

Introduction

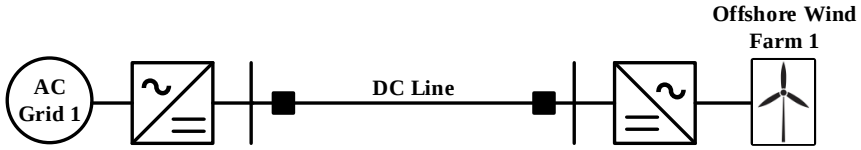
1.1 Background

High-Voltage Direct Current (HVDC) corridors play an essential role in integrating renewable energy resources (RESs), harvesting their power, and feeding it into the power grid, especially offshore wind farms which are interconnected to the onshore grid via submarine HVDC cables [1,2]. Furthermore, grid stability issues resulting from uncertainty, volatility, and intermittency of wind energy sources become more controllable with HVDC interconnections rather than direct AC interconnections [3]. Moreover, the distance between the offshore wind platform and the onshore interfacing point of connection adds another restriction on utilizing submarine AC cables since their charging currents increase for long distances and the compensation cost for these currents will be high, whereas submarine DC cables have nearly negligible charging currents [4]. An example of such an offshore wind harvesting HVDC grid is the proposed Princess Elisabeth Island (PEI) energy hub project, which is intended to collect up to 3.5 GW of offshore wind power over the Belgium's North Sea [5].

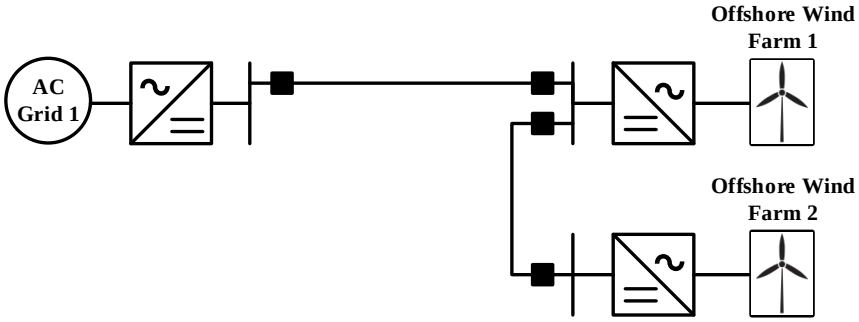
HVDC networks can be established in different configurations: 1) a simple back-to-back connection (Figure 1.1a) which is the perfect candidate in case of interconnecting asynchronous grids; 2) point-to-point links (Figure 1.1b) that enable bulk power transfer between two distant terminals; 3) multi-terminal HVDC grids with two configurations, i.e., star-connected (Figure 1.1c) terminals and meshed grids (Figure 1.1d). Multi-terminal HVDC grids are increasingly adopted in existing HVDC projects and will be further used in future projects since they permit more power transfer capability, increased system reliability, interconnecting large scale renewable resources located at different locations, and



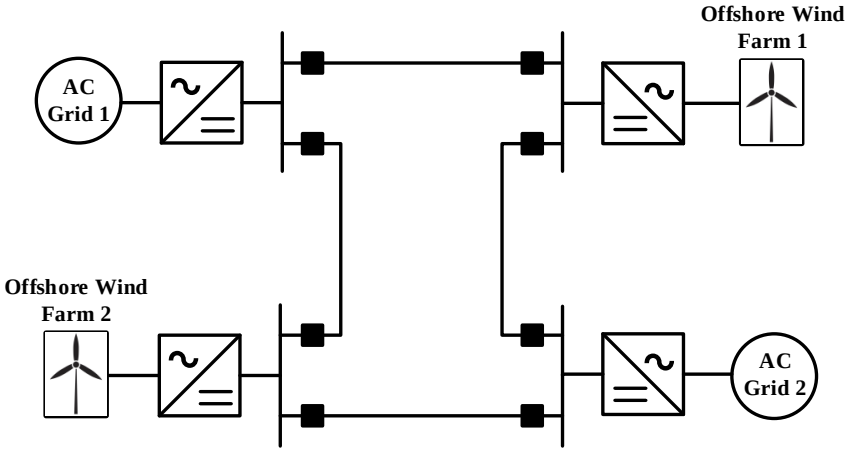
(a) A back-to-back connection.



(b) A point-to-point (two-terminal) link.



(c) A three-terminal star-connected grid.



(d) A four-terminal meshed grid.

Figure 1.1: Various HVDC transmission schemes.

Table 1.1: Existing HVDC Projects Overview.

HVDC Project	Country	Commissioning Year	Capacity	DC Voltage Level	Grid Configuration	Number of Terminals
SunZia [9]	USA	2025	3 GW	$\pm$525 kV	Point-to-point	Two
Greenlink [10]	UK/Ireland	2024	500 MW	$\pm$320 kV	Point-to-point	Two
Zhangbei [11]	China	2021	4.5 GW	$\pm$500 kV	Meshed	Four
NordLink [12]	Germany/ Norway	2021	1.4 GW	$\pm$525 kV	Point-to-point	Two
North Sea Link [13]	Norway/UK	2021	1.4 GW	$\pm$525 kV	Point-to-point	Two
Wudongde [14]	China	2020	8 GW	$\pm$800 kV	Star-connected	Three
Changji-Guquan [15]	China	2019	12 GW	$\pm$1100 kV	Point-to-point	Two
Maritime Link [16]	Canada	2018	500 MW	$\pm$200 kV	Point-to-point	Two
Zhoushan [17]	China	2014	1 GW	$\pm$200 kV	Meshed	Five
Nan'ao [18]	China	2013	200 MW	$\pm$160 kV	Star-connected	Three

they are considered as the key solution to realize future supergrids [6]. Supergrids refer to large-scale, cross-border transmission networks that interconnect multiple countries or regions using high-capacity, long-distance HVDC links to integrate renewable energy sources and enhance grid flexibility, reliability, and market integration [7]. Numerous HVDC projects have been installed and commissioned worldwide varying from point-to-point connections to multi-terminal HVDC grids. China and Europe possess the dominant share of these projects. For example, the Chinese power utility is recognized as the largest hybrid (AC/DC) grid worldwide with more than 50 HVDC projects in service and a capacity of greater than 70 GW [8]. Table 1.1 presents a brief overview of a selected number of large existing HVDC projects.

HVDC systems can be classified based on the converter technology into line-commutated converters (LCCs) and voltage-sourced converters (VSCs). VSCs exhibit various operational merits over LCCs as highlighted in Table 1.2 [19, 20]. In addition, the constant DC link voltage of VSCs facilitates their parallel operation which is an important feature to build multi-terminal HVDC grids. Modular multilevel converters (MMCs) are extensively exploited in recent HVDC projects and will be used in future projects due to their notable features, such as modularity, scalability, low switching frequency and losses, and low filtering requirements [21–24].

Table 1.2: Comparison between LCCs and VSCs.

Comparison Aspect	**LCCs**	**VSCs**
Semiconductor Switch	Thyristor	IGBT
Switch Controllability	semi-controllable	fully-controllable
Commutation Failure	Yes	No
DC Link	fixed current direction	fixed voltage polarity
Power Reversal	slow (requires voltage reversal)	simple and fast (no need for voltage reversal)
Harmonics	low-order harmonics	high-order harmonics
Filter Size	large	small
Active and Reactive Power Control	coupled control	decoupled control
Reactive Compensation Requirement	Yes	No
Reactive Support Provision	No	Yes
Black-Start Capability	No	Yes

1.2 Protection of Multi-terminal HVDC Grids

Protection is one of the major obstacles in realizing reliable and secure multi-terminal HVDC grids. Implementation of a reliable, sensitive, and selective protection system for HVDC networks is more challenging as compared to conventional AC systems since DC faults result in a large and nearly instantaneous rise of the DC current which has no zero-crossings. The large DC fault current is due to the low-impedance, low-inertia of HVDC networks and the rapid discharge rate of the converters' capacitors. This issue imposes stringent constraints on the fault clearing time to be in the range of a few milliseconds, e.g., 6 ms for the Zhangbei HVDC project [25], including 3 ms for the fault interruption process. Therefore, the design of ultra-fast protection schemes along with fast fault current interrupters such as direct current circuit breakers (DCCBs) is essential for the secure operation of HVDC grids.

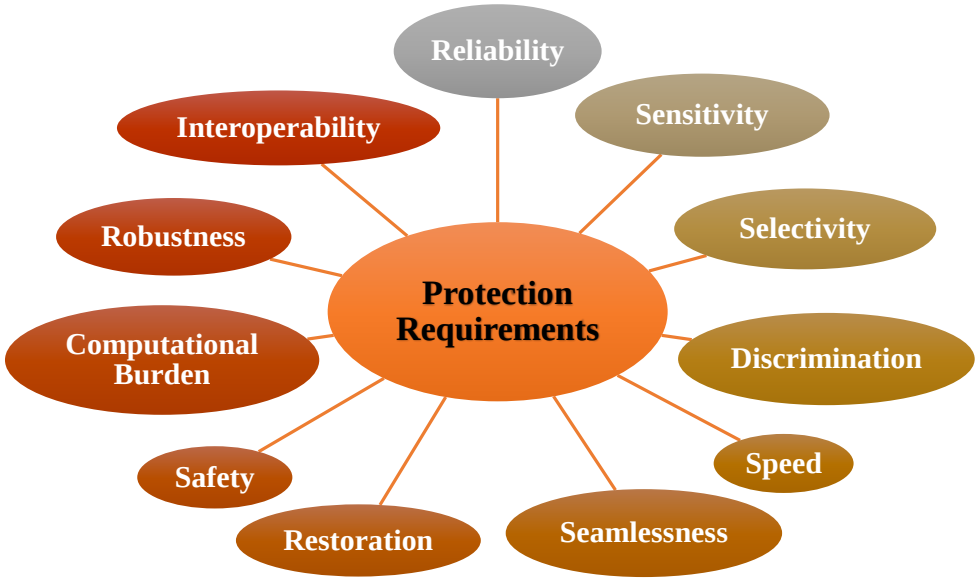


Figure 1.2: Protection requirements for HVDC grids.

1.2.1 HVDC protection system requirements

As HVDC systems expand from point-to-point interconnections to multi-terminal grids, protection requirements become more stringent and challenging to be fulfilled. The fundamental protection principles that must be satisfied for multi-terminal HVDC protection schemes are depicted in Figure 1.2 and demonstrated as follows [26–28]:

- **Reliability:** a reliable DC protection system should be dependable, i.e., operate correctly when required in case of all intended faults, and secure, i.e., do not operate incorrectly in case of unintended faults or normal operating condition.
- **Sensitivity:** the protection algorithm should be sensitive to all internal fault scenarios, including severe faults such as solid close faults and high-resistance faults.
- **Selectivity:** defined as the ability of the protection scheme to accurately identify the faulted segment and distinguish between internal and external faults.
- **Discrimination:** the protection algorithm should be able to distinguish between forward and reverse faults, identify the fault type (pole-to-pole (PTP) or pole-to-ground (PTG)), and determine the faulty pole in case of PTG faults.

- **Speed:** the protection scheme should initiate a trip signal, in case of internal faults, within a few milliseconds in order to prevent damages to converters' semiconductor switches with limited overcurrent capabilities. Furthermore, fast fault tripping is mandatory to ensure fault clearing before converters are blocked due to overcurrent or undervoltage conditions; thus, avoiding any current contribution from the AC-side towards the fault.

- **Seamlessness:** defined as the ability of the protection scheme to facilitate the stable and secure operation of the remaining healthy portion of the grid after clearing the faulted segment in case of permanent faults.

- **Restoration:** defined as the ability of the employed control and protection system to quickly restore the pre-fault stable operation of the system.

- **Robustness:** defined as the capability of the protection scheme to detect all fault events and distinguish them from other non-fault severe conditions such as power swings under different operating modes.

- **Computational Burden:** the proposed protection algorithm should detect the fault with minimum computations and sampling rates to comply with the stringent protection speed requirement.

- **Safety:** the utilized protection system should provide a safe protective shield for system components and personnel, besides ensuring public safety.

- **Interoperability:** defined as the adaptability of the protection scheme to coordinate with other protection philosophies in case of multi-vendor multi-terminal grids [29].

1.2.2 Classification of HVDC grid protection schemes

There are two main classifications for HVDC grid protection algorithms. First, protection schemes can be classified based on the intended protection function and speed into *primary* and *backup* protection schemes. Backup protection schemes are divided, according to the primary failure condition, into *breaker failure* and *relay failure* backup protection schemes. Second, protection algorithms can be classified into single-ended (communication-less or non-pilot) and double-ended (communication-based or pilot) schemes based on their need for a communication channel. Single-ended schemes have been proposed mainly to avoid communication failure and compensate for the delayed operation of double-ended schemes due to communication delays. Therefore, single-ended protection schemes are essential to

realize ultra-fast fault detection and classification. On the other hand, precise determination of the fault location within the faulted segment by a *fault location identification scheme* is extremely important to guarantee fast restoration of the system.

1.3 Statement of the Problem

Although single-ended primary protection schemes have been already proposed, an improved scheme is still required to tackle the shortcomings that have not been sufficiently investigated in the literature such as limited fault resistance coverage, reliance on grid-specific and/or simulation-based thresholds, and failure in detecting severe fault conditions, *e.g.*, close solid faults. These shortcomings are discussed in more detail in Chapter 2. Furthermore, the general applicability of existing schemes to various grid configurations and their reliable performance under severe fault conditions have not been investigated. Compared to primary protection schemes, much less attention has been dedicated to backup protection schemes of multi-terminal HVDC grids. There is a significant need for implementing a reliable breaker failure backup protection scheme that rapidly detects unsuccessful breaker operations. Furthermore, it is essential to develop a reliable relay failure backup protection scheme that can detect primary protection failures and initiate a backup trip signal for the primary breaker, enhancing the security of HVDC grids. The existing fault location identification schemes require further improvements since their accuracy deteriorates under severe fault conditions such as local-end solid faults and remote-end high-resistance faults. Moreover, the performance of fault location schemes in large multi-terminal grids has not been evaluated.

1.4 Research Objectives

The main objective of this study is to design highly reliable protection schemes for multi-terminal HVDC grids that achieve the aforementioned protection requirements and tackle the deficiencies in existing schemes. The main objectives of this thesis are summarized as follows:

- Design a primary protection scheme that can rapidly detect internal faults and reliably discriminate them from external faults under severe fault conditions.
- Design a fault location identification scheme to precisely determine the exact fault location after identifying the faulted segment by primary protection.

- Design a breaker failure backup protection scheme to reliably and rapidly detect breaker failure events.
- Design a relay failure backup protection scheme to reliably identify primary protection failure events.

1.5 Research Methodology

In order to achieve the aforementioned research objectives, the following methodology is employed:

- Offline design and validation: Protection algorithms are designed using MATLAB environment.
- PSCAD/EMTDC environment is used to simulate the test grid. Then, grid measurements from PSCAD are exported to MATLAB environment to evaluate the effectiveness of the designed algorithms.
- Real-time validation: A hardware-in-the-loop (HIL) test setup is established to experimentally evaluate the proposed protection scheme. The test grid is built in OPAL-RT, while the designed algorithm is implemented in the dSPACE controller, which functions as the protection relay.

1.6 Thesis Outline

The rest of this thesis is organized as follows: Chapter 2 provides a comprehensive literature review of existing HVDC grid protection schemes. The proposed primary, fault location, breaker failure, and relay failure schemes are demonstrated in Chapters 3 to 6, respectively. In Chapter 7, the experimental validation results are presented. Chapter 8 concludes the thesis and provides recommendations for future research. The author's publications completed during their PhD studies are listed in Appendix A.

Chapter 2

Literature Review

2.1 Introduction

Several HVDC protection schemes are proposed in the literature aiming to achieve fast, reliable, and selective identification of DC faults. This chapter presents a comprehensive review of HVDC protection schemes. First, the evolution of DC fault current is investigated, and the available fault clearing strategies and switchgear are discussed in Section 2.2. Second, in Sections 2.3 to 2.5, existing schemes in the literature are reviewed and compared with each other, highlighting their features and shortcomings. It should be noted that this review focuses on existing protection algorithms that employ half- and full-bridge MMC as well as two- and three-level VSCs, since the majority of existing HVDC projects are based on these topologies, particularly MMC.

2.2 Fundamentals of DC faults

As reported in the joint paper of the European network of transmission system operators for electricity (ENTSO-E) and Europacable [30], DC cable faults are scarce and a few cable-fault incidents were historically reported by transmission system operators (TSOs). Root causes of DC cable (underground and submarine) faults are as follows: 1) cable insulation breakdown due to aging; 2) uncoordinated digging works; 3) overheating due to persistent overloading operation; 4) improper cable burial; and 5) anchor and pack ice damages. On the other hand, DC faults are more frequent in case of overhead transmission lines due to

Table 2.1: Common roots of DC faults.

Employed Transmission Facility	Common Roots	Fault Type	Fault Nature
Overhead Lines	1. Direct lightning strikes.	PTG	Temporary
	2. Indirect back flashover across insulators.	PTG	Temporary
	3. Sudden contact between conductors or between one conductor and ground due to external objects (such as trees or birds).	PTG/ PTP	Temporary
	4. Swinging of conductors due to severe storms.	PTP	Temporary
	5. Broken conductors.	PTG	Permanent
	6. Insulation failure due to aging or pollution.	PTG	Permanent
	7. Tower collapse due to natural disasters.	PTG	Permanent
Underground Cables	1. Insulation failure due to aging, overloading, etc.	PTG	Permanent
	2. Uncoordinated digging works.	PTG	Permanent
	3. Improper cable burial.	PTG	Permanent
	4. Improper installation of cable joints.	PTG	Permanent
Submarine (Undersea) Cables	1. Insulation failure due to aging, overloading, etc.	PTG	Permanent
	2. Anchor and pack ice damages.	PTG	Permanent
	3. Fishing gears.	PTG	Permanent
	4. Improper installation of cable joints.	PTG	Permanent

their exposure to unexpected and uncontrolled climate conditions. Table 2.1 summarizes the most common causes of DC faults in various HVDC transmission facilities.

2.2.1 DC fault stages

DC fault currents are extremely large due to the small impedance of DC networks [6, 7]. Additionally, the fast discharge rate of the converters' capacitors accelerates the rise of fault current to high levels in the first few milliseconds after the fault incident [31]. Three main stages can be identified during a short-circuit DC fault [32, 33]. The first stage is the capacitor discharge stage at which the DC link capacitors or submodule capacitors of MMC rapidly discharge into the fault. The high rate of rise of the fault current during this stage triggers the converters' overcurrent protective measures, resulting in converter blocking. The second stage is the inductive discharge stage caused mainly by the MMC arm reactors, since inductive currents cannot be instantaneously interrupted after converters

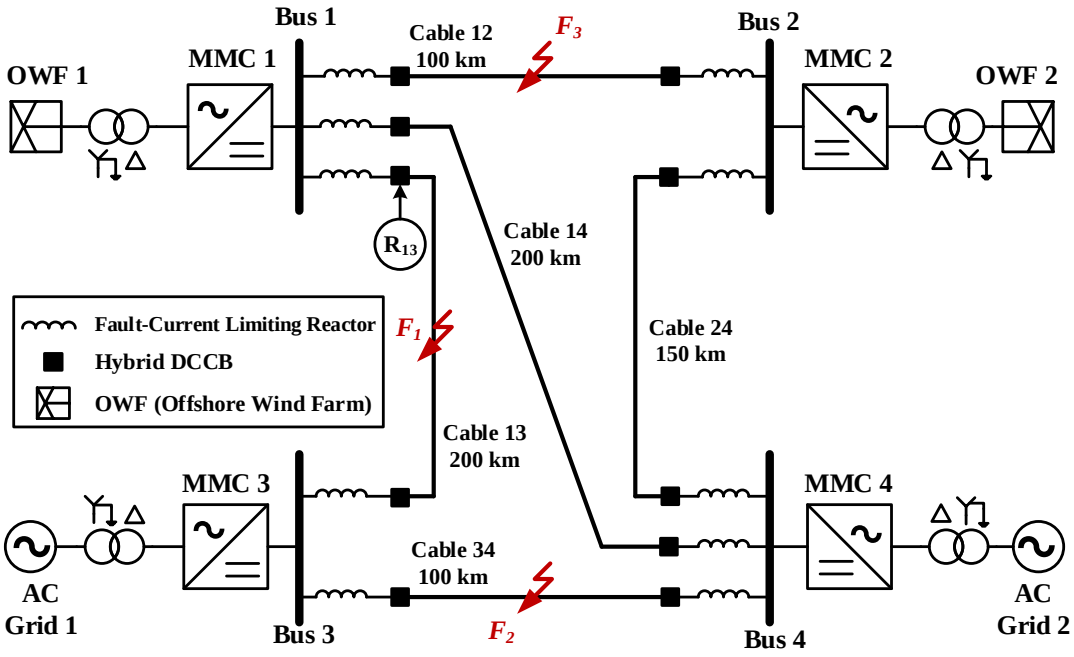


Figure 2.1: Four-terminal HVDC test grid.

are blocked. The third stage, which is automatically triggered after the inductive currents reach zero, is the AC infeed stage where the converters behave as uncontrolled rectifiers feeding the DC-side fault with large steady-state currents from the AC network. It is worth mentioning that DC fault currents should be interrupted during the first stage to avoid losing the controllability of converters and exceeding the interrupting capabilities of the employed DCCBs [34].

To demonstrate the aforementioned fault current stages, a half-bridge MMC-based four-terminal HVDC grid, shown in Figure 2.1, is simulated in PSCAD/EMTDC [35]. A PTP fault F_1 located at the middle of cable 13 is initiated at 0.71 s. The positive-pole current I_{13_p} measured by relay R_{13} is shown in Figure 2.2. As depicted in Figure 2.2, the capacitor discharge stage starts at t_{dis} once the first fault-induced backward traveling wave (TW) reaches bus 1 and is detected by R_{13}. Then, after a few milliseconds depending on the initial energy stored in the submodule capacitors, withstand capabilities of semiconductor switches, and fault parameters, the inductive discharge stage starts at t_{ind}. Finally, the AC infeed stage commences at t_{ac} once the arm inductors are completely discharged. Half-bridge MMCs are commonly modeled by a reduced RLC equivalent circuit, shown in Figure 2.3 [36], which precisely describes the initial fault stage. This equivalent cir-

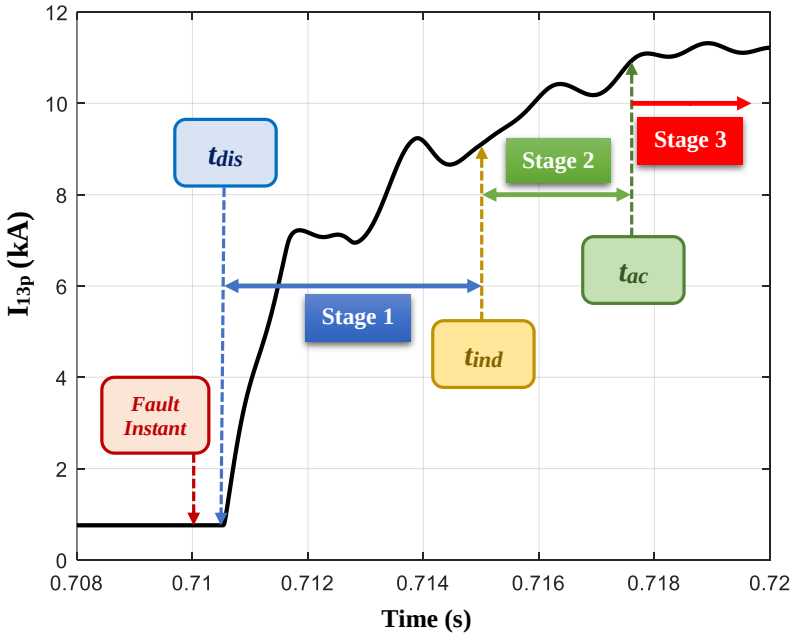


Figure 2.2: Positive-pole current during various stages of a DC fault.

cuit is frequently employed to evaluate various protection algorithms without increasing neither the computational burden nor the simulation time compared to the case when detailed models are employed. The equivalent circuit parameters can be calculated from (2.1-2.3) [37, 38]:

$$R_{eq} = \frac{2}{3}(R_{arm} + N_{SM}\ R_{on}), \tag{2.1}$$

$$L_{eq} = \frac{2}{3}L_{arm}, \tag{2.2}$$

$$C_{eq} = \frac{6\ C_{SM}}{N_{SM}}, \tag{2.3}$$

where R_{eq}, L_{eq}, and C_{eq} are the MMC equivalent resistance, inductance, and capacitance, respectively. R_{arm} is the arm resistance. N_{SM} is the number of submodules per arm. R_{on} is the on-state resistance per submodule, namely, the on-resistance of each insulated-gate bipolar transistor (IGBT). In the case of full-bridge MMCs, the same equivalent circuit can be adopted considering an on-state resistance twice that of a half-bridge MMC since two IGBT switches will be turned on per submodule in this case [24].

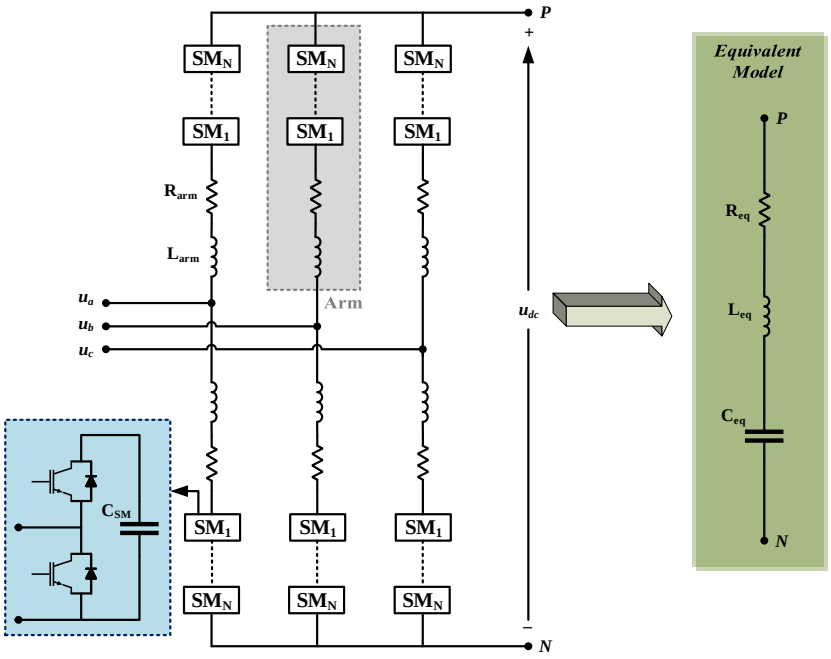


Figure 2.3: RLC equivalent circuit of a half-bridge MMC.

To limit the large fault currents and their high rate of rise during the first stage, DC boundary reactors (also called fault-limiting or smoothing reactors) are installed at both ends of each transmission line or cable segment within the HVDC grid. DC reactors enable dividing the HVDC grid into separate protection zones to facilitate the identification of the faulted segment and thus ensuring selectivity. This approach has been widely used in the literature to design HVDC grid protection schemes, particularly single-ended schemes where communication channels are not required [39]. The size of these reactors should be carefully selected since by increasing the reactor size, dynamic stability issues arise with power flow reversal; thus, affecting the control of converters. In addition, large reactors are more expensive and have larger footprint and losses. For example, the minimum reactor size that prevents converters from blocking during DC faults can be estimated from the proposed formula in [40]:

$$L_{dc}^{min} = \frac{1}{2}\frac{u_{dc}}{\Delta I}t_c - \frac{1}{3}L_{arm} \ , \tag{2.4}$$

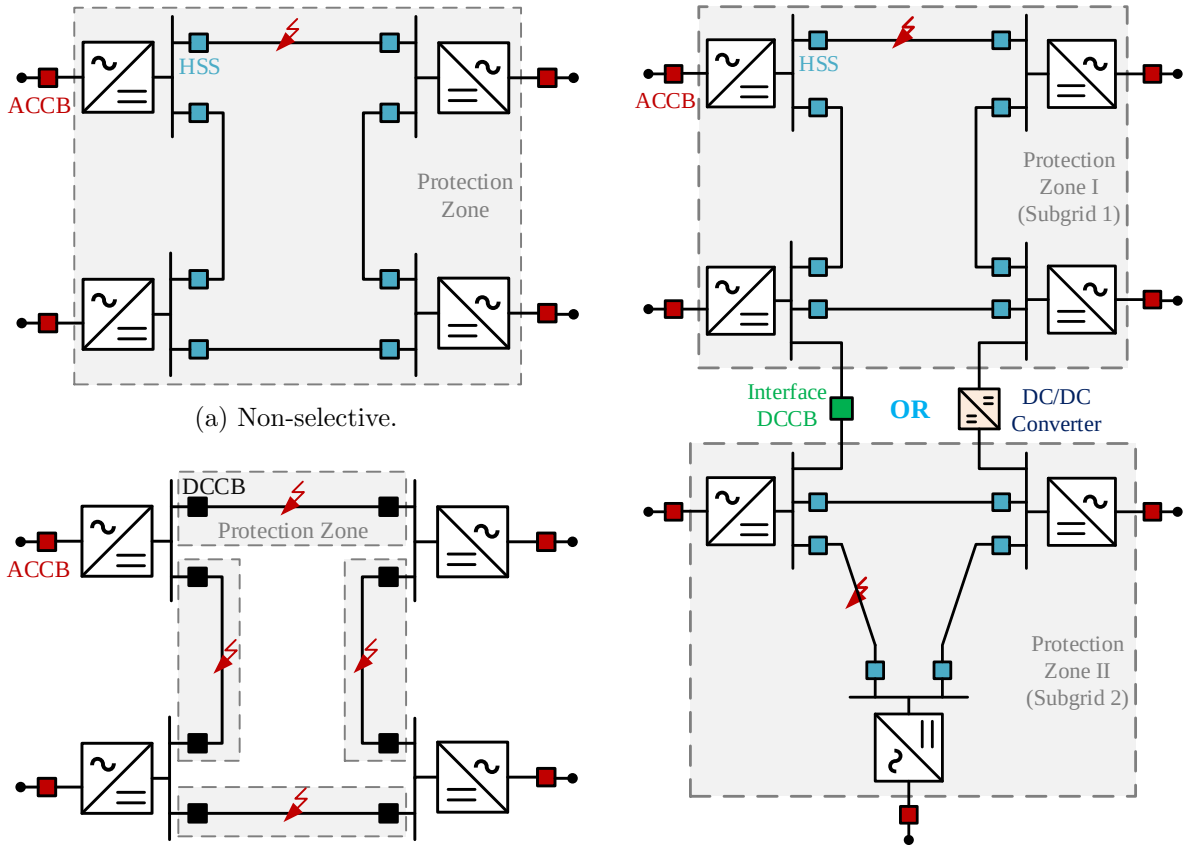
where L_{dc}^{min} is the minimum inductance per pole, L_{arm} is the MMC arm inductance, and ΔI is the permissible current rise within the specified fault clearing time t_c.

2.2.2 DC fault clearing philosophies

Designing a complete protection system for a multi-terminal HVDC grid requires specifying the strategy used to clear DC faults. A fault clearing strategy (or philosophy) can be defined as the approach taken by the protection system to clear DC faults [41]. According to [42], fault clearing strategies can be classified into three main categories, namely, non-selective, partially-selective, and fully-selective. Based on the desired protection system requirements and the constraints imposed on the grid, an appropriate protection philosophy is selected [42]. Accordingly, proper fault current interrupters are selected, and grid protection zones are specified.

In non-selective fault clearing strategies, the entire HVDC grid is de-energized in case of DC fault events utilizing either AC circuit breakers (ACCBs) or fault-blocking converters. Then, high-speed switches (HSSs) [43] installed at both ends of each line isolate the faulted segment; therefore, permitting restoration of the remaining healthy portion of the grid. In this strategy, the entire DC grid is considered as one protection zone as shown in Figure 2.4a. Although there is no selectivity in this strategy, it has a reduced cost since DCCBs are not required. However, this strategy is more suitable for point-to-point configurations since the loss of the entire HVDC grid during faults will impose severe stability issues. On the contrary, in fully-selective fault clearing strategies, only the faulted segment is tripped without affecting the remaining healthy grid via installing DCCBs at both ends of each segment. This strategy is the most reliable and selective choice for multi-terminal HVDC grids since individual protection zones are specified for protecting various grid components, similar to AC protection systems, as shown in Figure 2.4b. The high cost of DCCBs is the main disadvantage of this strategy. A compromised solution is the partially-selective fault clearing strategy or the grid-splitting strategy where the entire grid is divided into two or more protection zones, called subgrids, separated by interface DCCBs or DC/DC converters as shown in Figure 2.4c. A fault within a subgrid results in its tripping via the interfacing equipment and ACCBs of the faulted subgrid. Then, HSSs open to isolate the faulted segment, similar to the non-selective philosophy, resulting in the rapid restoration of the healthy part of the isolated subgrid.

DCCBs are the major components of fully-selective fault clearing strategies. DCCBs comprise three parallel paths with coordinated conduction during fault events, namely, the main conduction or load current path, the commutation or current-zero creation path, and the energy absorption path [44]. The main conduction path carries the normal load current, while the role of the commutation path is to transfer the large fault current from the main conduction path into the energy absorption path. The latter path primarily consists of surge arresters, such as metal-oxide varistors (MOVs), that dissipate the fault energy, drive



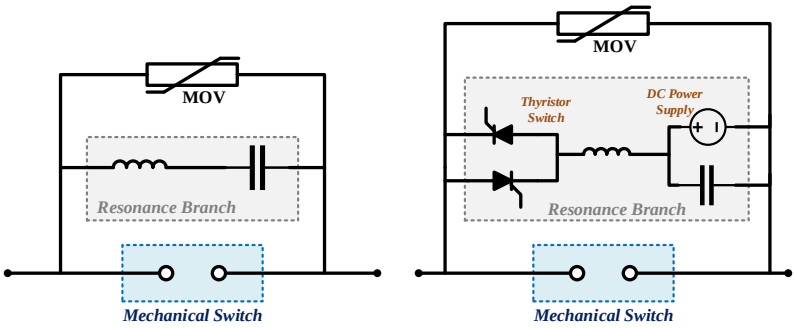
(a) Non-selective.

(b) Fully-selective.

(c) Partially-selective.

Figure 2.4: Protection zones of various fault clearing strategies.

the fault current into zero, and protect DCCB components from transient overvoltages [45]. There are three main types of DCCBs, i.e., mechanical (Figure 2.5) [45, 46], solid-state (Figure 2.6) [31], and hybrid (Figure 2.7) [45]. Typical mechanical DCCBs can interrupt fault currents up to 16 kA within 10 ms [46] which is relatively slow. On the other hand, solid-state DCCBs, where normal load current conduction and fault current commutation are achieved by the same branch consisting of a series set of semiconductor switches, can achieve an ultra-fast operation in the range of microseconds due to the absence of mechanical moving parts. Nevertheless, the employed semiconductor switches result in large on-state conduction losses. Hybrid DCCBs are the ultimate topologies that combine the fast operation of solid-state breakers with the reduced conduction losses of mechanical DCCBs. As shown in Figure 2.7, the main conduction path of hybrid DCCBs consists of an



(a) Passive-resonance. (b) Active-resonance.

Figure 2.5: Typical mechanical DCCB topologies.

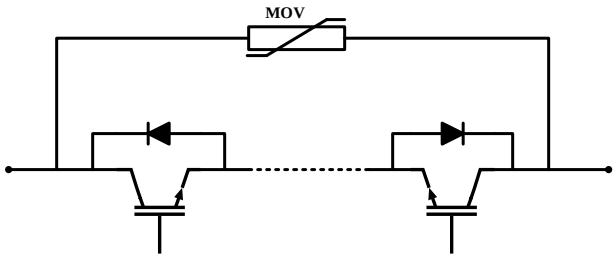


Figure 2.6: An IGBT-based solid-state DCCB.

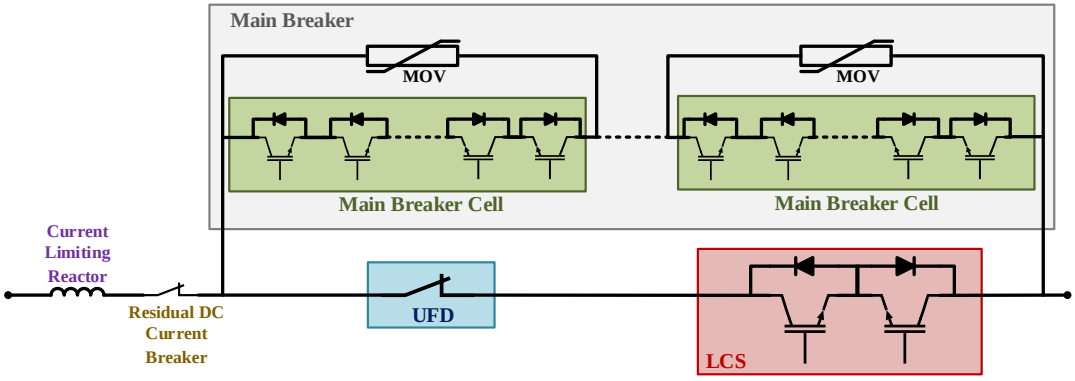


Figure 2.7: A hybrid DCCB.

ultra-fast disconnector (UFD), which provides instantaneous off-line isolation, and a load commutation switch (LCS), which consists of a reduced set of series semiconductor switches with much lower on-state conduction losses compared to solid-state breakers [47]. For

example, the Zhangbei HVDC grid in China, the world's first multi-terminal meshed grid, employs hybrid DCCBs that can fully interrupt substantial DC fault currents ($\geq 25\ kA$) in less than 3 ms [48].

2.3 HVDC grid protection schemes

A large number of DC protection algorithms have been proposed in the literature with various criteria and methodologies in order to achieve fast and selective fault detection. A suitable protection algorithm should be able to meet the aforementioned protection requirements in Section 1.2.1. Besides, it should be adaptable so that it can be applied to various converter topologies and grid configurations. Figure 2.8 shows a detailed classification of HVDC grid protection schemes. Protection schemes can be categorized into primary and backup schemes. Moreover, primary schemes can be further classified, based on the need for remote-terminal information, into single- and double-ended schemes. Figure 2.8 shows the various principles based on which single- and double-ended algorithms are formed. This section discusses the fundamental differences between single- and double-end primary protection schemes. In addition, a quick overview of the proposed backup protection algorithms is presented.

2.3.1 Primary protection schemes

HVDC primary protection schemes can be classified into two main categories: *double-ended schemes* and *single-ended schemes*. Double-ended schemes utilize communication channels to exchange measurement data or signals between boundary relays at both ends of each transmission line or cable segment based on which trip or no-trip decisions are made. Double-ended schemes are inherently selective, even for severe fault conditions such as high-resistance faults, since protection zones are formed between boundary relays without requiring DC boundary reactors [49]. However, their slow operation, due to communication delays, is a major shortcoming that impedes their applicability as fast primary protection schemes; yet they can be effectively utilized as backup schemes. Fast communication channels with adequate bandwidth, such as optical-fiber cables, should be used to limit this delay, increase the reliability of communication channels, and enhance their immunity against noise such that double-ended schemes can be safely utilized for primary protection [50]. Furthermore, synchronization between the exchanged data should be carefully considered to avoid malfunctioning during normal operation or external faults. A compre-

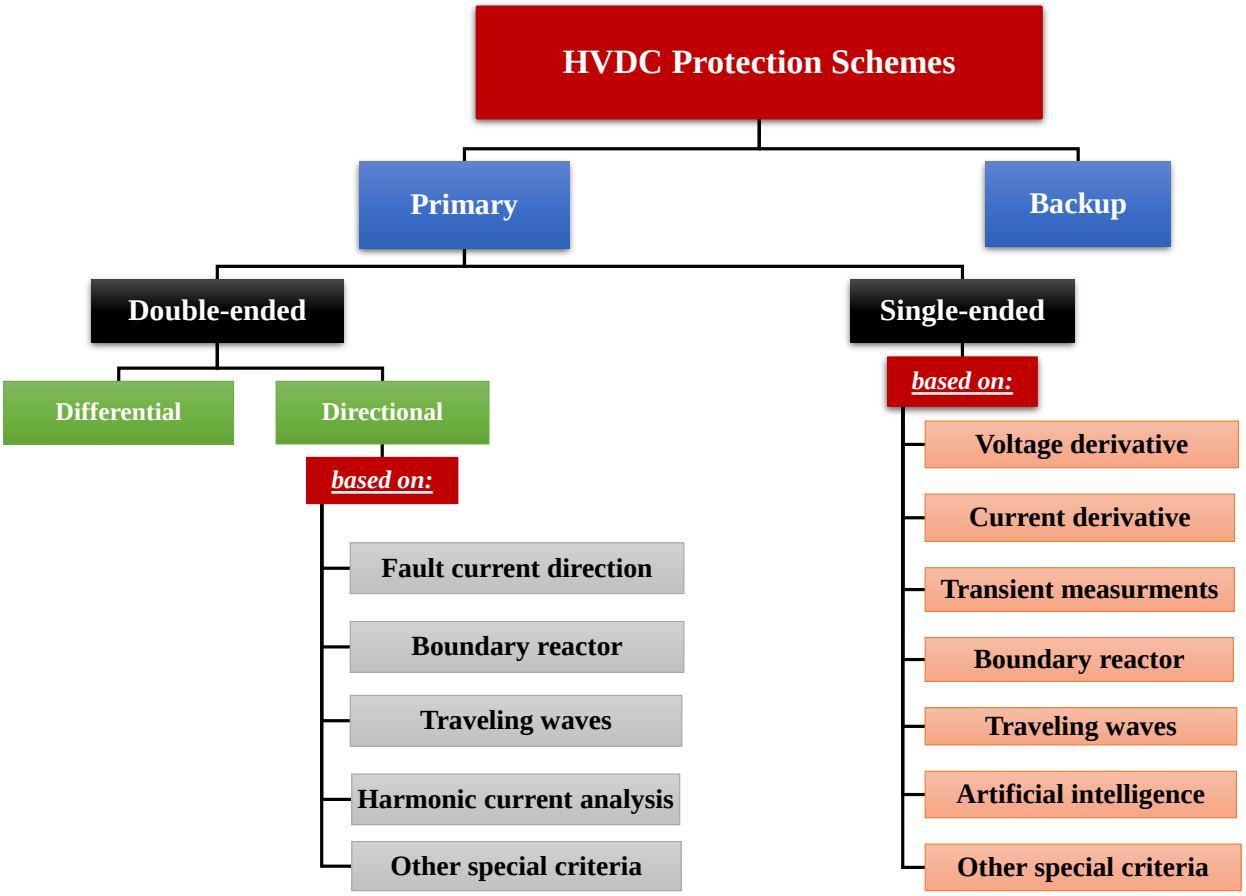


Figure 2.8: Classification of HVDC grid protection schemes.

hensive survey that covers existing double-ended protection schemes for VSC-HVDC grids are presented in Section 2.4.

On the contrary, single-ended schemes only require local measurements, and there is no need for remote-end data. Compared to double-ended schemes, single-ended schemes are more economical (no need for communication channels) and faster (no communication delays) [51]. However, their level of selectivity is deteriorated, particularly during high-resistance faults [52]. Therefore, DC boundary reactors are necessary to divide the entire grid into individual protection zones such that internal and external faults can be reliably discriminated. Moreover, precise and noise-free local measurements are necessary to guarantee the secure operation of single-ended schemes. Existing single-ended protection schemes and their principles are discussed in Section 2.5.

2.3.2 Backup protection schemes

Backup protection schemes are not required to be as fast as primary protection schemes. Therefore, double-ended schemes can be employed to provide selective and reliable backup protection. Backup protection is essential to ensure power system protection in case of primary protection failure. Primary protection failure can occur when corresponding breakers fail to clear the fault, *breaker failure*, or the primary relay fails to detect the fault, *relay failure*. Existing breaker and relay failure backup protection schemes are discussed in detail in Chapters 5 and 6, respectively, highlighting their shortcomings and introducing the proposed backup protection schemes.

2.4 Double-ended schemes

Double-ended schemes can be categorized according to the exchanged information into two major groups, i.e., differential and directional schemes. Differential schemes depend on exchanging information such as fault current measurements. Therefore, they require high bandwidth communication channels and synchronized exchanged data. On the other hand, directional schemes are employed to enhance the speed of double-ended schemes, reduce the communication channel loading, and loosen the stringent synchronization requirements. Directional schemes use logic (binary) data, representing the orientations or polarities of measurement quantities or specific extracted features from measurements. Therefore, selective, reliable, and fast unit protection algorithms with limited communication capacity are realized [53].

2.4.1 Differential protection schemes

Similar to AC differential protection schemes, DC differential schemes employ operating and restraining signals that are calculated based on the difference between and the average of boundary measurements, respectively. For instance, the principle of operation of current differential schemes is that during normal operation or external faults, the differential current approaches zero since measured currents at both ends of the protection zone have the same direction and approximately the same magnitude. On the contrary, during internal faults, the differential current will reach a much larger value. Therefore, by comparing the differential current with a non-zero threshold, to compensate for stray capacitive currents and other measurement errors, a reliable and selective fault indicator is achieved [54]. For

example, current measurement information is exchanged between both ends of each protection zone in the differential scheme introduced in [54], where the positive and negative pole currents at both ends of each segment are denoised using Discrete Wavelet Transform (DWT). Then, their extracted energy contents are employed to form the operating and restraining signals of the proposed criterion. The ratios between the operating and restraining signals of each line are utilized to discriminate between internal and external faults and identify the faulty pole. The large moving data window (1000 samples) required in this algorithm and the heavy wavelet computations significantly delay the fault detection process.

In [55], fault-tolerant inductor-capacitor-inductor (LCL) VSCs, which are capable of limiting fault currents for extended periods, are employed along with mechanical DCCBs such that a low-speed, yet highly reliable and highly selective protection system is realized based on a current differential protection criterion. However, the large operating time of the proposed algorithm ($30 - 60\ ms$) may adversely impact the overall transmission network's stability, security, and supply continuity. A similar scheme is proposed in [56] but with full-bridge MMCs exploiting their distinctive fault-handling capabilities such that slower and more cost-effective mechanical DCCBs with smaller ratings can be utilized. However, enhanced control of these converters can substitute the need for DCCBs; thus, achieving improved speed at a much lower cost. A fast differential algorithm has been recently proposed in [57] which realizes a compromise between selectivity and speed. In [57], transmission lines are modeled by the approximated Bergeron model based on which the line-mode components of measured currents at boundary relays are rapidly computed. Then, their differential component is utilized to detect internal faults. Although the Bergeron line model strengthens the immunity of the proposed scheme against malfunctioning during system disturbances and external faults, its precision needs further investigation considering line-distributed capacitances. In summary, the common ground of the above differential protection schemes is that accurate, synchronized, and denoised current measurements should be exchanged through an efficient communication medium to guarantee their reliable operation. In addition, the speed of the proposed algorithms does not comply with the stringent speed requirements recently imposed for multi-terminal HVDC grids [58].

2.4.2 Directional protection schemes

Directional algorithms result in faster double-ended protection schemes that require communication channels with limited capacity. They vary based on the exchanged pilot signals, e.g., the directions of fault current measurements, the polarities of reactor voltages, and

the signs of traveling waves' transient energies. This section discusses various types of existing directional protection schemes.

Fault current direction

Digital signals that represent the direction of fault currents at both terminals can be utilized as pilot signals alongside local measurements for selective fault detection. Similar to AC systems, the developed scheme may be a tripping scheme (where the local tripping command will be initiated only if a fault confirmation signal is received from the remote end) or a blocking scheme (where the local tripping command will be initiated if a blocking signal from the remote end is not received). A tripping scheme is proposed in [59] based on exchanging the sign of fault current directions. It is concluded that an internal fault is detected if the two terminal currents have the same sign, whereas opposite signs indicate an external fault. In [60], orientations of the transient fault currents at both line ends are determined by Wavelet Transform Modulus Maximum (WTMM). Then, the extracted orientations are compared with each other based on which internal and external faults are identified. However, the required large sampling frequency of 100 kHz increases the computational burden of this algorithm. In [61], the transient fault current increments in addition to their polarities at both line ends are evaluated and employed to discriminate between internal (opposite polarities) and external (same polarities) faults and precisely estimate the fault distance. The main deficiency of these schemes is that their reliability deteriorates during high-resistance faults as incorrect current polarities may be extracted due to the resulting small fault currents. The maximum fault resistance coverage is 300 Ω which is achieved in [60, 61]. In addition, the proposed scheme in [60] is the only one evaluated with multi-terminal grids rather than point-to-point interconnections as in the case of other schemes.

Boundary reactor-based pilot signals

Although DC boundary reactors are not required with double-ended schemes for grid segmentation, they may be utilized as current limiters to reduce the sharp rise of fault current. In [62], the polarities of boundary reactor voltages at both line ends are exchanged and compared to decide whether the detected fault is internal (positive polarities) or external (opposite polarities). In addition, the faulty pole is identified by integrating the reactor voltage over a data window to eliminate the coupling effect between the faulty and healthy poles. Likewise, transient properties of boundary reactor voltages are extracted by Wavelet transform in [63] based on which a pilot discrimination criterion is proposed. The major

demerit of these schemes is that DC boundary reactors are not optimally exploited since their ability to filter the high-frequency transients can be employed to implement adequate single-ended schemes without requiring communication channels as will be discussed in Section 2.5.4.

Traveling wave-based pilot signals

During DC faults, TWs are initiated at the fault point, then propagate in both directions along the faulted segment until reaching the boundary terminals where one part of these waves is refracted into the healthy part of the grid and the other part is reflected into the faulted segment and so forth [64]. TW-based algorithms are widely used to design unit and non-unit protection schemes. The permissive scheme designed in [65] classifies forward and reverse faults by calculating the energy content ratio of the incident backward fault wave over the reflected forward wave at terminal relays. Then, a permissive (or blocking) signal is sent to the other end to initiate (or prevent) the tripping signal of local DCCBs in case of forward (or reverse) faults. To decrease communication delays and TW attenuations in long cables, reference [66] proposes a protection algorithm that utilizes multiple intelligent sensors at cable joints and along the entire cable length. The proposed algorithm is based on a directional comparison criterion, where a trip signal is initiated if two consecutive sensors detect a forward fault. Moreover, proactive (or two-stage) DCCBs [44], which discard the initial trip signal if the fault is not confirmed before the breaker opens, are employed to further reduce the total fault detection and clearing time. Therefore, the algorithm speed and security are greatly improved. However, the main deficiency of this scheme is the increased cost of additional sensors.

Another pilot scheme is proposed in [67] based on comparing the orientations of transient energies (TEs) computed from the initial fault voltage TWs at both cable ends. The proposed algorithm effectively discriminates between internal (both TEs are negative) and external (one or two TEs are positive) faults. It also identifies the faulty pole based on the ratio between the computed TEs of positive and negative poles of the faulted segment. In addition, it estimates the fault location based on detecting the initial voltage surge arrival instants at both cable terminals, which are extracted by Stationary Wavelet Transform (SWT). However, the reliable performance of the proposed scheme requires a substantial sampling frequency (1 MHz), which increases the computational burden. The major shortcoming of TW-based schemes is that TW attenuations in case of lengthy transmission lines are not investigated. With severe attenuations, misleading estimation of the exchanged data will result in the maloperation of the proposed schemes, particularly under severe fault conditions.

Harmonic current-based pilot schemes

In such schemes, converters' harmonic currents at both line terminals are extracted and analyzed to identify internal and external faults. In [68], first carrier frequency harmonic (FCFH) currents are extracted by Discrete Fourier Transform (DFT) at both cable ends. Based on their magnitudes during a specified window length, the protection units at both terminals detect internal faults and distinguish them from external faults. The proposed algorithm was only applied to point-to-point configurations and did not consider high-resistance faults. A similar, yet improved scheme is proposed in [69] based on FCFH currents extracted by Hilbert-Huang Transform (HHT) which has several advantages over Fourier and wavelet transforms in terms of instantaneous frequency detection precision in the time domain. Furthermore, compared with the previous scheme, the algorithm was evaluated in a multi-terminal grid rather than a simple point-to-point configuration. In addition, a larger range of fault resistances was tested. It is worth mentioning that harmonic-based schemes require high computation capacity and they are easily affected by noise and disturbances. Therefore, their sensitivity and selectivity may deteriorate under severe fault scenarios.

Special methodologies for pilot schemes

Recently, new mathematical approaches, which require lower computation capacity compared with conventional methods, have been exploited to design fast and effective DC protection schemes. Morphological Gradient (MG) theory is employed in [70] to develop the Multi-resolution Morphological Gradient (MMG) algorithm, which efficiently extracts the desired waveform information even during loss of communication. In [70], MMG, which eliminates the errors resulting from data-synchronization mismatches, is applied to line-mode voltage TWs. The proposed scheme discriminates between internal and external faults by estimating the correlation coefficient between MMGs of line-mode voltage TWs at line terminals (the forward wave at one end and the backward wave at the other end). Finally, faulty pole identification is achieved based on calculating the ratio of MMG for the positive and negative poles of the faulted segment. However, the operating time of this algorithm (5 ms) needs to be reduced to comply with the recent HVDC protection system speed requirements.

The cosine distance criterion is another recent approach proposed in [71]. This criterion is based on comparing the orientations of the reference internal fault voltages and currents with the corresponding orientations of the actual superimposed fault quantities via calculating the cosine distance function. Protection algorithms based on Hausdorff

Distance (HD) approach are proposed in [49, 72]. The HD between two nonempty sets can be mathematically defined as the maximum distance of a set to the nearest point in the other set. The proposed methods in [49, 72] provide major advantages in terms of noise-tolerance capability and elimination of the compulsory data synchronization requirement. The fundamental principle proposed in both algorithms is based on evaluating the degree of similarity, via HD theory, between the initial fault voltage backward and forward TWs at line terminals (the forward wave at one terminal and the backward wave at the other terminal) to detect and discriminate between internal and external faults. Moreover, the faulty pole is identified in [72] based on the ratio of TEs of the positive pole over its counterpart of the negative pole. However, due to the relatively low speed of this scheme, it can be employed for backup protection rather than primary protection. The major disadvantage of these schemes is that they are not straightforward to implement due to their dependence on complicated mathematical approaches. In addition, their general applicability with various grid configurations is not investigated.

2.4.3 Comparison between double-ended schemes

Table 2.2 presents a summarized comparison among the reviewed double-ended schemes. The comparison is based on various aspects such as the exchanged data, mathematical approach, sampling frequency, and data window length based on which the algorithm can make decisions. Furthermore, the configuration of test grids and the converter technologies employed to evaluate the proposed schemes are provided. Moreover, the speed of the considered algorithms and their fault resistance coverage, beyond which the selective and reliable performance of the proposed algorithms will no longer be guaranteed, are compared. It is worth noting that the reported operation times of the algorithms depend on the propagation speed of TWs and the communication delay which depends on the employed communication medium and the lengths of overhead lines and/or cables within the test grid.

Based on Table 2.2, it is evident that differential schemes are generally slower than directional schemes. To the best of the author's knowledge, the fastest differential algorithm is the one reported in [57] with an operating time of 7.5 ms, given that the longest transmission line within the test grid has a length of 800 km. However, this operating time is still large considering the recent HVDC protection system speed requirements. Furthermore, stringent synchronization requirements are mandatory to accurately estimate the differential current and avoid relay maloperation during severe external faults. On the contrary, directional schemes have shorter operating times as they only require the exchange of binary signals with less stringent synchronization requirements. The minimum

Table 2.2: Comparison between existing double-ended protection schemes.

Reference (Category)	Exchanged Data	Mathematical Analysis Tool	Algorithm Triggering Criterion	Sampling Frequency (kHz)	Window Length (Number of Samples)	Tested Grid Configuration	Converter Topology	Fault Resistance Coverage	Operation Time(ms)
[54] (differential)	current measurements	DWT	high-frequency transients	100	1000	three-terminal star-connected	three-level NPC-VSC	300 Ω	10
[55] (differential)	current measurements	direct data processing	differential current	10	instantaneous measures	four-terminal meshed grid	two-level LCL-VSC	N/A	30 – 60
[56] (differential)	current measurements	direct data processing	differential current	N/A	instantaneous measures	CIGRE test grid	full-bridge MMC	400 Ω	20
[57] (differential)	current measurements	phase modal transformation	differential current (1-mode)	10	instantaneous measures	three-terminal star-connected	LCC/MMC (hybrid)	500 Ω	7.5
[59] (directional)	current polarity	direct data processing	current direction change	2	10	point-to-point	two-level VSC	100 Ω	10
[60] (directional)	fault current direction	WTMM	same as the main algorithm	100	instantaneous measures	four-terminal meshed grid	two-level VSC	300 Ω	3
[61] (directional)	current polarity	direct data processing	abrupt current variations	20	instantaneous measures	point-to-point	half-bridge MMC	300 Ω	N/A
[62] (directional)	reactor voltage polarity	phase modal transformation	reactor voltage gradient	50	25	four-terminal meshed grid	half-bridge MMC	400 Ω	3
[66] (directional)	fault current direction	direct data processing	voltage/current variations	N/A	instantaneous measures	four-terminal meshed grid	half-bridge MMC	1000 Ω	5
[67] (directional)	TE polarity	integration of wave power	abrupt voltage variations	1000	500	four-terminal meshed grid	half-bridge MMC	150 Ω	2.57
[68] (directional)	FCFH current detection flag	DFT	same as the main algorithm	N/A	27	point-to-point	two-level VSC	100 Ω	N/A
[69] (directional)	FCFH current detection flag	HHT	same as the main algorithm	100	512	CIGRE test grid	two-level/three-level VSC	500 Ω	N/A
[70] (directional)	line mode voltage	MMG	MMG value	10	31	four-terminal meshed grid	half-bridge MMC	1000 Ω	5
[71] (directional)	fault detection signal	cosine distance function	same as the main algorithm	5	10	four-terminal meshed grid	half-bridge MMC	1000 Ω	3
[72] (directional)	forward and backward voltage waves	improved HD hypothesis	instantaneous frequency obtained from HHT	20	40	four-terminal meshed grid	half-bridge MMC	1000 Ω	7.22

operating time of the reviewed directional schemes is 2.57 ms, which is reported in [67] given that the longest cable within the test grid is 200 km long. In addition, the fault resistance coverage of this scheme is 150 Ω, which is relatively small compared to other unit protection schemes. The largest fault resistance coverage is 1000 Ω, which is achieved

by the proposed directional schemes in [66, 70–72], while the lowest coverage is 100 Ω as reported in [59, 68].

Compared with differential schemes, directional schemes usually require a large sampling frequency and a high computation capacity. The directional scheme proposed in [67] has the largest sampling frequency of 1 MHz. In contrast, the lowest sampling frequency is 2 kHz as reported in [59]; however, the fault resistance coverage of this algorithm is small in addition to its slow speed. Regarding the employed test grid, three- and four-terminal grids are commonly used to evaluate the proposed schemes. Regarding the converter topology, MMCs are the commonly employed converter topologies in the reviewed papers, particularly half-bridge MMC. Half-bridge MMCs are the most commonly employed converters due to their simplicity and reduced cost and losses compared to full-bridge MMCs. However, full-bridge MMCs have a superior advantage which is the fault-blocking capability that can be exploited to relax the stringent speed requirements and reduce the ratings of DCCBs.

In summary, it can be concluded that communication-based schemes can attain a high level of selectivity since the multi-terminal grid is divided into separate protection zones at line boundaries where the information is exchanged; thus, the faulted segment can be reliably identified. Furthermore, recently proposed pilot schemes can comply with protection system speed requirements, particularly with short distances up to 200 km [67, 71]. Consequently, these algorithms can provide primary and backup protection. However, with longer transmission lines/cables and the imposed synchronization requirements, their utilization will be merely restricted to backup protection. Fiber-optic links are typically utilized by existing double-ended schemes as the communication medium for exchanging data between boundary relays due to their high reliability and immunity against communication failures and erroneous data transmission. Furthermore, they are robust against electromagnetic interference, and their large bandwidth facilitates the transmission of a large amount of data.

2.5 Single-ended schemes

Double-ended schemes are mostly slow due to the inevitable communication delays, which become longer as the transmission line or cable length increases. Furthermore, various errors in the exchanged data may occur due to noise and loss of synchronization. Consequently, double-ended schemes are practically recommended to provide backup protection, while single-ended protection schemes are required to provide fast primary protection.

The main challenge that hinders the design of single-ended schemes is achieving high selectivity, especially during remote faults with large resistances. Furthermore, to guarantee high accuracy, a large sampling frequency is commonly required, which increases the algorithm's computational burden. Additionally, attenuation of TWs associated with long transmission lines should be carefully considered to avoid the maloperation of single-ended algorithms [73]. Various approaches and methodologies have been proposed to design selective, sensitive, and reliable single-ended protection schemes that will be reviewed in this section.

2.5.1 Voltage derivative-based schemes

One of the earliest approaches that have been adopted to design single-ended protection schemes is based on the continuous computation of the rate-of-change-of-voltage (ROCOV) or voltage-derivative values based on local voltage measurements. Since DC faults are accompanied by a rapid voltage decline, the ROCOV value can be exploited to detect fault events. For instance, the proposed scheme in [74] utilizes the line-side reactor voltage measurements to estimate the ROCOV value, which is compared to a pre-adjusted threshold for DC fault detection and localization. The authors of [75, 76] have further improved the selectivity, reliability, and fault resistance coverage of ROCOV-based schemes by proposing an extra directional feature based on the ratio of ROCOV values measured at both sides of boundary reactors. In addition, the proposed scheme is augmented with a directional comparison ROCOV-based criterion to selectively detect high-resistance faults. This directional criterion has been further improved in bipolar grids with a metallic return path via inserting small reactors at both ends of the return conductor [76]. In [77], a double-stage scheme is proposed. In the first stage, the fault is detected based on an undervoltage criterion. The second stage is the discrimination stage based on undervoltage and voltage-derivative criteria to discriminate between internal and external forward faults as well as a current-derivative criterion to identify forward faults from reverse faults. However, these schemes require large sampling frequencies to accurately calculate the ROCOV value. Additionally, their selectivity deteriorates during high-resistance faults.

2.5.2 Current derivative-based schemes

Analogous to voltage derivative-based schemes, current derivative-based schemes have been proposed, in which the instantaneous increase of fault current and the corresponding rate-of-change-of-current (ROCOC) value are utilized to detect fault events. In addition, the

ROCOC criterion can be integrated with other criteria to develop selective algorithms and improve the algorithm's reliability and immunity against maloperations. In [78], five ROCOC indices are calculated based on which various faults are detected (including faults that involve the metallic return conductor in asymmetric bipolar configurations) and the faulty pole is identified. Another ROCOC-based scheme is proposed in [79] which provides both primary and backup protection for multi-terminal HVDC grids. In [79], a statistical Bayesian classifier is adopted to select the necessary thresholds and establish proper time-coordination between primary and backup relays. The main disadvantage of these schemes is the limited fault resistance coverage since the ROCOC value is drastically impacted as the fault current decreases with higher fault resistances. The proposed scheme in [78] can detect faults with resistances up to 50 Ω (limited coverage).

2.5.3 Transient schemes based on voltage and current measurements

DC faults are associated with abrupt increases in the fault current and sudden dips in the measured voltage. Therefore, direct measurements of local voltages and currents can provide fault indicators and can be employed in the design of rapid fault detection algorithms. It is worth noting that reliable voltage and current measurement devices with a high bandwidth should be utilized to provide precise and noise-free measurements based on which correct decisions can be made by the proposed algorithms [80]. In [81], the proposed fault detection criterion depends on transient voltage measurements at both sides of the boundary reactors, where the ratio of the transient voltages (ROTV) at both reactor sides is used to distinguish between internal and external faults. In [82], fault detection and identification (FDI) units are arranged at each bus to promptly detect faults, discriminate between bus and line faults, and selectively identify the faulted line or busbar based on local current measurements.

In [83], the proposed criterion depends on cable sheath voltage measurement which is typically zero during normal operation while having a non-zero value during the fault. Furthermore, in [83], the amplitude and polarity of the measured sheath voltage are utilized to identify the faulted segment and determine the faulty pole. The proposed scheme in [84] utilizes the transient fault voltage measurements to estimate the first peak time (FPT), which represents the time duration between the sudden voltage dip instant and the instant when the first peak is detected in the filtered voltage waveform, based on which the protection criterion is established. In [85], the change in the average voltage of positive and negative poles is employed to selectively detect various fault events. However, the employed data window length is large (5 ms).

In [86], the magnitudes and derivatives of the line-mode and zero-mode components of the local fault current are extracted based on modulus decomposition transformation. Then, the extracted values are projected on a protection phase plane, which is divided into fault regions according to the fault type. Consequently, internal faults can be detected and discriminated from external faults, and the faulty pole can be identified as well. The proposed scheme in [87] utilizes local fault voltage and current measurements to estimate three independent fault indicators, i.e., pole-current variations, pole-to-earth voltage variations, and converter neutral current variations, based on which different faults can be detected. In [88, 89], initial fault currents are analyzed and calculated by proposing a transient high-frequency equivalent model for the employed meshed grid. Then, a fault detection and discrimination criterion is proposed based on estimating the transient energy of the superimposed high-frequency components of local current measurements. In [89], the derived current expressions during the initial fault stage are used to detect and discriminate between internal and external faults. In summary, there are two major shortcomings of transient-based schemes: first, their sensitivity and selectivity reduce as the fault resistance increases. Second, the grounding impedance value as well as the number of grounding points and their locations have a substantial impact on the transient fault voltages and currents, particularly in large multi-terminal grids. This aspect has not been sufficiently investigated in the reviewed schemes, which restrict their application to certain grid configurations.

2.5.4 Boundary reactor-based schemes

As previously highlighted in Section 2.2.1, DC boundary reactors are installed at both ends of each transmission line or cable segment in HVDC grids to limit the sharp increase of fault currents and divide the grid into separate protection zones. Various protection schemes based on boundary reactor measurements have been proposed in the literature. In [90], the estimated value of the boundary reactor power is utilized to detect and discriminate between internal and external faults. However, the proposed scheme is not reliable in detecting high-resistance faults. Therefore, an auxiliary pilot backup criterion is developed for such faults. In [91], the proposed criterion depends on voltage measurements across boundary reactors to detect and discriminate various faults and identify the faulty pole. Depending on the rate of change of the reactor voltage, the proposed scheme in [92] can detect fault events. Besides, internal faults are discriminated from external faults depending on the voltage polarities and amplitudes of reactors that are connected to the same bus. However, in [92], only PTP faults are tested without providing a faulty-pole identification criterion. In [93], the proposed algorithm detects DC faults by calculating the difference

between the ratios of the root mean square values of transient voltages at both sides of boundary reactors. Moreover, the faulted pole is identified by calculating the instantaneous zero-sequence voltage (IZSV) at the converter's AC side. The concept of asymmetric pole inductors has been recently proposed in [94], where the value of the DC reactor installed at the positive pole is different from that of the negative pole. The difference between the inductor voltages of the two poles is utilized as the fault detection criterion. However, this scheme is incapable of detecting unsymmetrical DC faults, i.e., PTG faults. The lack of clear criteria to optimally select the size of boundary reactors in large multi-terminal grids is the major shortcoming of these schemes.

2.5.5 Traveling wave-based schemes

Similar to double-ended schemes, TW propagation theory has been widely applied in the design of single-ended schemes. In such schemes, fault-induced TWs are detected and their high-frequency contents and arrival instants are extracted using various signal processing tools based on which DC faults are detected. For example, DWT applied to local fault voltage TWs is exploited in [95] to identify the faulted segment. In [96], DWT is applied to local current measurements to design the protection criterion, where fault discrimination is achieved by detecting the high-frequency components associated with internal faults. During external faults, these components are attenuated due to shunt capacitors installed at the grid tie buses and the stray capacitances at each bus. The proposed discrimination criterion employs the ratio of the high- to low-frequency TEs to distinguish between internal and external faults. However, the proposed scheme lacks generalization since it is tested in a special grid structure that contains tie buses. The proposed scheme in [97] locally extracts the distinctive frequency contents of the first incident current TW utilizing DWT to distinguish between internal and external faults. In [98], DWT is used to extract high-frequency components of line-mode voltages and currents of the fault-induced forward and backward TWs to discriminate between forward and reverse faults.

In [99], the high-frequency content extraction is performed by Short-Time Fourier Transform (STFT) applied to local fault current measurements to develop a frequency-domain-based relaying algorithm. Moreover, a time-domain-based detection criterion is proposed based on estimating the correlation degree between the DC link capacitor discharge current and the local fault current. In [100], the orientations and high-frequency content of the initial fault current TW extracted by Fast Fourier Transform (FFT) are utilized to construct the fault detection and identification criteria. However, the proposed method requires a large sampling frequency and large computations.

Recently, HHT has been used in several protection schemes due to its capability of extracting instantaneous features with a physical meaning in the time domain. For instance, in [101], the average frequency of the transient voltage signal is estimated by HHT and the marginal Hilbert spectrum (MHS). Then, the estimated value is compared with a predefined distance-frequency curve to assess the fault location. However, this scheme requires extensive calculations to find the distance-frequency curve for each segment within the grid. In addition, the selectivity of this scheme is examined only for low-resistance (1 Ω) faults. In [102], the instantaneous energy density, estimated by HHT, is selected as the fault detection criterion. However, the frequency band, within which the density level is estimated, depends on the operating point of the system. Moreover, the fault resistance coverage of this scheme is relatively small (50 Ω).

In [103], a protection algorithm is proposed based on the zero- and line-mode components of the fault-induced backward TWs extracted by Phase-Modal Transformation (PMT). Similarly, PMT is employed in [104], where internal faults are detected by using the line-mode component of the boundary reactor voltage, and the faulty pole is identified based on the zero-mode component. In [105], a PMT-based algorithm is proposed which uses two criteria to detect fault events: 1) the derivative of the line-mode forward TW and 2) a directional criterion based on the surge arrival time difference (SATD) between line-mode components of backward and forward TWs. The major shortcoming of TW-based schemes is that TW attenuations in case of lengthy transmission lines are not investigated. With severe attenuations, the proposed schemes will maloperate, particularly under severe fault conditions. In addition, rapid detection of close faults based on TWs is challenging since the initial fault-induced backward TW can not be detected.

2.5.6 Artificial intelligence-based schemes

Various protection schemes based on artificial neural networks (ANNs) have been proposed that benefit from intelligent fault detectors and classifiers. In [106], an ANN-based scheme depending on local fault current measurements is proposed. However, this scheme has a long operating time of 5 ms. In [107], Wavelet transform along with Principal Component Analysis (PCA) are applied to local current measurements to extract distinctive features, which are utilized as inputs to a Genetic Fuzzy System (GFS) to discriminate between internal and external faults. Furthermore, in [108], an artificial intelligence-based discrimination criterion is proposed based on the fault-induced TW propagation features extracted by a convolutional neural network (CNN). It is worth mentioning that artificial intelligence-based schemes require high computational capacity, exhaustive simulations, and large data sets to train the proposed algorithms.

2.5.7 Special non-unit schemes

Recently, various mathematical approaches have been used to design efficient single-ended protection algorithms. The authors of [109] have developed a non-unit protective scheme based on the MG theory. In [109], MG theory is used to extract the amplitude and arrival instant of the initial fault wavefront from local voltage measurements to detect fault events. In [110], this scheme is modified based on the multiplication of the estimated second-level MG values of line-mode components of the fault voltage and current TWs. The proposed scheme in [111] depends on detecting sudden changes of fault transients associated with local fault voltage and current TWs using the Median Absolute Deviation (MAD) statistical approach. However, solid and noise-free faults are only considered to evaluate this scheme; thus, the MAD-based fault detection criterion may fail under severe fault conditions.

In [112, 113], the Levenberg-Marquart curve fitting technique is applied to the zero-mode component of the first incident TW of the measured fault current to extract index coefficients, which are utilized to distinguish internal from external faults. A similar scheme is developed in [114], where the fault resistance and location are estimated based on the magnitude and distortion degree of the incident fault current TW. Moreover, in [114], the effect of fault resistance is eliminated by utilizing adaptive thresholds, which are adjusted based on the extracted fault information from a curve-fitting criterion. Although the proposed scheme can reliably identify PTG faults with large fault resistances, it fails to detect PTP faults. Furthermore, it requires a large sampling frequency and a large computational capacity. Finally, a recent algorithm is proposed in [115] based on the statistical random matrix theory (RMT) applied to local current measurements. The major disadvantage of these schemes is that they are not straightforward to implement due to their dependence on complicated mathematical techniques. In addition, their general applicability with various grid configurations is not investigated.

2.5.8 Comparison between single-ended schemes

A comparison between existing single-ended schemes is presented in Table 2.3. The same comparison aspects as those used for double-ended schemes are investigated in addition to the size of boundary reactors employed in existing schemes. From Table 2.3, it can be concluded that single-ended schemes are fast with operating times less than 1 ms [76,82,100,110]. The algorithm proposed in [85] has the longest operation time of 5 ms. The speed of the remaining schemes complies with the protection system speed requirements (3 ms or less), except for the one in [101] (4 ms). The smallest sampling frequency is 10 kHz, which is employed in [89, 98, 102, 111]. The highest sampling frequency (2 MHz)

Table 2.3: Comparison between existing single-ended protection schemes.

Reference (Category)	Mathematical Analysis Tool	Algorithm Triggering Criterion	Sampling Frequency (kHz)	Window Length (Number of Samples)	Tested Grid Configuration	Converter Topology	Boundary Reactor Size(mH)	Fault Resistance Coverage	Operation Time(ms)
[76] (ROCOV)	direct data processing	same as the main algorithm	25	N/A	three-terminal meshed grid	half-bridge MMC	40	200 Ω	0.2
[78] (ROCOC)	direct data processing	same as the main algorithm	N/A	N/A	three-terminal star-connected	half-bridge MMC	40	50 Ω	1
[77] (ROCOV/ROCOC)	direct data processing	undervoltage	100	10	four-terminal meshed grid	half-bridge MMC	20 – 40	60 Ω	2.11
[82] (Transient)	direct data processing	same as the main algorithm	50	20	four-terminal meshed grid	half-bridge MMC	50	N/A	0.5
[85] (Transient)	direct data processing	average voltage change	20	100	four-terminal meshed grid	half-bridge MMC	300	500 Ω	5
[89] (Transient)	direct data processing	current derivative	10	20	four-terminal meshed grid	two-level VSC	100	500 Ω	3
[90] (DC Reactor)	direct data processing	same as the main algorithm	N/A	N/A	point-to-point	two-level VSC	5 – 145	N/A	2.6
[91] (DC Reactor)	direct data processing	DC reactor overvoltage	N/A	N/A	four-terminal meshed grid	half-bridge MMC	150	380 Ω	1
[93] (DC Reactor)	DWT	voltage derivative	20	40	four-terminal meshed grid	half-bridge MMC	150	300 Ω	2
[95] (TW)	DWT	current variation	96	10	five-terminal meshed grid	half-bridge MMC	150	500 Ω	1
[98] (TW)	DWT	voltage & current derivatives	10	30	three-terminal star-connected	LCC/MMC (hybrid)	75 – 150	300 Ω	3
[100] (TW)	FFT	same as the main algorithm	2000	1000	CIGRE test grid	half-bridge MMC	N/A	200 Ω	0.5
[101] (TW)	HHT	undervoltage & current derivative	50	200	four-terminal meshed grid	half-bridge MMC	50	1 Ω	4
[102] (TW)	HHT	same as the main algorithm	10	16	seven-terminal meshed grid	two-level VSC	N/A	50 Ω	2
[104] (TW)	PMT	voltage derivative	N/A	N/A	four-terminal meshed grid	half-bridge MMC	150	200 Ω	1.1
[105] (TW)	PMT	voltage gradient	20	6	four-terminal meshed grid	half-bridge MMC	200 – 300	800 Ω	1
[108] (Artificial Intelligence)	CNN	accumulated TW energy	50	50	four-terminal meshed grid	half-bridge MMC	100	300 Ω	3
[110] (Special)	PMT/MG	undervoltage	20	N/A	four-terminal meshed grid	half-bridge MMC	50	300 Ω	0.6
[111] (Special)	MAD	same as the main algorithm	10	50	four-terminal meshed grid	LCL half-bridge MMC	20	N/A	3

and the largest window length (1000 samples) are associated with the FFT-based scheme proposed in [100].

Three significant aspects should be carefully considered when evaluating the performance of single-ended schemes. First, the fault resistance coverage of single-ended schemes should be large enough such that critical fault scenarios can be detected. The maximum fault resistance coverage is 800 Ω, which is achieved by the proposed scheme in [105]. In contrast, only faults with 1 Ω resistance are simulated in the proposed scheme in [101]. Second, the size of boundary reactors should be optimized since large reactors may result in severe stability issues, particularly with power flow reversal which is common in multi-terminal grids. Small reactors are superior in terms of stability and cost, yet their role in damping the sharp rise of fault currents may be seriously impacted. In [105], large reactor sizes in the range of 200-300 mH are employed to achieve the large fault resistance coverage of 800 Ω. The lowest reported reactor size is 5 mH which is tested with the proposed scheme in [90]. Third, severe external faults such as solid local- and remote-end bus faults should be evaluated, and the proposed algorithms should be able to discriminate these faults from high-resistance internal faults. Note that this aspect may also affect the selection process of reactor sizes according to the required filtering level that guarantees successful discrimination between internal and external faults.

Comparing double-ended schemes (Table 2.2) with single-ended schemes (Table 2.3), it is evident that single-ended schemes have relatively higher sampling frequencies and less fault resistance coverage compared to double-ended schemes. However, single-ended schemes are faster than double-ended schemes, mainly due to the exclusive dependency on local measurements, and hence, the absence of communication delays. Furthermore, single-ended schemes are more accurate as they do not rely on communicated data; thus, they are not affected by communication and synchronization errors. In summary, there is a trade-off between selectivity and speed in single- and double-ended schemes. Based on the aforementioned discussions in Sections 2.4 and 2.5, selective single-ended schemes are the appropriate candidates for primary protection, whilst double-ended schemes should be employed as reliable backup protection algorithms. Furthermore, an exemplary single-ended scheme should be augmented with a powerful mathematical tool capable of rapidly extracting the internal fault signature under severe fault conditions. Although relatively fast double-ended schemes have been proposed in the literature, communication delay, data synchronization mismatch, and incidental communication failure are the major obstacles that endanger their reliable operation for primary protection.

Although single-ended primary protection schemes have been already proposed, an improved scheme is still necessary to tackle the following shortcomings that have not been sufficiently investigated in the literature:

1. Severe fault conditions are not intensively investigated as the performance of most existing schemes deteriorates under these conditions.

2. Fault resistance coverage needs to be improved without requiring large reactor sizes as the case in [85, 105].

3. The general applicability of existing schemes in large multi-terminal grids with various configurations is not examined.

4. Most existing schemes use fixed thresholds based on extensive simulations which impede their general applicability; rather, adaptive thresholds based on analytical derivations should be adopted.

2.6 Conclusion

A comprehensive survey of existing HVDC grid protection schemes is presented in this chapter. There is a trade-off between selectivity and speed in single- and double-ended protection schemes. Highly selective single-ended protection schemes are the appropriate candidates for providing primary protection. Furthermore, single-ended schemes should be augmented with a powerful signal processing tool capable of rapidly extracting the internal fault signature under severe fault conditions. On the other hand, double-ended protection schemes can be employed as reliable backup protection algorithms. The inevitable communication delays as well as data synchronization and incidental communication failures impede the use of double-ended schemes as primary protection schemes. Reliable primary protection, backup protection, and fault location identification schemes are necessary to entirely protect the grid and tackle the shortcomings of existing schemes. All protection requirements should be thoroughly satisfied under various grid configurations and severe fault conditions.

Chapter 3

Primary Protection Scheme

3.1 Introduction

To attain reliable future supergrids with low carbon emissions, multi-terminal HVDC grids are considered as a promising candidate [58,116]. Protection of HVDC grids is a crucial step that requires further advancements to ensure the secure integration of RESs [117, 118]. A comprehensive review over existing primary protection schemes is presented in Chapter 2. Among the reviewed categories, TW-based schemes exhibit a more superior performance in terms of speed and fault resistance coverage since the fault-induced TWs can be used to form a reliable fault detection criterion. For instance, the proposed TW-based scheme in [100] detects various faults in 0.5 ms based on FFT. However, its fault resistance coverage is not large enough (200 Ω); in addition, it requires a large sampling frequency (2 MHz). Another example is the proposed TW-based scheme in [105] that detects various faults with a fault resistance as large as 800 Ω based on mathematical morphology. However, large boundary reactor sizes ($200 - 300$ mH) are required to reliably distinguish between high-resistance internal faults and external faults; thus, resulting in dynamic stability issues that arise with power flow reversal [94]. In summary, although TW-based schemes are superior to other schemes for HVDC grid protection, further improvements to achieve rapid fault detection and large fault resistance coverage are necessary.

TW-based protection schemes employ fault-induced TWs alongside their propagation characteristics to detect internal faults. Therefore, they require a robust signal processing technique to detect fault-induced TWs. Effective utilization of signal processing techniques in fault detection can facilitate the extraction of internal fault signatures; thus, resulting in protection schemes that do not require grid-dependent thresholds or predefined settings

[119]. Hence, signal processing-based protection schemes can be applied to HVDC grids with various operating points and configurations [120]. HHT is an adaptive and robust signal processing technique that can extract instantaneous features, i.e., instantaneous frequency and energy, from fault-induced TWs [121]. These instantaneous features can be used to promptly detect internal faults. Compared to Fourier transform, STFT, and the S transform, HHT retains the same domain, i.e., the time domain, during the transformation; thus, resulting in the extraction of real-time or instantaneous features. Since there is a compromise between frequency and time resolution in Wavelet transform, the extracted instantaneous features by HHT are more precise in time. Therefore, compared to Wavelet transform, HHT is more tailored to capturing rapidly varying transients associated with internal faults [122]. In addition, the selection of a proper mother wavelet is challenging and has a significant impact on the resulting transform coefficients. In contrast, HHT is an adaptive transform that does not require a predefined basis function [121].

This chapter proposes a fast, reliable, and selective single-ended primary protection scheme for multi-terminal HVDC grids that addresses the shortcomings in existing schemes. In the proposed scheme, HHT is applied to local voltage measurements to extract the instantaneous frequency and energy features. Abrupt changes in these features during internal faults are detected as outliers. Simultaneous outliers in the extracted features correspond to internal faults, which offers a setting-less fault detection criterion; thus, eliminating the need for simulation-based and grid-specific thresholds. This chapter is organized as follows: in Section 3.2, TW propagation theory and the fundamental mathematical description of HHT are presented. The simulated test system is introduced in Section 3.3. The instantaneous features extracted by HHT during various internal and external faults are analyzed in Section 3.4. The proposed protection algorithm is described in Section 3.5, and the simulation results are exhibited in Section 3.6. Finally, the conclusions are highlighted in Section 3.7.

3.2 Fault-Induced Traveling Waves and Hilbert-Huang Transform

In this section, propagation properties of fault-induced TWs are introduced. Then, two stages of HHT are elaborated and the instantaneous features extracted by HHT are presented.

3.2.1 Propagation of Traveling Waves

DC faults result in abrupt changes in voltage and current values at the fault point. As a result, high-frequency electromagnetic TWs are induced at the fault point, which propagate towards line terminals with a speed approximately equal to light speed [123]. The fundamental dynamic equations that describe the propagation phenomenon of fault-induced voltage (v) and current (i) TWs, as a function of time (t) and distance from the fault point (x), are as follows [124]:

$$\frac{\partial^2 v(x,t)}{\partial x^2} = \gamma^2 \, \frac{\partial^2 v(x,t)}{\partial t^2} \ , \tag{3.1}$$

$$\frac{\partial^2 i(x,t)}{\partial x^2} = \gamma^2 \, \frac{\partial^2 i(x,t)}{\partial t^2} \ , \tag{3.2}$$

where γ is the propagation constant given by:

$$\gamma = \sqrt{Z \, Y}, \tag{3.3}$$

where Z and Y are the per unit series impedance and shunt admittance of the line, respectively. The time-domain solution of (3.1) and (3.2) is given by [125]:

$$v(x,t) = \underbrace{v_b(t - \frac{x}{\nu_{TW}})}_{Backward\ Component} + \underbrace{v_f(t + \frac{x}{\nu_{TW}})}_{Forward\ Component} \tag{3.4}$$

$$\begin{aligned} i(x,t) = & \underbrace{i_b(t - \frac{x}{\nu_{TW}})}_{Backward\ Component} + \underbrace{i_f(t + \frac{x}{\nu_{TW}})}_{Forward\ Component} \\ = & \frac{1}{Z_c} \, v_b(t - \frac{x}{\nu_{TW}}) - \frac{1}{Z_c} \, v_f(t + \frac{x}{\nu_{TW}}) \ , \end{aligned} \tag{3.5}$$

$$\nu_{TW} = \frac{1}{\sqrt{Z \, Y}} \ , \tag{3.6}$$

$$Z_c = \sqrt{\frac{Z}{Y}} \ , \tag{3.7}$$

where ν_{TW} is the TW propagation velocity and Z_c is the characteristic impedance of the line. v_b and v_f are the backward (incident) and forward (reflected) voltage TWs, respectively. Similarly, i_b and i_f are the backward and forward current TWs, respectively. It is worth mentioning that the forward direction is from the line terminal (measurement point) to the fault point. Equations (3.4) and (3.5) show that the voltage and current at any point along the line, at a certain time instant from the fault inception, consist of backward and forward components. If the voltage and current measurements at line terminals are denoted by $v_m(t)$ and $i_m(t)$, respectively, the backward and forward voltage TWs at the relay location can be expressed as follows [124]:

$$v_b(t) = \frac{v_m(t) - Z_c\, i_m(t)}{2}\ , \tag{3.8}$$

$$v_f(t) = \frac{v_m(t) + Z_c\, i_m(t)}{2}\ . \tag{3.9}$$

Since the first incident backward TW at the relay location carries the internal fault signature, it will be used in this chapter to design a fast and reliable primary protection scheme.

3.2.2 Hilbert-Huang Transform

Equations (3.8) and (3.9) describe the fault-induced TWs at the relay location. In terms of frequency content, the fault-induced TWs consist of high-frequency components with different amplitudes [126]. Thus, a robust signal processing technique should be employed to extract the instantaneous features associated with the fault-induced TWs from the measured signals [124]. HHT is an adaptive and empirical signal processing technique capable of reliably analyzing nonlinear and non-stationary signals, e.g., transient fault signals [121]. Compared to Wavelet transform and STFT, where the mother wavelet and the window length are selected based on numerous simulation studies, HHT does not require prior settings [122].

HHT generates an analytic complex-valued signal $z(t)$ from real-valued data, e.g., a measurement signal $y(t)$. From the complex-valued $z(t)$, real-time instantaneous features such as the instantaneous frequency $IF(t)$ and instantaneous energy $IE(t)$ can be extracted. HHT has two stages. In the first stage, empirical mode decomposition (EMD) is employed to decompose $y(t)$ into a set of intrinsic mode functions (IMFs) through the sifting process [121, 127]. An IMF should be locally symmetric and the number of extrema

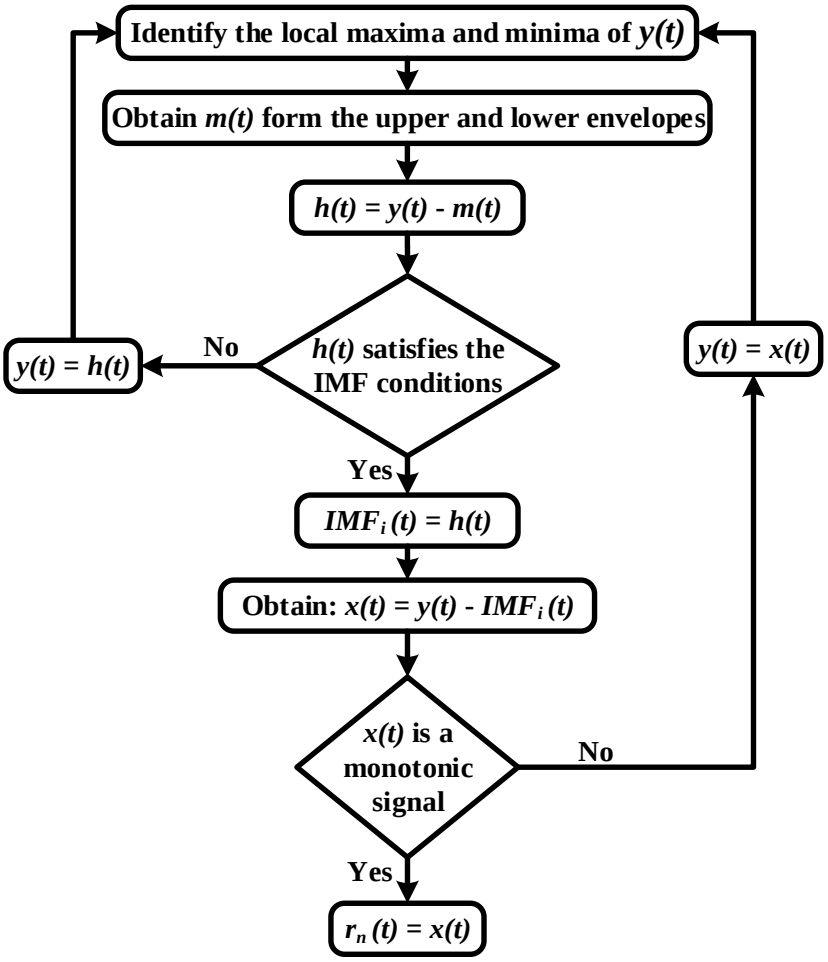


Figure 3.1: Simplified steps of the EMD sifting process.

and zero crossings of the IMF should be equal or differ at most by one. These two conditions are vital to guarantee that the estimated $IF(t)$ reflects the embedded frequency variations [121]. Mathematically, the EMD of $y(t)$ can be represented as:

$$y\left(t\right) = \sum_{i=1}^{n} IMF_i\left(t\right) + r_n\left(t\right), \tag{3.10}$$

where $r_n(t)$ is called the residue. $r_n(t)$ is a monotonic signal for which the IMF conditions can not be satisfied anymore [127].

Figure 3.1 summarizes the steps of the sifting process. After identifying the local maxima and minima of $y(t)$, the local maximum points are interpolated by a cubic spline

to form the upper envelope. Similarly, the lower envelope is obtained by connecting the local minimum points with a second spline. Then, to achieve a symmetric IMF, the local average of the two envelopes $m(t)$ is subtracted from $y(t)$ to obtain $h(t)$. This step is repeated until the first IMF is extracted. Then, the obtained IMF is subtracted from $y(t)$ to obtain $x(t)$. If $x(t)$ is not monotonic, these steps will be repeated to obtain the remaining IMFs. The sifting process is completed once $x(t)$ becomes monotonic. The sifting process results in the first extracted IMF to have the highest frequency component and $r_n(t)$ to be a monotonic signal. An advantage of EMD is that any superimposed riding waves, e.g., harmonics and measurement noise, on $y(t)$ will be inherently eliminated through the sifting process; thus, improving the robustness of the extracted instantaneous features.

In the second stage, Hilbert transform $H[.]$ is applied to the obtained IMF(s), and $z(t)$ is formed as [121]:

$$b\left(t\right) = H\left[IMF_i\left(\tau\right)\right] = \frac{1}{\pi}\int_{-\infty}^{+\infty}\frac{IMF_i\left(\tau\right)}{t-\tau}d\tau, \tag{3.11}$$

$$z\left(t\right) = IMF_i\left(t\right) + j\ b(t). \tag{3.12}$$

Finally, the instantaneous features $IF(t)$ and $IE(t)$ are calculated based on (3.13) and (3.14), respectively, where $IF(t)$ is the derivative of the phase angle of $z(t)$ and $IE(t)$ is the square of the amplitude of $z(t)$.

$$IF_i\left(t\right) = \frac{1}{2\pi}\ \frac{d}{dt}\left\{\tan^{-1}\frac{b(t)}{IMF_i\left(t\right)}\right\} \tag{3.13}$$

$$IE_i\left(t\right) = IMF_i(t)^2 + b(t)^2 \tag{3.14}$$

$IF(t)$ is the time-varying (local) frequency value of mono-component signals, which are defined as signals that have a single positive instantaneous frequency value at any time instant [121]. In other words, $IF(t)$ represents the intra-wave frequency variations due to the nonlinearity and non-stationarity of $y(t)$. To calculate $IF(t)$, $y(t)$ is decomposed into locally symmetric IMFs, which represent the various modes of oscillations, i.e., frequency components, embedded in $y(t)$. Therefore, the estimated $IF(t)$ can capture any abrupt changes in $y(t)$ in real-time [121]. In conventional transforms such as Fourier transform, the calculated (global) frequency corresponds to sinusoidal components with constant amplitudes that are embedded in the signal. However, the global frequency is not sufficient to describe non-stationary signals, where the frequency and amplitude of the decomposed components are continuously changing [122].

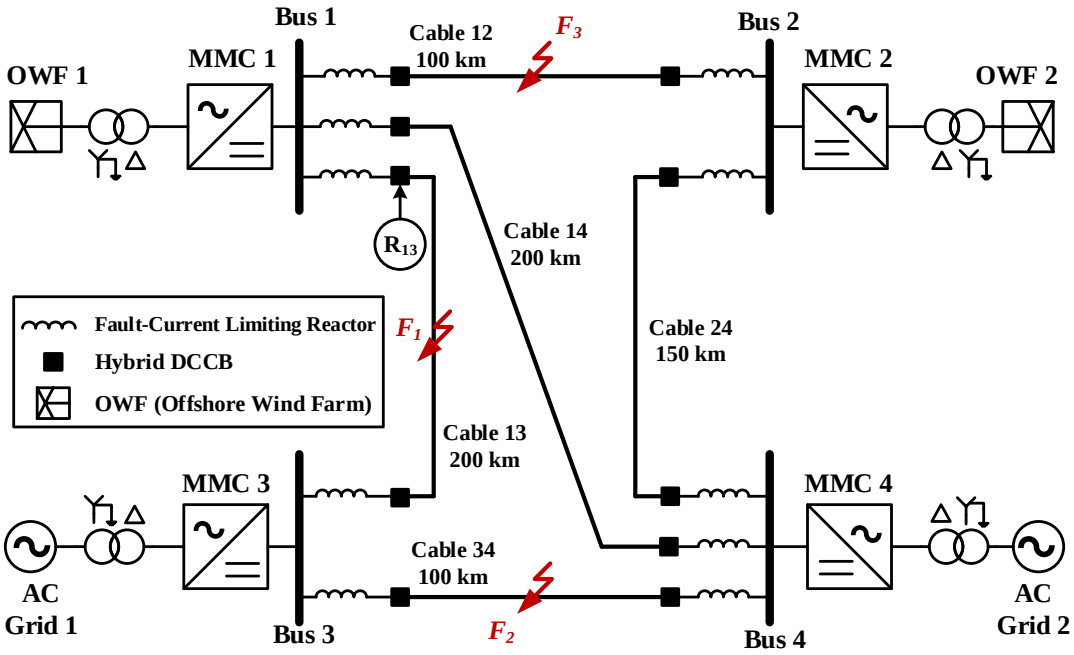


Figure 3.2: Four-terminal HVDC test grid.

3.3 Test Grid

The same four-terminal symmetrical monopolar HVDC grid, introduced in Chapter 2, is employed in this chapter, Figure 3.2. Half-bridge MMCs are installed at the four terminals. Five cables with different lengths are employed to connect the four terminals. At both ends of each cable, hybrid DC circuit breakers (DCCBs) and boundary reactors are implemented. The hybrid DCCBs are capable of interrupting the fault current within 2 ms [35]. The grid parameters are listed in Table 3.1. Active power control is provided by MMC 1 and MMC 2, while droop control is provided by MMC 3 and MMC 4. Further details regarding the grid parameters and converter control strategy can be found in [35].

3.4 Internal Fault Signature Based on HHT

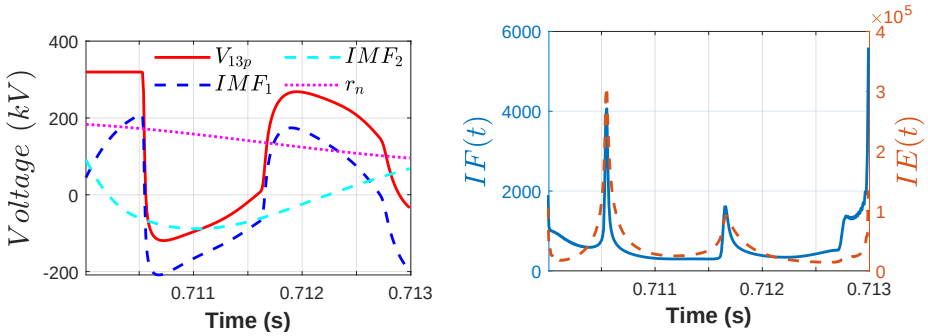
In this section, the instantaneous features extracted by HHT for internal and external faults are presented. In addition, the robustness of these features to fault location and resistance as well as measurement noise is demonstrated.

Table 3.1: Test grid parameters

	Parameter	Terminals 1-3	Terminal 4	Unit
AC Side	Rated power	900	1200	MVA
	Rated voltage	400		kV
	Grid reactance	17.7	13.4	Ω
	Grid resistance	1.77	1.34	Ω
	Transformer reactance	0.15		$p.u.$
MMC	Rated voltage	380		kV
	Number of SMs per arm	50		–
	SM capacitance	1465	1950	μF
	Arm inductance	84.8	63.6	mH
	Arm resistance	0.885	0.67	Ω
DC Side	Rated voltage	±320		kV
	Boundary inductance	50		mH

3.4.1 Internal Faults

In this chapter, R_{13} is the relay of interest that provides primary protection for cable 13. An internal PTP fault F_1 occurs at 0.71 s in the middle of cable 13. Figure 3.3 shows the positive-pole voltage waveform V_{13_p}, associated IMFs, and the instantaneous features of IMF_1. As shown in Figure 3.3a, V_{13_p} is decomposed into IMF_1, corresponding to the oscillation mode of the voltage waveform, IMF_2, and the residue. Based on (3.8), once the first backward TW (v_b) reaches the relay location, a sudden dip occurs in the voltage waveform; thus, resulting in a change in the oscillation mode of the signal and an abrupt increase in $IF(t)$, as shown in Figure 3.3b. Similarly, as depicted in Figure 3.3b, $IE(t)$ variations are correlated with the voltage waveform transients since $IE(t)$ corresponds to the instantaneous amplitude of the signal, according to (3.14). Therefore, the sudden dip in the voltage will result in a sudden change in $IE(t)$. In this fault scenario, two IMFs are



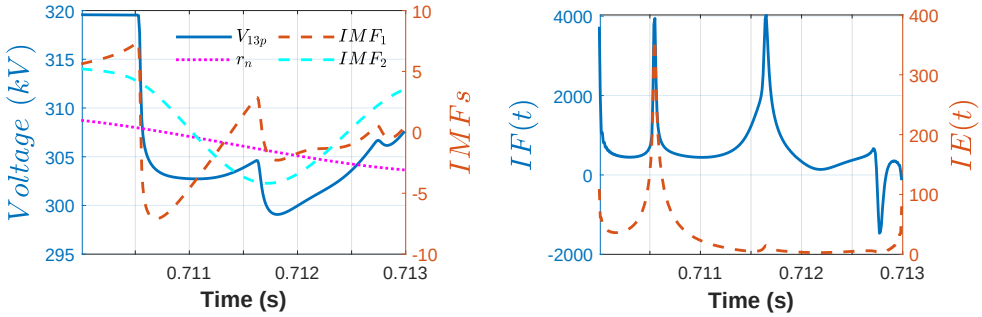
(a) EMD of V_{13_p}. (b) $IF(t)$ and $IE(t)$.

Figure 3.3: V_{13_p} and the corresponding features for F_1.

obtained. However, only the first IMF preserves the fault signature since the sudden dip in V_{13_p} appears only in IMF_1, as shown in Figure 3.3a. This results in simultaneous abrupt changes in $IF(t)$ and $IE(t)$, as shown in Figure 3.3b. IMF_2 has a smooth change when the fault wave arrives at R_{13} and consequently does not capture the fault signature. Therefore, the instantaneous features of IMF_2 will not be correlated with fault transients. It should be noted that the second incident TW reflected at the fault point causes a second abrupt change in $IF(t)$ and $IE(t)$, as shown in Figure 3.3b. However, these changes are less sharp with smaller amplitudes compared with the first abrupt change due to the attenuation of the second backward TW.

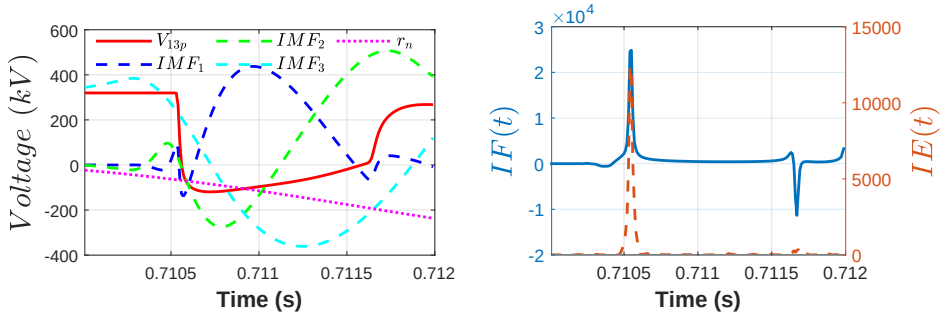
To emphasize the importance of the EMD stage and the robustness of the extracted instantaneous features by HHT, the fault parameters are changed and the obtained IMFs as well as the instantaneous features of IMF_1 are investigated. The impact of high-resistance faults on the extracted features is shown in Figure 3.4, where the fault resistance (R_F) is 1000 Ω. Similar to the solid fault scenario, the fault signature is only exhibited in IMF_1 and results in simultaneous abrupt changes in the instantaneous frequency and energy. The same conclusion is obtained when V_{13_p} has a signal-to-noise ratio (SNR) of 40 *db*, Figure 3.5.

The impact of fault location on the extracted instantaneous features is shown in Figure 3.6, where four internal solid PTP faults along cable 13 are simulated. Regardless of the fault location, simultaneous abrupt changes in $IF(t)$ and $IE(t)$ are observed when an internal fault occurs. Moreover, for faults close to R_{13}, the successive TW reflections between the relay location and fault point result in subsequent changes in $IF(t)$ and $IE(t)$ with smaller amplitudes compared with the initial abrupt changes, Figure 3.6b. The number of obtained IMFs depends mainly on the fault location and data window length. Considering



(a) EMD of V_{13_p}. (b) $IF(t)$ and $IE(t)$.

Figure 3.4: V_{13_p} and the corresponding features for F_1 with $R_F = 1000\ \Omega$.



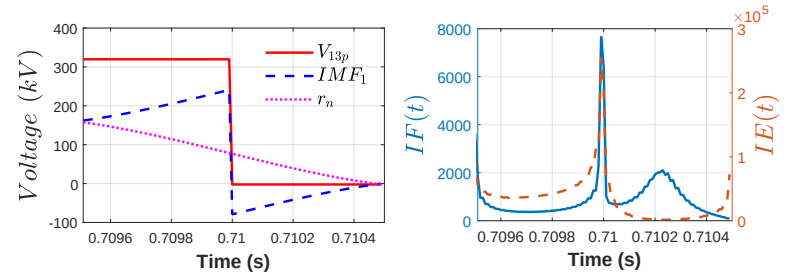
(a) EMD of V_{13_p}. (b) $IF(t)$ and $IE(t)$.

Figure 3.5: V_{13_p} and the corresponding features for F_1 with $SNR = 40\ db$.

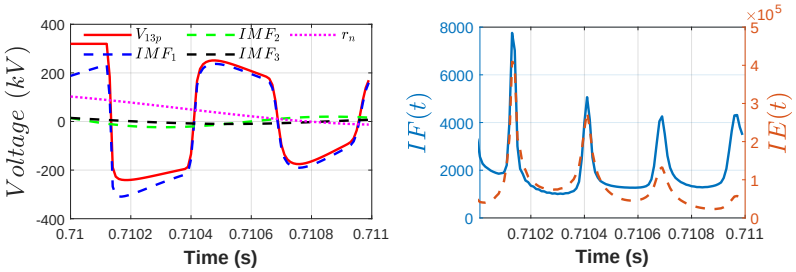
a 1 ms window for the four fault scenarios, only one IMF is obtained for the faults located at 125 km and the end of cable 13 as shown in Figure 3.6c and Figure 3.6d, respectively. In Figure 3.6a, a solid fault at the beginning of cable 13 causes V_{13_p} to immediately drop to zero, and only one IMF is obtained. Based on the analyses presented in this section, it is evident that only the first IMF carries the fault signature. Furthermore, the instantaneous features extracted from IMF_1 by HHT can be used for fault detection since the abrupt changes in these features are directly related to the fault-induced TWs.

3.4.2 External Faults

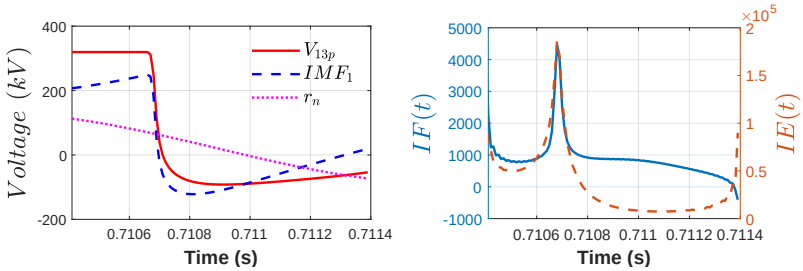
In this section, the extracted features for two external fault scenarios are studied. Fault F_2 is a forward external PTP fault in the middle of cable 34, whereas F_3 is a reverse external PTP fault in the middle of cable 12. The EMD of V_{13_p} and the extracted features of IMF_1 for F_2 and F_3 are shown in Figures 3.7 and 3.8, respectively. As shown in



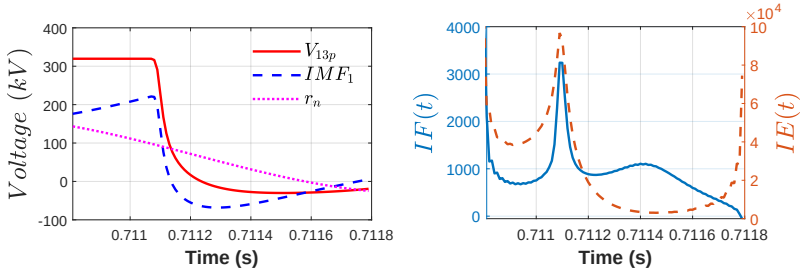
(a) PTP fault at the beginning of cable 13.



(b) PTP fault at 25 km from bus 1.

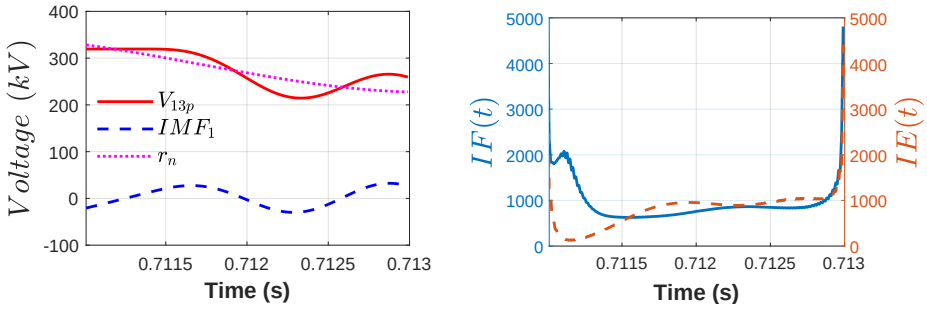


(c) PTP fault at 125 km from bus 1.



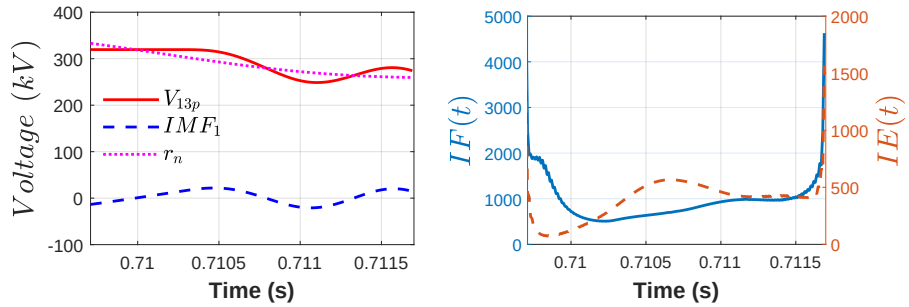
(d) PTP fault at the end of cable 13.

Figure 3.6: EMD of V_{13_p} and the corresponding extracted features for various internal faults along cable 13.



(a) EMD of V_{13_p}. (b) $IF(t)$ and $IE(t)$.

Figure 3.7: V_{13_p} and the corresponding features for a forward external fault F_2.

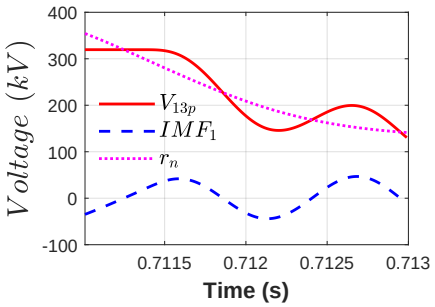


(a) EMD of V_{13_p}. (b) $IF(t)$ and $IE(t)$.

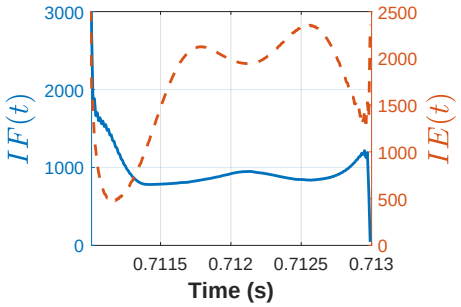
Figure 3.8: V_{13_p} and the corresponding features for a reverse external fault F_3.

Figures 3.7a and 3.8a, there are no sudden dips in V_{13_p} and IMF_1. The reason is that the first backward TW v_b will be drastically attenuated and its sharp wavefront and high-frequency components will be smoothed out after passing through two boundary reactors and before reaching R_{13}. Therefore, compared to internal faults such as F_1, no abrupt changes are observed in $IF(t)$ and $IE(t)$, Figures 3.7b and 3.8b. To study the impact of boundary reactor size on the extracted features, F_2 and F_3 are re-simulated with a smaller boundary inductance of 25 mH. The EMD of V_{13_p} and the extracted features of IMF_1 for F_2 and F_3 are shown in Figures 3.9 and 3.10, respectively. As the boundary inductance decreases, the dip in v_{13_p} increases. Therefore, $IE(t)$ will have a larger peak compared to those of Figures 3.7b and 3.8b. However, no abrupt changes are observed in $IF(t)$ and $IE(t)$ since there are no sudden dips in V_{13_p} and IMF_1.

Breaker operation during external faults is one of the transients that might result in relay maloperation. To investigate this scenario, F_2 is simulated and the impact of primary breaker operation of cable 34 on R_{13} is examined, Figure 3.11. Primary breakers of cable

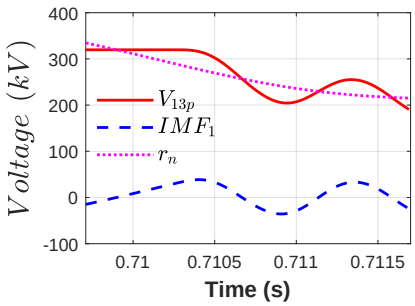


(a) EMD of V_{13_p}.

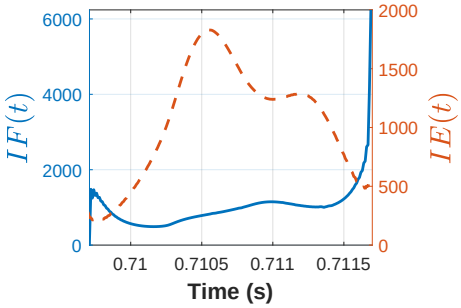


(b) $IF(t)$ and $IE(t)$.

Figure 3.9: V_{13_p} and the corresponding features for F_2 with $L_{dc} = 25\ mH$.



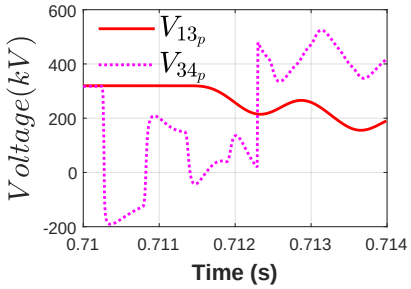
(a) EMD of V_{13_p}.



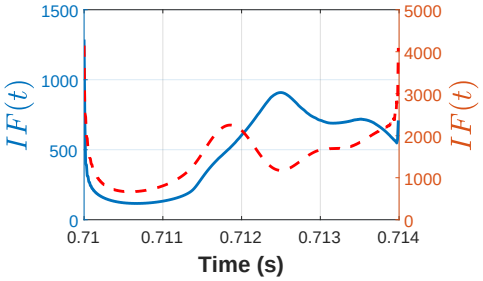
(b) $IF(t)$ and $IE(t)$.

Figure 3.10: V_{13_p} and the corresponding features for F_3 with $L_{dc} = 25\ mH$.

34 are set to isolate the fault 2 ms after fault detection, which results in a sudden increase in V_{34_p}, corresponding to the developed counter voltage across the breaker caused by the surge arrester, as shown in Figure 3.11a. However, as shown in Figure 3.11b, no abrupt changes are observed in $IF(t)$ and $IE(t)$, calculated by R_{13}, since there are no sudden dips in V_{13_p}. Other scenarios such as changes in the system operating point may impact the performance of the proposed scheme. To investigate those cases, the reference DC voltage of bus 1 is reduced to $\pm 288\ kV$ (10% drop) while running the simulation, Figure 3.12. As shown in Figure 3.12b, similar waveforms as those shown in Figure 3.11b are obtained with no abrupt changes in $IF(t)$ and $IE(t)$ since there are no resulting sudden dips in V_{13_p}, as shown in Figure 3.12a. In summary, it can be concluded that the instantaneous features $IF(t)$ and $IE(t)$ extracted from IMF_1 by HHT can be used to form a fast fault detection criterion that can reliably distinguish between internal and external faults under various fault conditions.

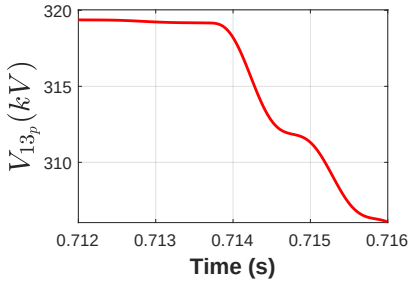


(a) V_{13_p} and V_{34_p}.

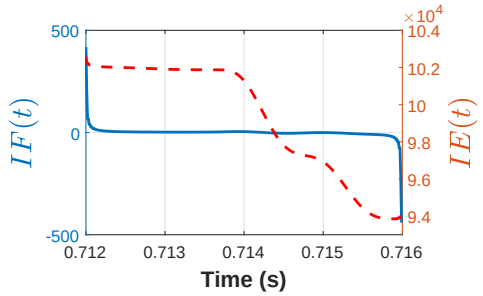


(b) $IF(t)$ and $IE(t)$ at R_{13}.

Figure 3.11: V_{13_p}, V_{34_p}, and the corresponding features for F_2 considering breaker operation.



(a) V_{13_p}.



(b) $IF(t)$ and $IE(t)$.

Figure 3.12: V_{13_p} and the corresponding features during the change of the reference DC voltage.

3.5 Proposed Fault Detection Algorithm

In this chapter, a fast and reliable primary protection algorithm is proposed, which only uses local voltage measurements of the positive and negative poles. The proposed algorithm consists of three stages, as shown in Figure 3.13. In the first stage, the instantaneous features of both poles, i.e., IF_p, IF_n, IE_p, and IE_n, are extracted by applying HHT to a 1 ms moving window of measured voltages of positive and negative poles. The employed sampling frequency is 100 kHz such that the extracted instantaneous features capture the fault-induced TWs, which have high-frequency components in the order of hundreds of kHz [123]. It is worth mentioning that modern digital signal processors have sufficiently large sampling rates to process the measured signals and execute the required computations of the proposed algorithm [128]. It is worth noting that $IF(t)$ remains below 50 kHz across all simulated fault scenarios. This complies with the Nyquist theorem and ensures

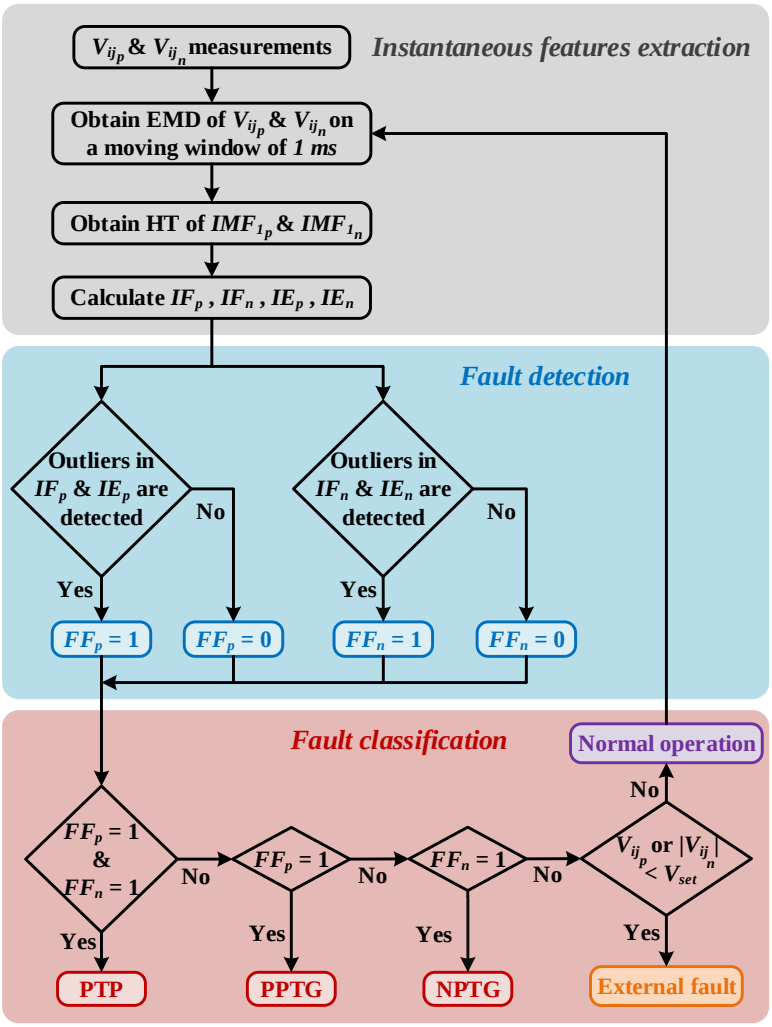


Figure 3.13: Flowchart of the proposed primary protection scheme.

that the extracted fault-induced frequency components are accurately captured at the employed sampling rate. The proposed scheme does not require a startup criterion that may fail under severe fault conditions, which prevents the protection scheme from being triggered. Most startup criteria in the literature depend on voltage derivative [74] and voltage gradient [129]. These criteria not only require grid-specific thresholds but also may fail during high-resistance faults.

The second stage is the fault detection stage, where a fault flag FF is triggered during an internal fault event if simultaneous outliers in the instantaneous frequency and energy are detected. In statistics, outliers are defined as singular data points that falls significantly

outside the remaining points in a data set [130]. Mathematically, a data point a_i in a window of N samples is detected as an outlier if its value is above the window average μ by at least three times the standard deviation σ of the window [131].

$$a_i \geq \mu + 3\ \sigma\ , \tag{3.15}$$

where,

$$\mu = \frac{1}{N}\sum_{i=1}^{N} a_i\ , \tag{3.16}$$

$$\sigma = \sqrt{\frac{\sum_{i=1}^{N}(a_i - \mu)^2}{N-1}}\ . \tag{3.17}$$

The results of applying the proposed outlier-based fault detection criterion to the internal fault scenario F_1 are shown in Figure 3.14. At $t = 0.71054\ s$, the fault-induced TWs reach the relay location, which results in a sudden dip in V_{13_p} and simultaneous abrupt changes in $IF(t)$ and $IE(t)$ at the same instant, as shown in Figure 3.3b. Once these abrupt changes arise around the center of the moving window, simultaneous outliers will be observed. For F_1, the simultaneous outliers are detected by the data window captured at $t = 0.7108\ s$, as shown in Figure 3.14. Employing outlier detection provides a robust and setting-less fault detection criterion in the proposed scheme as internal faults, regardless of fault parameters and conditions, are associated with abrupt changes in voltage measurements. These changes result in simultaneous sharp notches in $IF(t)$ and $IE(t)$ that can be reliably detected as outliers. This feature not only improves the reliability and robustness of the proposed scheme under severe fault conditions but also guarantees its applicability to large multi-terminal HVDC grids with various configurations. It should be noted that the first and last ten values of the extracted instantaneous features are discarded to avoid any maloperation due to the edge effect of HHT, which is caused by the fitting process of the maximum and minimum splines [121].

The third stage is the fault classification stage, where the fault type is identified based on the calculated FF values in the second stage. As shown in Figure 3.13, a PTP fault is identified if both FF values of the positive and negative poles are unity. If only the FF of the positive pole is triggered, the fault is a positive-pole-to-ground (PPTG) fault. If only the FF of the negative pole is triggered, the fault is a negative-pole-to-ground (NPTG) fault. If both FF values are zero, an undervoltage criterion is employed to check for external faults. The undervoltage threshold V_{set} is selected as 0.85 $p.u.$ such that a 15%

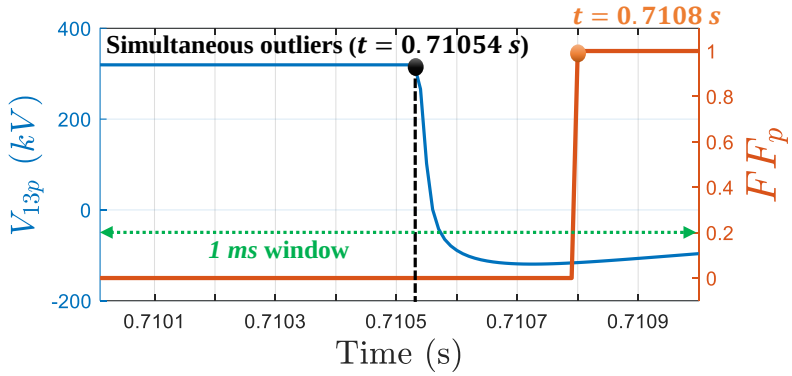
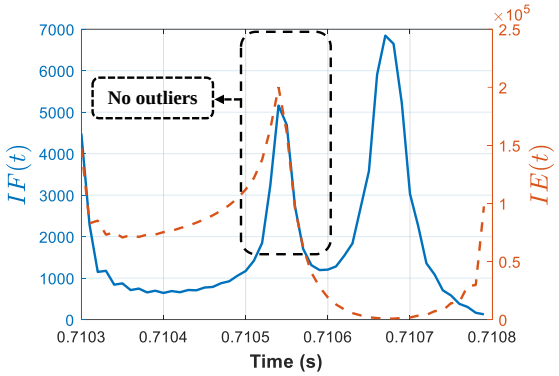


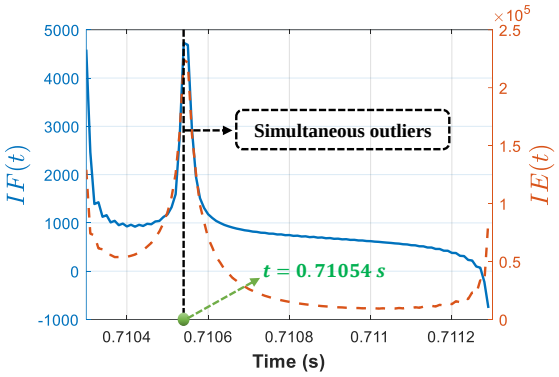
Figure 3.14: V_{13_p}, FF_p, and the detect outliers in $IF(t)$ and $IE(t)$ during the fault F_1.

voltage drop, as recommended in [77], is allowed during normal grid operation. It is worth mentioning that since the FF values of positive and negative poles are simultaneously calculated, no additional fault classification criterion is required to identify the fault type. This is an advantage compared to most existing schemes in the literature, such as the one proposed in [105], where the zero-mode voltage integral is used to identify the faulted pole(s). Therefore, the proposed scheme is fast and requires less computation compared to existing schemes. Fault classification is essential for isolating the faulted pole and ensuring supply continuity in case of pole-to-ground faults via the sound pole; therefore, enhancing the transmission system stability and security. Furthermore, fault type information is required for fault location and reclosing schemes to determine the exact fault location and distinguish between permanent and temporary faults; thus, achieving rapid system restoration [132].

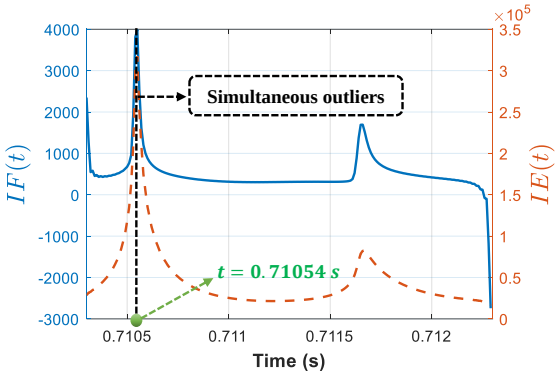
The moving window length of the proposed algorithm is selected such that fast fault detection is attained provided that the extracted instantaneous features are directly correlated with the fault-induced TWs. The algorithm will maloperate if short moving windows are selected as the extracted instantaneous features may not capture the internal fault signature due to insufficient voltage samples. For instance, Figure 3.15a depicts the instantaneous features for F_1 when a 0.5 ms moving window is employed. As shown, no outliers are detected since there are no abrupt changes in $IF(t)$ and $IE(t)$ as compared to Figure 3.15b, where a 1 ms moving window is employed, and simultaneous outliers are detected at time $t = 0.71054$ s. In addition, a second peak in $IF(t)$ is obtained in Figure 3.15a, which is not correlated with fault-induced TWs and may result in false detection of an internal fault. On the other hand, longer moving windows will unnecessarily slow down fault detection speed of the proposed algorithm. In Figure 3.15c, the extracted features when a 2 ms moving window is employed are shown. It can be seen that the same outliers as of Figure 3.15b are obtained.



(a) 0.5 ms moving window.



(b) 1 ms moving window.



(c) 2 ms moving window.

Figure 3.15: The extracted instantaneous features and detected outliers for F_1 with various window lengths.

3.6 Simulation Results

The reliability and selectivity of the developed primary protection scheme under various internal and external fault scenarios are demonstrated in this section.

3.6.1 Internal Faults

The analyses presented in Section 3.4.1 show that the instantaneous features of IMF_1 extracted by HHT have the internal fault signature under various fault parameters and conditions. In this section, 165 internal fault scenarios along cable 13 are simulated. R_F is changed from 0.01 Ω (solid fault) to 1000 Ω in steps of 100 Ω. For each R_F value, various fault types (PTP, PPTG, and NPTG) are simulated along the entire cable length starting from the local end, right after R_{13}, towards the remote end in steps of 50 km. All faults are initiated at 0.71 s. All simulated scenarios are successfully detected as internal faults in less than 1 ms, and the correct FFs are triggered.

The algorithm operating time is defined as the time interval between the instant when a FF is triggered and the arrival time of v_b at R_{13}. The largest operating time of the proposed algorithm is 0.73 ms, which is associated with a solid PPTG fault at the remote end of the cable. The operating time of the algorithm for PPTG and NPTG faults is the same when other fault parameters are identical. Moreover, the algorithm operating time in case of PPTG and NPTG faults is slightly longer than PTP faults due to the mutual coupling between the faulted and healthy poles, which slightly delays the abrupt changes in the instantaneous features. For instance, the operating time of a solid PTP fault at the remote end of the cable is 0.71 ms, while that of a PPTG is 0.73 ms. The computation time of modern digital signal processors is in the range of a few microseconds [133]. With a sampling frequency of 100 kHz, a new sample will be acquired after 10 μs, which is a sufficient time for modern digital signal processors to perform the required computations. Consequently, the fault detection time of the proposed algorithm will not exceed 1 ms for all fault scenarios.

As the fault location moves away from R_{13}, the operating time increases due to the attenuation of v_b, which delays the abrupt changes in the instantaneous features, Figure 3.16. For the same reason, as shown in Figure 3.17, the operating time increases as R_F increases. A special scenario is a remote-end fault located at 200 km from bus 1, for which the operating time decreases as R_F increases, Figure 3.18. The reason is that v_b and the first reflected TW will simultaneously reach R_{13}; besides, as R_F increases, the magnitude

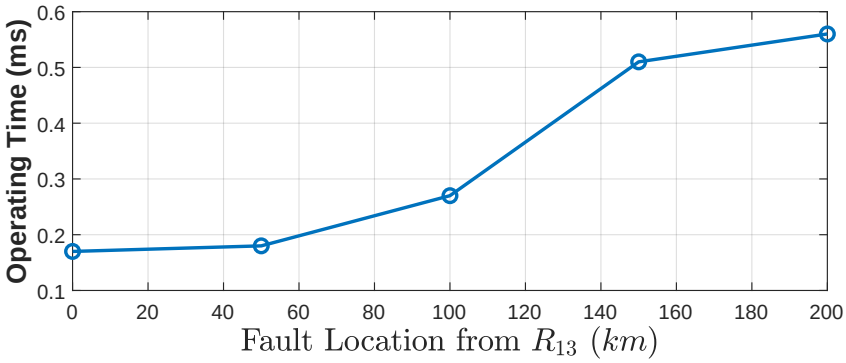


Figure 3.16: Operating time for various solid PTP faults along cable 13.

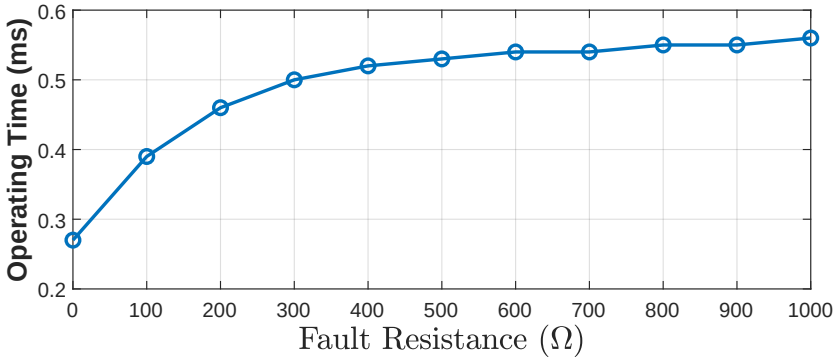


Figure 3.17: Operating time for F_1 with R_F changing from 0.01 Ω to 1000 Ω.

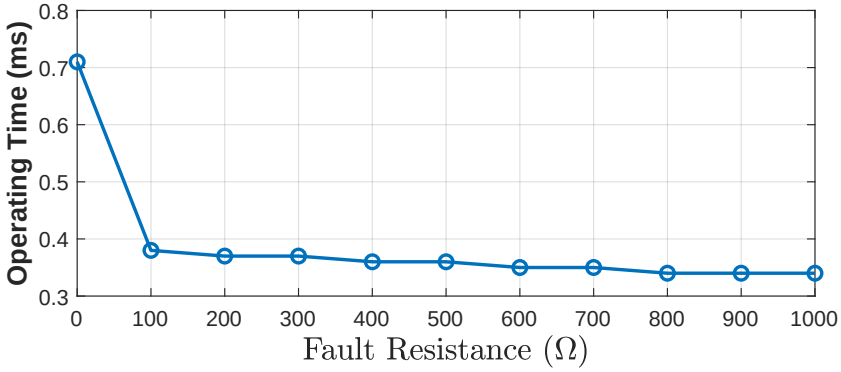


Figure 3.18: Operating time for a PTP fault at 200 km from bus 1 with R_F changing from 0.01 Ω to 1000 Ω.

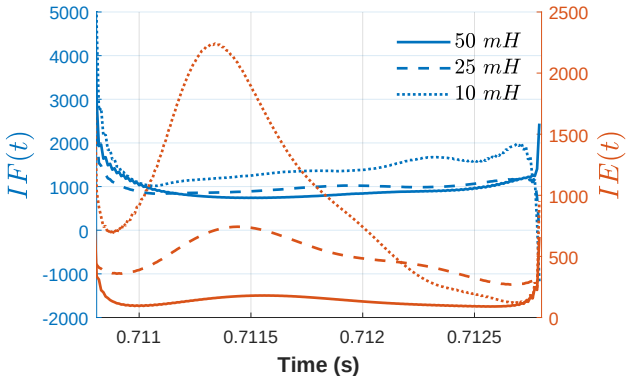
of the reflected wave increases [124]; thus, accelerating the detection of abrupt changes in the instantaneous features.

3.6.2 External Faults

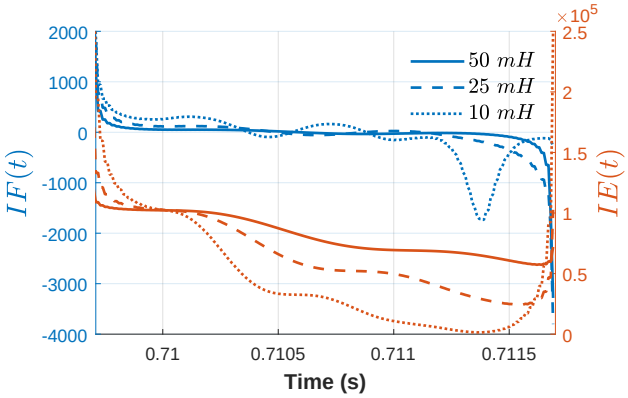
In this section, 36 solid PTP, PPTG, and NPTG external faults at the beginning, middle, and end of cables 34, 12, 14, and 24 are simulated. Two solid PTP faults at buses 1 and 3 are studied as well. The resulting FF values for R_{13} are all zero; thus, confirming the selectivity and reliability of the proposed scheme under various external faults, including critical ones at buses and the beginning of adjacent cables. Furthermore, as shown in Figures 3.7 and 3.8, there are no abrupt changes in the voltage waveform during external faults regardless of the fault direction. Therefore, forward and reverse external faults result in no abrupt changes in the extracted instantaneous features; thus, no outliers are detected by the proposed scheme. This is one of the advantages of the proposed method as the majority of existing schemes use fault direction, obtained from current measurements, in the initial step to prevent relay operation during reverse external faults. Then, a second criterion is applied to distinguish between internal and forward external faults [101].

During internal faults, the proposed fault detection criterion depends only on the first incident TW before it is reflected at the boundary reactor. Therefore, the size of boundary reactors has no impact on the performance of the proposed scheme during internal faults. On the other hand, boundary reactors filter out the fault-induced high-frequency components during external faults. Hence, the sudden dip in the voltage waveform will be smoothed, and consequently, no abrupt changes in the extracted instantaneous frequency and energy will be observed. As a result, no outliers will be detected by the proposed fault detection criterion. Thus, external faults can be successfully discriminated from internal faults, and the maloperation of the proposed scheme during external faults is avoided. The inductance of the boundary reactors in the test system shown in Figure 3.2 is 50 mH. To evaluate the impact of the inductance on the performance of the proposed fault detection criterion during external faults, critical external fault scenarios are studied. These scenarios include a forward PTP fault at the beginning of cable 34 and two reverse PTP faults at the beginning of cables 12 and 14 with reactor sizes of 50 mH, 25 mH, and 10 mH. Figure 3.19 shows the extracted instantaneous features of these fault scenarios. In all these fault scenarios, regardless of the reactor size, no abrupt changes in $IF(t)$ and $IE(t)$ are observed, and no outliers are detected. This confirms the correct performance of the proposed algorithm even in an HVDC grid with a small boundary inductance of 10 mH. This is one of the main advantages of the proposed scheme as smaller reactors are less costly, have a smaller footprint, and have lower losses. In addition, larger inductances may impose dynamic stability issues, particularly with power flow reversal [94].

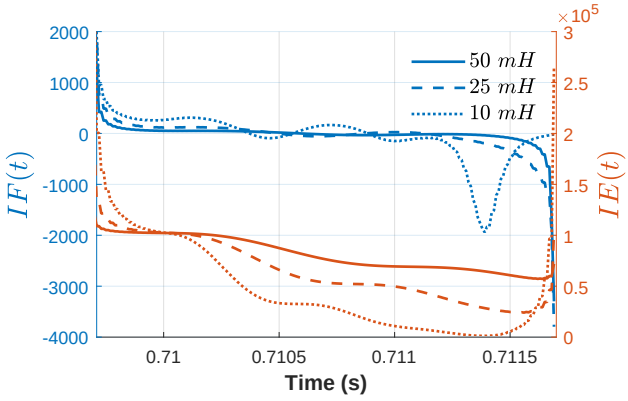
It should be noted that the minimum size of boundary reactors, where the performance of the proposed scheme is not impacted, is not fixed at 10 mH for all HVDC grids. Rather,



(a) Fault on cable 34.



(b) Fault on cable 12.



(c) Fault on cable 14.

Figure 3.19: $IF(t)$ & $IE(t)$ for external faults under various boundary reactor sizes.

it depends on system parameters such as system voltage, line impedance, the equivalent impedance of MMCs, and the typical rate of change of the system voltage during the fault. Those parameters change from one system to another. Thus, the minimum size of boundary reactors can be determined based on simulation studies for each grid individually. However, the proposed scheme manifests its applicability to multi-terminal grids with weak boundary conditions and will not require large boundary reactors compared to the existing schemes. For instance, the proposed scheme in [104] will work well only if the limiting reactors are larger than 100 mH. Moreover, a large boundary reactor of 300 mH is required in [105] to distinguish between internal and external faults. As mentioned in [134], the size of boundary reactors in HVDC grids is usually between $100 - 200$ mH. For instance, the Zhangbei four-terminal HVDC grid in China, the world's first multi-terminal meshed grid, utilizes 150 mH boundary reactors at both ends of each line within the grid [48]. The presence of boundary reactors, regardless of their size, ensures the effectiveness of the proposed algorithm since their smoothing effect prevents simultaneous abrupt changes in the extracted instantaneous frequency and energy (Figure 3.19). Consequently, external faults can be reliably distinguished from internal faults; thus, avoiding the maloperation of the proposed scheme during external faults. The designed scheme is capable of reliably detecting simultaneous faults within the HVDC grid. If two faults occur nearly simultaneously on different lines, each fault is detected independently by its respective primary relay. If both faults occur on the same line, the nearest local relay to each fault will detect and isolate the fault based on local voltage measurements. This localized detection ensures that the scheme remains effective even under simultaneous fault conditions.

3.6.3 Impact of Measurement Noise

To study the impact of measurement noise on the performance of the proposed scheme, $SNRs$ of 40 and 50 db for the voltage measurements are considered. Internal PTP faults with $R_F = 500\ \Omega$ and $1000\ \Omega$ are simulated at the beginning, middle, and end of cable 13. Additionally, external faults are simulated at the beginning of cables 34, 12, and 14. As shown in Table 3.2, all the simulated internal faults are successfully detected by the proposed scheme, i.e., all FFs are unity. On the other hand, all FFs are zero for all external faults; thus, confirming the security of the proposed scheme during severe external faults. It is worth mentioning that the proposed scheme may maloperate with lower SNR values. However, the typical range of SNR values in transmission systems is $80-90$ db [135]. This range is guaranteed through proper shielding of sensors and using filters and signal processing techniques such as averaging and noise cancellation algorithms [136].

Table 3.2: Performance of the proposed scheme in the presence of measurement noise

Fault Type	**Faulted Cable**	**Fault Location** (km)	SNR (db)	R_F (Ω)	FF_p & FF_n	**Operating Time** (ms)
PTP	Cable 13	0	50	500	1	0.21
		100			1	0.34
		200			1	0.50
PTP	Cable 13	0	40	500	1	0.23
		100			1	0.39
		200			1	0.51
PTP	Cable 13	0	50	1000	1	0.24
		100			1	0.43
		200			1	0.48
PTP	Cable 13	0	40	1000	1	0.26
		100			1	0.47
		200			1	0.49
PTP	Cable 34	0	40-50	0.01	0	-
	Cable 12	0			0	-
	Cable 14	0			0	-

3.6.4 Comparison with Other Schemes

Table 3.3 shows a detailed comparison between the proposed scheme and existing schemes in the literature. Compared with HHT-based schemes [69, 101, 102], the proposed scheme detects high-resistance faults up to 1000 Ω, which is double the maximum achievable coverage in [69]. Moreover, internal faults are rapidly detected in less than 1 ms, which is half the operating time of the fastest HHT-based algorithm (proposed in [102]); thus, complying with the stringent HVDC grid primary protection speed requirements. In addition, the proposed scheme reliably detects severe internal faults, such as remote high-resistance faults, and distinguishes them from critical external faults like solid bus faults. The proposed scheme in [101] fails to detect these fault scenarios, and they are not investigated in [69, 102].

Table 3.3: Comparison between the proposed scheme and existing schemes

Reference	Signal Processing Technique	Fault Detection Criterion	Tested Grid Configuration	Boundary Reactor Size	R_F Coverage	Operating Time	Sampling Frequency
[97]	DWT	Energy of Wavelet coefficients	Three-terminal star-connected grid	Not reported	50 Ω	3 ms	50 kHz
[95]	DWT	Instantaneous current-differential	Five-terminal meshed grid	150 mH	500 Ω	1 ms	96 kHz
[98]	DWT	Forward/backward TW ratio	Three-terminal star-connected grid	150 mH	300 Ω	3 ms	10 kHz
[100]	FFT	TW frequency spectral ratio	CIGRE nine-terminal benchmark grid	Not reported	200 Ω	0.5 ms	2 MHz
[104]	Modal-Domain Analysis	Line-mode reactor voltage	Four-terminal meshed grid	150 mH	200 Ω	1.1 ms	100 kHz
[120]	S Transform	Gaussian function	Seven-terminal meshed grid	Not reported	10 Ω	1.3 ms	10 kHz
[105]	Mathematical Morphology	TW surge arriving time difference	Four-terminal meshed grid	300 mH	800 Ω	1 ms	20 kHz
[102]	HHT	Density of $IE(t)$	Seven-terminal meshed grid	Not reported	50 Ω	2 ms	10 kHz
[101]	HHT	Average frequency	Four-terminal meshed grid	50 mH	1 Ω	4 ms	25 kHz
[69]	HHT	Harmonics	CIGRE nine-terminal benchmark grid	Not reported	500 Ω	Not reported	100 kHz
Proposed Scheme	HHT	Outliers	Four-terminal meshed grid	50 mH	1000 Ω	1 ms	100 kHz

Compared with existing TW-based schemes [95,97,98,100,104,105,120], whose thresholds are selected based on intensive simulations and applied only to a specific test grid, the proposed scheme provides a robust and setting-less fault detection criterion that does not rely on the grid configuration or parameters. Furthermore, the proposed scheme reliably detects high-resistance faults in HVDC grids with small boundary reactors (up to 10 mH), while large boundary reactors ($200 - 300$ mH) are required to detect such faults in [105]. It should be noted that boundary reactor sizes reported in Table 3.3 are the typical values of the reported test grid. Additionally, the proposed scheme does not require an additional criterion to identify the faulted pole or the fault direction, which is the case in [101,105,120]. Compared to DWT-based schemes [95, 97, 98], the proposed HHT-based scheme achieves higher resistance coverage and operates with smaller boundary reactor sizes, enhancing its sensitivity and applicability in practical HVDC networks. In terms of computational complexity, the EMD stage in HHT is more intensive than DWT, but remains feasible for real-time implementation, as demonstrated in Chapter 7. Furthermore, the HHT-based scheme can be realized on standard DSP platforms without requiring extensive filter banks or multi-resolution analysis, resulting in comparable or even lower hardware costs in practice [127].

TW-based schemes are typically implemented in microprocessor-based relays capable of fast data acquisition and processing; thus, ensuring rapid fault detection and isolation [137]. A practical example is the well-known control and protection system called Modular Advanced Control for HVDC (MACH™), developed by Hitachi Energy and practically installed in many HVDC projects. The MACH control and protection system is equipped with state-of-the-art microcontrollers and digital signal processors to facilitate the implementation of TW-based schemes [138]. Finally, it is worth mentioning that the proposed scheme is conceptually scalable to large multi-terminal HVDC grids with any number of terminals. This is primarily due to its setting-less fault detection criterion, which relies only on local voltage measurements and does not require system-wide communication. As a result, the scheme is computationally modular and can be executed independently at each terminal, making it a promising protection solution for future large-scale HVDC grids.

3.7 Conclusion

A robust single-ended protection scheme for multi-terminal HVDC grids is proposed in this chapter. The proposed scheme rapidly detects internal faults and reliably distinguishes them from external faults. HHT is applied to local voltage measurements to extract the instantaneous frequency and energy features. Internal faults are identified when simultaneous outliers in both instantaneous frequency and energy are detected. The main advantages of the proposed scheme are summarized as follows:

- Rapid detection and discrimination of internal faults in less than 1 ms.
- A setting-less fault detection criterion, which is based on outlier-detection, is proposed, eliminating the need for simulation-based and grid-specific thresholds. This ensures its applicability to multi-terminal HVDC grids with various configurations and parameters.
- The proposed scheme detects internal faults with high resistances up to 1000 Ω without requiring large boundary reactor sizes. Additionally, it reliably distinguishes between internal and external faults even when the boundary reactor size is as small as 10 mH.
- The proposed scheme reliably detects severe internal faults such as close solid faults and remote high-resistance faults, whereas it is blocked during critical external faults such as bus faults and faults at the beginning of adjacent lines.

- No additional fault classification or faulted pole selection criteria are required since FF values can directly identify the faulted pole(s). Therefore, the proposed scheme is fast and computationally efficient compared to other schemes that require an additional criterion for faulted pole identification.
- The proposed scheme is highly robust to fault resistance, fault location, boundary reactor size, and measurement noise.

Chapter 4

Fault Location Identification Scheme

4.1 Introduction

Fault location identification schemes are substantial to minimize the duration of HVDC grid outages and accelerate the restoration of its normal operation [139, 140]. In HVDC grids, DC fault currents reach high levels within a few milliseconds due to the low network inertia and impedance [34, 141]. Therefore, primary relays are required to rapidly detect faults in less than 3 ms [142]. Thus, fault location identification schemes have limited fault data to estimate the fault location. Fault location schemes are classified into single-ended and double-ended schemes [143, 144]. Single-ended schemes estimate the fault location based on local measurements and by determining the arrival instants of the first two backward traveling waves (BTWs) reflected from the fault location [145, 146]. In double-ended schemes, the fault location is estimated based on the two time instants when the initial fault-induced BTWs reach both terminal relays [123]. Single-ended schemes are less accurate, have lower fault resistance coverage, and require higher sampling frequency compared to double-ended schemes [139]. The reason is that the detection of the second reflected BTW is challenging, primarily due to attenuation caused by successive reflections at the relay and fault location. Additionally, during remote faults, the BTW reflected from the remote terminal arrives at the local relay before that reflected from the fault location; thus, resulting in an inaccurate estimation of the fault location [147].

Various double-ended TW-based fault location identification schemes have been proposed in the literature [123, 139, 148–150]. In [139], a convolution-based algorithm is proposed to estimate the fault location. However, the fault location estimation error is relatively high as it depends on curve fitting methods. In addition, this scheme can not locate

high-resistance PTP faults. In [123], voltage measurements are optimally segmented, then a search algorithm is applied to detect BTWs. However, the error of this scheme is large, and the fault resistance coverage is limited. HHT-based fault location schemes have better accuracy than other TW-based schemes [148–150]. The reason is that HHT can accurately detect the arrival time of BTWs in real time based on the extracted instantaneous features that are instantly affected by fault transients [122]. In [148], the product of the instantaneous amplitude and frequency is compared with a threshold to capture the wavefront arrival instants at both terminals. The proposed criterion in [149] depends on a modified instantaneous frequency spectrum to detect BTWs, while the proposed one in [150] is based on an amplitude-frequency coefficient (AFC) extracted by HHT. The main deficiencies of existing HHT-based fault location schemes are: 1) limited fault resistance coverage; 2) long data window requirement; 3) high sampling frequency requirement to accurately capture BTWs; and 4) dependence on threshold values that rely on network configuration and parameters. A double-ended fault location scheme is proposed in this chapter. Based on HHT, the arrival instants of the initial fault-induced BTWs at both line terminals are determined to estimate the fault location. The organization of the remainder of this chapter is as follows. In Section 4.2, TW propagation theory is briefly revisited, and the fault location formula employed in this chapter is derived. In Section 4.3, the instantaneous features extracted by HHT are analyzed during internal faults, based on which the arrival instants of BTWs are identified. The proposed scheme is described in Section 4.4, and the simulation results are presented in Section 4.5. Finally, the conclusions derived from this chapter are outlined in Section 4.6.

4.2 Traveling Wave Propagation Theory

TW propagation theory states that transmission network faults induce electromagnetic TWs that travel from the fault location towards line terminals, where reflections and refractions occur, as shown in Figure 4.1 [124]. TW propagation can be mathematically represented by a second-order differential equation as follows [124]:

$$\frac{\partial^2 u(r,t)}{\partial r^2} = \gamma^2 \, \frac{\partial^2 u(r,t)}{\partial t^2} \ , \tag{4.1}$$

where u is the voltage TWs and r is the distance from fault location at time t. γ is the propagation constant calculated based on the series impedance and shunt admittance of the line as given in (4.2). The reciprocal of γ represents the TW propagation velocity v_{TW} (4.3).

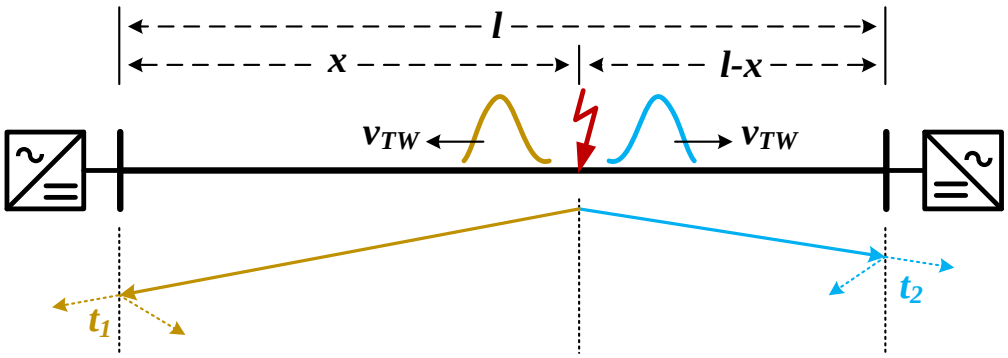


Figure 4.1: Propagation of the fault-induced TWs.

$$\gamma = \sqrt{Z\,Y} \tag{4.2}$$

$$v_{TW} = \frac{1}{\sqrt{Z\,Y}} \tag{4.3}$$

The arrival instants of the initial fault-induced BTWs at both line terminals t_1 and t_2 can be expressed as:

$$t_1 = \frac{x}{v_{TW}} \qquad \& \qquad t_2 = \frac{l-x}{v_{TW}}\ , \tag{4.4}$$

where x is the fault location and l is the line length. Based on (4.4), fault location is calculated as:

$$x = \frac{l + v_{TW}(t_1 - t_2)}{2}\ . \tag{4.5}$$

4.3 Fault Analysis With Hilbert-Huang Transform

In this section, the test grid and the extracted instantaneous features that will be later used in the proposed fault location identification scheme are presented.

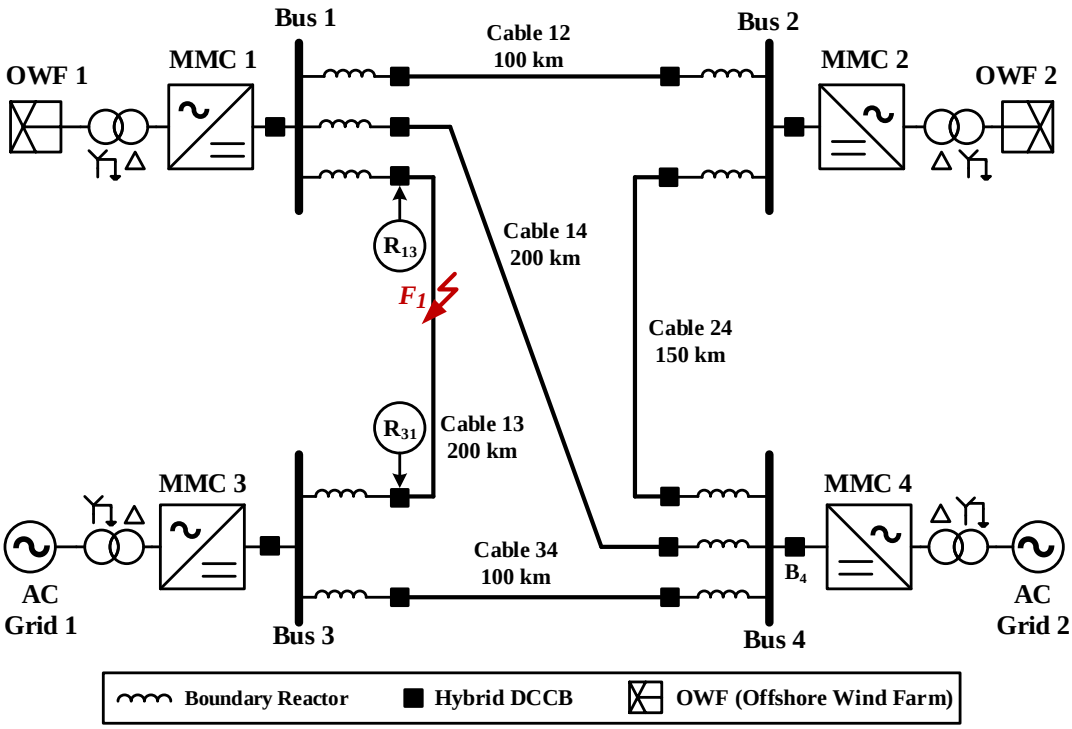


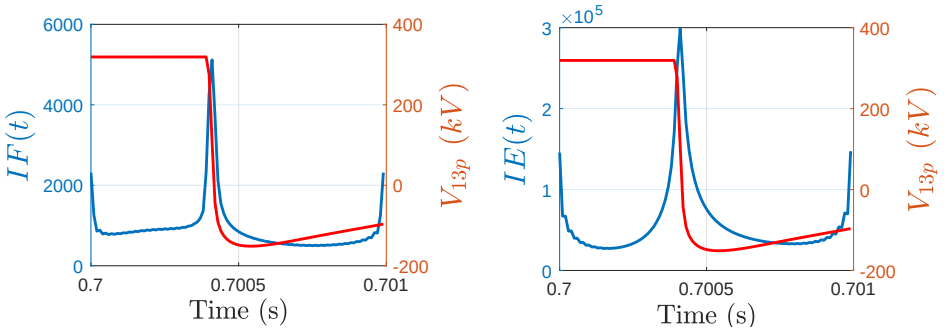
Figure 4.2: Test Grid.

4.3.1 Test Grid

The same HVDC grid employed in previous chapters is shown in Figure 4.2 with two relays added at both terminals of cable 13, *i.e.*, the local relay R_{13} and the remote relay R_{31}. The proposed scheme is applied to R_{13} and R_{31} to capture the time instants t_1 and t_2, respectively, required for estimating the fault location.

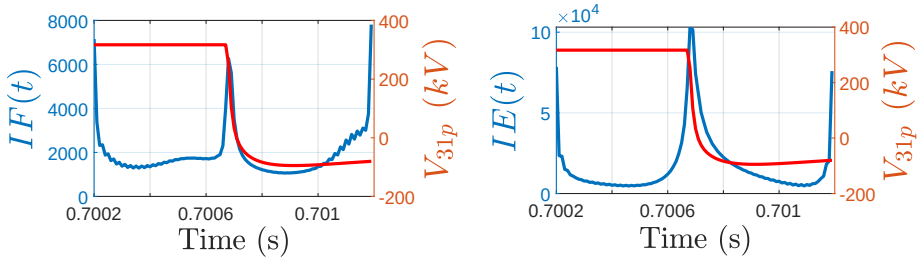
4.3.2 Instantaneous Features Extraction By HHT

The instantaneous frequency $IF(t)$ and the instantaneous energy $IE(t)$, extracted by HHT, are employed to capture the BTW arrival time instants t_1 and t_2. The same HHT steps presented in Section 3.2.2 are employed in this chapter to extract $IF(t)$ and $IE(t)$. Figures 4.3 and 4.4 shows the instantaneous features extracted by HHT from positive-pole voltages V_{13_p} and V_{31_p} during a PTP fault (F_1), that occurs at 0.7 s on cable 13 at 75 km from R_{13}. As shown in Figures 4.3 and 4.4, positive-pole voltages suddenly drop at the instant when the fault-induced BTWs reach terminal relays. The high-frequency components associated with the fault-induced BTWs appear in the first IMF extracted during



(a) V_{13_p} and $IF(t)$. (b) V_{13_p} and $IE(t)$.

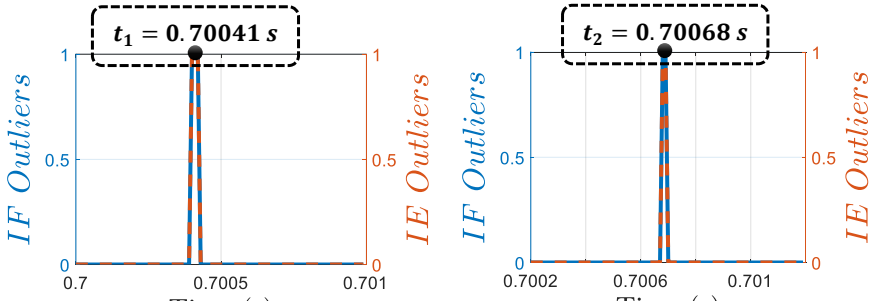
Figure 4.3: V_{13_p} and the corresponding features extracted at R_{13} for F_1.



(a) V_{31_p} and $IF(t)$. (b) V_{31_p} and $IE(t)$.

Figure 4.4: V_{31_p} and the corresponding features extracted at R_{31} for F_1.

the EMD stage. Therefore, an abrupt change in the extracted instantaneous frequency occurs at the same instant when the voltage suddenly drops, as shown in Figures 4.3a and 4.4a. Similarly and simultaneously, an abrupt change in the extracted instantaneous energy occurs, as shown in Figures 4.3b and 4.4b. The reason is that the sudden voltage dip causes a sudden change in the extracted instantaneous amplitude and, hence, abruptly changes $IE(t)$. The time instants when simultaneous abrupt changes arise in $IF(t)$ and $IE(t)$ extracted at R_{13} and R_{31} correspond to t_1 and t_2, respectively. Therefore, the instantaneous features extracted by HHT can be reliably used to identify the time instants t_1 and t_2, required for estimating the fault location. It should be noted that the sifting process results in irregular edges in $IF(t)$ and $IE(t)$ [121]. As these edges can drastically impact the accuracy of the proposed scheme, they are eliminated prior to estimating t_1 and t_2.



(a) R_{13}. (b) R_{31}.

Figure 4.5: Detected outliers at relays and captured arrival instants of BTWs.

4.4 Proposed Fault Location Identification Scheme

The abrupt changes in $IF(t)$ and $IE(t)$ can be detected as outliers. Based on the outlier definition in (3.15), simultaneous outliers in $IF(t)$ and $IE(t)$ are detected at R_{13} and R_{31} during F_1 at $t_1 = 0.70041\ s$ and $t_2 = 0.70068\ s$, respectively, as shown in Figure 4.5. Given that $v_{TW} = 183.5\ km/ms$ [35], the fault location x is calculated from (4.5) as 75.2275 km, where F_1 actually occurs at 75 km from R_{13}. It is worth mentioning that off-line estimation of fault location is valuable for the maintenance crew to restrict the area where fault-pinpointing field tests, such as the sniffer test, are executed to determine the exact fault location [151]. Figure 4.6 summarizes the steps of the proposed scheme for R_{13}. If a fault is detected by the primary protection relay, the proposed fault location identification scheme starts to operate. Firstly, HHT is applied to a 1 ms data window to extract $IF(t)$ and $IE(t)$ from voltage measurements. From the fault data recorded by the primary relay, the initial window should equally have pre-fault and post-fault samples such that the sudden voltage drop associated with the fault is processed by HHT. Then, the outlier detection criterion is applied to the extracted features. The instant when simultaneous outliers are detected by R_{13} is recorded as t_1. If simultaneous outliers are not detected, the data window will be updated to include more post-fault samples until simultaneous outliers are detected. Finally, t_2 is received from R_{31}, and x is calculated from (4.5). The sampling frequency is 100 kHz. It should be noted that a 1 ms window is optimally selected since it has sufficient samples to accurately extract the instantaneous features by HHT [119, 121]. Shorter windows may result in misleading peaks in the extracted features. On the other hand, fault location schemes with longer windows are not compatible with fast primary protection schemes due to limited post-fault samples.

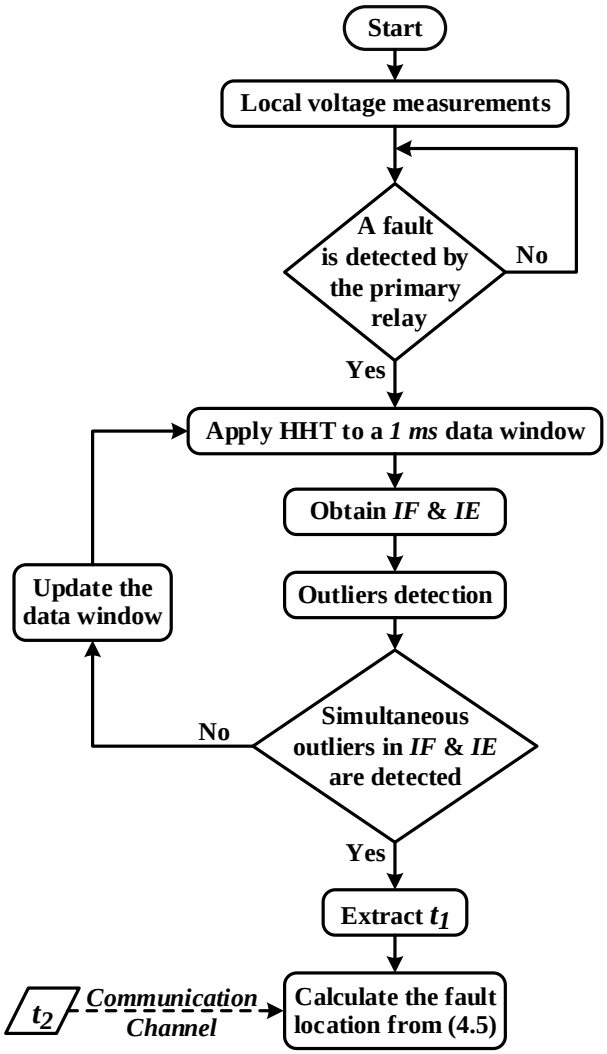


Figure 4.6: Flowchart of the proposed fault location scheme of R_{13}.

4.5 Simulation Results

The accuracy of the proposed scheme is evaluated in this section. Various fault scenarios obtained by changing the fault type, location, and resistance are simulated. Then, the proposed scheme is compared with existing fault location schemes, highlighting its superior performance.

Table 4.1: Fault location calculated by the proposed scheme for various solid internal faults

Fault Type	x_{act} (km)	t_1 (s)	t_2 (s)	x (km)	$\%error$
PTP	5	0.70002	0.70106	4.58	0.21
PPTG	25	0.70013	0.70095	24.765	0.1175
NPTG	50	0.70027	0.70082	49.5375	0.231
PTP	75	0.70041	0.70068	75.2275	0.114
PTP	100	0.70054	0.70054	100	0
PTP	125	0.70068	0.7004	125.69	0.345
PPTG	150	0.70082	0.70027	150.4625	0.231
NPTG	175	0.70095	0.70013	175.235	0.1175
PTP	195	0.70107	0.70002	196.3375	0.6688

4.5.1 Solid Internal Faults

Numerous solid fault scenarios, including PTP, PPTG, and NPTG faults, along cable 13 are simulated. Table 4.1 shows the obtained results. All faults are triggered at 0.7 s. Positive-pole voltages are processed to capture t_1 and t_2 during PTP and PPTG faults, whereas negative-pole voltages are used during NPTG faults. For each scenario, the fault distance from R_{13} is calculated based on (4.5), besides the percentage error is calculated as follows [145]:

$$\%error = \frac{\mid x - x_{act} \mid}{l_{13}} * 100\% \ , \tag{4.6}$$

where x_{act} is the actual fault location from R_{13}, and l_{13} is the length of cable 13 which is 200 km. As shown in Table 4.1, the maximum $\%error$ is less than 0.7%, which manifests the high precision of the proposed scheme.

4.5.2 Fault Resistance Coverage

To evaluate the robustness of the proposed fault location identification scheme to fault resistance, various fault scenarios are simulated with fault resistances $R_F = 500\ \Omega$ and

Table 4.2: Fault location calculated by the proposed scheme for various non-solid internal faults

Fault Type	x_{act} (km)	R_F (Ω)	t_1 (s)	t_2 (s)	x (km)	$\%error$
PTP	5	500	0.70002	0.70106	4.58	0.21
PTP	5	1000	0.70002	0.70106	4.58	0.21
PTP	25	500	0.70013	0.70096	23.8475	0.576
PPTG	25	1000	0.70013	0.70096	23.8475	0.576
PTP	75	500	0.7004	0.70068	74.31	0.345
NPTG	75	1000	0.7004	0.70068	74.31	0.345
PTP	100	500	0.70054	0.70054	100	0
PTP	100	1000	0.70054	0.70055	99.0825	0.459
PPTG	125	500	0.70069	0.70041	125.69	0.345
PTP	125	1000	0.70069	0.70041	125.69	0.345
NPTG	175	500	0.70096	0.70013	176.1525	0.576
PTP	175	1000	0.70096	0.70013	176.1525	0.576

1000 Ω. The results are tabulated in Table 4.2. It is evident that the proposed scheme is highly accurate during faults with R_F values up to 1000 Ω.

4.5.3 Comparison

The proposed scheme is compared to existing double-ended fault location identification schemes in terms of the maximum tolerable fault resistance (Max R_F), data window length, sampling frequency, and the maximum percentage error, as shown in Table 4.3. The proposed scheme has a remarkably higher fault resistance coverage than existing fault location schemes. Although the proposed schemes in [148–150] have relatively better accuracy than the proposed scheme, their accuracy deteriorates when R_F exceeds 300 Ω. Compared to [139,148,150], a significantly smaller data window is utilized by the proposed scheme. Therefore, the proposed scheme can be employed along with recent primary protection schemes that rapidly detect faults within 1 ms [119]. Compared to [149, 150], a

Table 4.3: Comparison between the proposed scheme and the existing double-ended schemes

Reference	**Criterion**	**Max** R_F (Ω)	**Data Window Length** (ms)	**Sampling Frequency** (kHz)	**Maximum Percentage Error** $(\%)$
[139]	Convolution	500	5	10	1.3
[123]	Segmented signals	450	1	250	2.12
[148]	AFC	300	10	100	0.18
[149]	IF Spectrum	300	Not reported	1000	0.33
[150]	AFC	300	5	1000	0.5
Proposed Scheme	Outlier detection	1000	1	100	0.67

significantly smaller sampling frequency is required, resulting in a reduced computational burden. Furthermore, the arrival instants of BTWs are captured by the proposed scheme based on detecting outliers without adjusting any thresholds, which is the case in most existing schemes [123, 139, 148–150].

4.6 Conclusion

Accurate identification of fault location in multi-terminal HVDC grids contributes to reducing the downtime of the faulted segment and determining critical locations frequently exposed to fault incidents. A fast, accurate, and reliable fault location identification scheme is proposed in this chapter. The arrival time of the initial fault-induced BTW is identified when simultaneous outliers in the instantaneous frequency and energy extracted by HHT are detected. The double-ended scheme identifies the fault location based on the two arrival instants estimated by terminal relays. Several simulation results are presented, demonstrating the accuracy and robustness of the proposed scheme to high-resistance faults. The main advantages of the proposed scheme are summarized as follows:

- Fault location is identified with high precision with a maximum percentage error less than 0.7%.
- The arrival instants of BTWs are estimated based on a setting-less outlier-based criterion; thus, expanding the applicability of the proposed scheme to large multi-terminal HVDC grids with different configurations and parameters.
- Fault location is rapidly identified within 1 ms before tripping the faulted line by primary breakers.
- The proposed scheme is robust to high-resistance faults up to 1000 Ω.

Chapter 5

Breaker Failure Backup Protection Scheme

5.1 Introduction

Persistent faults in multi-terminal HVDC grids can lead to grid component damage due to excessive current and voltage levels and may result in the disconnection of a substantial portion of the grid [144]. In addition, uncleared faults may cause converters blocking, and consequently loss of their controllability [26]. Primary protection failure occurs when corresponding breakers fail to clear the fault, i.e., *breaker failure*, or the primary relay fails to detect the fault, i.e., *relay failure* [34]. DCCBs may fail to trip due to [44, 152] i) significant stress caused by fault energy and transient overvoltages, ii) fault arc restrike, iii) commutation failure between conduction and energy absorption branches of DCCBs, iv) performance degradation due to aging and frequent switching, and v) failure of the breaker surge arrester due to fractures and punctures. Therefore, a fast and reliable breaker failure backup protection scheme is required to protect HVDC grids during breaker failure events.

Several schemes have been proposed in the literature to detect breaker failure incidents in HVDC grids. The proposed scheme in [55] compares the breaker current with a pre-specified threshold 20 ms after the trip instant. However, this large delay considerably jeopardizes the grid's reliability and security and may damage grid equipment [153]. The breaker failure detection speed is significantly improved in [154,155] by employing statistical classifiers based on linear discriminant analysis and K-nearest neighbor techniques applied to local voltages and currents. However, their performance with high fault resistances is not evaluated. In addition, intensive simulations are required to train the classifiers and

set the algorithm thresholds. In [156], the quickest change detection algorithm, another statistical method, is applied to the breaker voltage to detect breaker failure events. However, additional measurement devices are required in [156] to measure the voltage across each breaker; thus, resulting in an increased cost. In [157], the breaker counter voltage during tripping is estimated based on local voltage and current measurements and then compared with the corresponding calculated value to detect breaker failure events. The proposed scheme depends on simulation-based thresholds and the approximated nonlinear resistance of the breaker surge arrester. A voltage-derivative-based scheme is proposed in [158] to detect unsuccessful breaker operations. However, the derivative-based criterion depends on thresholds that are obtained from simulations. In addition, the derivative value is adversely impacted by fault resistance and measurement noise [144].

In summary, the main shortcomings in existing breaker failure backup protection schemes include: i) delayed detection time, ii) additional voltage sensors requirement, iii) reliance on simulation-based thresholds, and iv) additional parameter or measurement requirements that may deteriorate the algorithm accuracy under severe fault conditions, e.g., surge arrester resistance or breaker counter voltage. Compared to primary protection schemes, much less attention has been dedicated to breaker failure backup protection of multi-terminal HVDC grids. Based on the aforementioned shortcomings, there is a significant need for implementing a reliable breaker failure backup protection scheme that rapidly detects unsuccessful breaker operations. This chapter proposes a novel breaker failure backup protection scheme for multi-terminal HVDC grids. The basic principle of the proposed scheme is that a successful breaker trip is always associated with a sudden increase in local voltage measurements corresponding to the counter voltage generated across the breaker during breaker operation. In the proposed scheme, detected outliers in the instantaneous features extracted by HHT are employed to infer the occurrence of abrupt changes in local voltage measurements. A breaker failure event is detected if simultaneous outliers in the instantaneous frequency and energy are not observed following a trip signal issued by the primary relay. The remaining of the paper is organized as follows: Section 5.2 investigates the instantaneous frequency and energy extracted by HHT during successful breaker operation and breaker failure scenarios. Then, the proposed breaker failure backup protection scheme is presented. In Section 5.3, several simulation studies are presented to validate the reliability and effectiveness of the proposed scheme under severe fault conditions. The conclusions are outlined in Section 5.4.

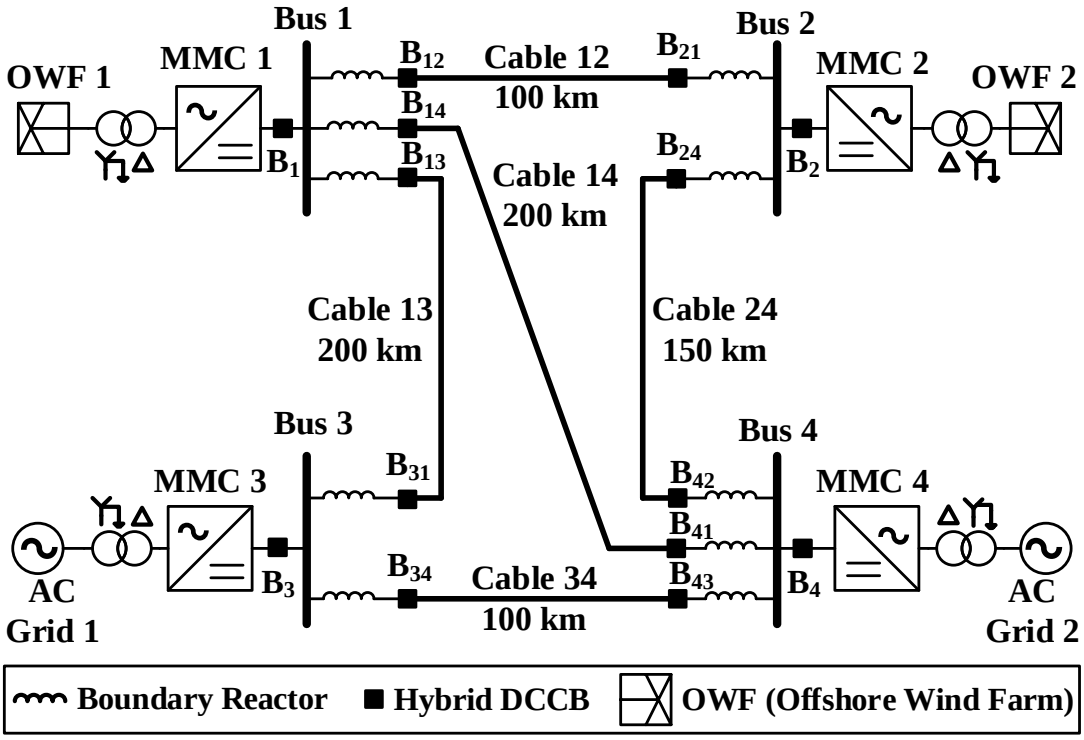


Figure 5.1: Four-terminal HVDC test grid.

5.2 Breaker Failure Backup Protection Scheme

In this section, first, the impact of breaker failure on local voltage measurements is analyzed. Then, the instantaneous frequency and energy extracted by HHT are presented during successful breaker operation and breaker failure. Finally, the proposed breaker failure backup protection scheme is presented.

5.2.1 Test System

The same HVDC grid employed in previous chapters is presented again in Figure 5.1. Selective fault clearing strategy is accomplished by inserting hybrid DCCBs at both terminals of each cable, which are capable of clearing the fault within 2 ms [44]. The breaker model consists of a switch in parallel with a surge arrester, which is responsible for absorbing the fault energy [35]. The switch opens 2 ms after receiving the trip signal in order to simulate a hybrid DCCB [159]. The voltage rating of the surge arrester is 480 kV, which is 150% of

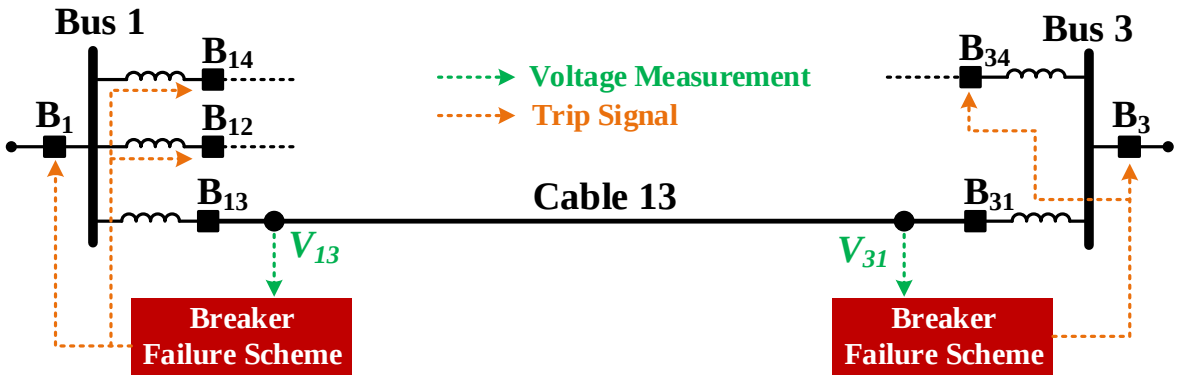


Figure 5.2: Breaker Failure Backup protection system of cable 13.

the DC voltage rating. Figure 5.2 shows the breaker failure backup protection system for cable 13. The proposed breaker failure backup protection scheme is implemented at both terminals of each cable. Only local voltage measurements are required for the proposed scheme to detect breaker failure events. If a fault at cable 13 is detected by the primary relay and the primary breaker B_{13} fails to isolate the fault, trip signals issued by the proposed scheme will be sent to the remaining breakers connected to Bus 1, i.e., B_1, B_{12}, and B_{14}. Likewise, if B_{31} fails to trip, B_3 and B_{34} will receive backup trip signals from the proposed scheme implemented at Bus 3.

5.2.2 Local Voltage Measurement During Breaker Operation

To analyze the impact of breaker operation on local voltage measurements, an internal solid PTP fault in the middle of cable 13 is simulated. The permanent fault is triggered at 0.7 s. The fault is assumed to be successfully detected by the primary relay immediately after the fault-induced TWs reach the local terminal at Bus 1. Therefore, a trip signal is issued to the primary breaker, i.e., B_{13}. Figure 5.3 shows V_{13_p} for the two possible scenarios of successful and unsuccessful breaker operation. As shown in Figure 5.3, a successful breaker trip is associated with an abrupt change in the voltage waveform, 2 ms after fault detection. This sudden increase corresponds to the developed counter voltage across the breaker caused by the surge arrester. This sudden increase in the voltage waveform is about 480 kV, i.e., the voltage rating of the surge arrester. On the contrary, if the breaker fails to clear the fault, the voltage oscillations will persist, and no abrupt changes will occur. Consequently, breaker failure events can be rapidly detected if there are no abrupt changes in the voltage waveform during the anticipated trip time.

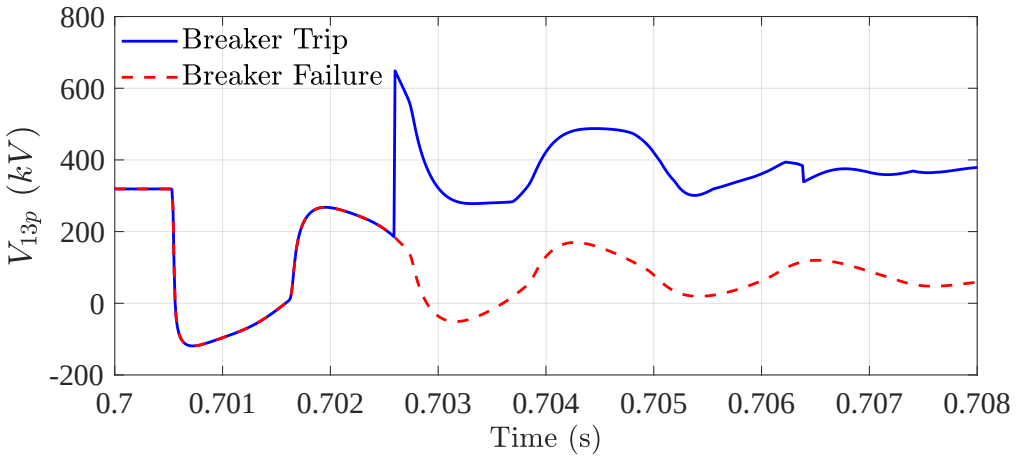


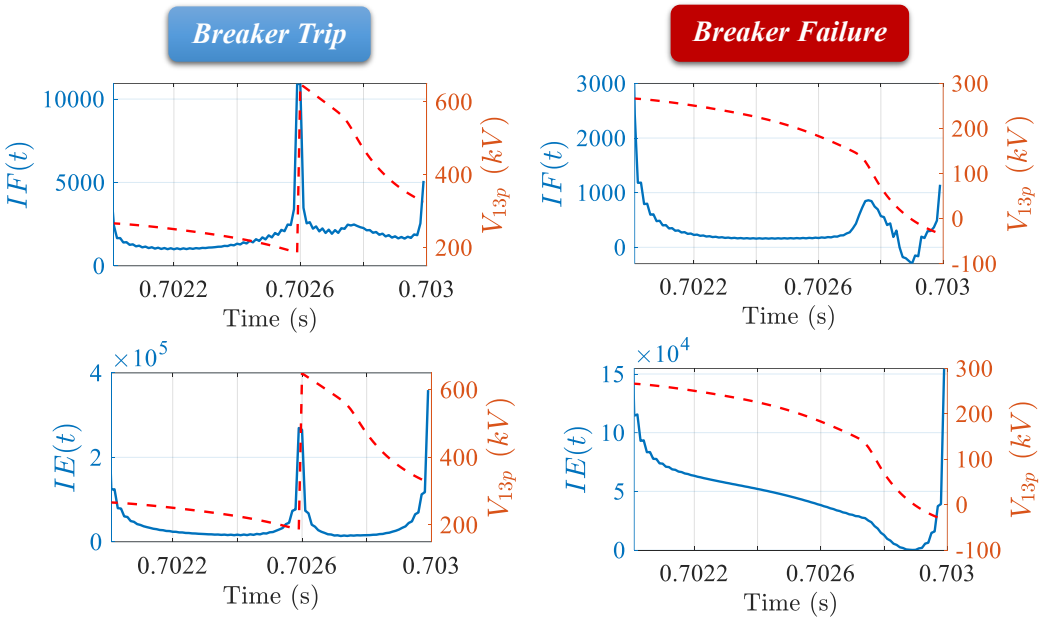
Figure 5.3: Positive-pole voltage waveform during successful breaker trip and breaker failure.

5.2.3 IF and IE During Breaker Operation

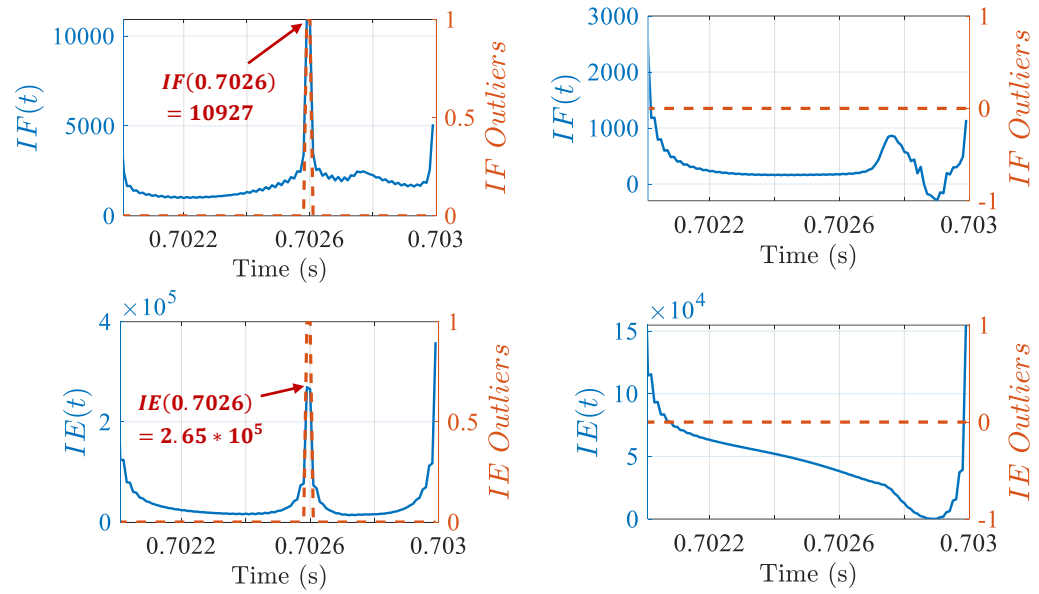
Figure 5.4a shows the extracted instantaneous features by HHT, i.e., $IF(t)$ and $IE(t)$, for a 1 ms window of V_{13_p} during successful breaker trip and breaker failure. The same HHT steps presented in Section 3.2.2 are employed in this chapter to extract $IF(t)$ and $IE(t)$. As shown in Figure 5.4a (left side), the abrupt change in V_{13_p} associated with successful breaker operation causes $IF(t)$ and $IE(t)$ waveforms to be similar to an impulse function. The reason is that the abrupt change in V_{13_p} results in a sudden change in the oscillation mode of the signal; thus, promptly increasing the extracted instantaneous frequency. In addition, the sudden increase in the amplitude of V_{13_p} results in a prompt increase in the extracted instantaneous energy [119]. On the contrary, if the breaker fails to trip, no abrupt changes will occur in V_{13_p}. Therefore, $IF(t)$ and $IE(t)$ waveforms will be smooth and without any abrupt changes, as shown in Figure 5.4a (right side). Therefore, breaker failure events can be detected if there are no abrupt changes in $IF(t)$ and $IE(t)$.

5.2.4 Outlier Detection

The outlier definition in (3.15) is applied to the extracted instantaneous frequency and energy shown in Figure 5.4a. As shown in Figure 5.4b (left), simultaneous outliers in $IF(t)$ and $IE(t)$ are detected at 0.7026 s during successful breaker operation. On the other hand, no outliers are detected during breaker failure, as shown in Figure 5.4b (right). It is worth mentioning that the proposed scheme depends on the detected outliers in both



(a) Instantaneous frequency and instantaneous energy of V_{13_p}.



(b) Outlier detection.

Figure 5.4: The extracted instantaneous features of V_{13_p} and detected outliers during successful breaker trip and breaker failure.

the instantaneous frequency and energy to increase the reliability and robustness of the proposed criterion. In addition, maloperation of the proposed scheme due to individual outliers in $IF(t)$ or $IE(t)$ during fault transients (after fault detection and before primary breaker operation) are avoided. To mitigate the HHT edge effect, the proposed scheme discards the outliers that occur within the first and last ten samples of the 1 ms data window.

5.2.5 Proposed Scheme

Figure 5.5 shows the flowchart of the proposed breaker failure backup protection scheme. The proposed algorithm commences once a trip signal is issued by the primary relay. Therefore, the proposed scheme is not vulnerable to maloperation during normal operation of the system, changes in system operating points, or external faults. HHT is applied to a 1 ms moving window of the measured voltage to extract the instantaneous frequency and energy. If simultaneous outliers in $IF(t)$ and $IE(t)$ are detected, a successful breaker trip is concluded. Otherwise, breaker failure is detected given that sufficient time, $T_{elapsed}$, has been devoted for the corresponding breaker to trip. In this chapter, $T_{elapsed}$ is equal to 3 ms, which is 1 ms more than the anticipated breaker trip time. It is important to note that $T_{elapsed}$ is established based on the breaker speed, which is readily available for any HVDC grid. For example, the Zhangbei HVDC grid in China, the world's first multi-terminal meshed grid, employs hybrid circuit breakers that can fully interrupt substantial DC fault currents ($\geq$ 25 kA) in less than 3 ms [48]. Additionally, $T_{elapsed}$ setting remains unaffected by changes in grid configuration or parameters.

5.3 Simulation Results

Several simulation studies are presented in this section to evaluate the performance of the proposed breaker failure backup protection scheme under different fault conditions, such as various fault locations, fault resistances, and boundary inductances. Furthermore, the proposed scheme is applied to a bipolar HVDC grid to emphasize its general applicability. In addition, the main advantages of the proposed scheme and its superiority compared to existing schemes are demonstrated.

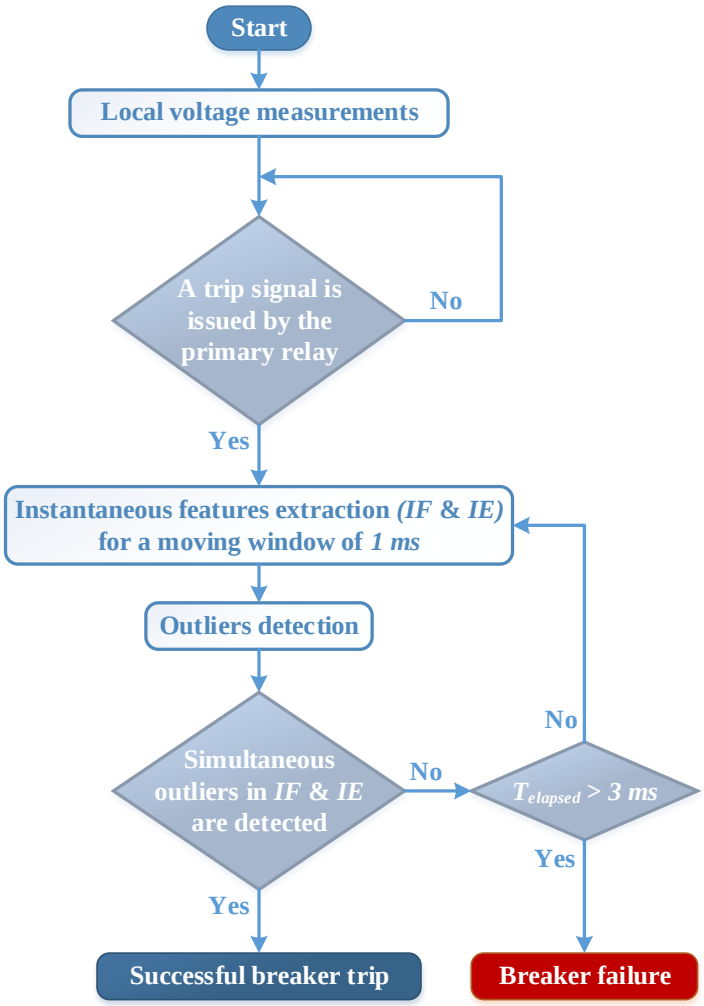
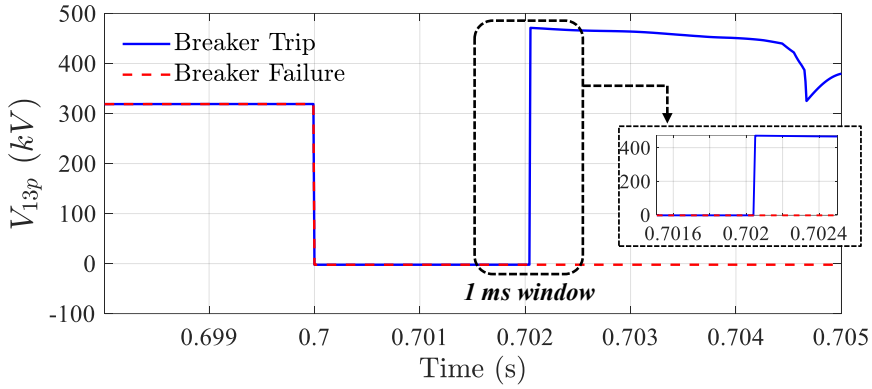


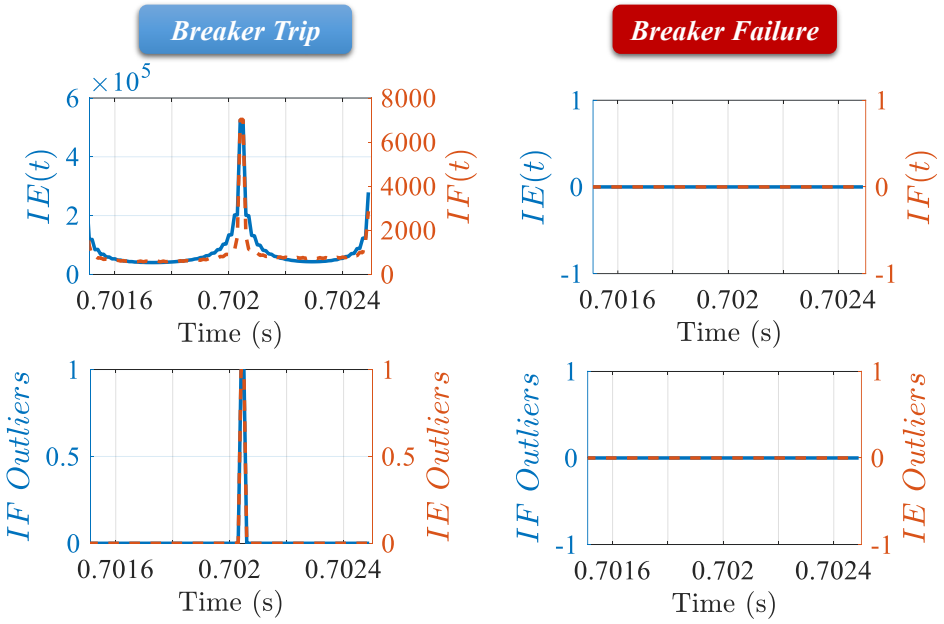
Figure 5.5: Proposed breaker failure backup protection scheme.

5.3.1 Fault Location

Various internal faults along the entire length of cable 13 are simulated. B_{13} is considered as the primary breaker under investigation. The fault location is changed, and the performance of the proposed breaker failure scheme during successful breaker trip and breaker failure is evaluated. All faults are permanent and were initiated at 0.7 s. Figure 5.6 shows V_{13_p} and the extracted instantaneous features as well as the detected outliers for a solid PTP fault at the beginning of cable 13. As shown in Figure 5.6, V_{13_p} immediately drops to zero at 0.7 s since the fault resistance is zero, and the fault location is just right after



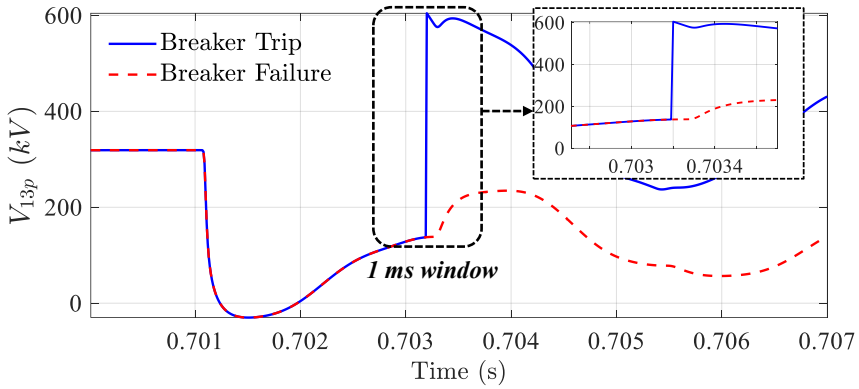
(a) V_{13_p} with a zoomed 1 ms window.



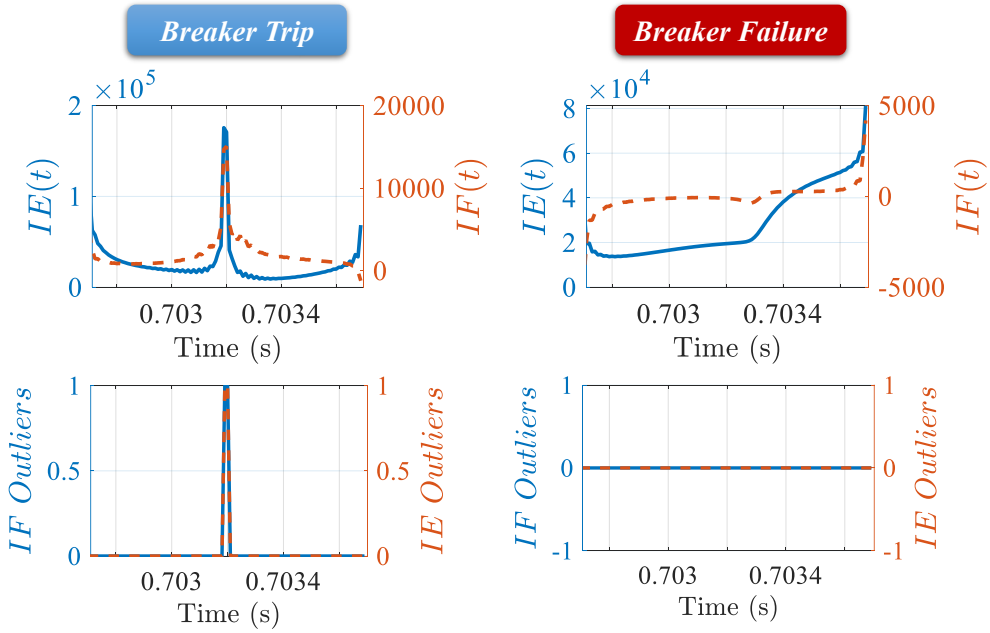
(b) $IF(t)$, $IE(t)$, and detected outliers.

Figure 5.6: A solid PTP fault at the beginning of cable 13 during successful and unsuccessful breaker trip.

the primary relay. When the breaker successfully trips, the abrupt increase in V_{13_p}, which occurs 2 ms after fault detection, causes the waveforms of $IF(t)$ and $IE(t)$ to have abrupt changes that are detected as simultaneous outliers by the proposed scheme indicating successful breaker operation. On the other hand, when the breaker fails to trip, V_{13_p} remains zero, resulting in zero instantaneous features with no outliers. In this case, the proposed



(a) V_{13_p} with a zoomed 1 ms window.



(b) $IF(t)$, $IE(t)$, and detected outliers.

Figure 5.7: A solid PTP fault at the end of cable 13 during successful and unsuccessful breaker trip.

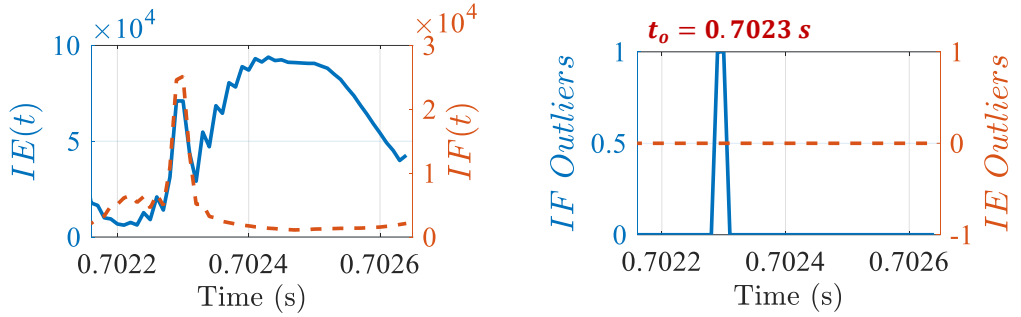
scheme detects a breaker failure. In Figure 5.7, the fault location is changed to be at the remote end of cable 13. Likewise, simultaneous outliers are detected in $IF(t)$ and $IE(t)$ when the breaker successfully trips, whereas no outliers are detected during breaker failure. It is evident that the proposed scheme can reliably distinguish between successful breaker trip and breaker failure regardless of the fault location.

Table 5.1: Detection time of successful operation of B_{13} for various fault locations

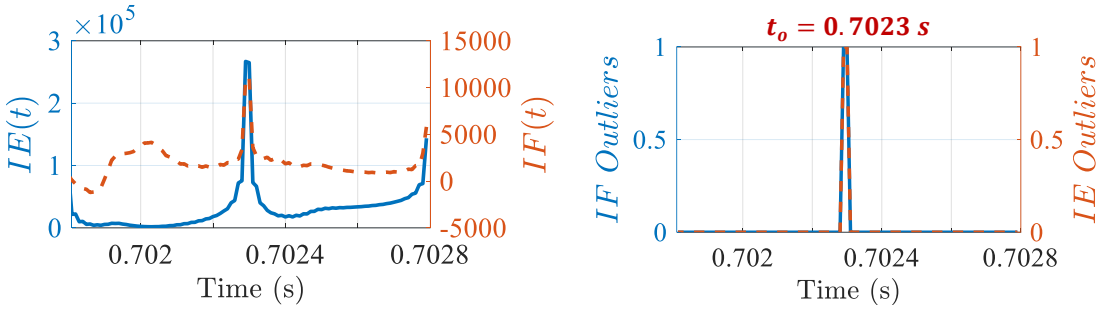
Fault Distance From Bus 1 (km)	t_f (s)	t_o (s)	t_d (ms)
0	0.7	0.70205	2.05
50	0.70026	0.7023	2.04
100	0.70053	0.7026	2.07
150	0.70081	0.7029	2.09
200	0.70108	0.7032	2.12

The fault location affects the fault detection instant when the fault-induced TWs arrive at the relay location. Therefore, the time instant of breaker operation and, accordingly, the detection instant of simultaneous outliers in $IF(t)$ and $IE(t)$ will vary by changing the fault location. However, this will not impact the reliable performance of the proposed scheme. As the fault distance increases, the time instant, when simultaneous outliers are detected, increases as well. Table 5.1 shows the detection time of simultaneous outliers for various fault locations. t_f is the time instant when the fault is detected by the primary relay and a trip signal is sent to the primary breaker. t_f is the instant corresponding to the sudden voltage dip in V_{13_p}, which occurs when the fault-induced TWs arrive at the relay location. t_o is the time instant when simultaneous outliers in $IF(t)$ and $IE(t)$ are detected indicating successful breaker operation. t_d is the time difference between t_o and t_f, which is the required time by the proposed algorithm to detect successful breaker operation. As shown in Table 5.1, t_d is less than 3 ms; thus, successful breaker operation can be identified by the proposed scheme within 1 ms from the intended breaker trip instant. If the breaker fails to trip, a breaker failure will be detected by the proposed scheme 3 ms ($T_{elapsed}$) after receiving the trip signal, i.e., 1 ms after the intended breaker trip instant.

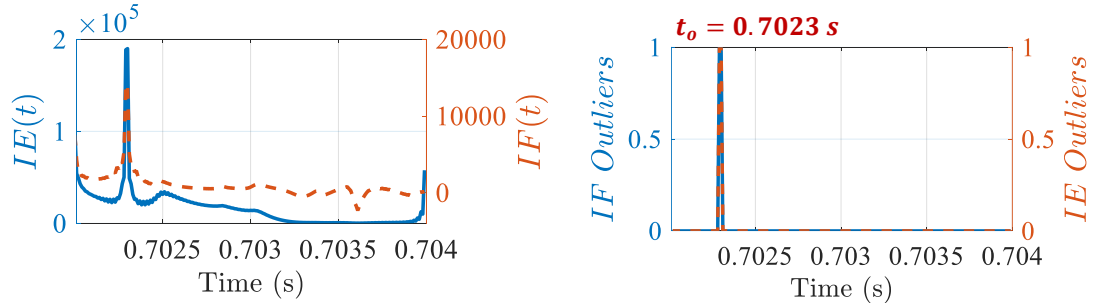
It is worth mentioning that the window length is selected such that sufficient samples are available for HHT calculations to guarantee accurate estimation of the extracted instantaneous features [127]. The sampling frequency is 100 kHz, and the window length is 1 ms. To investigate the impact of window length, the extracted instantaneous features and the corresponding outliers during successful breaker operation for a fault on cable 13 at 50 km from Bus 1 under various window lengths are shown in Figure 5.8. When a 0.5 ms window is used, the instantaneous energy outlier is not detected since $IE(t)$ has an erroneous second peak. Consequently, a breaker failure event will be incorrectly detected. On the other hand, when a 2 ms window is used, simultaneous outliers in $IF(t)$ and $IE(t)$



(a) 0.5 ms window.



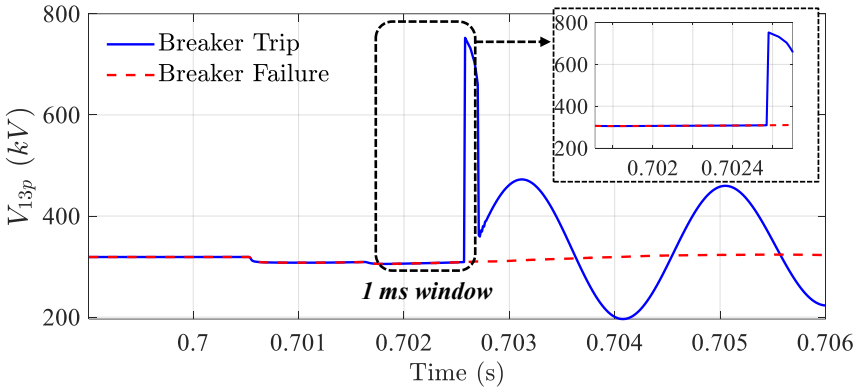
(b) 1 ms window.



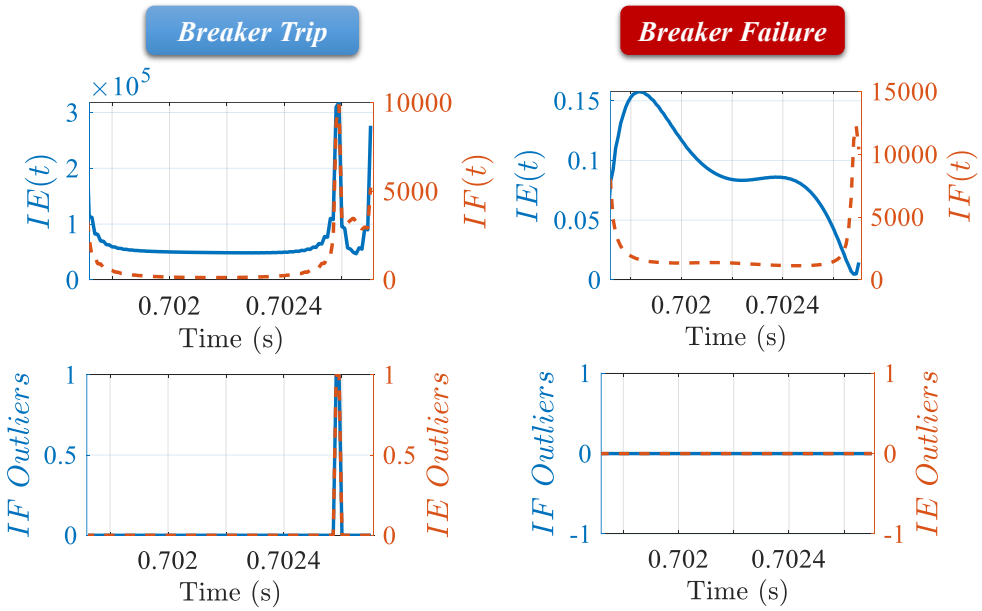
(c) 2 ms window.

Figure 5.8: Instantaneous features and detected outliers under various window sizes for a fault at 0.7 s on cable 13, 50 km from Bus 1.

are detected at $t_o = 0.7023$ s, which is the same instant when a 1 ms window is used. Therefore, inaccurate features may be extracted if small windows are employed, whereas long windows will unnecessarily slow down the proposed scheme. The sampling frequency of 100 kHz is employed so that the extracted instantaneous frequency and energy can reliably capture abrupt changes in the voltage waveform during successful breaker operation within the employed window length.



(a) V_{13_p} with a zoomed 1 ms window.

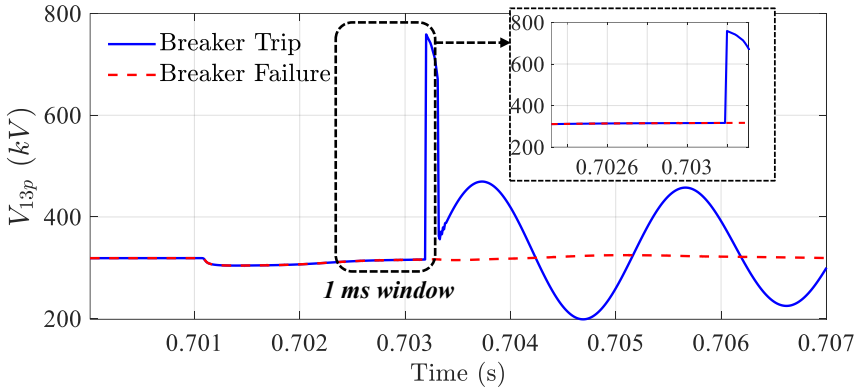


(b) $IF(t)$, $IE(t)$, and detected outliers.

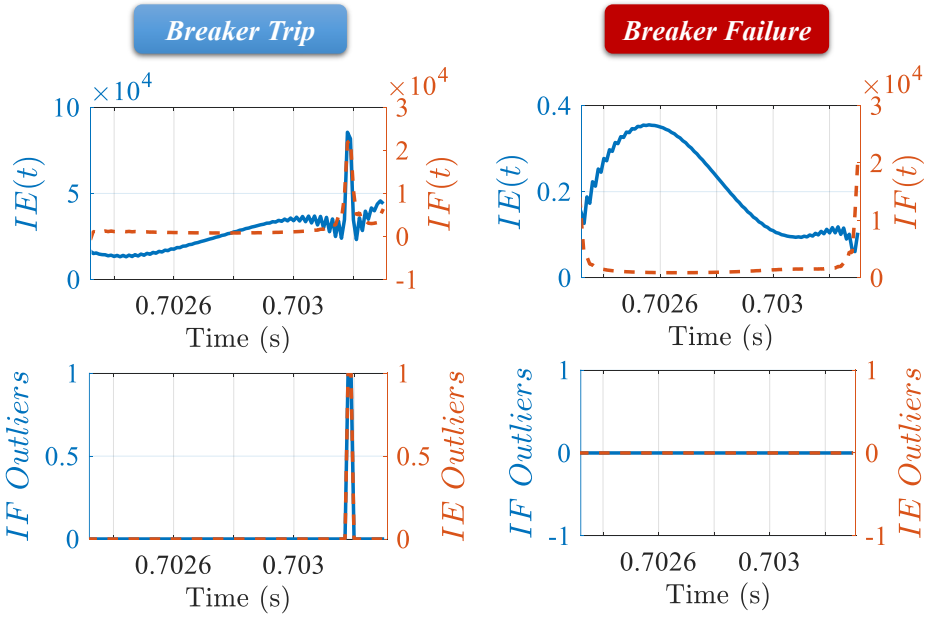
Figure 5.9: A PTP fault at the middle of cable 13 with $R_F = 1500\ \Omega$ during successful and unsuccessful breaker trip.

5.3.2 Fault Resistance

To investigate the impact of fault resistance (R_F) on the proposed scheme, two critical internal faults are simulated where $R_F = 1500\ \Omega$ and the fault location is at the middle and remote end of cable 13, as shown in Figures 5.9 and 5.10, respectively. Figures 5.9 and 5.10 show that the reliable performance of the proposed breaker failure scheme is



(a) V_{13_p} with a zoomed 1 ms window.



(b) $IF(t)$, $IE(t)$, and detected outliers.

Figure 5.10: A PTP fault at the end of cable 13 with $R_F = 1500\ \Omega$ during successful and unsuccessful breaker trip.

guaranteed regardless of the fault resistance value. The reason is that a successful breaker trip results in an abrupt increase in V_{13_p} and simultaneous detection of outliers in $IF(t)$ and $IE(t)$ regardless of R_F value. Furthermore, the detection time of simultaneous outliers is not impacted by R_F since the instant when the abrupt increase in V_{13_p} occurs does not depend on R_F. Rather, it depends mainly on the breaker speed. For instance, $t_o = 0.7026\ s$

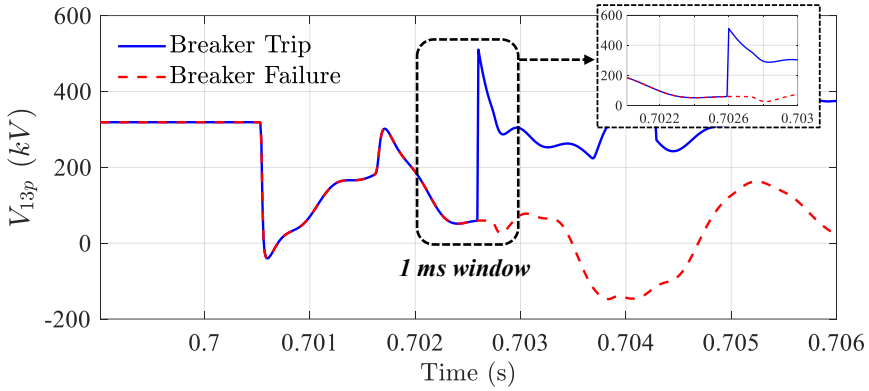
for the middle-cable fault case (Figure 5.9b) and $t_o = 0.7032\ s$ for the remote-end fault case (Figure 5.10b), which are the same instants compared to the corresponding solid fault cases, Table 5.1. It is worth mentioning that during the successful breaker operation when R_F is large, the fault energy is quickly released. Therefore, a quick drop in V_{13_p} occurs following the first abrupt increase. The reason is that the released fault energy depends on the fault current [160], which is inversely proportional to the R_F value. However, as shown in Figures 5.9 and 5.10, the detection of outliers in $IF(t)$ and $IE(t)$, and consequently the performance of the proposed scheme is not impacted by the energy absorption speed during the breaker interruption process.

5.3.3 Boundary Reactors

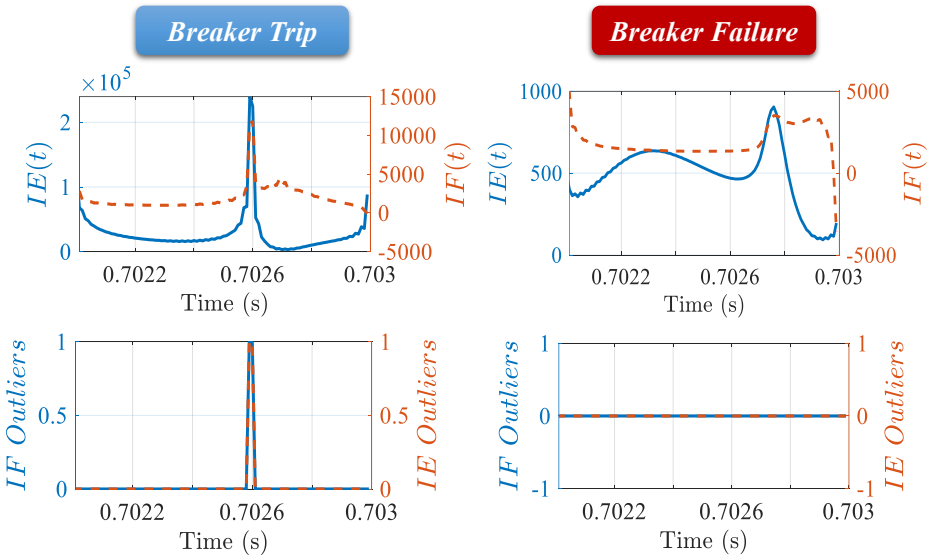
In multi-terminal HVDC grids, DC reactors are typically installed at the boundaries of each line to limit the sharp rate of rise of fault current and to provide individual protection zones for each line [161]. As the reactor size increases, dynamic stability issues may arise during power flow reversal [94]. Therefore, small boundary reactors are desired, particularly when converters can control the fault current within the interruption capability of DCCBs [161]. To examine the impact of small reactors on the proposed scheme, the size of the grid boundary reactors is changed from 50 mH to 10 mH, and a solid PTP fault at the middle of cable 13 is simulated. As shown in Figure 5.11, the proposed scheme correctly discriminates between successful breaker trip and breaker failure, even with a small reactor size. In this fault scenario, $t_o = 0.7026\ s$ which is the same as the detection instant of a middle-cable fault case with a 50 mH boundary reactor. Therefore, the performance of the proposed method is not impacted by the size of boundary reactors.

5.3.4 Impact of Measurement Noise

To investigate the impact of measurement noise on the proposed scheme, a solid PTP fault at the middle of cable 13 is simulated, and a 40 db white Gaussian noise is added to V_{13_p}. As shown in Figure 5.12, the proposed scheme detects simultaneous outliers in $IF(t)$ and $IE(t)$ during successful breaker operation. In contrast, a breaker failure event is detected when no outliers are captured. In this fault scenario, t_o is not impacted by measurement noise ($t_o = 0.7026\ s$).



(a) V_{13_p} with a zoomed 1 ms window.

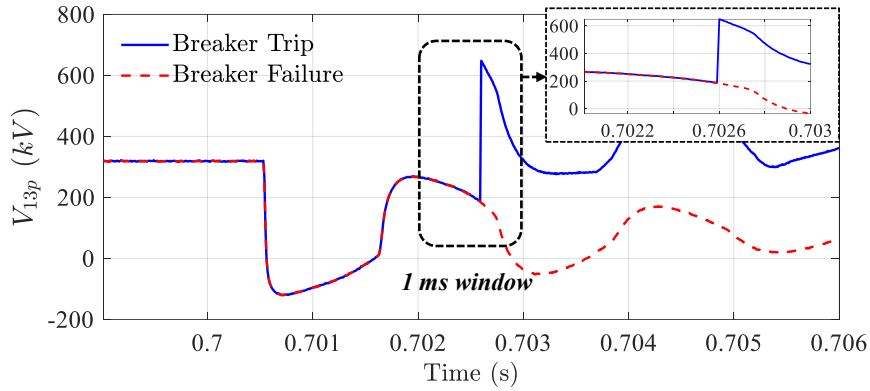


(b) $IF(t)$, $IE(t)$, and detected outliers.

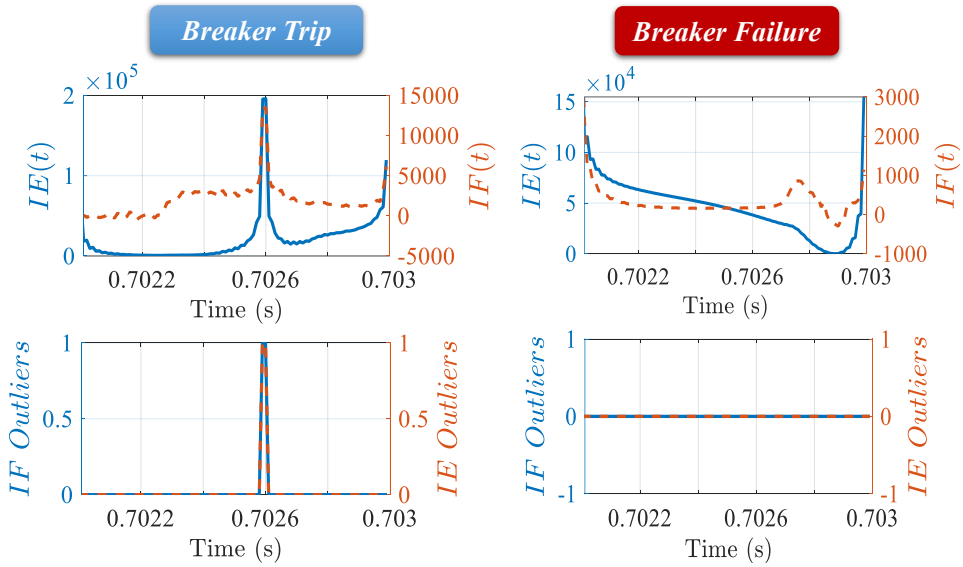
Figure 5.11: A solid PTP fault at the middle of cable 13 with a boundary reactor of 10 mH during successful and unsuccessful breaker trip.

5.3.5 Applicability to Other HVDC Grids

In this section, the proposed scheme is applied to a two-terminal, MMC-based bipolar HVDC grid, as depicted in Figure 5.13, to demonstrate its setting-less feature. The grid operates at a rated DC voltage of ±320 kV, with AC voltages of 240 kV and 230 kV on the rectifier and inverter sides, respectively. Terminal converters are connected by a



(a) V_{13_p} with a zoomed 1 ms window.



(b) $IF(t)$, $IE(t)$, and detected outliers.

Figure 5.12: A solid PTP fault at the middle of cable 13 with a 40 db white Gaussian noise during successful and unsuccessful breaker trip.

400 km long transmission line. Detailed grid parameters, control strategies, and equivalent models are outlined in [162]. The same breaker model used in the four-terminal grid (Figure 5.1) is utilized here. A solid PPTG fault is simulated at the midpoint of the line. The proposed scheme, with identical parameters (such as the outlier detection criteria, sampling frequency, window length, and $T_{elapsed}$), is applied to the positive-pole voltage at the rectifier side V_{R_p}. As shown in Figure 5.14, the scheme reliably differentiates between successful breaker operation and breaker failure. This evidence confirms that the

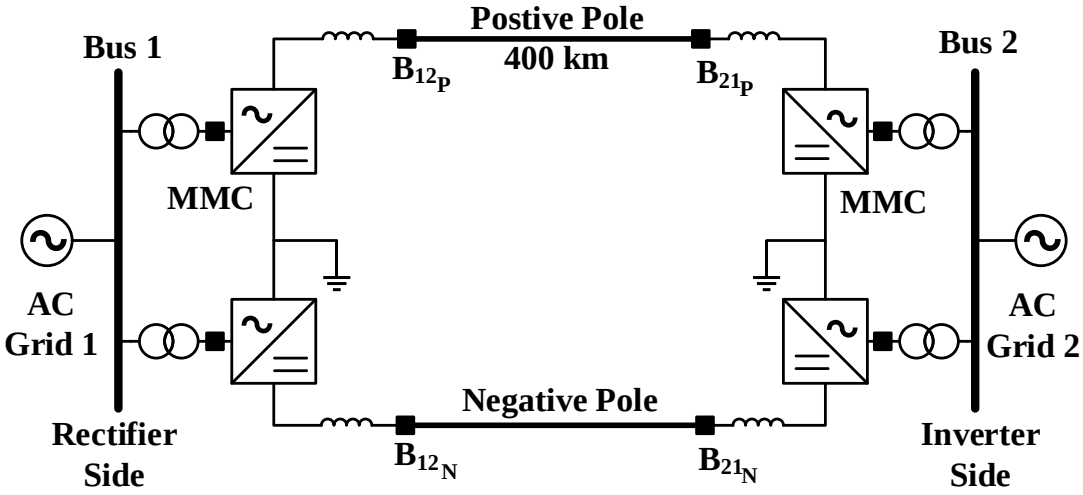
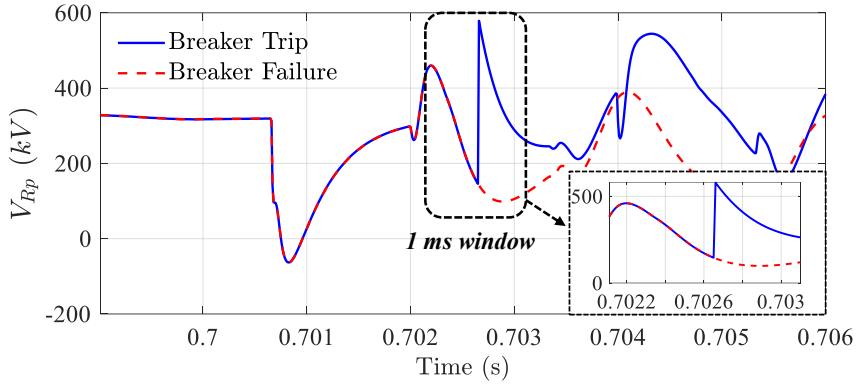


Figure 5.13: Two-terminal HVDC test grid.

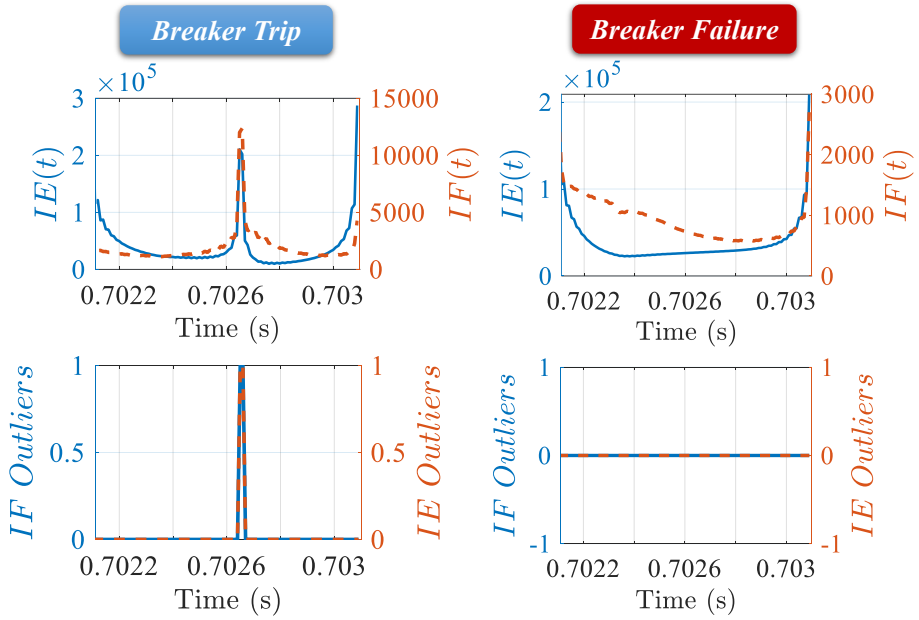
parameters of the proposed scheme are universal and can be applied to HVDC grids with various configurations and parameters. It should be noted that the breaker model used in these simulations (a time-controlled switch connected in parallel with a surge arrester) is adaptable and can represent different breaker technologies [35]. The time delay of the switch can be adjusted to reflect the speed of various breaker technologies, while the surge arrester branch remains consistent across all models. Since the proposed scheme depends primarily on detecting sudden increases in the voltage waveform, which corresponds to the counter voltage developed across the breaker due to the surge arrester, it can reliably differentiate between successful breaker operation and failure, regardless of the specific breaker technology employed.

5.3.6 Comparison with Existing Breaker Failure Backup Protection Schemes

Table 5.2 compares the proposed scheme with existing schemes in the literature. Compared with existing schemes, the proposed outlier-based scheme has the minimum breaker failure detection time and the largest fault resistance coverage without requiring additional sensors or simulation-based thresholds. Furthermore, estimation of breaker parameters, e.g., breaker counter voltage and the surge arrester nonlinear resistance, are not required, as compared to [157]. The sampling frequency of the proposed scheme is relatively large compared to existing schemes. However, as reported in [163], a sampling frequency of 100 kHz is a typical value used in HVDC grid protection schemes. In addition, modern digital sig-



(a) V_{R_p} with a zoomed 1 ms window.



(b) $IF(t)$, $IE(t)$, and detected outliers.

Figure 5.14: A solid PPTG fault at the middle of the line during successful and unsuccessful breaker trip.

nal processors (DSPs) have large sampling rates, in the range of tens of MHz, to rapidly process the measured signals and execute the required computations of the proposed algorithm [164, 165]. Furthermore, voltage measurement sensors used in HVDC grids have a wide frequency band. For example, resistive-capacitive voltage divider sensors can sample voltage signals with sampling frequencies up to 500 kHz, while the maximum sampling frequency of optical voltage sensors is 30 MHz [163].

Table 5.2: Comparison between the proposed scheme and existing breaker failure backup protection schemes

Ref	Criterion	Additional Sensors	Simulation-Based Thresholds	R_F Coverage	Operating Time	Sampling Frequency
[55]	Current magnitude	No	No	Not reported	20 ms	10 kHz
[153]	Quadratic discriminant analysis	No	Yes	10 Ω	2 ms	10 kHz
[154]	Linear discriminant analysis	No	Yes	Not reported	3 ms	50 kHz
[155]	K-nearest neighbor	No	Yes	Not reported	3 ms	50 kHz
[156]	Quickest change detection	Yes	Yes	10 Ω	4 ms	50 kHz
[157]	Breaker counter voltage estimation	No	Yes	Not reported	5 ms	100 kHz
[158]	Voltage derivative	Yes	Yes	200 Ω	3 ms	10 kHz
Proposed Scheme	Outliers	No	No	1500 Ω	1 ms	100 kHz

5.4 Conclusion

This chapter proposes a fast, reliable, and setting-less breaker failure backup protection scheme for multi-terminal HVDC grids. A breaker failure event is detected if simultaneous outliers in the instantaneous frequency and energy extracted by HHT are not observed.

The major advantages of this scheme are:

- Fast detection of breaker failure events in less than 1 ms from the intended breaker trip instant.
- Use of local voltage measurements to detect breaker failure events.
- No need for additional voltage sensors to measure the voltage across the breaker.
- Avoiding delayed detection of breaker failure events by omitting the need for monitoring the breaker current to check its progression towards zero.
- Applicable to HVDC grids with various configurations and parameters due to the use of a setting-less outlier-based criterion.
- Robustness to high fault resistances (up to 1500 Ω), small boundary reactors (up to 10 mH), and measurement noise (up to 40 db).
- Capability to reliably distinguish between successful breaker trip and breaker failure during severe fault scenarios such as solid faults at local ends and critical fault scenarios such as high-resistance faults at remote ends.

Chapter 6

Relay Failure Backup Protection Scheme

6.1 Introduction

Primary protection schemes for multi-terminal HVDC grids may fail to detect critical internal fault scenarios such as local-end solid faults and remote-end high-resistance faults [144]. In addition, these schemes may maloperate and may not be able to distinguish between internal and severe external faults, such as solid bus faults [166]. Sustained faults result in abnormal voltages and currents; thus, endangering grid equipment and causing converters to block, *i.e.*, acting as uncontrolled converters [1]. Furthermore, DC fault currents momentarily increase to high levels in a few milliseconds due to low inertia and impedance of HVDC grids [167]. Therefore, a fast and reliable relay failure backup protection scheme is required to protect HVDC grids in case of primary protection failure [157, 168].

Several relay failure backup protection schemes for HVDC grids have been proposed in the literature. To rapidly detect primary relay failure, single-ended backup protection schemes based on local measurements are proposed in [155, 156, 169]. In [155], the K-nearest neighbor technique is applied to local voltage and current measurements to provide reverse backup protection. However, extensive simulations are required to determine the algorithm thresholds. Furthermore, high-resistance faults are not investigated in [155]. The quickest change detection algorithm is employed in [156] to provide forward backup protection using local voltage measurements. However, the fault resistance coverage of the algorithm proposed in [156] is limited to 10 Ω only. A double-stage current-derivative-based backup scheme is proposed in [169]. However, this scheme maloperates when the fault

resistance exceeds 200 Ω. Since speed requirement of backup protection of HVDC grids is slightly lower than that of primary protection, double-ended backup protection schemes can be employed due to their higher selectivity and sensitivity compared to single-ended schemes [144]. For instance, a backup protection scheme is proposed in [57] based on current differential protection. However, the exchanged measurements between line ends require communication channels with high bandwidth and should be strictly synchronized. In addition, line-distributed capacitances affect the accuracy of the calculated differential current and may result in backup protection maloperation.

Pilot backup protection schemes, which rely on limited information exchange, *e.g.*, logic signals representing the fault direction, are proposed to conserve the selectivity of differential schemes while reducing the communication channel bandwidth and relieving the strict synchronization requirement [166]. A pilot backup protection scheme is proposed in [170] based on the magnitude and direction of reactive energy estimated by Hilbert transform [171]. However, since reactive energy is reduced by fault resistance, the coverage of this scheme is limited to 200 Ω. In [62], internal and external faults are distinguished based on the polarities of boundary reactor voltages at terminal relays, where positive polarities indicate an internal fault and opposite polarities indicate an external fault. In [172], wavelet packet energy entropy (WPEE), applied to current measurements, is utilized to discriminate between internal and external faults. However, a large post-fault data window of 10 ms is required, which reduces the algorithm speed. In addition, estimated values of WPEE are drastically decreased when the fault resistance exceeds 100 Ω; thus, deteriorating the algorithm selectivity. Moreover, selecting a proper mother wavelet and adjusting the algorithm thresholds are laborious due to their reliance on extensive simulations, grid configuration, and parameters. The proposed scheme in [173] provides remote backup protection in both forward and reverse directions based on polarities and arrival instances of the fault-induced TWs extracted by morphological undecimated wavelet decomposition (MUWD). This scheme is slow, requires a high sampling frequency (500 kHz), and provides limited fault resistance coverage (100 Ω). In [174], the ratio of the backward over forward TW voltages at terminal relays are exchanged to decide whether the fault is internal or external. However, [174] requires large boundary reactors (200 mH), which may endanger system stability during power flow reversal [94].

In summary, existing relay failure backup protection schemes have the following major shortcomings:

- Use of a start-up criterion: most existing schemes depend on derivative-based criteria to initiate the algorithm. The start-up criterion may fail during critical fault condi-

tions such as high-resistance faults [155, 156, 170, 174], and consequently, the backup scheme will not be triggered.

- Limited fault resistance coverage [170, 172, 173]: recent primary protection schemes can detect internal faults with fault resistances up to 1000 Ω [175–177]. As backup protection is the last line of defense against extreme fault conditions, its fault resistance coverage should be greater than that of primary protection. Furthermore, this coverage should be determined for remote-end internal faults rather than middle-of-line faults, which is the case in [62, 170].

- Delayed operation: most existing schemes suffer from delayed operation since they use large post-fault data windows with lengths greater than 5 ms [57, 172, 173], which is the recommended operating time of backup protection of multi-terminal HVDC grids [174].

While primary protection schemes for multi-terminal HVDC grids have been extensively studied in the literature, backup protection has received significantly less attention. Based on the shortcomings above, it is essential to develop a reliable relay failure backup protection scheme that can detect primary protection failures and initiate a backup trip signal for the primary breaker, enhancing the security of HVDC grids. This chapter proposes a fast and reliable single-ended relay failure backup protection scheme for multi-terminal HVDC grids. The proposed scheme encompasses two components, i.e., a fault detection component and a directional component. The fault detection component detects internal and external faults in both directions based on Bayesian Model Averaging (BMA) [178]. Then, the fault direction is identified by the directional component based on the polarities of the faulted pole or zero-mode currents, according to the fault type. The proposed scheme can distinguish between internal, forward, and reverse external faults. Additionally, it can provide fast local backup protection in forward and reverse directions during internal and reverse external faults.

The remainder of the chapter is structured as follows: Section 6.2 introduces the HVDC test grid used in this study. The fault detection and directional components are outlined in Section 6.3 and Section 6.4, respectively. The proposed relay failure backup protection scheme is detailed in Section 6.5. In Section 6.6, several simulation studies are presented to demonstrate the reliability and effectiveness of the proposed scheme under various fault conditions. In Section 6.7, the BMA algorithm is utilized to detect breaker failure events based on local voltage measurements. Finally, conclusions of this chapter are summarized in Section 6.8.

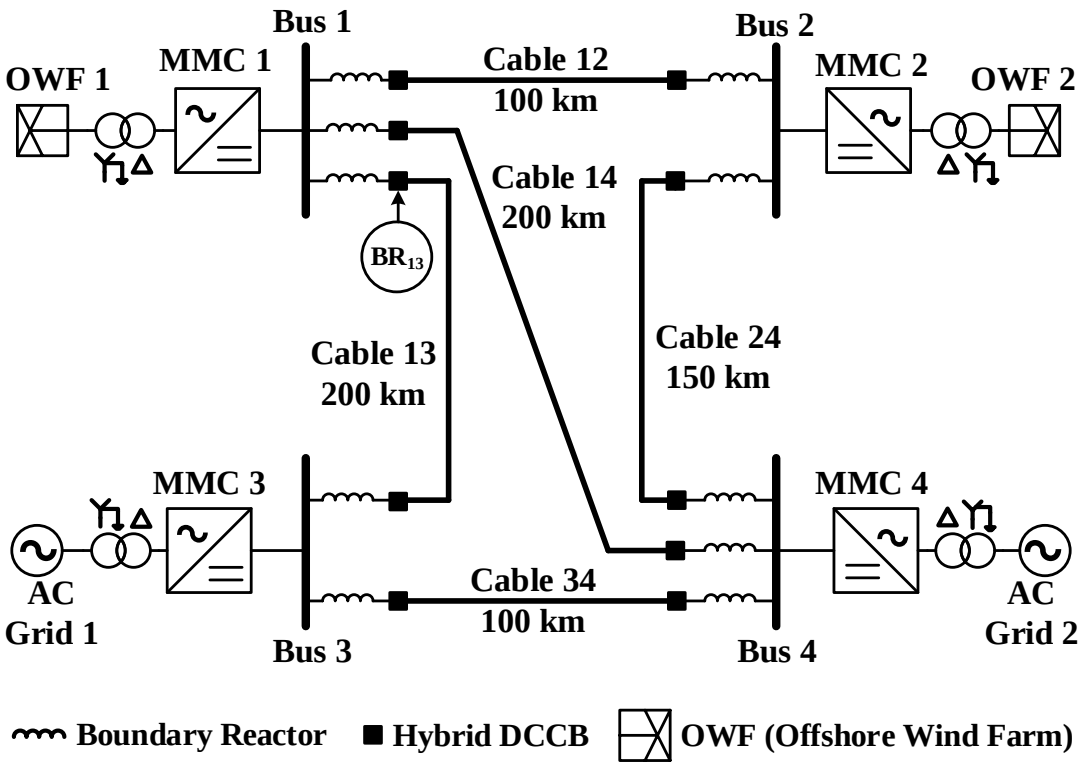


Figure 6.1: Four-terminal HVDC test grid.

6.2 HVDC Test Grid

The same HVDC grid employed in previous chapters is depicted in Figure 6.1 with the backup relay under investigation (BR_{13}) located at the beginning of cable 13. The system operates with a sampling frequency of 50 kHz.

6.3 Fault Detection Component

DC faults, regardless of fault resistance, typically cause sudden dips in the voltage waveform [119]. As the fault resistance increases, the voltage dip and its steepness reduce, resulting in the maloperation of derivative-based fault detection algorithms [144]. Furthermore, varying fault conditions, such as fault type and location, system configuration, and the presence of measurement noise, introduce significant variations in the resulting voltage waveforms. Therefore, a robust and adaptive abrupt change detection algorithm is required to reliably

identify abrupt changes in the voltage waveform under various fault conditions, ensuring fast and accurate fault detection.

BMA provides a reliable statistical technique for adaptive data modeling and abrupt change identification [179]. Various fault scenarios generate different voltage waveforms. To enable the identification of abrupt changes for all fault scenarios, BMA accounts for data model uncertainty and infers the optimal model by averaging across a set of candidate models, weighted by their posterior probabilities [179]. BMA addresses model selection uncertainty by incorporating all candidate models, rather than utilizing a fixed model. Furthermore, BMA is capable of identifying potential change points within the data and estimating the probability that these points signify abrupt changes, providing a probabilistic framework for detecting abrupt changes in any voltage waveform.

The BMA algorithm is described in the following steps [178]:

- *Step 1:* Consider a voltage signal $v(t)$ with N samples is modeled by a piecewise linear component $T(t)$ and a residual component $\epsilon(t)$ as follows:

$$v(t) = T(t) + \epsilon(t) \ , \tag{6.1}$$

  where $T(t)$ is modeled by a series of straight line segments defined by their slope a and intercept b and separated by m change points:

$$T(t) = a_j \ t + b_j \quad for \ \tau_j < t < \tau_{j+1}, \quad j = 0, \ldots, m \ , \tag{6.2}$$

  where $\tau_j = t_o$ is the initial time instant of the data window and $\tau_{m+1} = t_N$ is the time instant corresponding to the last sample N. Therefore, the parameters of a candidate model $\mathcal{M}_i$ can be represented as follows:

$$\mathcal{M}_i = \begin{cases} t_{cp_r} & r = 1, \ldots, m \\ a_j & j = 0, \ldots, m \\ b_j & j = 0, \ldots, m \end{cases} \quad , \quad i = 1, \ldots, M \ , \tag{6.3}$$

  where M is the number of candidate models and t_{cp_r} are the time instants associated with the model change points.

- *Step 2:* While it may seem that there will be an infinite number of candidate models, a finite set of M models can be selected by employing a probabilistic search method called the Markov Chain Monte Carlo (MCMC) sampling technique, which is explained in [179]. MCMC is used to explore the space of possible models by sampling

from the posterior distribution over candidate time series models. These models differ in structural features such as the number and locations of change points. MCMC is preferred over other sampling methods, such as importance sampling or rejection sampling, due to its scalability and ability to approximate complex posterior distributions without requiring exhaustive enumeration, making it well-suited for fault detection under extreme fault conditions [179].

- *Step 3:* Each model $\mathcal{M}_i$ is assigned a posterior probability $P(\mathcal{M}_i \mid v)$ to quantify how well it fits $v(t)$. $P(\mathcal{M}_i \mid v)$ is estimated based on Bayes' theorem as follows [180]:

$$P(\mathcal{M}_i \mid v) = \frac{P(v \mid \mathcal{M}_i)\ P(\mathcal{M}_i)}{\sum_{k=1}^{M} P(v \mid \mathcal{M}_k)\ P(\mathcal{M}_k)}\ , \tag{6.4}$$

  where $P(v \mid \mathcal{M}_i)$ is defined as the likelihood, which is the probability of observing v given that the model $\mathcal{M}_i$ is valid. A normal distribution is selected to model $P(v \mid \mathcal{M}_i)$ to simplify the algorithm computations [178]. $P(\mathcal{M}_i)$ is the prior probability of $\mathcal{M}_i$, which reflects our existing knowledge about the model before observing $v(t)$. A uniform prior distribution is selected to model $P(\mathcal{M}_i)$ to reflect equal initial likelihoods for all models, indicating no prior preference for any specific model. The denominator $\sum_{k=1}^{M} P(v \mid \mathcal{M}_k)\ P(\mathcal{M}_k)$ is a normalization term, summing over all possible models.

- *Step 4:* The best values of the optimal model parameters are obtained by weighting each model's estimation based on its posterior probability obtained in *Step 3*.

$$\mathbb{E}[\theta \mid v] = \sum_{i=1}^{M} P(\mathcal{M}_i \mid v)\ \mathbb{E}[\theta \mid \mathcal{M}_i, v]\ , \tag{6.5}$$

  where θ is the parameter of interest from (6.3), *i.e.*, m, t_{cp_r}, a_j, and b_j. $\mathbb{E}[\theta \mid v]$ is the expected value of θ, averaged over all candidate models. $\mathbb{E}[\theta \mid \mathcal{M}_i, v]$ is the estimate of θ under model $\mathcal{M}_i$. Equation (6.5) shows how BMA considers model selection uncertainty by incorporating all candidate models based on their posterior probabilities, providing a more robust estimate than relying on a single model.

- *Step 5:* The probability that a detected change point truly represents an abrupt change is calculated as follows:

$$\begin{aligned} P_{AC} &= P(t_{cp_r} \mid v) = \\ &\frac{1}{M} \sum_{i=1}^{M} \mathbb{I}\ (t_{cp_r} \in \text{change points of } \mathcal{M}_i)\ , \end{aligned} \tag{6.6}$$

where P_{AC} is the probability of detecting an abrupt change in v at t_{cp_r}. $\mathbb{I}(t_{cp_r} \in$ change points of $\mathcal{M}_i)$ is an indicator function that is 1 if t_{cp_r} represents a change point instant in model $\mathcal{M}_i$, and 0 otherwise. The value of P_{AC} lies between 0 and 1. For instance, if $P_{AC} = 1$ at a specific time instant t_{cp_r}, it indicates that all the candidate models agree that there is a significant change in v at that instant, revealing the existence of an abrupt change.

Within the context of fault detection, P_{AC} is simply the fault probability, which describes the probability that the detected change point corresponds to a fault event. As P_{AC} approaches one, it strongly indicates the presence of a fault. Therefore, a fault event is detected by the proposed scheme if:

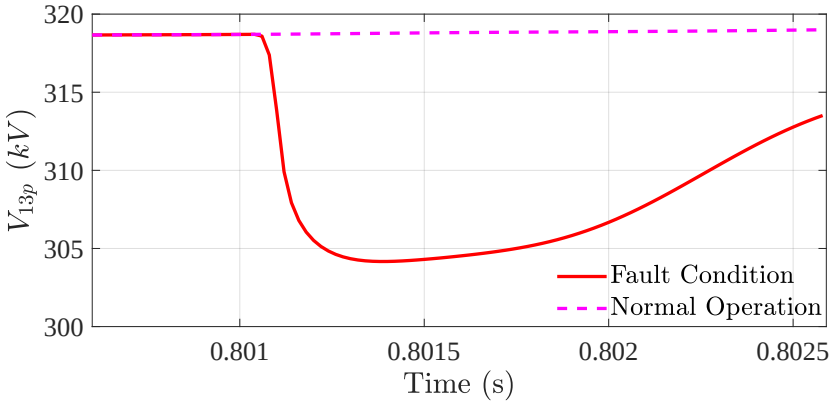
$$P_{AC} \geq P_{set,1}, \tag{6.7}$$

where $P_{set,1}$ is a threshold used to distinguish between abrupt changes during fault events and regular change points during non-fault conditions such as changes in system operating points.

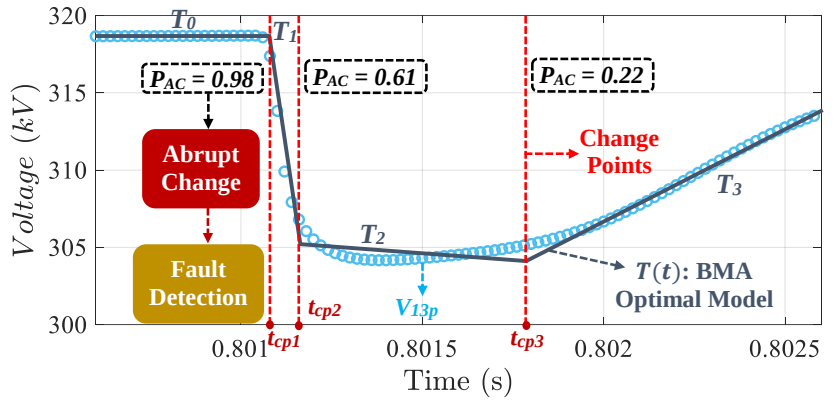
The BMA algorithm is applied to a critical fault scenario, where an internal PPTG fault located at the remote end of cable 13 is simulated. The fault starts at 0.8 s with a fault resistance $R_F = 1500\ \Omega$. Figure 6.2 shows the positive-pole voltage waveform V_{13_p}, the optimal data model estimated by BMA, the detected change points, and the corresponding P_{AC} values during fault condition and normal operation. As shown in Figure 6.2b, the estimated model is divided into four line segments (T_0, T_1, T_2, and T_3) with three change points ($m = 3$) at the following time instants: $t_{cp_1} = 0.80106\ s$, $t_{cp_2} = 0.80118\ s$, and $t_{cp_3} = 0.80176\ s$. The obtained BMA optimal model $T(t)$ is given in (6.8), where the time t is in seconds.

$$T(t) = \begin{cases} T_0: & V_{13_p} = 318.7 \quad kV \\ T_1: & V_{13_p} = -112875\ t + 90738.2 \quad kV \\ T_2: & V_{13_p} = -1563.8\ t + 1558 \quad kV \\ T_3: & V_{13_p} = 11285.5\ t - 8744.2 \quad kV \end{cases} \tag{6.8}$$

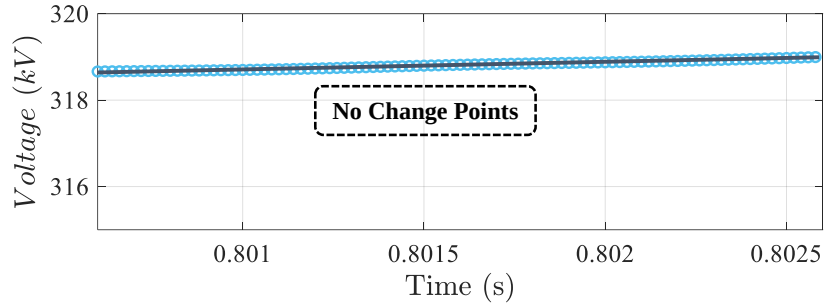
The sudden dip in V_{13_p} during the fault, Figure 6.2b, is detected as an abrupt change at t_{cp_1} with $P_{AC} = 0.98$, confirming the fault and emphasizing the robustness of the proposed fault detection criterion to high-resistance faults. By contrast, V_{13_p} during normal operation is modeled by a single line segment without change points, as shown in Figure 6.2c.



(a) V_{13_p}.

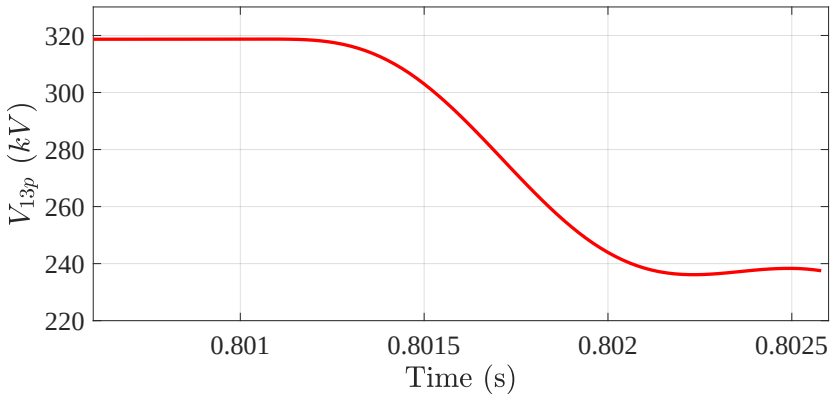


(b) BMA optimal model and detected change points during the fault.

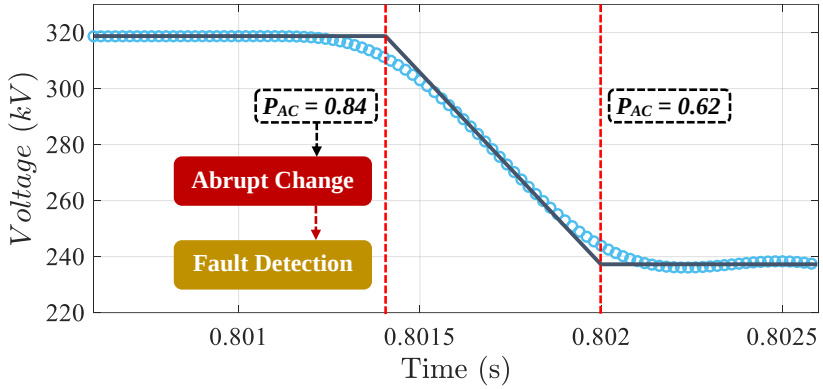


(c) BMA optimal model and detected change points during normal operation.

Figure 6.2: BMA performance during normal operation and an internal PPTG fault at the remote end of cable 13 with $R_F = 1500\ \Omega$.



(a) V_{13_p}.

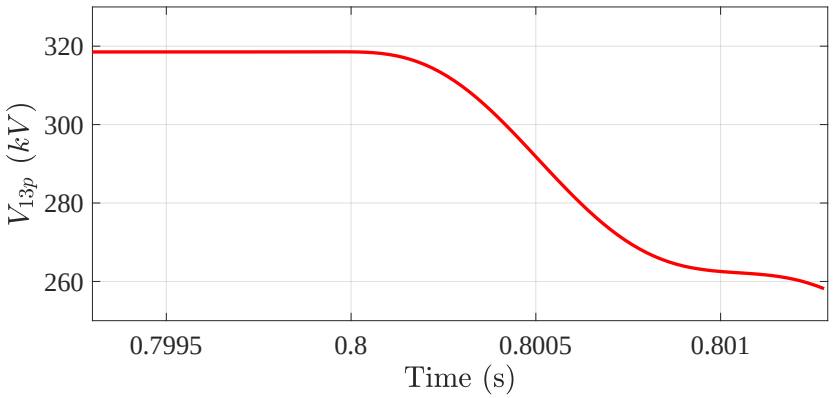


(b) BMA optimal model and detected change points.

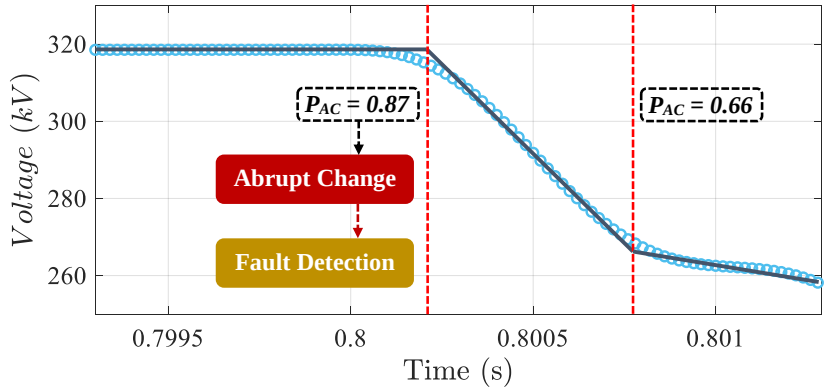
Figure 6.3: BMA performance during a solid forward external PPTG fault at the beginning of cable 34.

Therefore, the proposed fault detection criterion can reliably discriminate between critical internal faults with high resistances and normal operation, ensuring high sensitivity without maloperation during normal conditions.

Besides internal fault detection, the proposed criterion can identify external faults in both forward and reverse directions. To demonstrate this, forward and reverse external PPTG faults (with respect to the backup relay BR_{13}) at the beginning of cables 34 and 12, respectively, are simulated. As shown in Figures 6.3 and 6.4, the proposed criterion successfully detect these faults, with P_{AC} values of 0.84 for the forward fault and 0.87 for the reverse fault. It is also observed that the values of P_{AC} for external faults are lower compared to internal faults, as boundary reactors smooth the voltage waveforms before



(a) V_{13_p}.



(b) BMA optimal model and detected change points.

Figure 6.4: BMA performance during a solid reverse external PPTG fault at the beginning of cable 12.

they are captured by BR_{13}. In summary, in this section, a robust fault detection criterion based on BMA is proposed, where abrupt changes in the voltage waveform during faults are detected based on the value of P_{AC}. This method offers a highly reliable fault detection criterion, capable of identifying high-resistance internal faults and forward/reverse external faults.

6.4 Fault Directional Component

After detecting the fault, the directional component is used to determine the fault direction with respect to the backup relay BR_{13}. Current measurements are widely employed to indicate the fault direction based on their polarities [90]. A positive current polarity indicates the flow of current from BR_{13} towards bus 3, and vice versa [113]. However, this criterion may maloperate in the presence of high-resistance faults [181]. Alternatively, the polarity of zero-mode currents is robust to the fault resistance value [181]. Therefore, the polarity of zero-mode currents are used in the proposed scheme to identify the fault direction for pole-to-ground (PTG) faults, i.e., PPTG and NPTG faults. Zero-mode and line-mode currents (i_0 and i_1) are calculated from positive and negative pole currents (i_p and i_n) based on the following transformation matrix [181]:

$$\begin{bmatrix} i_0 \\ i_1 \end{bmatrix} = \frac{1}{\sqrt{2}} \begin{bmatrix} 1 & 1 \\ 1 & -1 \end{bmatrix} \begin{bmatrix} i_p \\ i_n \end{bmatrix} \tag{6.9}$$

The polarity of i_0 during PTG faults is determined by accumulating i_0 samples over a data window of N samples, as defined in (6.10). ξ_{PTG} is the zero-mode current polarity during PTG faults. The accumulation of i_0 samples provides a more robust criterion for polarity identification compared to relying on a single sample [105].

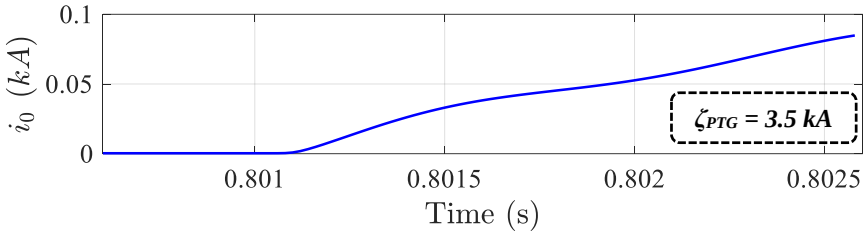
$$\xi_{PTG} = \sum_{k=1}^{N} i_{0_k} \tag{6.10}$$

A binary variable S is defined to indicate the fault direction based on the fault type, i.e., PPTG fault (S_{PPTG}) or NPTG fault (S_{NPTG}), as given in (6.11) or (6.12), respectively (S_{PPTG} and S_{NPTG} are complementary).

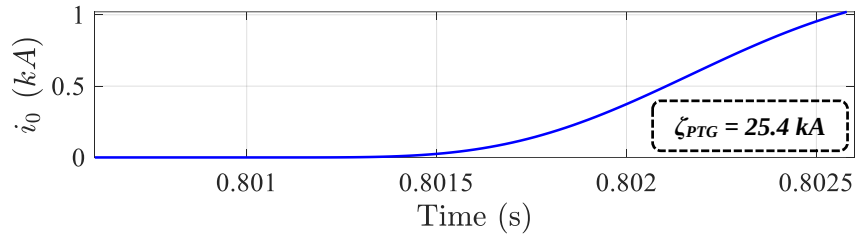
$$S_{PPTG} = \begin{cases} 1 & \xi_{PTG} > 0 \ \rightarrow \ \text{Forward Fault} \\ 0 & \xi_{PTG} < 0 \ \rightarrow \ \text{Reverse Fault} \end{cases} \tag{6.11}$$

$$S_{NPTG} = \begin{cases} 1 & \xi_{PTG} < 0 \ \rightarrow \ \text{Forward Fault} \\ 0 & \xi_{PTG} > 0 \ \rightarrow \ \text{Reverse Fault} \end{cases} \tag{6.12}$$

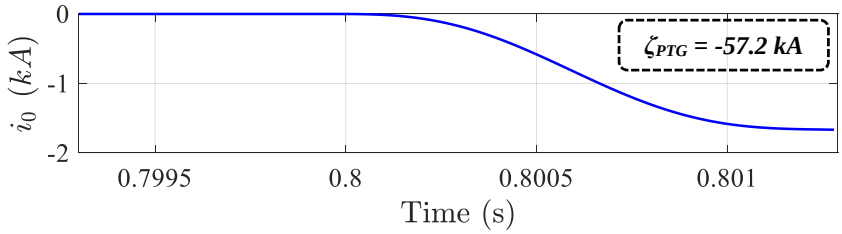
During PTP faults, i_0 remains zero due to the symmetry of the fault. Therefore, i_p is used instead of i_0 to determine the fault direction, given that high-resistance faults are



(a) An internal fault at the remote end of cable 13 ($R_F = 1500\ \Omega$).



(b) A solid forward external fault at the beginning of cable 34.



(c) A solid reverse external fault at the beginning of cable 12.

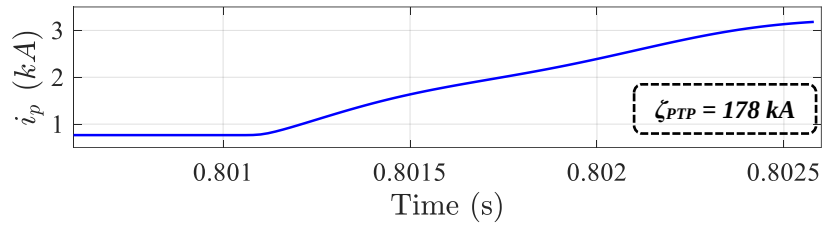
Figure 6.5: Zero-mode current waveforms under internal, forward, and reverse external PPTG faults.

typically associated with PTG faults, while the fault resistance of PTP faults is generally very low [113]. The polarity of i_p (ξ_{PTP}) is calculated as shown in (6.13), and the directional criterion for PTP faults (S_{PTP}) is expressed in (6.14).

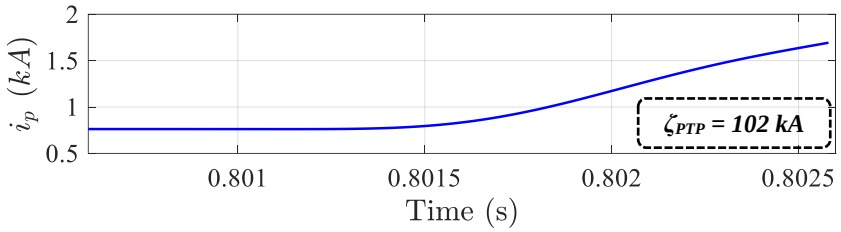
$$\xi_{PTP} = \sum_{k=1}^{N} i_{p_k} \tag{6.13}$$

$$S_{PTP} = \begin{cases} 1 & \xi_{PTP} > 0 \ \rightarrow \ \text{Forward Fault} \\ 0 & \xi_{PTP} < 0 \ \rightarrow \ \text{Reverse Fault} \end{cases} \tag{6.14}$$

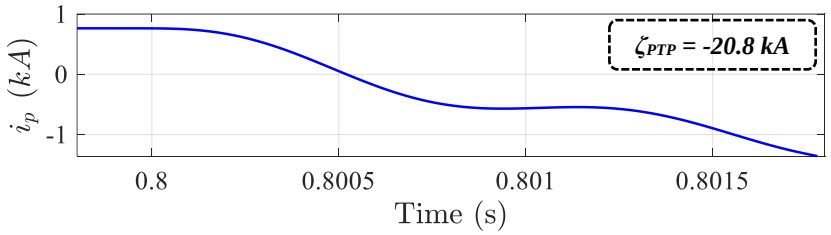
The directional criterion is applied to the same three fault scenarios investigated in Section 6.3, *i.e.*, an internal PPTG fault at the remote end of cable 13 with $R_F = 1500\ \Omega$



(a) An internal fault at the remote end of cable 13 ($R_F = 100\ \Omega$).



(b) A solid forward external fault at the beginning of cable 34.



(c) A solid reverse external fault at the beginning of cable 12.

Figure 6.6: Positive-pole current waveforms under internal, forward, and reverse external PTP faults.

and solid PPTG faults at the beginning of cables 34 and 12. Figure 6.5 depicts the obtained zero-mode current waveforms and the corresponding values of ξ_{PTG}. As shown, ξ_{PTG} is positive in case of forward PPTG faults (internal and forward external faults), while ξ_{PTG} is negative in case of reverse PPTG faults (reverse external faults). Therefore, the polarity of zero-mode currents can reliably identify the fault direction during PTG faults. Similarly, the polarity of positive-pole currents is used to identify the fault direction during PTP faults. Figure 6.6 shows the positive-pole current waveforms and the corresponding values of ξ_{PTP} for the same fault scenarios, yet the fault type is PTP and R_F of the internal fault case is 100 Ω. Again, ξ_{PTP} is positive in case of forward PTP faults and negative in case of reverse PTP faults.

6.5 Proposed Relay Failure Backup Protection Scheme

Figure 6.7 shows the flowchart of the proposed relay failure backup protection scheme. The proposed scheme commences once positive or negative pole voltages drop below a certain value V_{set}. The value of V_{set} should be selected to accommodate all fault scenarios, including high-resistance internal faults, typically associated with small voltage dips. As shown in Figure 6.2a, a large fault resistance of 1500 Ω results in approximately 5% sudden drop in the voltage waveform. Therefore, V_{set} is selected as 310 kV, corresponding to 3% voltage drop. Then, the proposed fault detection criterion estimates the values of P_{AC} of positive and negative poles (P_{AC_p} and P_{AC_n}) and compares them with $P_{set,1}$. The value of $P_{set,1}$ should be selected such that all fault events are reliably detected while avoiding relay maloperation during non-fault transients.

To demonstrate how $P_{set,1}$ is selected, two transient non-fault scenarios are considered, and the values of P_{AC} for these scenarios are calculated. First, the reference DC voltage at Bus 1 drops by 5% during the simulation (the same drop as in the internal fault scenario). As shown in Figure 6.8, only one change point is identified with a small P_{AC} value of 0.35, indicating a non-fault condition. The second transient scenario that may result in relay maloperation is the trip of external breakers during external faults. To investigate the impact of external breaker operation on the proposed fault detection criterion, a forward external PPTG fault at the middle of cable 34 is simulated, Figure 6.9. The fault is successfully detected and cleared by the primary protection of cable 34. The developed counter voltage during successful breaker operation results in a sudden increase in V_{34_p}, as shown in Figure 6.9a. However, there are no abrupt changes in V_{13_p}, and two change points with small P_{AC} values are identified by the BMA algorithm, as shown in Figure 6.9b. Based on the investigated scenarios, P_{AC} during fault scenarios is much higher than other transient scenarios, and therefore, $P_{set,1}$ is adjusted at 0.7.

The next step is to identify the fault type. If both P_{AC_p} and P_{AC_n} are larger than $P_{set,1}$, the fault type is PTP. If only P_{AC_p} (P_{AC_n}) satisfies (6.7), a PPTG (NPTG) fault is identified. Based on the identified fault type, the fault direction S relative to the backup relay BR_{13} is determined, as explained in Section 6.4. Based on the value of S, forward faults are distinguished from reverse faults. If a forward fault is identified, the value of P_{AC} is compared with a higher threshold, $P_{set,2}$, to discriminate between internal and forward external faults. The sudden dip in the voltage during internal faults causes the value of P_{AC} to be almost one (as shown in Figure 6.2b), while the sudden dip in the voltage during forward external faults will be smoothed due to boundary reactors, resulting in lower value of P_{AC} (as shown in Figure 6.3b). For the most critical forward external fault, a solid PTP fault at bus 3, P_{AC} is 0.86. Therefore, the value of $P_{set,2}$ is selected as 0.95.

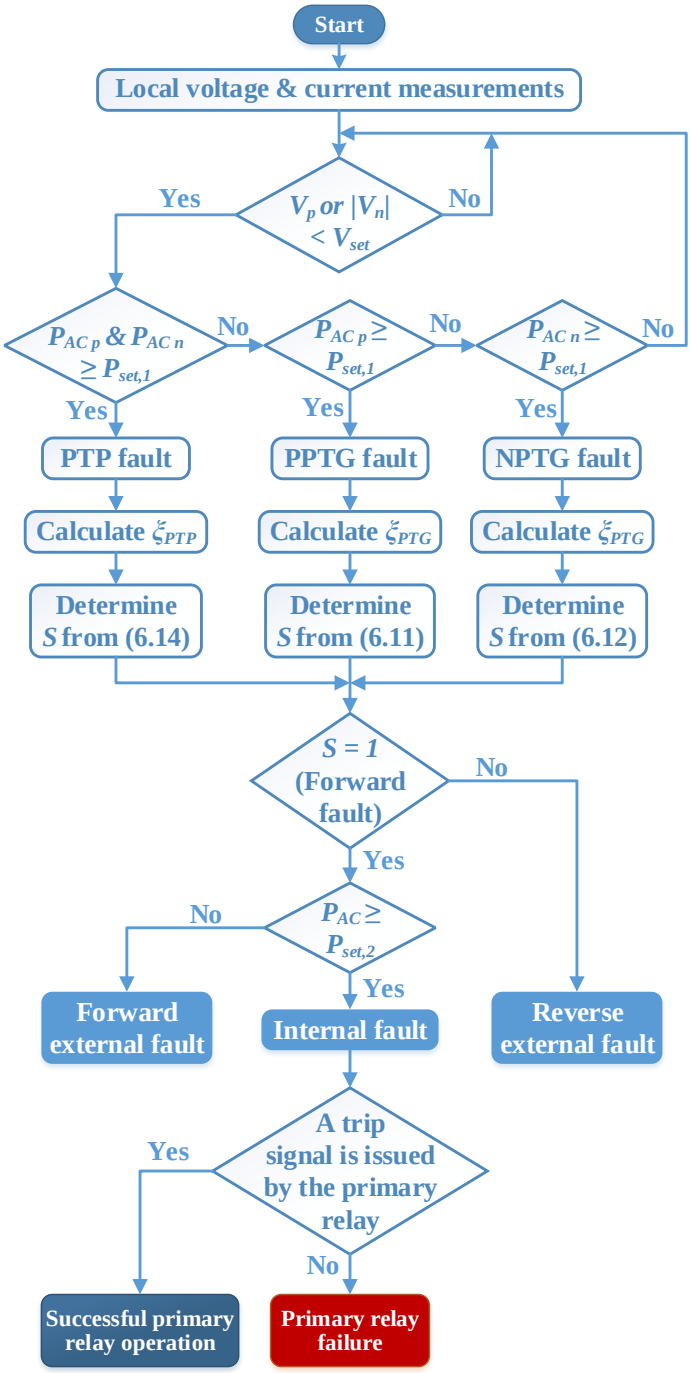


Figure 6.7: Proposed relay failure backup protection scheme.

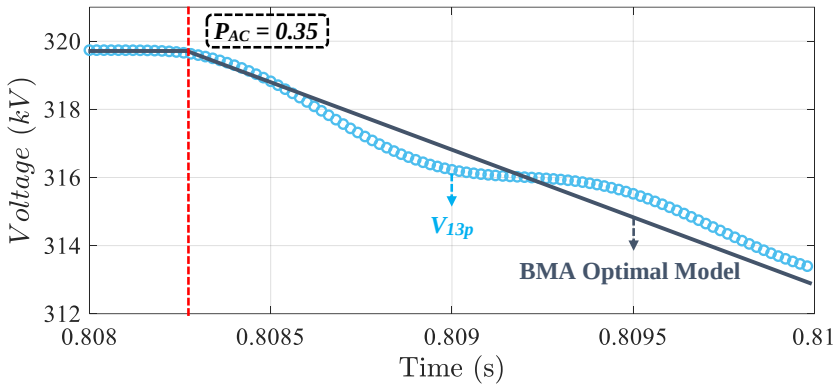
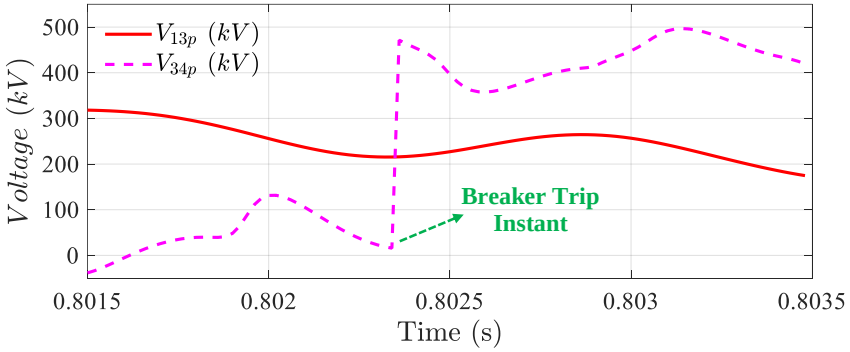
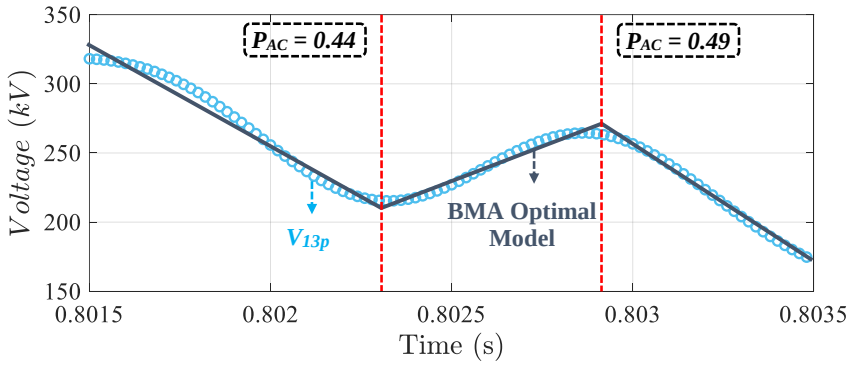


Figure 6.8: BMA optimal model and detected change points for a 5% drop in the reference DC voltage at Bus 1.



(a) V_{13_p} and V_{34_p}.



(b) BMA optimal model and detected change points.

Figure 6.9: BMA performance during successful breaker operation for a solid forward external PPTG fault at the middle of cable 34.

In summary, internal, forward, and reverse external faults are identified based on the following criterion:

$$\begin{cases} S = 1 \ \& \ P_{AC} \geq P_{set,2} & \text{Internal fault} \\ S = 1 \ \& \ P_{set,1} \leq P_{AC} < P_{set,2} & \text{Forward external fault} \\ S = 0 \ \& \ P_{AC} \geq P_{set,1} & \text{Reverse external fault} \end{cases} \tag{6.15}$$

If an internal fault is identified and the primary relay does not issue a trip signal, a backup trip signal will be sent to the primary breaker of cable 13. According to HVDC grid protection speed requirement, the maximum permissible time for primary relays to detect internal faults is less than 3 ms [144]. Therefore, a time delay of 3 ms is used to coordinate between primary and backup protection. One notable advantage of the proposed scheme is that it immediately detects primary relay failure events once the 3 ms time delay has elapsed. Likewise, if a reverse external fault is identified by the proposed scheme and the intended primary relay fails to detect the fault, BR_{13} will send a backup trip signal to the primary breaker of cable 12.

6.6 Simulation Results

In this section, numerous fault scenarios are simulated to evaluate the performance of the proposed relay failure backup protection scheme under various fault conditions. Furthermore, the superiority of the proposed scheme in comparison to existing schemes is demonstrated.

6.6.1 Performance of the proposed relay failure scheme

Several internal and external fault scenarios are simulated to evaluate the performance of the proposed relay failure backup protection scheme. The backup relay BR_{13} is selected as the local relay under investigation. Various fault types (PTP, PPTG, and NPTG) at different locations are simulated with R_F changing from zero to 1500 Ω. The obtained values of P_{AC}, ξ_{PTG} (or ξ_{PTP}), and S for all the simulated scenarios are shown in Tables 6.1 and 6.2 for internal and external faults, respectively. These values are calculated based on the first data window in which the fault is detected, *i.e.*, P_{AC} becomes larger than $P_{set,1}$. For PPTG and NPTG faults, the calculated values of the faulted pole are given, whereas for PTP faults, those of the positive pole are only shown. Based on extensive simulations,

Table 6.1: Performance of the proposed relay failure backup protection scheme under various internal faults

Fault Type	**Location**	**Distance** (km)	**From**	R_F (Ω)	P_{AC}	ξ_{PTG}	ξ_{PTP}	S	**Decision**
PPTG	cable 13	0	bus 1	0	1	183	–	1	Internal fault
NPTG	cable 13	100	bus 1	0	1	−177	–	1	Internal fault
PTP	cable 13	200	bus 1	0	0.99	–	338	1	Internal fault
PPTG	cable 13	0	bus 1	100	1	43.9	–	1	Internal fault
NPTG	cable 13	100	bus 1	100	1	−32.7	–	1	Internal fault
PTP	cable 13	200	bus 1	100	0.98	–	178	1	Internal fault
PPTG	cable 13	0	bus 1	1500	1	3.8	–	1	Internal fault
NPTG	cable 13	0	bus 1	1500	1	−3.8	–	1	Internal fault
PPTG	cable 13	100	bus 1	1500	1	2.6	–	1	Internal fault
NPTG	cable 13	100	bus 1	1500	1	−2.6	–	1	Internal fault
PPTG	cable 13	200	bus 1	1500	0.98	3.5	–	1	Internal fault
NPTG	cable 13	200	bus 1	1500	0.98	−3.5	–	1	Internal fault

a 2 ms moving window of the measured voltage is required to reliably capture the abrupt change associated with the fault, especially during external faults, and to precisely calculate the value of P_{AC}. The sampling frequency is 50 kHz; thus, the moving window contains 100 samples ($N = 100$), sufficient for accurate statistical inference [178]. To minimize the computational burden of the proposed scheme, without impacting its performance, the moving window is updated every ten samples.

As shown in Tables 6.1 and 6.2, it is evident that the proposed relay failure backup protection scheme successfully detects all faults and reliably discriminates between internal and external faults in both forward and reverse directions. Furthermore, the reliable performance of the proposed scheme is demonstrated under critical internal faults (remote high-resistance faults) and severe external faults (solid bus faults). Since the window length is 2 ms, all fault scenarios are rapidly detected by the proposed fault detection criterion in less than 2 ms depending on the number of post-fault samples required to detect the abrupt change associated with the fault. It should be mentioned that the proposed fault detection

Table 6.2: Performance of the proposed relay failure backup protection scheme under various external faults

Fault Type	**Location**	**Distance** (km)	**From**	R_F (Ω)	P_{AC}	ξ_{PTG}	ξ_{PTP}	S	**Decision**
External Bus Faults									
PTP	bus 3	–	–	0	0.86	–	162	1	Forward external fault
PTP	bus 1	–	–	0	0.95	–	−206	0	Reverse external fault
External Cable Faults									
PTP	cable 34	0	bus 3	0	0.84	–	102	1	Forward external fault
PTP	cable 34	50	bus 3	0	0.81	–	98.7	1	Forward external fault
PTP	cable 34	100	bus 3	0	0.8	–	89.3	1	Forward external fault
PTP	cable 12	0	bus 1	0	0.9	–	−20.8	0	Reverse external fault
PTP	cable 12	50	bus 1	0	0.86	–	−11.6	0	Reverse external fault
PTP	cable 12	100	bus 1	0	0.84	–	−15.5	0	Reverse external fault

criterion can be tailored to provide primary fault detection by exploiting the fact that the value of P_{AC} during internal faults is higher than that of external faults. In this case, $P_{set,2}$ can be used as the threshold of the primary criterion. In addition, a shorter data window may be used because of the steepness of the sudden dip in the voltage waveform during internal faults compared to external faults. However, in that scenario, a larger boundary reactor will be required to guarantee reliable discrimination between internal and external faults, especially during external bus faults.

6.6.2 Sensitivity to the size of boundary reactors

This section evaluates the sensitivity of the proposed relay failure backup protection scheme to the size of boundary reactors. Two high-resistance internal fault cases are examined: PPTG and NPTG faults at the midpoint and end of cable 13, respectively, with $R_F = 1500\,\Omega$. Additionally, two external fault scenarios are considered: forward and reverse PTP faults at buses 3 and 1, respectively. The simulations consider boundary reactor sizes of 25 mH and 10 mH. As shown in Table 6.3, the proposed scheme successfully identifies all fault scenarios. As the inductance of boundary reactors decreases, their ability to suppress fault current and smooth the voltage waveform is reduced, resulting in a steeper voltage dip during external faults and higher fault currents. Consequently, the values of P_{AC} during external faults are higher than those presented in Table 6.2. It is evident that the performance of the proposed scheme remains unaffected by the inductance of boundary reactors. A significant advantage of the proposed scheme is its applicability to HVDC grids with weak boundary conditions up to 10 mH. Furthermore, large boundary reactors might introduce dynamic stability issues during power flow reversal [94].

6.6.3 Sensitivity to measurement noise

This section evaluates the performance of the proposed relay failure backup protection scheme under measurement noise. The same fault scenarios in Section 6.6.2 (with $L_{dc} = 50\ mH$) are examined, where signal-to-noise ratios (SNR) of 30 and 40 db for voltage and current measurements are considered. As shown in Table 6.4, the proposed scheme successfully detects all fault scenarios and discriminates between internal and external faults, confirming its robustness to measurement noise.

6.6.4 Comparison with existing schemes

Table 6.5 compares the proposed scheme with existing relay failure backup protection schemes. Compared with existing schemes, the proposed scheme demonstrates superior performance in terms of fault resistance coverage, sensitivity to boundary reactor size, speed, and measurement noise withstand capability. One of the most significant advantages of the proposed scheme is its large fault resistance coverage of up to 1500 Ω, whereas the coverage of existing schemes does not exceed 500 Ω. Another notable advantage of the proposed scheme is its applicability to HVDC grids with small boundary reactors (up to 10 mH), whereas other schemes will fail if boundary reactors are less than $75 - 100\ mH$

Table 6.3: Performance of the proposed relay failure backup protection scheme under different boundary conditions

Fault Type	**Location**	**Distance** (km)	**From**	R_F (Ω)	P_{AC}	ξ_{PTG}	ξ_{PTP}	S	**Decision**
				$L_{dc} = 25\ mH$					
PPTG	cable 13	100	bus 1	1500	1	4	–	1	Internal fault
NPTG	cable 13	200	bus 1	1500	0.98	−4.6	–	1	Internal fault
PTP	bus 3	–	–	0	0.88	–	280	1	Forward external fault
PTP	bus 1	–	–	0	0.96	–	−331	0	Reverse external fault
				$L_{dc} = 10\ mH$					
PPTG	cable 13	100	bus 1	1500	1	5.3	–	1	Internal fault
NPTG	cable 13	200	bus 1	1500	0.98	−4.9	–	1	Internal fault
PTP	bus 3	–	–	0	0.89	–	468	1	Forward external fault
PTP	bus 1	–	–	0	0.98	–	−441	0	Reverse external fault

[57, 169, 172]. As the size of boundary reactors reduces, cost, footprint, and losses will reduce [182].

The single-ended directional criterion of the proposed scheme can efficiently identify the fault direction based on the polarities of local pole or zero-mode currents without any need for communication channels; thus, avoiding communication delays and failure and eliminating the need for synchronization between terminal relays. In contrast, strictly synchronized current measurements should be exchanged in [57] to distinguish between internal and external faults. The proposed fault detection criterion can detect solid internal faults at the beginning of cables, whereas the proposed scheme in [170], based on reactive energy, fails to detect those faults since the pole voltage drops to zero, and hence, the estimated reactive energy is zero. Considering protection speed, the proposed scheme can rapidly detect and discriminate between internal, forward and reverse external faults in less than 2 ms, which is faster than most existing schemes. In addition, the proposed scheme

Table 6.4: Performance of the proposed relay failure backup protection scheme under different noise levels

Fault Type	**Location**	**Distance** (km)	**From**	R_F (Ω)	P_{AC}	ξ_{PTG}	ξ_{PTP}	S	**Decision**
				$SNR = 40$ db					
PPTG	cable 13	100	bus 1	1500	0.97	2.6	–	1	Internal fault
NPTG	cable 13	200	bus 1	1500	0.98	−3.6	–	1	Internal fault
PTP	bus 3	–	–	0	0.79	–	162	1	Forward external fault
PTP	bus 1	–	–	0	0.86	–	−210	0	Reverse external fault
				$SNR = 30$ db					
PPTG	cable 13	100	bus 1	1500	0.96	2.7	–	1	Internal fault
NPTG	cable 13	200	bus 1	1500	0.98	−3.1	–	1	Internal fault
PTP	bus 3	–	–	0	0.75	–	161	1	Forward external fault
PTP	bus 1	–	–	0	0.85	–	−206	0	Reverse external fault

sends backup trip signals to primary breakers in case of primary relay failure during internal and reverse external faults; thus, providing local backup protection in forward and reverse directions.

6.7 Breaker Failure Detection Based on BMA

This section demonstrates how BMA distinguishes between successful breaker operation and breaker failure by investigating the following case study (Figure 5.1). Figure 6.10a presents V_{13_p} during breaker trip and failure scenarios for a PTP fault at the middle of cable 13. The fault type is permanent, and it starts at 0.7 s. As illustrated in Figure 6.10a, the primary distinction between breaker trip and failure scenarios is the sudden increase

Table 6.5: Comparison between the proposed scheme and existing relay failure backup protection schemes

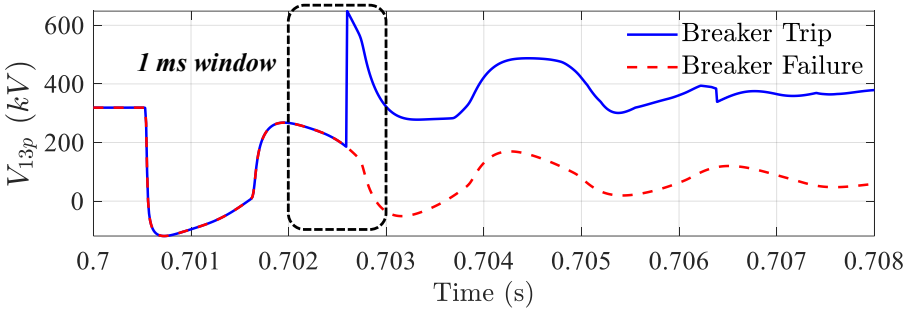
Reference	Fault Detection Criterion	Directional Criterion	Boundary Reactor Size	Minimum Permissible L_{dc}	Minimum Permissible Noise Level	R_F Coverage	Operating Time	Sampling Frequency
[155]	K-nearest neighbor	Not employed	50 mH	Not investigated	Not investigated	Not investigated	3 ms	50 kHz
[156]	Quickest change detection	Not employed	100 mH	Not investigated	20 db	10 Ω	4 ms	50 kHz
[169]	Current derivative	Not employed	100 mH	100 mH	50 db	200 Ω	1 ms	20 kHz
[57]	Line-mode current differential protection	Not employed	150 mH	75 mH	30 db	500 Ω	7.5 ms	10 kHz
[170]	Reactive energy	Reactive energy flow directions	290 mH	Not investigated	Not investigated	200 Ω	40 ms	10 kHz
[62]	Boundary reactor voltage gradient	Polarities of boundary reactor voltages	200 mH	Not investigated	Not investigated	400 Ω	3 ms	50 kHz
[172]	WPEE	Not employed	100 mH	100 mH	Not investigated	100 Ω	10 ms	10 kHz
[173]	MUWD	Polarities of incident TWs	50 mH	Not investigated	30 db	100 Ω	3 ms	500 kHz
Proposed Scheme	BMA	Polarities of pole or zero-mode currents	50 mH	10 mH	30 db	1500 Ω	2 ms	50 kHz

in V_{13_p} in case of successful breaker operation around the anticipated breaker trip instant (2 ms after fault detection). This sharp increase results from the dissipation of fault energy through the surge arrester branch, generating a large counter voltage across the breaker [152]. Therefore, after receiving a trip signal from primary protection, the absence of abrupt changes in V_{13_p} indicates breaker failure. Hence, the BMA algorithm can be employed to infer the breaker status based on local voltage measurements without requiring additional measuring devices.

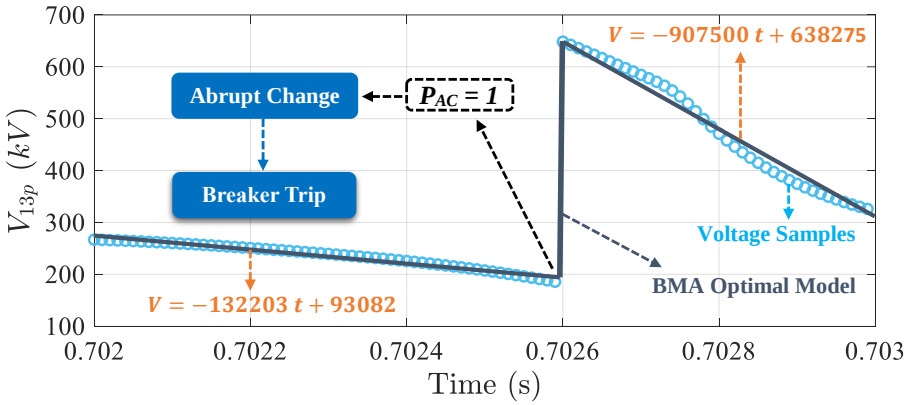
The BMA algorithm is applied to V_{13_p} over a 1 ms window during breaker trip and failure scenarios. As shown in Figure 6.10b, V_{13_p} is modeled as two line segments separated by a change point with $P_{AC} = 1$ due to the abrupt change in the voltage waveform during successful breaker operation. During breaker failure, Figure 6.10c, P_{AC} of the detected change point is small due to the smooth change of V_{13_p}. Consequently, an abrupt change can be detected if:

$$P_{AC} > P_{set}, \tag{6.16}$$

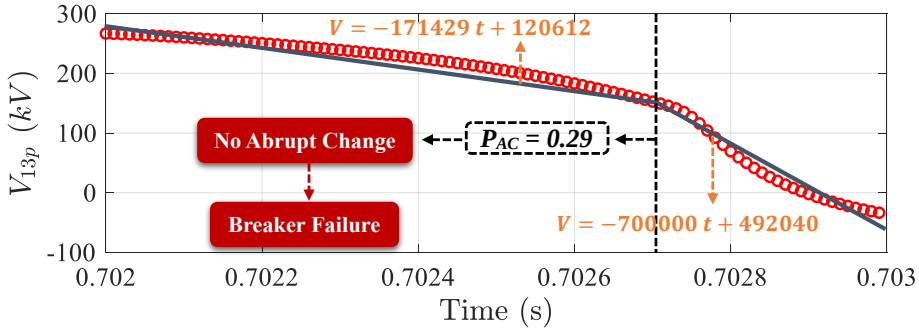
where P_{set} is a threshold that distinguishes between abrupt changes during successful breaker operation and regular change points during breaker failure.



(a) V_{13_p}.



(b) BMA model over a 1 ms window during breaker trip.



(c) BMA model over a 1 ms window during breaker failure.

Figure 6.10: Positive-pole voltage waveform and corresponding BMA models during successful breaker trip and breaker failure.

The procedure of the proposed BMA-based breaker failure backup protection scheme is described in Figure 6.11. If an internal fault occurs, the primary relay detects the fault and sends a trip signal to the primary breaker. After receiving the trip signal,

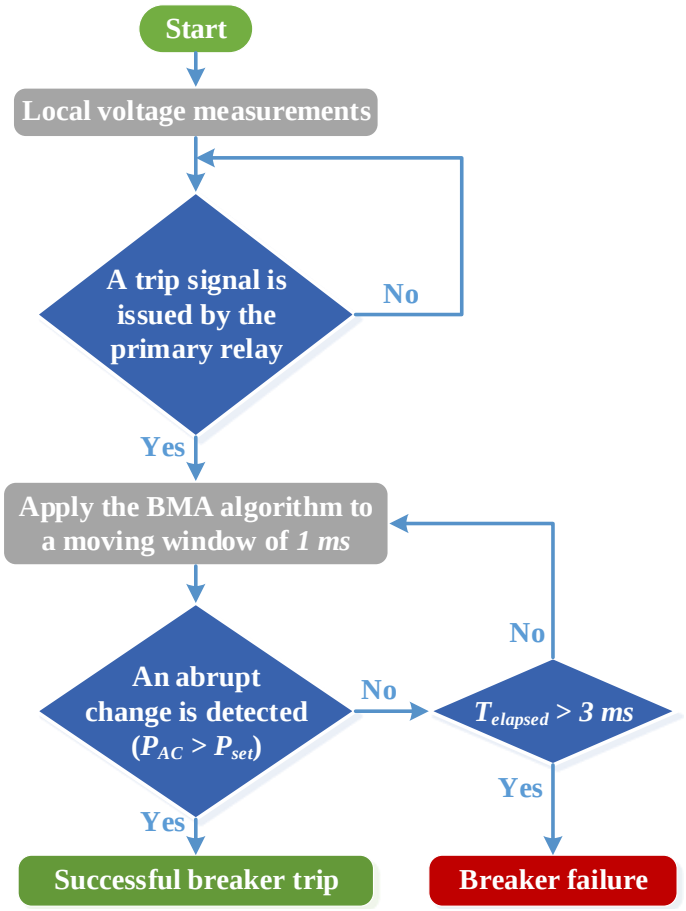
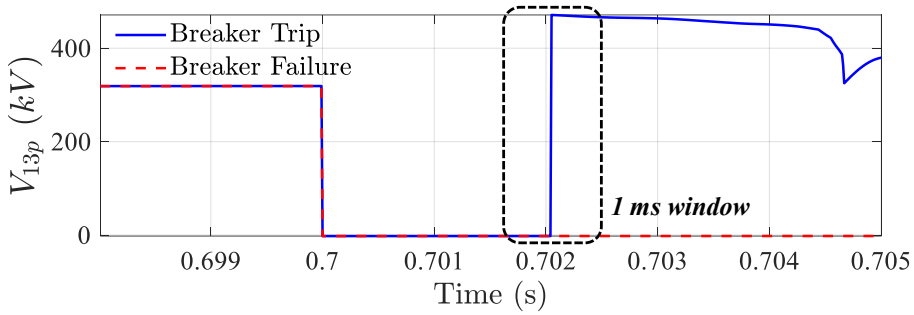


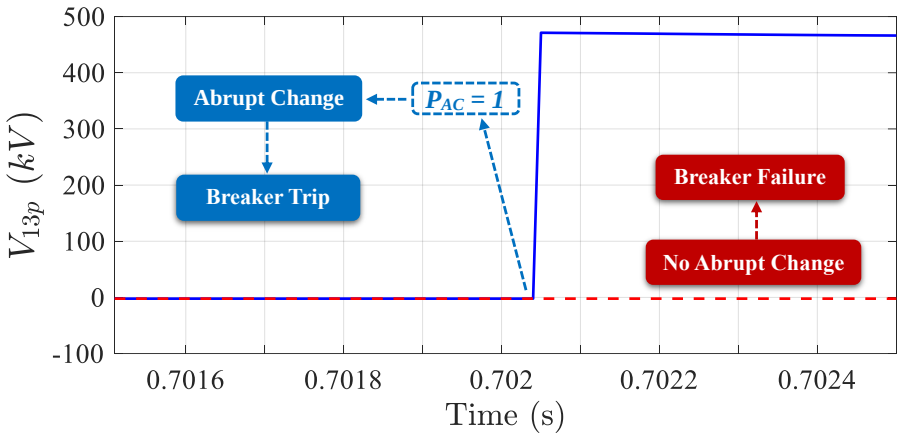
Figure 6.11: Proposed BMA-based breaker failure backup protection scheme.

the BMA algorithm is continuously applied to local voltage measurements using a 1 ms moving window. To minimize the computational burden of the proposed scheme, without impacting its performance, the moving window is updated every ten samples. If the breaker successfully trips, P_{AC} will be larger than P_{set} and an abrupt change is detected by the BMA algorithm. The value of P_{set} is selected as high as 0.95, Figure 6.10b. If no abrupt changes are detected after 3 ms ($T_{elapsed}$), a breaker failure event is identified, and backup trip signals are issued by the proposed scheme to other breakers connected to the same bus.

Various fault scenarios are simulated to demonstrate the efficient performance of the proposed BMA-based breaker failure scheme. Figure 6.12a shows V_{13_p} during breaker trip and failure scenarios for a solid PPTG fault at the local end of cable 13. As shown in Figure 6.12b (blue), successful breaker operation is associated with an abrupt change with



(a) V_{13_p}.

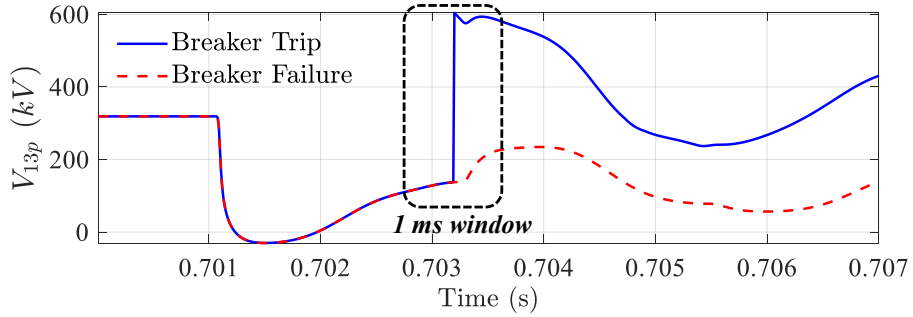


(b) A zoomed 1 *ms* window with the detected abrupt changes.

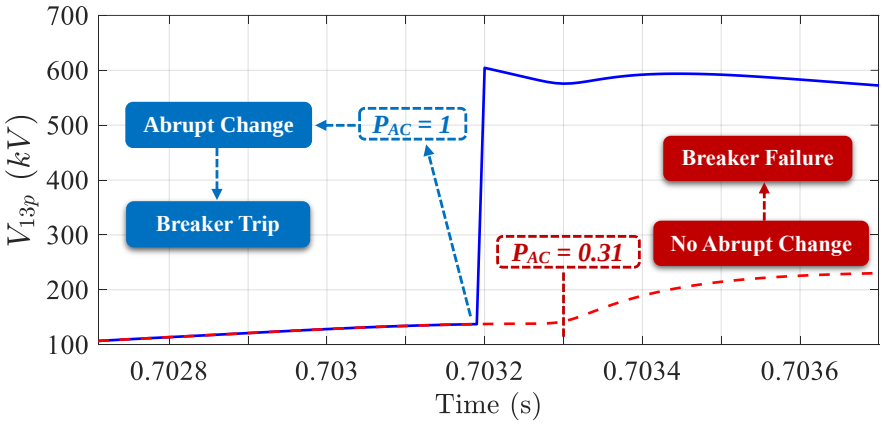
Figure 6.12: Performance of the proposed BMA-based breaker failure scheme during a solid PPTG fault at the beginning of cable 13 with successful breaker trip and failure.

$P_{AC} = 1$. On the other hand, no abrupt changes exist during breaker failure, Figure 6.12b (red). Similarly, a PPTG fault is simulated at the remote end of cable 13, and the proposed scheme reliably discriminates between successful breaker trip and breaker failure, as shown in Figure 6.13. Therefore, the performance of the proposed BMA-based breaker failure scheme is not impacted by fault location.

A PTP fault is simulated at the remote end of cable 13 with R_F equal to 1500 Ω. As depicted in Figure 6.14, breaker trip and failure scenarios are successfully distinguished by the proposed scheme. A significant advantage of the proposed BMA-based breaker failure scheme is its capability to detect breaker failure events, even if the fault resistance is as high as 1500 Ω. The proposed scheme is robust to high-resistance faults because the abrupt increase in V_{13_p} associated with the developed counter voltage depends mainly on the surge arrester voltage rating, not the fault resistance. It is worth mentioning that a



(a) V_{13_p}.

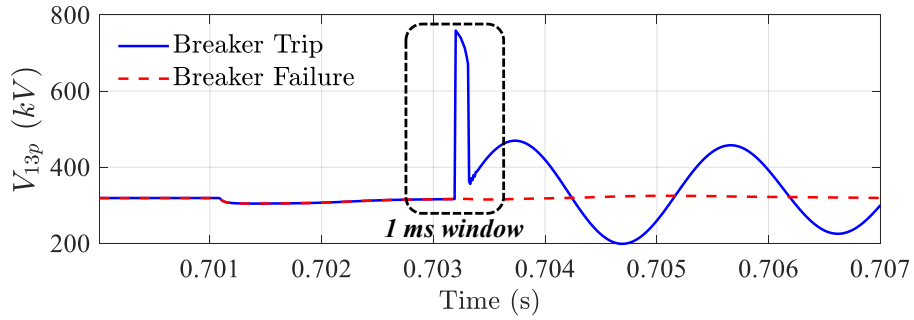


(b) A zoomed 1 ms window with the detected abrupt changes.

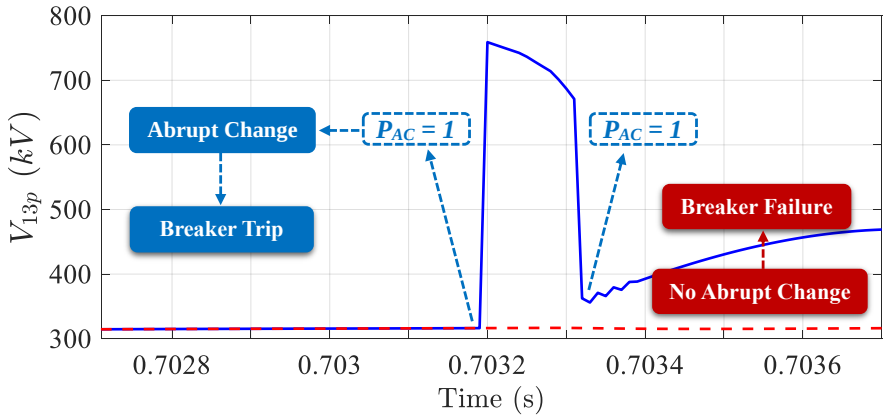
Figure 6.13: Performance of the proposed BMA-based breaker failure scheme during a solid PPTG fault at the end of cable 13 with successful breaker trip and failure.

second abrupt change is detected during successful breaker operation, without affecting the performance of the proposed scheme, as shown in Figure 6.14b. The second abrupt change occurs due to the rapid release of the fault energy, which is proportional to the limited fault current of this scenario as R_F is large [160].

To evaluate the robustness of the proposed BMA-based breaker failure scheme to weak boundary conditions, the size of boundary reactors is changed from 50 mH (default value) to 10 mH. A solid PTP fault is simulated in the middle of cable 13. As shown in Figure 6.15, the proposed scheme successfully distinguishes between breaker trip and failure scenarios as the detected change points during breaker failure have small P_{AC} values compared with that of the detected abrupt change during breaker trip. Therefore, the proposed BMA-based breaker failure scheme does not require large boundary reactors, which may complicate bidirectional power flow control in multi-terminal HVDC grids [94]. To in-



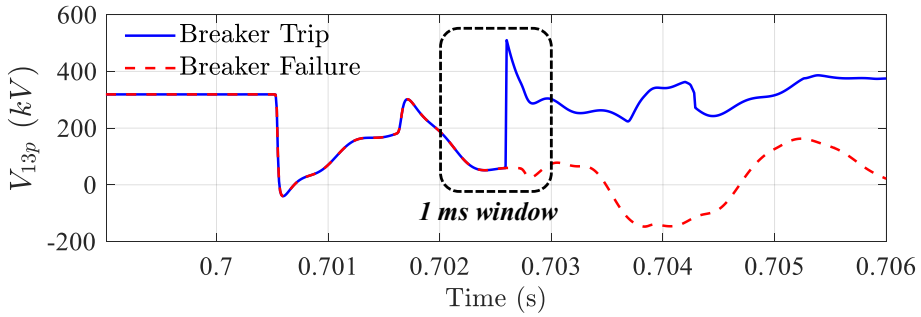
(a) V_{13_p}.



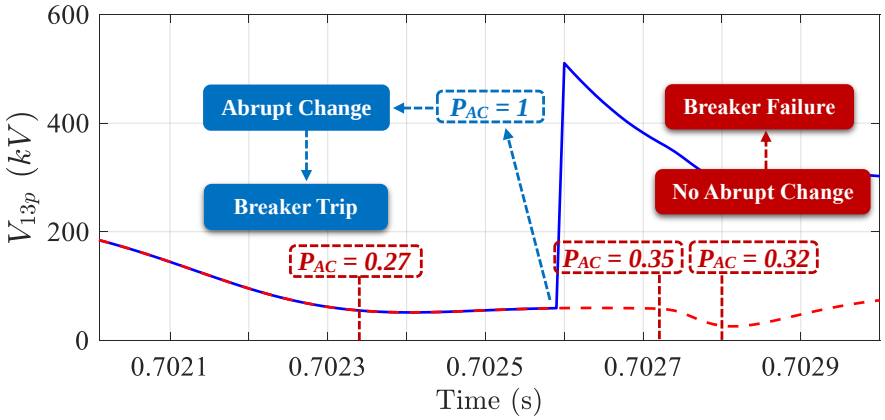
(b) A zoomed 1 ms window with the detected abrupt changes.

Figure 6.14: Performance of the proposed BMA-based breaker failure scheme during a PTP fault at the end of cable 13 with $R_F = 1500\ \Omega$ with successful breaker trip and failure.

vestigate the measurement noise withstand capability, a solid PTP fault is simulated in the middle of cable 13 with an SNR of 30 db, Figure 6.16. The BMA optimal models of this fault scenario (Figure 6.16b) are similar to those of the same fault scenario, yet without measurement noise (Figures 6.10b and 6.10c), since the averaging feature of the BMA algorithm helps in eliminating measurement noise. The simulation results of this fault scenario confirm that the proposed BMA-based breaker failure scheme is capable of detecting breaker failure events in the presence of measurement noise.



(a) V_{13_p}.

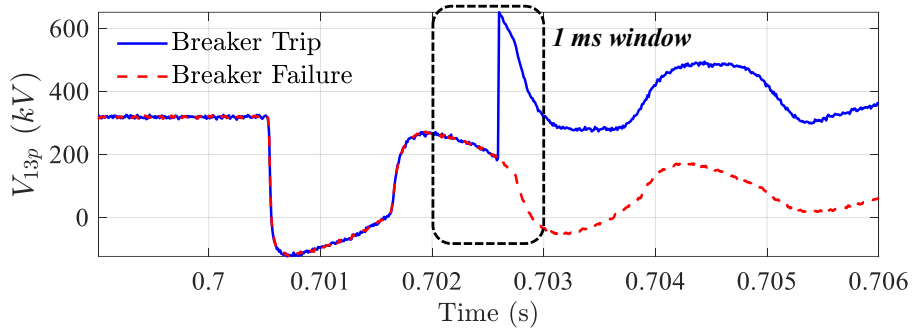


(b) A zoomed 1 ms window with the detected abrupt changes.

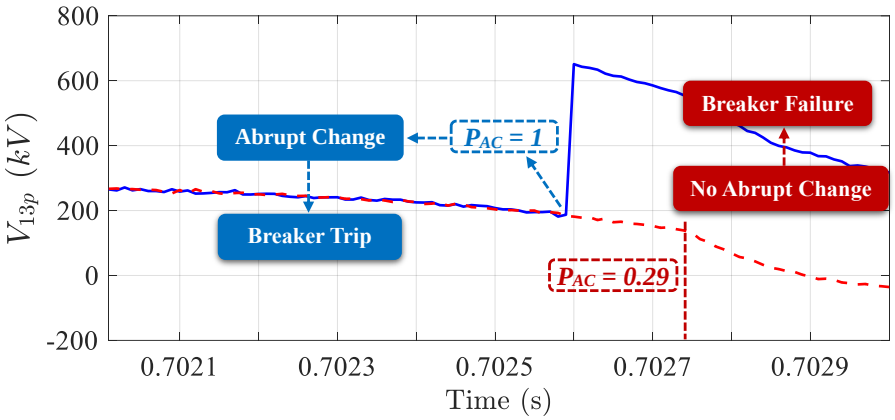
Figure 6.15: Performance of the proposed BMA-based breaker failure scheme during a solid PTP fault at the middle of cable 13 with $L_{dc} = 10\ mH$ with successful breaker trip and failure.

6.8 Conclusion

This chapter introduces a highly selective and sensitive single-ended relay failure backup protection scheme for multi-terminal HVDC grids based on BMA and the polarities of the faulted pole or zero-mode currents. The proposed scheme can reliably distinguish between internal, forward, and reverse external faults. Additionally, it can provide fast local backup protection in forward and reverse directions during internal and reverse external faults. The main features of the proposed relay failure scheme are:



(a) V_{13_p}.



(b) A zoomed 1 ms window with the detected abrupt changes.

Figure 6.16: Performance of the proposed BMA-based breaker failure scheme during a solid PTP fault at the middle of cable 13 with $SNR = 30$ db with successful breaker trip and failure.

- Reliable detection of critical internal faults, such as remote-end high-resistance faults, with a clear distinction from severe external faults, including solid bus faults.
- Rapid fault detection, enabling fast backup protection in case of primary protection failure.
- High sensitivity to internal faults with fault resistances as large as 1500 Ω.
- High robustness to measurement noise.
- Compatibility with HVDC grids with small boundary reactors (up to 10 mH).

The BMA algorithm is applied to local voltage measurements to provide breaker failure backup protection. If abrupt changes in local voltage measurements are detected by BMA following fault detection, successful breaker operation is inferred. Otherwise, breaker failure is identified. The reliable performance of the proposed BMA-based breaker failure backup protection scheme is demonstrated under various fault conditions, including different fault locations, high-resistance faults, small size of boundary reactors, and the presence of measurement noise.

Chapter 7

Real-Time Experimental Validation

7.1 Introduction

Real-time simulation is defined as a process in which a high-speed computer simulates a dynamic system (such as an electrical power grid) so that the progression of simulation time coincides with actual time [183]. This allows for the testing of hardware and software in a realistic and controlled environment. Within the context of power system protection, real-time simulation enables the testing of different protection schemes under various fault conditions without risking damage to the actual equipment. In addition, real-time simulation facilitates hardware-in-the-loop (HIL) tests, where real protection relays can interact with the power system model in real-time. This is a significant step to ensure that protection relays will operate correctly in real-world scenarios [184].

This chapter presents the experimental results of real-time validation of the HHT-based primary protection scheme proposed in Chapter 3, demonstrating its performance and effectiveness in a real-time HIL experimental setup. The remainder of this chapter is structured as follows: Section 7.2 details the experimental setup, including a description of the hardware components, their interconnections, and the software configuration. Section 7.3 presents the experimental results obtained from the executed fault scenarios, including internal and external faults, to validate the performance of the proposed scheme in real-time. Finally, Section 7.4 summarizes the key findings and conclusions drawn from the experimental validation.

7.2 Experimental Setup

Figure 7.1 outlines the experimental setup used for real-time validation, which features the interaction of two real-time platforms: the OPAL-RT OP5700 simulator and the dSPACE MicroLabBox controller. The OP5700 real-time simulator, developed by OPAL-RT Technologies, is a powerful tool to simulate complex systems in real-time, connect real-world hardware to those systems, and test the interactions in real-time [185]. In this experimental setup, the OP5700 real-time simulator is used to simulate the four-terminal HVDC grid (Figure 3.2) in real-time, as shown in Figure 7.1. The dSPACE MicroLabBox is a compact real-time system that provides a powerful and flexible platform to develop and test control systems and protection algorithms in real-time [186]. In this test setup, the primary protection scheme is implemented on the dSPACE MicroLabBox, which serves as the protection relay. Thus, the protection scheme can be comprehensively evaluated in a realistic environment.

Figure 7.2 shows the actual hardware test setup, where each platform is connected to one host PC, and the software required to program each platform is installed on the corresponding host PC. To simulate the four-terminal HVDC grid on the OP5700 real-time simulator, the HVDC grid is modeled using MATLAB/Simulink environment. Then, RT-Lab software, developed by OPAL-RT technologies, is employed to interact with the model in real-time, *e.g.*, initiate a fault event while running the model in real-time. On the dSPACE platform, the MATLAB/Simulink-based real-time interface (RTI) tool, developed by dSPACE, runs the HHT-based primary protection algorithm in real-time, allowing the dSPACE hardware to act as a real-world protection relay. The ControlDesk software, developed by dSPACE, is used to evaluate the performance of the implemented protection relay by visualizing the received voltage measurement and the issued trip signal during the fault [187].

In this experimental setup, cable 13 is selected as the protected cable, as shown in Figure 7.1. Figure 7.3 shows a simplified representation of the experimental setup. The local voltage measurement at bus 1 is continuously transmitted in real-time as an analog signal since the voltage waveform is inherently continuous. The analog ports of the OP5700 real-time simulator are DB37, while the analog ports of the dSPACE MicroLabBox are BNC. The connection between the two simulators, shown in Figure 7.2, is made using BNC lead connectors and BNC cables due to the unavailability of custom-made cables. The trip signal issued by the relay during the fault is fed back as a digital signal to terminal breakers on OPAL-RT to clear the fault in real-time. The value of the trip signal can be one (during internal faults) or zero (during normal operation or external faults). This high/low nature is perfectly suited for digital representation.

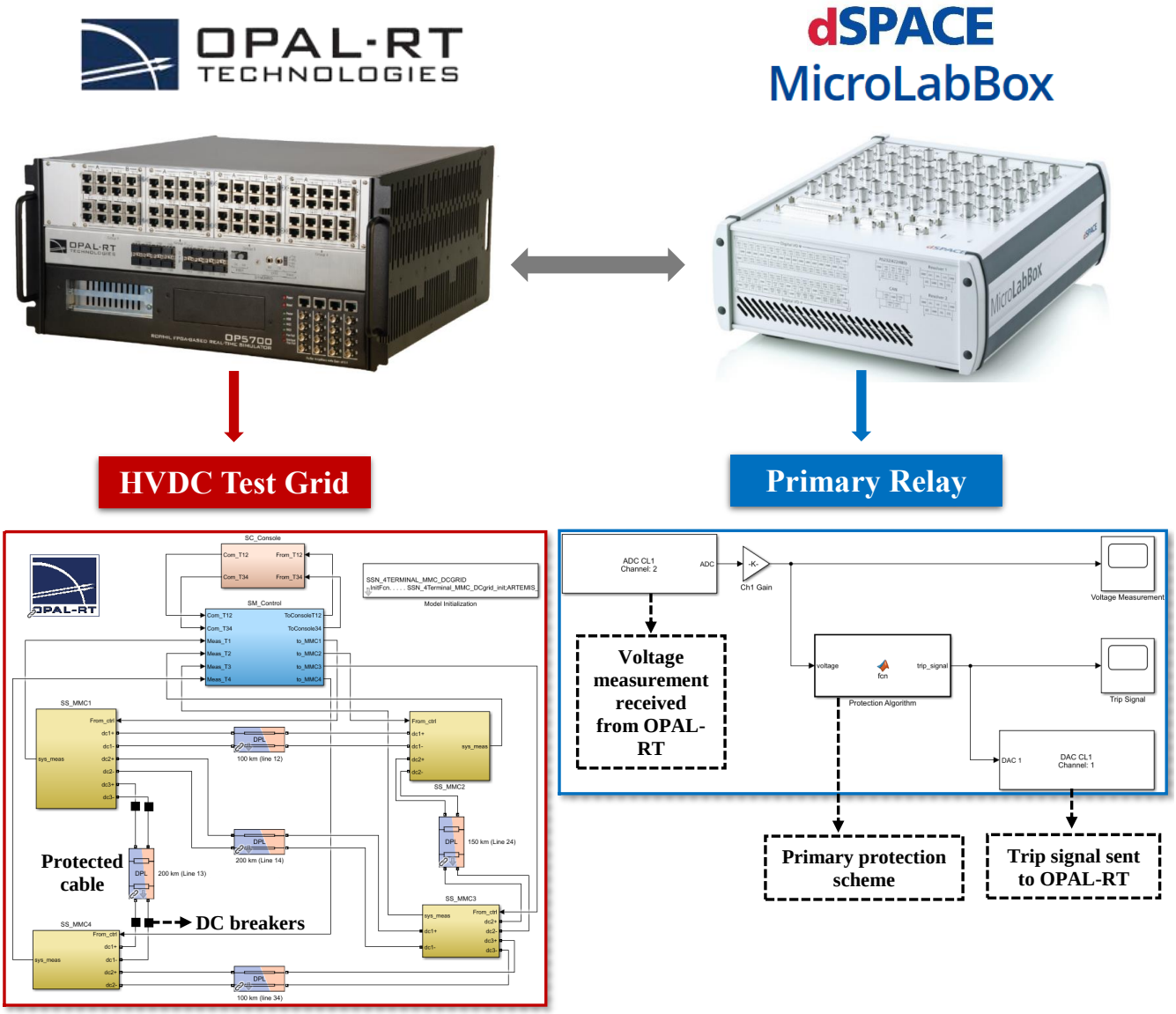


Figure 7.1: Experimental HIL test setup layout.



Figure 7.2: HIL test setup.

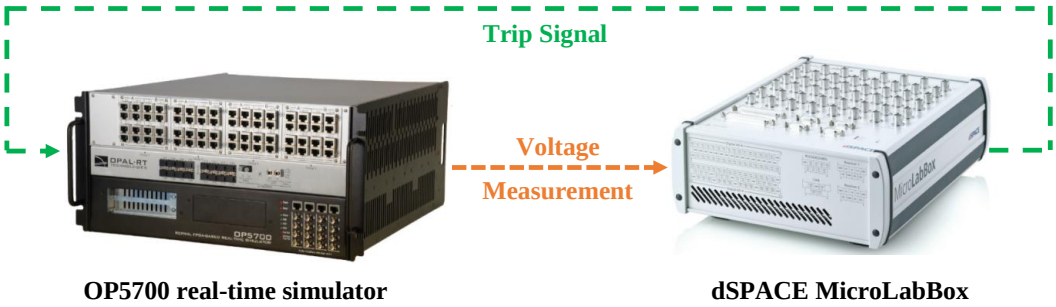


Figure 7.3: Simplified representation of the experimental setup.

7.3 Experimental Results

The experimental validation tests are performed in two stages. In the first stage, a preliminary open-loop test setup, where the trip signal on dSPACE is not fed back to OPAL-RT, is employed to evaluate the performance of the primary relay in distinguishing between internal and external faults in real-time. In the second stage, the trip signal is sent from dSPACE to OPAL-RT to form the closed HIL test setup, enabling real-time interaction between both platforms. According to the hardware specifications of dSPACE MicroLabBox, the sampling time cannot be less than 50 μs. Therefore, the sampling frequency used is 20 kHz. With a moving window of 100 samples required by the proposed primary protection scheme, the fault detection time is less than 5 ms.

Five fault scenarios are executed in real-time in the first stage. As mentioned in Section 7.2, the ControlDesk software is used to visualize the voltage signal received from OPAL-RT and the trip signal issued by the implemented relay on dSPACE. The first fault scenario involves a solid PTP fault at the beginning of cable 13. Figure 7.4 shows the positive-pole voltage waveform and the issued trip signal. As shown in Figure 7.4, the fault is initiated at 6.59 s, causing a sudden drop in the voltage waveform. The primary protection scheme, implemented on dSPACE, successfully detects the fault and immediately issues the corresponding trip signal at 6.592 s (within 2 ms). It is worth mentioning that the oscillations, noises, and irregularities in the voltage waveform in Figure 7.4 are mainly caused by inefficient cabling between OPAL-RT and dSPACE.

In the second and third scenarios, solid PTP faults occur at the middle and end of cable 13, initiated at 5.862 s and 4.656 s, respectively (Figures 7.5 and 7.6). In both cases, the protection scheme promptly detects the fault and issues the corresponding trip signals in real-time at 5.864 s (within 2 ms) and 4.659 s (within 3 ms), respectively. The fourth scenario considers a PTP fault at the middle of cable 13 with a fault resistance of 200 Ω, initiated at 5.853 s. As illustrated in Figure 7.7, the scheme reliably detects the fault and

issues the corresponding trip signal at 5.857 s (within 4 ms). In the fifth scenario, an external fault at the beginning of cable 34 is simulated. As shown in Figure 7.8, no trip signal is issued since there is no sudden drop in the voltage waveform compared to internal faults, as shown in Figure 7.9, where the sudden voltage dip during the first fault scenario is compared with the voltage drop during the external fault scenario.

In the second stage, the closed HIL test setup is employed. Two fault scenarios are re-simulated: the solid PTP middle-cable fault (Figure 7.10) and the solid PTP fault at the end of cable 13 (Figure 7.11). As shown in Figures 7.10 and 7.11, the trip signal is fed back to OPAL-RT to trip terminal breakers, which causes switching transients during the interruption process followed by the recovery voltage developing to the prefault voltage level. It is observed that following fault interruption, the recovery voltage exhibits a prolonged restoration period before reaching its pre-fault level, particularly in the last scenario (Figure 7.11), when compared to PSCAD offline simulations for the same fault case (Figure 7.12). This discrepancy between offline and real-time results primarily arises from the following factors:

- DC breaker modeling differences: In PSCAD, a detailed breaker model is used (as explained in Section 5.2.1), whereas in RT-Lab, due to software constraints and computational complexity, the breaker is represented by a simplified switch model in OPAL-RT. This approximation can significantly influence the transient response and recovery dynamics.
- Variations in model implementation: Some discrepancies exist in component modeling between the two environments, especially the MMC model and its associated control parameters, which can affect the system's dynamic behavior during post-fault recovery.

It should be noted that the communication delay between OPAL-RT and dSPACE is negligible, as it is significantly shorter than the used sampling time (50 μs). It was observed that when the trip signal is initiated on dSPACE at a given instant, breaker switching immediately begins in the next time step, as recorded from the dSPACE side. This indicates that the total communication time required to transmit the trip signal from dSPACE to OPAL-RT and to send the voltage signal from OPAL-RT to dSPACE is shorter than the simulation time step. Hence, it can be concluded that the communication delay has no impact on the obtained results. In summary, the presented results demonstrate the effectiveness of the proposed scheme in detecting various fault conditions and distinguishing between internal and external faults; thus, confirming its feasibility for practical implementation.

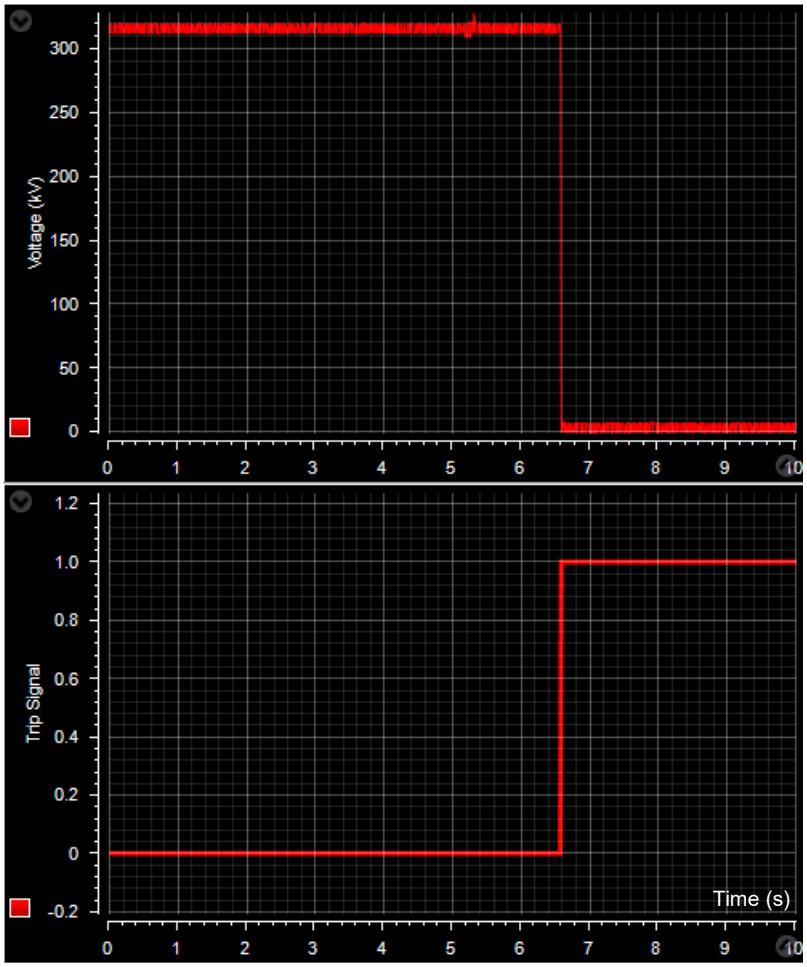


Figure 7.4: Real-time positive-pole voltage and corresponding trip signal during a solid PTP fault at the beginning of cable 13.

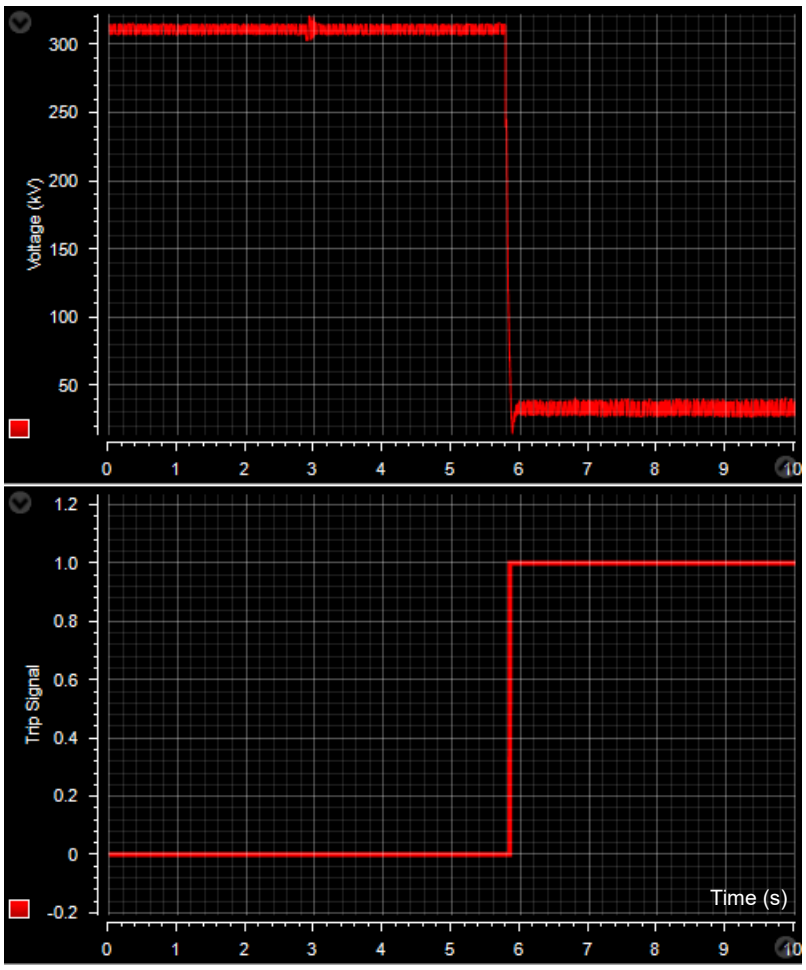


Figure 7.5: Real-time positive-pole voltage and corresponding trip signal during a solid PTP fault at the middle of cable 13.

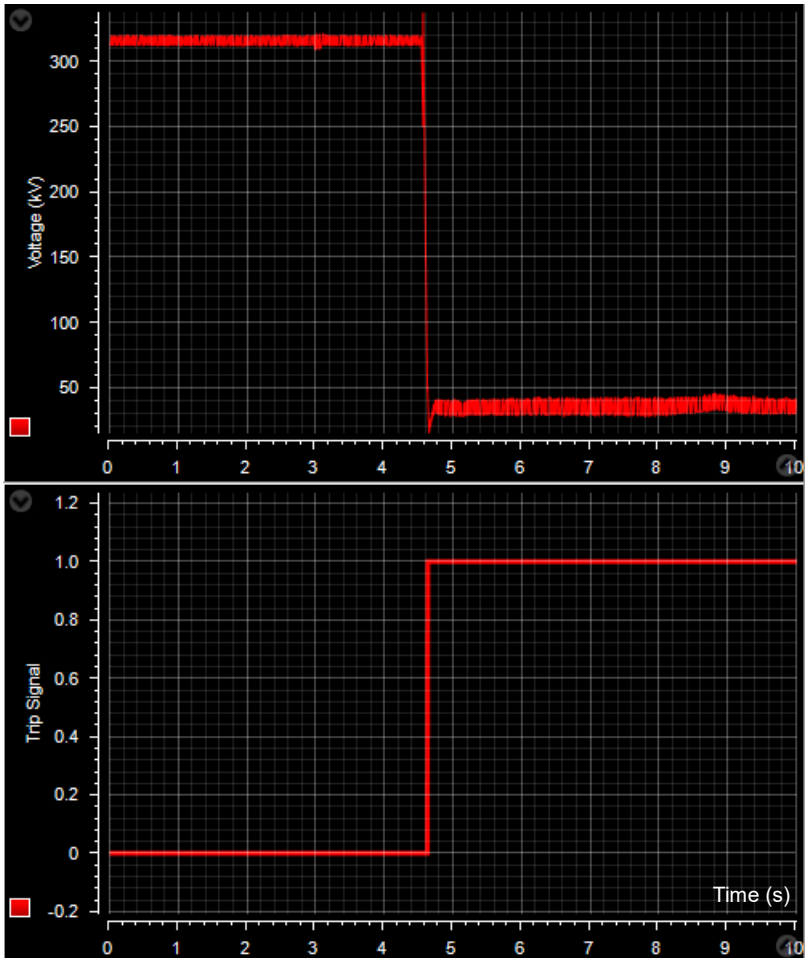


Figure 7.6: Real-time positive-pole voltage and corresponding trip signal during a solid PTP fault at the end of cable 13.

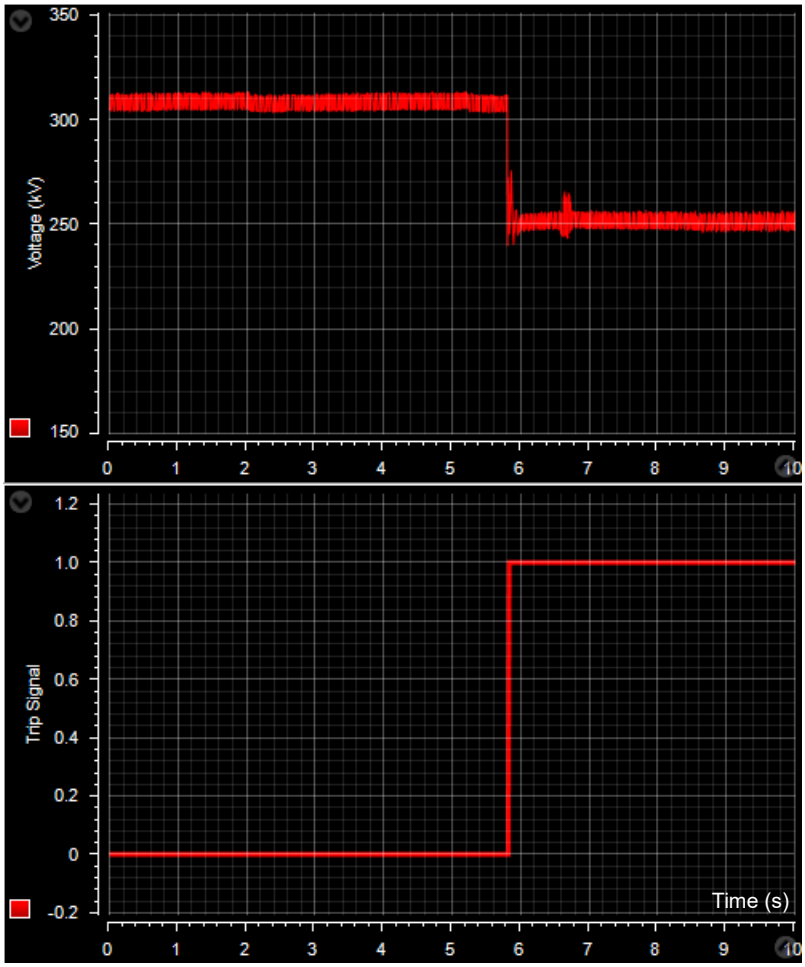


Figure 7.7: Real-time positive-pole voltage and corresponding trip signal during a PTP fault at the middle of cable 13 with $R_F = 200\ \Omega$.

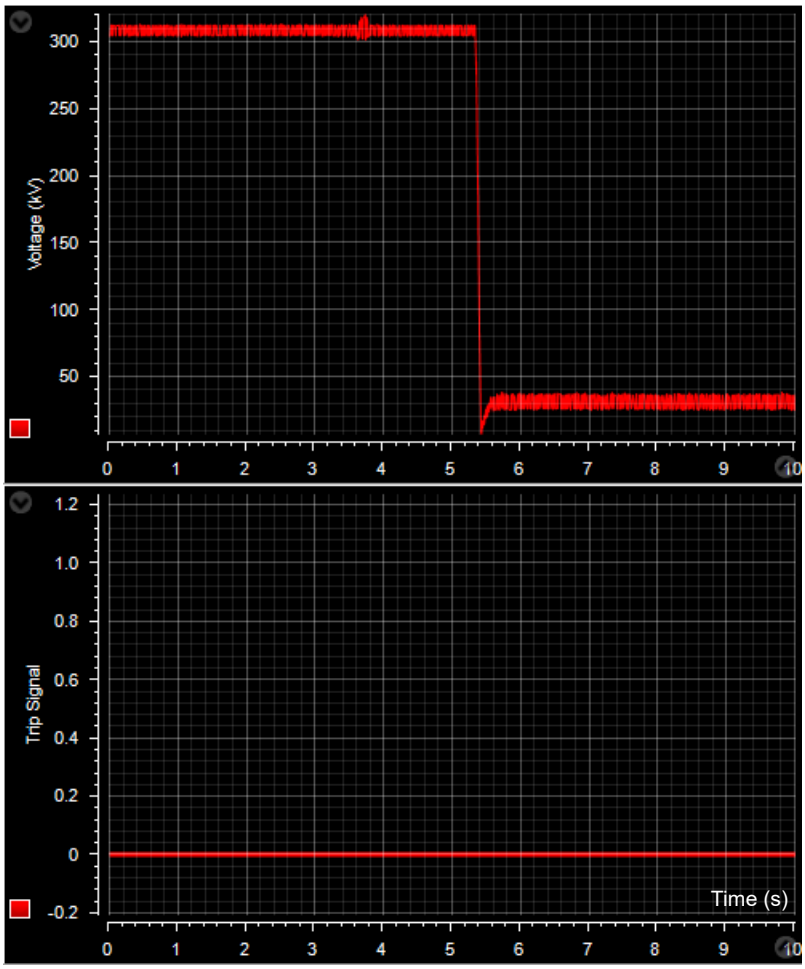


Figure 7.8: Real-time positive-pole voltage and corresponding trip signal during an external PTP fault at the beginning of cable 34.

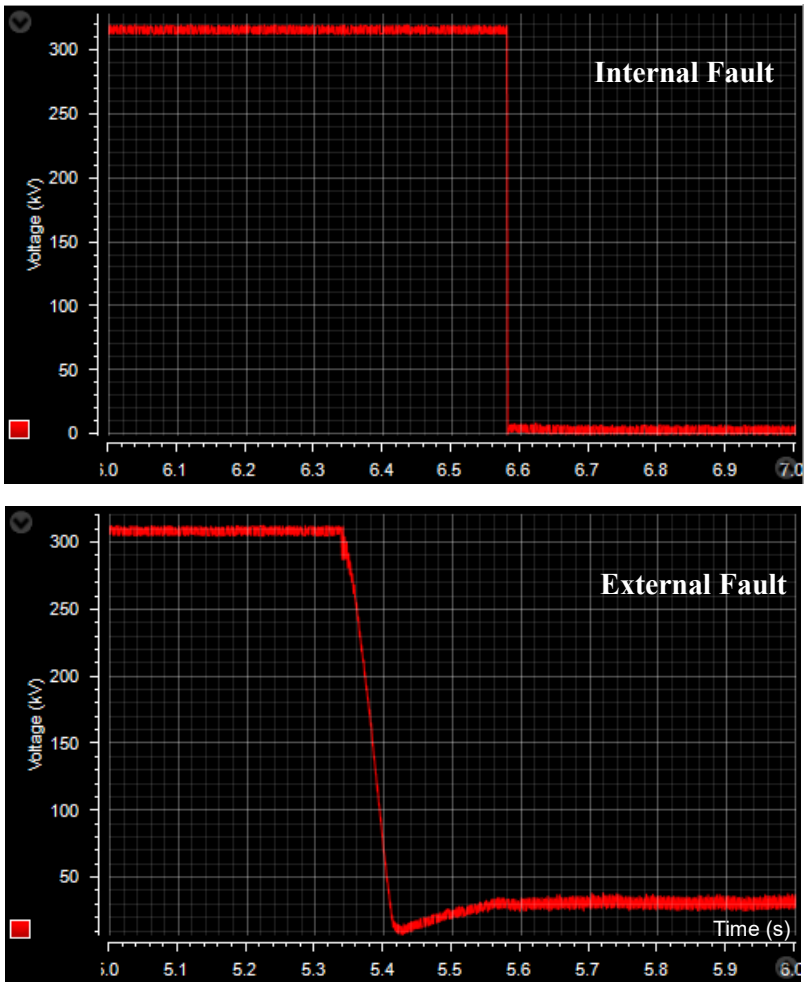


Figure 7.9: Positive-pole voltage drop during internal and external faults.

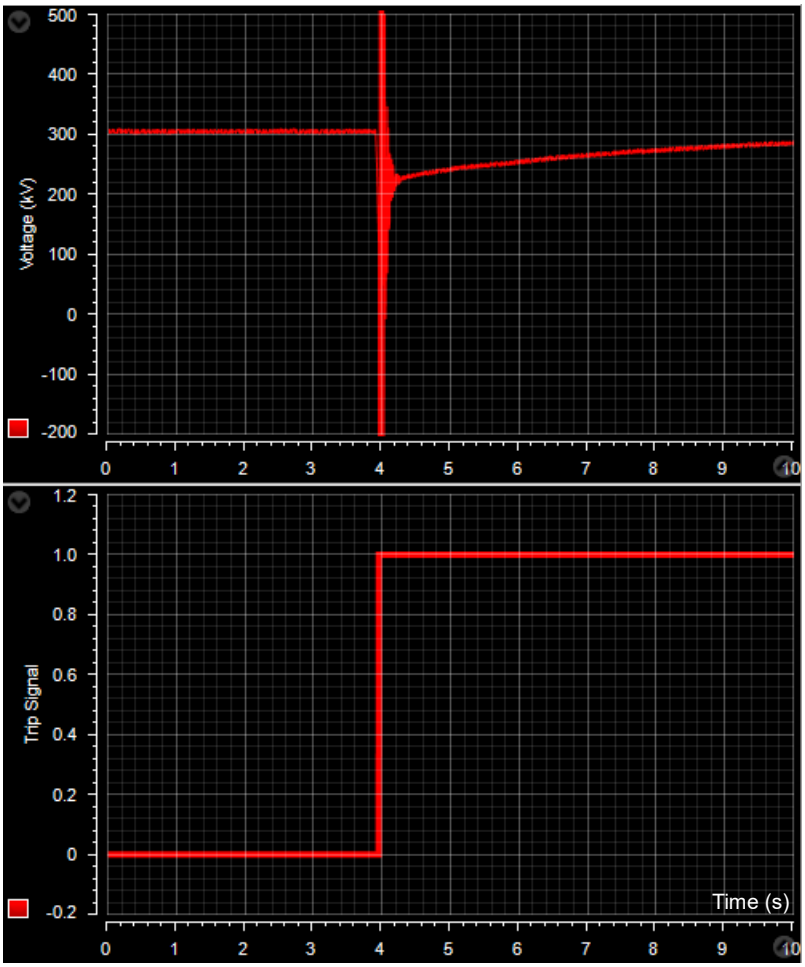


Figure 7.10: HIL real-time positive-pole voltage and corresponding trip signal during a solid PTP fault at the middle of cable 13.

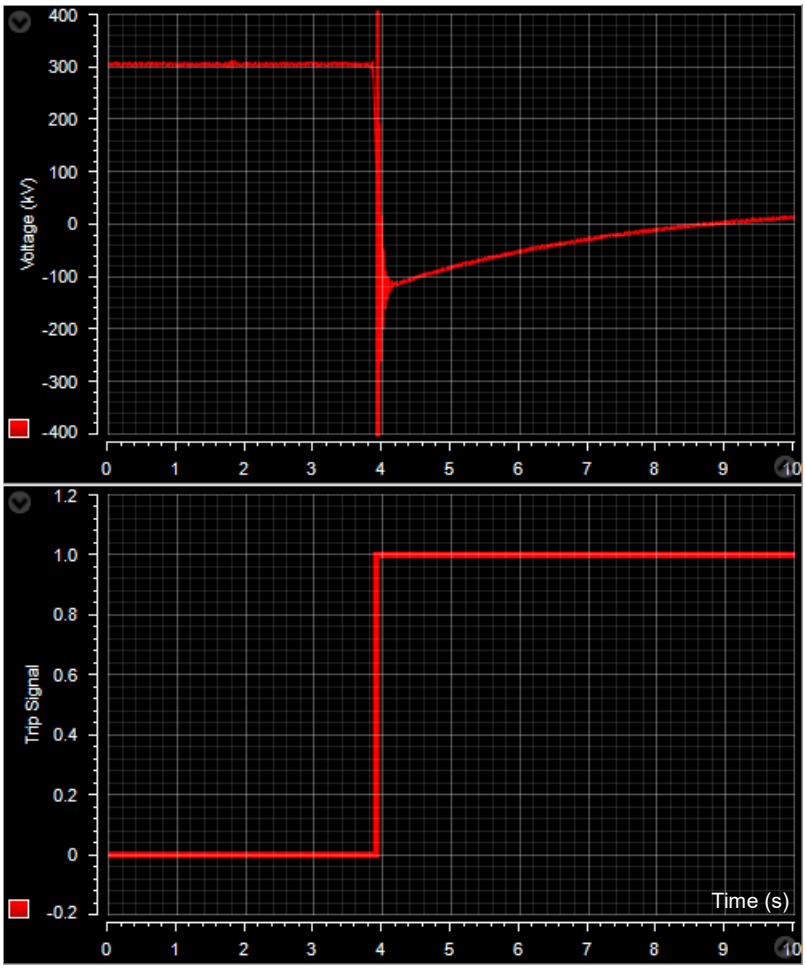


Figure 7.11: HIL real-time positive-pole voltage and corresponding trip signal during a solid PTP fault at the end of cable 13.

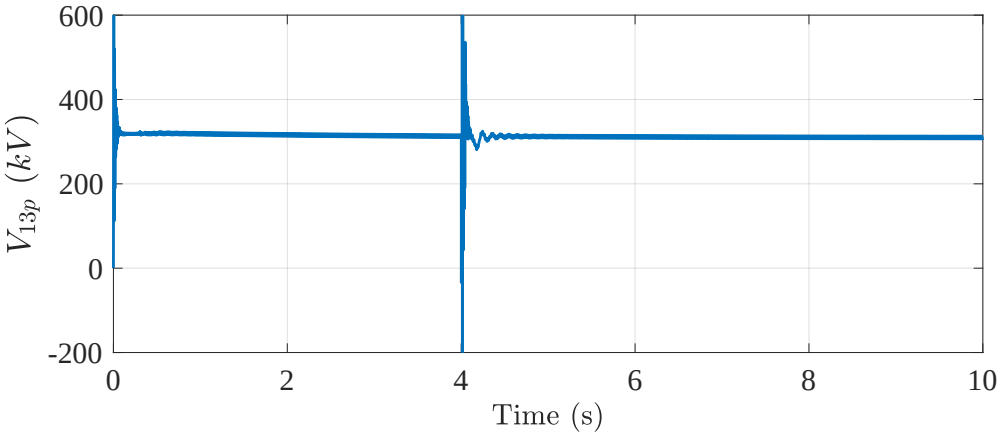


Figure 7.12: Offline positive-pole voltage during a solid PTP fault at the end of cable 13.

7.4 Conclusion

In this chapter, the proposed HHT-based primary protection scheme is tested in real-time via an experimental test setup. The HIL experimental setup consists of the OP5700 real-time simulator and the dSPACE MicroLabBox controller. Trip signals are successfully issued in real-time by the primary relay (implemented on the dSPACE controller) when internal faults are triggered within the HVDC grid (running in real-time on OPAL-RT). The real-time experimental results demonstrate the practical feasibility of the proposed scheme for physical relay implementation. While the HIL test setup based on OPAL-RT and dSPACE platforms provides a reliable and high-fidelity environment for real-time testing, it is important to acknowledge two main limitations. First, the sampling frequency is restricted to 20 kHz, which may limit the fault detection speed. Second, inefficient cabling between OPAL-RT and dSPACE can introduce signal oscillations and noise, potentially affecting relay performance under severe fault conditions.

Chapter 8

Conclusion and Future Work

8.1 Summary

This thesis focused on the protection of multi-terminal HVDC grids. To avoid the negative impacts of DC faults on the reliable operation of multi-terminal HVDC grids and to address the shortcomings of existing protection schemes, primary protection, backup protection, and fault location identification schemes are designed to reliably protect the HVDC grid. Numerous simulations in PSCAD/EMTDC software environment for a four-terminal HVDC grid are executed to demonstrate the rapid and reliable performance of the designed schemes under various fault conditions. The summary and main conclusions of each chapter are presented as follows:

- Chapter 1:

  This chapter introduces various HVDC grid configurations, protection challenges, and protection requirements of multi-terminal HVDC grids. In addition, the thesis's research objectives and the employed methodology are articulated.

- Chapter 2:

  In this chapter, a comprehensive review of existing HVDC grid protection schemes is presented, highlighting their features and shortcomings. Based on the presented comparative study, it is concluded that highly selective and sensitive single-ended protection schemes are required to provide primary protection, while double-ended protection schemes can be employed as backup protection. Furthermore, single-ended

schemes require a powerful signal processing tool capable of rapidly extracting the internal fault signature under severe fault conditions.

- Chapter 3:

  In this chapter, the designed primary protection scheme is introduced. Instantaneous frequency and energy are extracted by HHT applied to local voltage measurements, based on which the fault detection criterion is designed. A fault is detected if simultaneous outliers in the instantaneous frequency and energy are identified by the designed scheme. The effectiveness of the designed scheme is demonstrated by extensive simulations under various fault scenarios.

- Chapter 4:

  A double-ended fault location identification scheme for multi-terminal HVDC grids is designed in this chapter based on HHT. First, HHT is utilized to extract the instantaneous frequency and energy from voltage measurements at both line terminals. Then, a setting-less criterion based on outlier detection is employed to capture the arrival time of the initial fault-induced backward traveling waves. Based on the arrival instants at both line terminals, the fault location is identified with high precision. Various simulations are executed to demonstrate the accuracy and reliability of the designed scheme.

- Chapter 5:

  In this chapter, a setting-less breaker failure backup protection scheme for multi-terminal HVDC grids is designed. HHT is applied to local voltage measurements following the fault event. The instantaneous frequency and energy during successful breaker operation and breaker failure scenarios are investigated. Then, the outlier-based criterion is employed to detect breaker failure events. The rapid and reliable performance of the designed breaker failure scheme is evaluated under various fault conditions.

- Chapter 6:

  This chapter introduces a reliable single-ended relay failure backup protection scheme for multi-terminal HVDC grids. The designed scheme utilizes a statistical approach to detect various fault conditions and consists of fault detection and directional components. The designed statistically based fault detection component employs BMA to reliably and rapidly detect the fault event and classify its type. The directional component uses local current measurements to identify the fault direction and discriminate between internal and forward/reverse external faults. The designed scheme

provides fast local backup protection for internal and reverse external faults. The designed scheme has been extensively evaluated in PSCAD/EMTDC and its robustness to high-resistance faults, weak boundary conditions, and measurement noise has been demonstrated.

- Chapter 7:

  This chapter presents the experimental validation of the designed primary relay. The four-terminal HVDC grid is simulated in OPAL-RT in real-time. Local voltage measurements are exported to the dSPACE controller, where the designed primary protection scheme is built to process the received voltage signal in real-time. Trip signals are successfully issued in real-time by the primary relay corresponding to the triggered fault events in the HVDC grid.

8.2 Contributions

In this thesis, four protection schemes are designed for multi-terminal HVDC grids. The main contributions of this thesis are summarized as follows:

1. Primary Protection Scheme:

   - A fast, reliable, sensitive, and selective single-ended protection scheme is designed that detects high-resistance faults in less than 1 ms. Furthermore, bus and external faults are reliably discriminated from internal faults by the designed scheme, even when the size of the boundary reactors is as small as 10 mH.
   - Outlier detection is used, for the first time, in the design of HVDC grid protection schemes, to obtain a setting-less fault detection criterion; thus, enabling the designed protection scheme to be applicable to HVDC grids with various configurations and parameters.

2. Fault Location Identification Scheme:

   - A fast and accurate double-ended fault location identification scheme is designed. The arrival time of the initial fault-induced BTW is identified when simultaneous outliers in the instantaneous frequency and energy extracted by HHT are detected. The designed scheme identifies the location of the fault based on the two arrival instants estimated at both terminal relays.

3. Breaker Failure Backup Protection Scheme:

    - A robust single-ended breaker failure backup protection scheme is designed based on the instantaneous features extracted by HHT from local voltage measurements.
    - A setting-less criterion based on outlier detection is introduced, which is independent of grid configuration, parameters, and breaker technology.

4. Relay Failure Backup Protection Scheme:

    - A highly selective and sensitive single-ended relay failure backup protection scheme is designed based on BMA and the polarities of the faulted pole or zero-mode currents.
    - The BMA algorithm is applied to local voltage measurements to provide breaker failure backup protection.

8.3 Future Work

Future research can be carried out to address the following challenges related to the protection of multi-terminal HVDC grids:

- Design a reliable bus protection scheme capable of detecting bus faults and discriminating them from line faults.
- Design a reclosing scheme for multi-terminal HVDC grids to reliably discriminate between permanent and temporary faults. In addition, an adaptive reclosing scheme should be able to precisely detect the extinction (deionization) instant of transient fault arcs during temporary faults.
- The interoperability of the designed protection schemes with multi-vendor HVDC grids, where the protection relays within the grid are provided by different manufacturers, should be evaluated. This step is necessary to facilitate the expansion of existing small-scale HVDC grids to large-scale supergrids.

References

[1] J. Sahebkar Farkhani, Özgür Çelik, K. Ma, C. L. Bak, and Z. Chen, "A comprehensive review of potential protection methods for VSC multi-terminal HVDC systems," *Renewable and Sustainable Energy Reviews*, vol. 192, p. 114280, 2024.

[2] D. Van Hertem and M. Ghandhari, "Multi-terminal VSC HVDC for the European supergrid: Obstacles," *Renewable and Sustainable Energy Reviews*, vol. 14, no. 9, pp. 3156–3163, 2010.

[3] P. Rault, F. Colas, X. Guillaud, and S. Nguefeu, "Method for small signal stability analysis of VSC-MTDC grids," in *2012 IEEE Power and Energy Society General Meeting*, 2012, pp. 1–7.

[4] J. P. Daniel, S. Liu, E. Ibanez, K. Pennock, G. Reed, and S. Hanes, "National Offshore Wind Energy Grid Interconnection Study," 2014. [Online]. Available: https://www.osti.gov/biblio/1148347

[5] Tractebel Energy, "World's first energy island takes shape in Belgium's North Sea," Available online: https://tractebel-engie.com/en/news/2024/world-s-first-energy-island-takes-shape-in-belgium-s-north-sea#:~:text=Princess%20Elisabeth%20Island%20(PEI)%2C,expected%20to%20run%20through%202028.

[6] D. Jovcic, *High voltage direct current transmission: converters, systems and DC grids*. John Wiley & Sons, 2019.

[7] D. Van Hertem, O. Gomis-Bellmunt, and J. Liang, *HVDC grids: for offshore and supergrid of the future*. John Wiley & Sons, 2016.

[8] M. Han and A. Gole, *Modeling and Simulation of HVDC Transmission*. Institution of Engineering and Technology (IET), 2020.

[9] Hitachi Energy, "SunZia HVDC Project," Available online: https://www.hitachienergy.com/news-and-events/customer-success-stories/sunzia.

[10] Greenlink, "Greenlink Interconnector," Available online: https://www.greenlink.ie/.

[11] H. Pang and X. Wei, "Research on Key Technology and Equipment for Zhangbei 500kV DC Grid," in *2018 International Power Electronics Conference (IPEC-Niigata 2018 ECCE Asia)*, 2018, pp. 2343–2351.

[12] TenneT, "NordLink," Available online: https://netztransparenz.tennet.eu/our-grid/international-connections/nordlink/.

[13] "North Sea Link," Available online: https://northsealink.com/.

[14] X. Chen, H. Li, Y. Liang, and G. Wang, "A protection scheme for hybrid multi-terminal HVDC networks utilizing a time-domain transient voltage based on fault-blocking converters," *International Journal of Electrical Power & Energy Systems*, vol. 118, p. 105825, 2020.

[15] Hitachi Energy, "Changji-Guquan UHVDC Link," Available online: https://www.hitachienergy.com/case-studies/changji-guquan-uhvdc-link.

[16] "ABB commissions historical power interconnector in Canada," Available online: https://new.abb.com/news/detail/5053/abb-commissions-historical-power-interconnector-in-canada.

[17] G. Tang, Z. He, H. Pang, X. Huang, and X.-p. Zhang, "Basic topology and key devices of the five-terminal DC grid," *CSEE Journal of Power and Energy Systems*, vol. 1, no. 2, pp. 22–35, 2015.

[18] H. Rao, "Architecture of Nan'ao multi-terminal VSC-HVDC system and its multi-functional control," *CSEE Journal of Power and Energy Systems*, vol. 1, no. 1, pp. 9–18, 2015.

[19] A. Yazdani and R. Iravani, *Voltage-sourced converters in power systems: modeling, control, and applications*. John Wiley & Sons, 2010.

[20] M. P. Bahrman and B. K. Johnson, "The ABCs of HVDC transmission technologies," *IEEE Power and Energy Magazine*, vol. 5, no. 2, pp. 32–44, 2007.

[21] S. Du, A. Dekka, B. Wu, and N. Zargari, *Modular multilevel converters: analysis, control, and applications*. John Wiley & Sons, 2018.

[22] K. Sharifabadi, L. Harnefors, H.-P. Nee, S. Norrga, and R. Teodorescu, *Design, control, and application of modular multilevel converters for HVDC transmission systems*. John Wiley & Sons, 2016.

[23] A. Nami, J. Liang, F. Dijkhuizen, and G. D. Demetriades, "Modular Multilevel Converters for HVDC Applications: Review on Converter Cells and Functionalities," *IEEE Transactions on Power Electronics*, vol. 30, no. 1, pp. 18–36, 2015.

[24] M. N. Sakib, S. P. Azad, and M. Kazerani, "A Critical Review of Modular Multilevel Converter Configurations and Submodule Topologies from DC Fault Blocking and Ride-Through Capabilities Viewpoints for HVDC Applications," *Energies*, vol. 15, no. 11, 2022.

[25] M. Kong, X. Pei, H. Pang, J. Yang, X. Dong, Y. Wu, and X. Zhou, "A lifting wavelet-based protection strategy against DC line faults for Zhangbei HVDC Grid in China," in *2017 19th European Conference on Power Electronics and Applications (EPE'17 ECCE Europe)*, 2017, pp. 1–11.

[26] M. Zain Yousaf, H. Liu, A. Raza, and M. Baber Baig, "Primary and backup fault detection techniques for multi-terminal HVdc systems: a review," *IET Generation, Transmission & Distribution*, vol. 14, no. 22, pp. 5261–5276, 2020.

[27] I. Jahn, N. Johannesson, and S. Norrga, "Survey of Methods for Selective DC Fault Detection in MTDC Grids," *IET Conference Proceedings*, 2017.

[28] W. Leterme, I. Jahn, P. Ruffing, K. Sharifabadi, and D. Van Hertem, "Designing for High-Voltage dc Grid Protection: Fault Clearing Strategies and Protection Algorithms," *IEEE Power and Energy Magazine*, vol. 17, no. 3, pp. 73–81, 2019.

[29] I. Jahn, M. Nahalparvari, C. Hirsching, M. Hoffmann, P. Düllmann, F. Loku, A. Agbemuko, G. Chaffey, E. Prieto-Araujo, and S. Norrga, "An Architecture for a Multi-Vendor VSC-HVDC Station With Partially Open Control and Protection," *IEEE Access*, vol. 10, pp. 13 555–13 569, 2022.

[30] "Recommendations to improve HVDC cable systems reliability - A joint ENTSO-E and Europacable paper," Available online: https://www.entsoe.eu/2019/06/20/recommendations-to-improve-hvdc-cable-systems-reliability/.

[31] W. Leterme, "Communication-Less Protection Algorithms for Meshed VSC HVDC Cable Grids," Ph.D. dissertation, KU Leuven, Leuven, Belgium, 2016.

[32] N. A. Belda, C. A. Plet, and R. P. P. Smeets, "Analysis of Faults in Multiterminal HVDC Grid for Definition of Test Requirements of HVDC Circuit Breakers," *IEEE Transactions on Power Delivery*, vol. 33, no. 1, pp. 403–411, 2018.

[33] J. Yang, J. E. Fletcher, and J. O'Reilly, "Multiterminal DC Wind Farm Collection Grid Internal Fault Analysis and Protection Design," *IEEE Transactions on Power Delivery*, vol. 25, no. 4, pp. 2308–2318, 2010.

[34] M. Perez-Molina, D. Larruskain, P. Eguia Lopez, G. Buigues, and V. Valverde, "Review of protection systems for multi-terminal high voltage direct current grids," *Renewable and Sustainable Energy Reviews*, vol. 144, p. 111037, 2021.

[35] W. Leterme, N. Ahmed, J. Beerten, L. Ängquist, D. V. Hertem, and S. Norrga, "A new HVDC grid test system for HVDC grid dynamics and protection studies in EMT-type software," in *11th IET International Conference on AC and DC Power Transmission*, 2015.

[36] W. Leterme and D. Van Hertem, "Reduced Modular Multilevel Converter Model to Evaluate Fault Transients in DC Grids," *IET Conference Proceedings*, 2014.

[37] Y. Li, J. Li, G. Wu, L. Xiong, K. Jia, and Z. Xu, "DC Fault Analysis Models of Three Converter Topologies Considering Control Effects," *IEEE Transactions on Industrial Electronics*, vol. 67, no. 11, pp. 9480–9491, 2020.

[38] M. Langwasser, G. De Carne, M. Liserre, and M. Biskoping, "Fault Current Estimation in Multi-Terminal HVdc Grids Considering MMC Control," *IEEE Transactions on Power Systems*, vol. 34, no. 3, pp. 2179–2189, 2019.

[39] Y. Zhang, W. Cong, G. Li, K. Sun, and Y. Zhang, "Single-ended MMC-MTDC line protection based on dual-frequency amplitude ratio of traveling wave," *Electric Power Systems Research*, vol. 189, p. 106808, 2020.

[40] D. Döring, K. Würflinger, V. Staudt, M. Zeller, and G. Ebner, "Interactions between a half-bridge MMC and a hybrid DC breaker during fault current interruption compared to a full-bridge MMC," *IET Power Electronics*, vol. 13, no. 18, pp. 4168–4175, 2020.

[41] Y. Wang, Z. Yuan, J. Fu, Y. Li, and Y. Zhao, "A feasible coordination protection strategy for MMC-MTDC systems under DC faults," *International Journal of Electrical Power & Energy Systems*, vol. 90, pp. 103–111, 2017.

[42] CIGRE Joint Working Group B4/B5.59, "TB 739: Protection and local control of HVDC-grids," 2018, available online: https://e-cigre.org/publication/739-protection-and-local-control-of-hvdc-grids.

[43] P. Ruffing, N. Collath, C. Brantl, and A. Schnettler, "DC Fault Control and High-Speed Switch Design for an HVDC Network Protection Based on Fault-Blocking Converters," *IEEE Transactions on Power Delivery*, vol. 34, no. 1, pp. 397–406, 2019.

[44] F. Mohammadi, K. Rouzbehi, M. Hajian, K. Niayesh, G. B. Gharehpetian, H. Saad, M. Hasan Ali, and V. K. Sood, "HVDC Circuit Breakers: A Comprehensive Review," *IEEE Transactions on Power Electronics*, vol. 36, no. 12, pp. 13 726–13 739, 2021.

[45] R. P. P. Smeets and N. A. Belda, "High-voltage direct current fault current interruption: A technology review," *High Voltage*, vol. 6, no. 2, pp. 171–192, 2021.

[46] K. Tahata, S. E. Oukaili, K. Kamei, D. Yoshida, Y. Kono, R. Yamamoto, and H. Ito, "HVDC circuit breakers for HVDC grid applications," in *11th IET International Conference on AC and DC Power Transmission*, 2015.

[47] W. Lin, D. Jovcic, S. Nguefeu, and H. Saad, "Modelling of high-power hybrid DC circuit breaker for grid-level studies," *IET Power Electronics*, vol. 9, no. 2, pp. 237–246, 2016.

[48] T. An, D. Liu, F. Li, and L. Zhu, *Experience from the World's First HVDC Grid*. Cham: Springer International Publishing, 2023, pp. 1–42.

[49] Z. Li, Y. Ye, N. Tong, X. Lin, C. Li, N. Jin, and L. Chen, "High error-tolerable unit protection for VSC-MTDC independent of data synchronization," *International Journal of Electrical Power & Energy Systems*, vol. 124, p. 106393, 2021.

[50] J. Ma, Z. Xiao, Y. Li, J. Zhang, B. Wu, Z. Li, R. Ma, W. Huang, and P. Cheng, "A new pilot protection scheme for modular multi-level converter-based HVDC system based on voltage matching factor," *IET Generation, Transmission & Distribution*, vol. 16, no. 13, pp. 2573–2586, 2022.

[51] M. H. Nadeem, X. Zheng, N. Tai, M. Gul, M. Yu, and Y. He, "Non-communication based protection scheme using transient harmonics for multi-terminal HVDC networks," *International Journal of Electrical Power & Energy Systems*, vol. 127, p. 106636, 2021.

[52] N. Tong, X. Lin, Y. Li, Z. Hu, N. Jin, F. Wei, and Z. Li, "Local Measurement-Based Ultra-High-Speed Main Protection for Long Distance VSC-MTDC," *IEEE Transactions on Power Delivery*, vol. 34, no. 1, pp. 353–364, 2019.

[53] S. Yu, X. Wang, and C. Pang, "A Pilot Protection Scheme of DC Lines for MMC-HVDC Grid using Random Matrix," *Journal of Modern Power Systems and Clean Energy*, pp. 1–17, 2022.

[54] A. E. Abu-Elanien, A. A. Elserougi, A. S. Abdel-Khalik, A. M. Massoud, and S. Ahmed, "A differential protection technique for multi-terminal HVDC," *Electric Power Systems Research*, vol. 130, pp. 78–88, 2016.

[55] M. Hajian, L. Zhang, and D. Jovcic, "DC Transmission Grid With Low-Speed Protection Using Mechanical DC Circuit Breakers," *IEEE Transactions on Power Delivery*, vol. 30, no. 3, pp. 1383–1391, 2015.

[56] D. Jovcic, W. Lin, S. Nguefeu, and H. Saad, "Low-Energy Protection System for DC Grids Based on Full-Bridge MMC Converters," *IEEE Transactions on Power Delivery*, vol. 33, no. 4, pp. 1934–1943, 2018.

[57] H. Liu, B. Li, W. Wen, T. C. Green, J. Zhang, N. Zhang, and L. Chen, "Ultra-fast current differential protection with high-sensitivity for HVDC transmission lines," *International Journal of Electrical Power & Energy Systems*, vol. 126, p. 106580, 2021.

[58] M. Wang, W. Leterme, G. Chaffey, J. Beerten, and D. Van Hertem, "Multi-vendor interoperability in HVDC grid protection: State-of-the-art and challenges ahead," *IET Generation, Transmission & Distribution*, vol. 15, no. 15, pp. 2153–2175, 2021.

[59] G. Song, X. Chu, X. Cai, and S. Gao, "A novel pilot protection principle for VSC-HVDC cable lines based on fault component current," *International Journal of Electrical Power & Energy Systems*, vol. 53, pp. 426–433, 2013.

[60] G. Zou, Q. Feng, Q. Huang, C. Sun, and H. Gao, "A fast protection scheme for VSC based multi-terminal DC grid," *International Journal of Electrical Power & Energy Systems*, vol. 98, pp. 307–314, 2018.

[61] X. Zheng, M. H. Nadeem, N. Tai, S. Habib, B. Wang, M. Yu, and Y. He, "A transient current protection and fault location scheme for MMC-HVDC transmission network," *International Journal of Electrical Power & Energy Systems*, vol. 124, p. 106348, 2021.

[62] Q. Huang, G. Zou, S. Zhang, and H. Gao, "A Pilot Protection Scheme of DC Lines for Multi-Terminal HVDC Grid," *IEEE Transactions on Power Delivery*, vol. 34, no. 5, pp. 1957–1966, 2019.

[63] J. He, B. Li, Y. Li, H. Qiu, C. Wang, and D. Dai, "A Fast Directional Pilot Protection Scheme for the MMC-based MTDC Grid," *Proceedings of the Chinese Society of Electrical Engineering*, vol. 37, no. 23, pp. 6878–6887, 2017.

[64] W. Xiang, S. Yang, G. P. Adam, H. Zhang, W. Zuo, and J. Wen, "DC Fault Protection Algorithms of MMC-HVDC Grids: Fault Analysis, Methodologies, Experimental Validations, and Future Trends," *IEEE Transactions on Power Electronics*, vol. 36, no. 10, pp. 11 245–11 264, 2021.

[65] N. Tong, X. Lin, C. Li, Q. Sui, L. Chen, Z. Wang, N. Jin, and Z. Li, "Permissive pilot protection adaptive to DC fault interruption for VSC-MTDC," *International Journal of Electrical Power & Energy Systems*, vol. 123, p. 106234, 2020.

[66] W. Leterme and D. Van Hertem, "Cable Protection in HVDC Grids Employing Distributed Sensors and Proactive HVDC Breakers," *IEEE Transactions on Power Delivery*, vol. 33, no. 4, pp. 1981–1990, 2018.

[67] Y. Li, Y. Gong, and B. Jiang, "A novel traveling-wave-based directional protection scheme for MTDC grid with inductive DC terminal," *Electric Power Systems Research*, vol. 157, pp. 83–92, 2018.

[68] X. Zheng, N. Tai, Z. Wu, and J. Thorp, "Harmonic current protection scheme for voltage source converter-based high-voltage direct current transmission system," *IET Generation, Transmission & Distribution*, vol. 8, no. 9, pp. 1509–1515, 2014.

[69] M. Ashouri, F. Faria da Silva, and C. Leth Bak, "A Harmonic Based Pilot Protection Scheme for VSC-MTDC Grids with PWM Converters," *Energies*, vol. 12, no. 6, 2019.

[70] W. Xiang, H. Zhang, S. Yang, M. Zhou, W. Lin, and J. Wen, "A Differential Pilot Protection Scheme for MMC-Based DC Grid Resilient to Communication Failure," *IEEE Journal of Emerging and Selected Topics in Power Electronics*, vol. 9, no. 5, pp. 5631–5645, 2021.

[71] M. Farshad, "A Pilot Protection Scheme for Transmission Lines of Half-Bridge MMC-HVDC Grids Using Cosine Distance Criterion," *IEEE Transactions on Power Delivery*, vol. 36, no. 2, pp. 1089–1096, 2021.

[72] Q. Huai, L. Qin, K. Liu, A. Hooshyar, H. Ding, C. Gong, and Y. Xu, "A pilot line protection for MT-HVDC grids using similarity of traveling waveforms," *International Journal of Electrical Power & Energy Systems*, vol. 131, p. 107162, 2021.

[73] J. He, B. Li, Y. Li, W. Wang, H. Lyu, and B. Li, "Simplified calculation method of threshold value for the non-unit transient-voltage based protection in multi-terminal VSC-HVDC grid," *International Journal of Electrical Power & Energy Systems*, vol. 134, p. 107435, 2022.

[74] J. Sneath and A. D. Rajapakse, "Fault Detection and Interruption in an Earthed HVDC Grid Using ROCOV and Hybrid DC Breakers," *IEEE Transactions on Power Delivery*, vol. 31, no. 3, pp. 973–981, 2016.

[75] N. M. Haleem and A. D. Rajapakse, "Application of new directional logic to improve DC side fault discrimination for high resistance faults in HVDC grids," *Journal of Modern Power Systems and Clean Energy*, vol. 5, no. 4, pp. 560–573, 2017.

[76] N. Haleem and A. Rajapakse, "Local measurement based ultra-fast directional ROCOV scheme for protecting Bi-pole HVDC grids with a metallic return conductor," *International Journal of Electrical Power & Energy Systems*, vol. 98, pp. 323–330, 2018.

[77] W. Leterme, J. Beerten, and D. Van Hertem, "Nonunit Protection of HVDC Grids With Inductive DC Cable Termination," *IEEE Transactions on Power Delivery*, vol. 31, no. 2, pp. 820–828, 2016.

[78] N. M. Haleem and A. D. Rajapakse, "Fault-Type Discrimination in HVDC Transmission Lines Using Rate of Change of Local Currents," *IEEE Transactions on Power Delivery*, vol. 35, no. 1, pp. 117–129, 2020.

[79] A. Raza, A. Akhtar, M. Jamil, G. Abbas, S. O. Gilani, L. Yuchao, M. N. Khan, T. Izhar, X. Dianguo, and B. W. Williams, "A Protection Scheme for Multi-Terminal VSC-HVDC Transmission Systems," *IEEE Access*, vol. 6, pp. 3159–3166, 2018.

[80] J. Yang, J. Fletcher, J. O'Reilly, G. Adam, and S. Fan, "Protection scheme design for meshed VSC-HVDC transmission systems of large-scale wind farms," in *9th IET International Conference on AC and DC Power Transmission (ACDC 2010)*, 2010.

[81] J. Liu, N. Tai, and C. Fan, "Transient-Voltage-Based Protection Scheme for DC Line Faults in the Multiterminal VSC-HVDC System," *IEEE Transactions on Power Delivery*, vol. 32, no. 3, pp. 1483–1494, 2017.

[82] S. Pirooz Azad and D. Van Hertem, "A Fast Local Bus Current-Based Primary Relaying Algorithm for HVDC Grids," *IEEE Transactions on Power Delivery*, vol. 32, no. 1, pp. 193–202, 2017.

[83] S. H. Ashrafi Niaki, S. M. Hosseini, and A. A. Abdoos, "Fault detection of HVDC cable in multi-terminal offshore wind farms using transient sheath voltage," *IET Renewable Power Generation*, vol. 11, no. 13, pp. 1707–1713, 2017.

[84] Q. Huang, G. Zou, X. Wei, C. Sun, and H. Gao, "A non-unit line protection scheme for MMC-based multi-terminal HVDC grid," *International Journal of Electrical Power & Energy Systems*, vol. 107, pp. 1–9, 2019.

[85] M. Mehrabi-Kooshki, S. S. Mirhosseini, and S. Jamali, "Non-unit protection scheme for HVDC transmission lines based on energy of voltage difference," *IET Generation, Transmission & Distribution*, vol. 16, no. 11, pp. 2166–2187, 2022.

[86] J. Liao, N. Zhou, and Q. Wang, "DC Grid Protection Method Based on Phase Planes of Single-End Common-and Differential-Mode Components," *IEEE Transactions on Power Delivery*, vol. 36, no. 1, pp. 299–310, 2021.

[87] C. Troitzsch, A.-K. Marten, and D. Westermann, "Non-telecommunication based DC line fault detection methodology for meshed HVDC grids," *IET Generation, Transmission & Distribution*, vol. 10, no. 16, pp. 4231–4239, 2016.

[88] Y. Li, L. Wu, J. Li, L. Xiong, X. Zhang, G. Song, and Z. Xu, "DC Fault Detection in MTDC Systems Based on Transient High Frequency of Current," *IEEE Transactions on Power Delivery*, vol. 34, no. 3, pp. 950–962, 2019.

[89] Y. Li, J. Li, L. Xiong, X. Zhang, and Z. Xu, "DC Fault Detection in Meshed MTdc Systems Based on Transient Average Value of Current," *IEEE Transactions on Industrial Electronics*, vol. 67, no. 3, pp. 1932–1943, 2020.

[90] S. Li, W. Chen, X. Yin, D. Chen, and Y. Teng, "A Novel Integrated Protection for VSC-HVDC Transmission Line Based on Current Limiting Reactor Power," *IEEE Transactions on Power Delivery*, vol. 35, no. 1, pp. 226–233, 2020.

[91] C. Li, A. M. Gole, and C. Zhao, "A Fast DC Fault Detection Method Using DC Reactor Voltages in HVdc Grids," *IEEE Transactions on Power Delivery*, vol. 33, no. 5, pp. 2254–2264, 2018.

[92] R. Li, L. Xu, and L. Yao, "DC Fault Detection and Location in Meshed Multiterminal HVDC Systems Based on DC Reactor Voltage Change Rate," *IEEE Transactions on Power Delivery*, vol. 32, no. 3, pp. 1516–1526, 2017.

[93] Y. He, X. Zheng, N. Tai, J. Wang, M. H. Nadeem, and J. Liu, "A DC Line Protection Scheme for MMC-Based DC Grids Based on AC/DC Transient Information," *IEEE Transactions on Power Delivery*, vol. 35, no. 6, pp. 2800–2811, 2020.

[94] H. Dadgostar, M. Hajian, and K. Ahmed, "DC grids DC fault detection using asymmetric pole inductors," *Electric Power Systems Research*, vol. 193, p. 107016, 2021.

[95] D. Tzelepis, A. Dyśko, S. M. Blair, A. O. Rousis, S. Mirsaeidi, C. Booth, and X. Dong, "Centralised busbar differential and wavelet-based line protection system for multi-terminal direct current grids, with practical IEC-61869-compliant measurements," *IET Generation, Transmission & Distribution*, vol. 12, no. 14, pp. 3578–3586, 2018.

[96] A. E. Abu-Elanien, A. S. Abdel-Khalik, A. M. Massoud, and S. Ahmed, "A non-communication based protection algorithm for multi-terminal HVDC grids," *Electric Power Systems Research*, vol. 144, pp. 41–51, 2017.

[97] B. Mitra, B. Chowdhury, and A. Willis, "Protection Coordination for Assembly HVDC Breakers for HVDC Multiterminal Grids Using Wavelet Transform," *IEEE Systems Journal*, vol. 14, no. 1, pp. 1069–1079, 2020.

[98] B. Li, Y. Li, J. He, B. Li, S. Liu, B. Liu, and L. Xu, "An Improved Transient Traveling-Wave Based Direction Criterion for Multi-Terminal HVDC Grid," *IEEE Transactions on Power Delivery*, vol. 35, no. 5, pp. 2517–2529, 2020.

[99] Y. M. Yeap, N. Geddada, K. Satpathi, and A. Ukil, "Time- and Frequency-Domain Fault Detection in a VSC-Interfaced Experimental DC Test System," *IEEE Transactions on Industrial Informatics*, vol. 14, no. 10, pp. 4353–4364, 2018.

[100] K. A. Saleh, A. Hooshyar, E. F. El-Saadany, and H. H. Zeineldin, "Protection of High-Voltage DC Grids Using Traveling-Wave Frequency Characteristics," *IEEE Systems Journal*, vol. 14, no. 3, pp. 4284–4295, 2020.

[101] V. Albernaz Lacerda, R. M. Monaro, D. Campos-Gaona, D. V. Coury, and O. Anaya-Lara, "Distance protection algorithm for multiterminal HVDC systems using the Hilbert–Huang transform," *IET Generation, Transmission & Distribution*, vol. 14, no. 15, pp. 3022–3032, 2020.

[102] D. Li, A. Ukil, K. Satpathi, and Y. M. Yeap, "Hilbert–Huang Transform Based Transient Analysis in Voltage Source Converter Interfaced Direct Current System," *IEEE Transactions on Industrial Electronics*, vol. 68, no. 11, pp. 11 014–11 025, 2021.

[103] Y. Zhang, N. Tai, and B. Xu, "Fault Analysis and Traveling-Wave Protection Scheme for Bipolar HVDC Lines," *IEEE Transactions on Power Delivery*, vol. 27, no. 3, pp. 1583–1591, 2012.

[104] S. Yang, W. Xiang, R. Li, X. Lu, W. Zuo, and J. Wen, "An Improved DC Fault Protection Algorithm for MMC HVDC Grids Based on Modal-Domain Analysis," *IEEE Journal of Emerging and Selected Topics in Power Electronics*, vol. 8, no. 4, pp. 4086–4099, 2020.

[105] X. Yu and L. Xiao, "A DC Fault Protection Scheme for MMC-HVDC Grids Using New Directional Criterion," *IEEE Transactions on Power Delivery*, vol. 36, no. 1, pp. 441–451, 2021.

[106] Q. Yang, S. Le Blond, R. Aggarwal, Y. Wang, and J. Li, "New ANN method for multi-terminal HVDC protection relaying," *Electric Power Systems Research*, vol. 148, pp. 192–201, 2017.

[107] R. Bertho, V. A. Lacerda, R. M. Monaro, J. C. M. Vieira, and D. V. Coury, "Selective Nonunit Protection Technique for Multiterminal VSC-HVDC Grids," *IEEE Transactions on Power Delivery*, vol. 33, no. 5, pp. 2106–2114, 2018.

[108] N. Tong, Z. Tang, Y. Wang, C. S. Lai, and L. L. Lai, "Semi AI-based protection element for MMC-MTDC using local-measurements," *International Journal of Electrical Power & Energy Systems*, vol. 142, p. 108310, 2022.

[109] S. Jamali and S. S. Mirhosseini, "Protection of transmission lines in multi-terminal HVDC grids using travelling waves morphological gradient," *International Journal of Electrical Power & Energy Systems*, vol. 108, pp. 125–134, 2019.

[110] S. S. Mirhosseini, S. Jamali, and M. Popov, "Non-unit protection method for long transmission lines in MTDC grids," *IET Generation, Transmission & Distribution*, vol. 15, no. 11, pp. 1674–1687, 2021.

[111] L. Liu, Z. Liu, M. Popov, P. Palensky, and M. A. M. M. van der Meijden, "A Fast Protection of Multi-Terminal HVDC System Based on Transient Signal Detection," *IEEE Transactions on Power Delivery*, vol. 36, no. 1, pp. 43–51, 2021.

[112] C. Zhang, G. Song, and X. Dong, "A Novel Traveling Wave Protection Method for DC Transmission Lines Using Current Fitting," *IEEE Transactions on Power Delivery*, vol. 35, no. 6, pp. 2980–2991, 2020.

[113] C. Zhang, G. Song, T. Wang, L. Wu, and L. Yang, "Non-unit Traveling Wave Protection of HVDC Grids Using Levenberg–Marquart Optimal Approximation," *IEEE Transactions on Power Delivery*, vol. 35, no. 5, pp. 2260–2271, 2020.

[114] C. Zhang, G. Song, T. Wang, and X. Dong, "An Improved Non-Unit Traveling Wave Protection Method With Adaptive Threshold Value and Its Application in HVDC Grids," *IEEE Transactions on Power Delivery*, vol. 35, no. 4, pp. 1800–1811, 2020.

[115] H. Shu, G. Wang, X. Tian, S. Lei, X. Jiang, and Z. Bo, "Single-ended protection method of MMC-HVDC transmission line based on random matrix theory," *International Journal of Electrical Power & Energy Systems*, vol. 142, p. 108299, 2022.

[116] B. Li, J. He, Y. Li, and B. Li, "A review of the protection for the multi-terminal VSC-HVDC grid," *Protection and Control of Modern Power Systems*, vol. 4, no. 21, 2019.

[117] X. Zhang, M. Radwan, and S. P. Azad, "Modified distance protection of transmission lines originating from DFIG-based WPPs by considering the impact of fault-induced rotor frequency and LVRT requirements," *International Journal of Electrical Power & Energy Systems*, vol. 147, p. 108911, 2023.

[118] M. Radwan and S. P. Azad, "An Outlier-Based Single-Ended Protection Scheme for Multi-Terminal MMC-HVDC Grids Based on Hilbert-Huang Transform," *IEEE Transactions on Power Delivery*, vol. 39, no. 6, pp. 3535–3546, 2024.

[119] M. Radwan and S. P. Azad, "A single-ended protection scheme for multi-terminal HVDC grids based on Hilbert-Huang Transform," in *2023 IEEE Power & Energy Society General Meeting (PESGM)*, 2023, pp. 1–5.

[120] D. Li, A. Ukil, K. Satpathi, and Y. M. Yeap, "Improved s transform-based fault detection method in voltage source converter interfaced dc system," *IEEE Transactions on Industrial Electronics*, vol. 68, no. 6, pp. 5024–5035, 2021.

[121] N. E. Huang *et al.*, "The empirical mode decomposition and the Hilbert spectrum for nonlinear and non-stationary time series analysis," *Proceedings of the Royal Society of London. Series A: Mathematical, Physical and Engineering Sciences*, vol. 454, no. 1971, pp. 903–995, 1998.

[122] N. E. Huang and S. Shen, *Hilbert-Huang transform and its applications*, 2nd ed. World Scientific, 2014, vol. 16.

[123] M. Farshad and M. Karimi, "A Signal Segmentation Approach to Identify Incident/Reflected Traveling Waves for Fault Location in Half-Bridge MMC-HVdc Grids," *IEEE Transactions on Instrumentation and Measurement*, vol. 71, pp. 1–9, 2022.

[124] L. Tang, X. Dong, S. Shi, and B. Wang, "Analysis of the characteristics of fault-induced travelling waves in MMC-HVDC grid," *The Journal of Engineering*, vol. 2018, no. 15, pp. 1349–1353, 2018.

[125] C. R. Paul, *Analysis of Multiconductor Transmission Lines*. IEEE, 2008, ch. Time-Domain Analysis of Two-Conductor Lines, pp. 343–469.

[126] R. E. Torres-Olguin, "DC faults in HVDC: Detection, identification, and handling," in *Modeling, Operation, and Analysis of DC Grids*, A. Garcés, Ed. Academic Press, 2021, pp. 27–67.

[127] N. E. Huang and Z. Wu, "A review on Hilbert-Huang transform: Method and its applications to geophysical studies," *Reviews of Geophysics*, vol. 46, no. 2, 2008.

[128] W. Rebizant, J. Szafran, and A. Wiszniewski, *Digital signal processing in power system protection and control*. Springer, 2011.

[129] S. Yu, X. Wang, and X.-P. Zhang, "A sensitive single-end DC line fault detection method for MMC-HVDC grids using reactor voltage ratio," *International Journal of Electrical Power & Energy Systems*, vol. 148, p. 108953, 2023.

[130] K.-V. Yuen and G. A. Ortiz, "Outlier detection and robust regression for correlated data," *Computer Methods in Applied Mechanics and Engineering*, vol. 313, pp. 632–646, 2017.

[131] H. Wang, M. J. Bah, and M. Hammad, "Progress in Outlier Detection Techniques: A Survey," *IEEE Access*, vol. 7, pp. 107 964–108 000, 2019.

[132] S. Ghashghaei and M. Akhbari, "Fault detection and classification of an HVDC transmission line using a heterogenous multi-machine learning algorithm," *IET Generation, Transmission & Distribution*, vol. 15, no. 16, pp. 2319–2332, 2021.

[133] W. Rebizant, J. Szafran, and A. Wiszniewski, *Hardware and Functional Development of Protection Devices and Systems*. London: Springer London, 2011, pp. 13–27.

[134] M. Li, J. Ning, J. He, S. Mirsaeidi, and M. Nie, "Initial traveling wave waveform-based single-ended setting-less protection for VSC-MTDC grids," *CSEE Journal of Power and Energy Systems*, pp. 1–12, 2024.

[135] A. Bhandari, H. Yin, Y. Liu, W. Yao, and L. Zhan, "Real-Time Signal-to-Noise Ratio Estimation by Universal Grid Analyzer," in *2019 International Conference on Smart Grid Synchronized Measurements and Analytics (SGSMA)*, 2019, pp. 1–6.

[136] "IEEE Recommended Practice for Monitoring Electric Power Quality," *IEEE Std 1159-2019*, pp. 1–98, 2019.

[137] CIGRE Joint Working Group B4/A3.80, "Technical Brochure 873: Design, test and application of HVDC circuit breakers," 2022, accessed: 2024-07-07. [Online]. Available: https://www.e-cigre.org/publications/detail/873-design-test-and-application-of-hvdc-circuit-breakers.html

[138] Hitachi Review. Control and Protection for HVDC: An introduction to MACH. Accessed: 2024-07-07. [Online]. Available: https://www.hitachi.com/rev/archive/2023/r2023_04/04a04/index.html

[139] Y. Nie, Y. Liu, R. Pan, D. Lu, and R. Fan, "Convolution Based Time Domain Fault Location Method for Lines in MMC-HVDC Grids with Distributed and Frequency Dependent Line Model," *IEEE Transactions on Power Delivery*, pp. 1–14, 2023.

[140] M. Radwan and S. P. Azad, "A novel double-ended fault location identification scheme for multi-terminal HVDC grids based on Hilbert-Huang transform," in *2024 IEEE Power & Energy Society General Meeting (PESGM)*, 2024, pp. 1–5.

[141] R. Itiki, M. Manjrekar, S. G. Di Santo, and L. F. M. Machado, "Technical feasibility of Japan-Taiwan-Philippines HVdc interconnector to the Asia Pacific Super Grid," *Renewable and Sustainable Energy Reviews*, vol. 133, p. 110161, 2020.

[142] B. Wang, Y. Liu, D. Lu, R. Pan, and K. Yue, "Multi-section frequency dependent line model enabled underground cable fault location in MMC-HVDC grids using dynamic state estimation," *International Journal of Electrical Power & Energy Systems*, vol. 153, p. 109322, 2023.

[143] C. Zhang, G. Song, T. Wang, and L. Yang, "Single-Ended Traveling Wave Fault Location Method in DC Transmission Line Based on Wave Front Information," *IEEE Transactions on Power Delivery*, vol. 34, no. 5, pp. 2028–2038, 2019.

[144] M. Radwan and S. P. Azad, "Protection of Multi-Terminal HVDC Grids: A Comprehensive Review," *Energies*, vol. 15, no. 24, 2022.

[145] Q. Huai, K. Liu, A. Hooshyar, H. Ding, K. Chen, and Q. Liang, "Single-ended line fault location method for multi-terminal HVDC system based on optimized variational mode decomposition," *Electric Power Systems Research*, vol. 194, p. 107054, 2021.

[146] V. P. Dardengo, J. F. Fardin, and M. C. de Almeida, "Single-terminal fault location in HVDC lines with accurate wave velocity estimation," *Electric Power Systems Research*, vol. 194, p. 107057, 2021.

[147] J. C. C. Vieira, D. Fernandes, W. L. A. Neves, and F. V. Lopes, "Fault diagnosis in bipolar HVDC systems based on traveling wave theory by monitoring data from one terminal," *Electric Power Systems Research*, vol. 223, p. 109594, 2023.

[148] X. Zhu, S. Li, Y. Guo, X. Chen, C. He, and J. Deng, "Novel wavefront detection and fault location method based on Hilbert-Huang transform for long HVDC transmission lines," *Electric Power Systems Research*, vol. 211, p. 108213, 2022.

[149] W. Chen, D. Wang, D. Cheng, F. Qiao, X. Liu, and M. Hou, "Novel travelling wave fault location principle based on frequency modification algorithm," *International Journal of Electrical Power & Energy Systems*, vol. 141, p. 108155, 2022.

[150] D. Wang and M. Hou, "Travelling wave fault location algorithm for LCC-MMC-MTDC hybrid transmission system based on Hilbert-Huang transform," *International Journal of Electrical Power & Energy Systems*, vol. 121, p. 106125, 2020.

[151] K. H. Ali, A. A. Aboushady, S. Bradley, M. E. Farrag, and S. A. Abdel Maksoud, "An Industry Practice Guide for Underground Cable Fault-Finding in the Low Voltage Distribution Network," *IEEE Access*, vol. 10, pp. 69 472–69 489, 2022.

[152] N. A. Belda, R. P. P. Smeets, and R. M. Nijman, "Experimental Investigation of Electrical Stresses on the Main Components of HVDC Circuit Breakers," *IEEE Transactions on Power Delivery*, vol. 35, no. 6, pp. 2762–2771, 2020.

[153] M. Abedrabbo and D. Van Hertem, "A primary and backup protection algorithm based on voltage and current measurements for HVDC grids," in *International High Voltage Direct Current Conference (HVDC 2016)*, 2016, pp. 854–860.

[154] S. Pirooz Azad, W. Leterme, and D. Van Hertem, "Fast breaker failure backup protection for HVDC grids," *Electric Power Systems Research*, vol. 138, pp. 99–105, 2016.

[155] W. Leterme, S. Pirooz Azad, and D. Van Hertem, "A Local Backup Protection Algorithm for HVDC Grids," *IEEE Transactions on Power Delivery*, vol. 31, no. 4, pp. 1767–1775, 2016.

[156] J. Sun, M. Saeedifard, and A. P. S. Meliopoulos, "Backup Protection of Multi-Terminal HVDC Grids Based on Quickest Change Detection," *IEEE Transactions on Power Delivery*, vol. 34, no. 1, pp. 177–187, 2019.

[157] M. Wang, M. Zaja, J. Beerten, D. Jovcic, and D. Van Hertem, "Backup Protection Algorithm for Failures in Modular DC Circuit Breakers," *IEEE Transactions on Power Delivery*, vol. 36, no. 6, pp. 3580–3589, 2021.

[158] M. J. Pérez-Molina, D. M. Larruskain, P. Eguia, and O. Abarrategi, "Circuit Breaker Failure Protection Strategy for HVDC Grids," *Energies*, vol. 14, no. 14, 2021.

[159] W. Chen, R. Zeng, J. He, Y. Wu, X. Wei, T. Fang *et al.*, "Development and prospect of direct-current circuit breaker in China," *High Voltage*, vol. 6, no. 1, pp. 1–15, 2021.

[160] J. Gao, H. Yuan, A. Yang, M. Rong, R. Dai, Z. Peng, and X. Wang, "A Fault Detection Method Based on Successive Variational Mode Decomposition for the Energy Absorption Branch of Modular DC Circuit Breakers," *IEEE Transactions on Power Delivery*, vol. 38, no. 5, pp. 3688–3700, 2023.

[161] J. He, Z. Xie, B. Li, Y. Li, H. Lyu, and Y. Sheng, "A novel directional pilot protection independent of line parameters and boundary elements for MMC-HVDC grid," *International Journal of Electrical Power & Energy Systems*, vol. 150, p. 109094, 2023.

[162] PSCAD Knowledge Base. HVDC VSC transmission interconnecting two AC systems. Accessed: 2024-08-20. [Online]. Available: https://www.pscad.com/knowledge-base/article/222

[163] D. Tzelepis, V. Psaras, E. Tsotsopoulou, S. Mirsaeidi, A. Dyśko, Q. Hong *et al.*, "Voltage and Current Measuring Technologies for High Voltage Direct Current Supergrids: A Technology Review Identifying the Options for Protection, Fault Location and Automation Applications," *IEEE Access*, vol. 8, pp. 203 398–203 428, 2020.

[164] F. Savi, J. Harikumaran, D. Barater, G. Buticchi, C. Gerada, and P. Wheeler, "Femtocore: An Application Specific Processor for Vertically Integrated High Performance Real-Time Controls," *IEEE Open Journal of the Industrial Electronics Society*, vol. 2, pp. 479–488, 2021.

[165] T. Vince, M. Sroka, B. Fecko, B. Peryvertailo, R. Yatsiuk, and I. Anna, "A Universal DSP Module for Simultaneous Multiple RS232 Communication with Synchronous Measurements Reading Capability," in *2023 IEEE 5th International Conference on Modern Electrical and Energy System (MEES)*, 2023, pp. 1–5.

[166] Z. Wang, H. Li, H. Jin, H. Liu, Y. Liang, and G. Wang, "Pilot protection for flexible HVDC transmission lines based on transient voltage ratio characteristics," *International Journal of Electrical Power & Energy Systems*, vol. 162, p. 110263, 2024.

[167] R. H. Chandio, F. A. Chachar, J. B. Soomro, J. A. Ansari, H. M. Munir, H. M. Zawbaa, and S. Kamel, "Control and protection of MMC-based HVDC systems: A review," *Energy Reports*, vol. 9, pp. 1571–1588, 2023.

[168] M. Radwan and S. P. Azad, "A Fast and Setting-Less Breaker Failure Backup Protection Scheme for Multi-Terminal HVDC Grids," *IEEE Transactions on Power Delivery*, vol. 39, no. 6, pp. 3525–3534, 2024.

[169] M. J. Pérez-Molina, D. M. Larruskain, P. Eguía, and V. Valverde Santiago, "Local Derivative-Based Fault Detection for HVDC Grids," *IEEE Transactions on Industry Applications*, vol. 58, no. 2, pp. 1521–1530, 2022.

[170] S. Luo, X. Dong, S. Shi, and B. Wang, "A Directional Protection Scheme for HVDC Transmission Lines Based on Reactive Energy," *IEEE Transactions on Power Delivery*, vol. 31, no. 2, pp. 559–567, 2016.

[171] T. Cui, X. Dong, Z. Bo, and A. Juszczyk, "Hilbert-Transform-Based Transient/Intermittent Earth Fault Detection in Noneffectively Grounded Distribution Systems," *IEEE Transactions on Power Delivery*, vol. 26, no. 1, pp. 143–151, 2011.

[172] Q. Huai, K. Liu, L. Qin, X. Liao, S. Zhu, Y. Li, and H. Ding, "Backup-Protection Scheme for Multi-Terminal HVDC System Based on Wavelet-Packet-Energy Entropy," *IEEE Access*, vol. 7, pp. 49 790–49 803, 2019.

[173] M. Banafer and S. R. Mohanty, "A travelling wave based primary and backup protection for MMC-MTDC transmission system using morphological un-decimated wavelet scheme," *Electric Power Systems Research*, vol. 212, p. 108367, 2022.

[174] Y. Zhang, S. Wang, T. Liu, X. Li, H. Beng Gooi, A. M. Ghias, R. Xu, and T. Chang, "A backup protection scheme for the transmission lines based on the directional traveling wave and waveform similarity," *International Journal of Electrical Power & Energy Systems*, vol. 147, p. 108864, 2023.

[175] F. Deng, Z. Zhang, H. Zhong, X. Zeng, Y. Huang, Z. Zeng, and S. Feng, "Single-end traveling wave protection method in flexible DC transmission line based on dominant frequency attenuation characteristics," *International Journal of Electrical Power & Energy Systems*, vol. 152, p. 109220, 2023.

[176] K. Chen, Q. Hong, M. Li, J. He, Y. Tang, and C. D. Booth, "Polarity of current area based active injection protection scheme for hybrid MMC-HVDC grids," *International Journal of Electrical Power & Energy Systems*, vol. 152, p. 109261, 2023.

[177] Y. Liang, L. Jiang, H. Li, and G. Wang, "A novel voltage projection component-based protection scheme for hybrid multi-terminal HVDC transmission lines," *International Journal of Electrical Power & Energy Systems*, vol. 153, p. 109334, 2023.

[178] K. Zhao, M. A. Wulder, T. Hu, R. Bright, Q. Wu, H. Qin, Y. Li, E. Toman, B. Mallick, X. Zhang, and M. Brown, "Detecting change-point, trend, and seasonality in satellite time series data to track abrupt changes and nonlinear dynamics: A Bayesian ensemble algorithm," *Remote Sensing of Environment*, vol. 232, p. 111181, 2019.

[179] T. M. Fragoso, W. Bertoli, and F. Louzada, "Bayesian Model Averaging: A Systematic Review and Conceptual Classification," *International Statistical Review*, vol. 86, no. 1, pp. 1–28, 2018.

[180] W. M. Bolstad, *Understanding computational Bayesian statistics*. John Wiley & Sons, 2009, vol. 644.

[181] C. Zhang, G. Song, A. S. Meliopoulos, and X. Dong, "Setting-Less Nonunit Protection Method for DC Line Faults in VSC-MTdc Systems," *IEEE Transactions on Industrial Electronics*, vol. 69, no. 1, pp. 495–505, 2022.

[182] C. Zhang, B. Chen, J. Yan, and G. Song, "Setting-Less Pilot Protection for MTDC Systems with Weak or No Line Boundary Based on Model Differences Between Forward and Backward Faults," *IEEE Journal of Emerging and Selected Topics in Power Electronics*, 2024.

[183] P. K. Gupta and S. R. Samantaray, "Enhanced primary protection scheme for MTDC network using modified linear quadratic score," *Electric Power Systems Research*, vol. 242, p. 111418, 2025.

[184] S. Song, J. Lei, W. Ma, and Y. Wang, "Kalman Filter Based Detection Scheme for DC-Link Voltage Measurement Faults in MMC-HVDC Systems," *IEEE Transactions on Power Electronics*, vol. 40, no. 3, pp. 4199–4212, 2025.

[185] OPAL-RT Technologies. OP5700 System Description. Accessed: 2025-03-04. [Online]. Available: https://opal-rt.atlassian.net/wiki/spaces/PHDGD/pages/144630756/OP5700+System+Description

[186] dSPACE. MicroLabBox: Compact prototyping unit for the laboratory. Accessed: 2025-03-05. [Online]. Available: https://www.dspace.com/en/pub/home/products/hw/microlabbox.cfm

[187] dSPACE. ControlDesk: Experiment and Instrumentation Software for ECU Development. Accessed: 2025-03-05. [Online]. Available: https://www.dspace.com/en/pub/home/products/sw/experimentandvisualization/controldesk.cfm

APPENDICES

Appendix A

List of Publications

Below is a list of publications by the author completed during their doctoral studies.

A.1 Peer-Reviewed Journal Articles

[1] M. Radwan and S. P. Azad, "A Fast and Setting-Less Breaker Failure Backup Protection Scheme for Multi-Terminal HVDC Grids," *IEEE Transactions on Power Delivery*, vol. 39, no. 6, pp. 3525-3534, 2024.

[2] M. Radwan and S. P. Azad, "An Outlier-Based Single-Ended Protection Scheme for Multi-Terminal MMC-HVDC Grids Based on Hilbert-Huang Transform," *IEEE Transactions on Power Delivery*, vol. 39, no. 6, pp. 3535-3546, 2024.

[3] M. Radwan and S. P. Azad, "Protection of Multi-Terminal HVDC Grids: A Comprehensive Review," *Energies*, vol. 15, no. 24, 2022.

[4] X. Zhang, M. Radwan, and S. P. Azad, "Modified distance protection of transmission lines originating from DFIG-based WPPs by considering the impact of fault-induced rotor frequency and LVRT requirements," *International Journal of Electrical Power & Energy Systems*, vol. 147, no. 108911, 2023.

A.2 Conference Proceedings

[1] M. Radwan and S. P. Azad, "A novel double-ended fault location identification scheme for multi-terminal HVDC grids based on Hilbert-Huang transform," *2024 IEEE Power & Energy Society General Meeting (PESGM)*, Seattle, WA, USA, 2024.

[2] M. Radwan and S. P. Azad, "A single-ended protection scheme for multi-terminal HVDC grids based on Hilbert-Huang Transform," *2023 IEEE Power & Energy Society General Meeting (PESGM)*, Orlando, FL, USA, 2023.

A.3 Submitted Journal Articles

[1] M. Radwan and S. P. Azad, "A Statistical Approach for Relay Failure Backup Protection in Multi-terminal HVDC Grids," *IEEE Transactions on Power Delivery* (Under Review).

A.4 Submitted Conference Papers

[1] M. Radwan and S. P. Azad, "DC Breaker Failure Detection Scheme in Multi-Terminal HVDC Grids," *2025 IEEE Power & Energy Society General Meeting* (Accepted).